



Synthesis of amphiphilic linear and comb-like terpolymers with epoxidized double-bond and their self-assembly into magnetic vesicles with shape fixing ability under UV cross-linking

Diana Kazaryan

► To cite this version:

Diana Kazaryan. Synthesis of amphiphilic linear and comb-like terpolymers with epoxidized double-bond and their self-assembly into magnetic vesicles with shape fixing ability under UV cross-linking. Polymers. Université de Bordeaux, 2023. English. NNT : 2023BORD0225 . tel-04401363

HAL Id: tel-04401363

<https://theses.hal.science/tel-04401363>

Submitted on 17 Jan 2024

HAL is a multi-disciplinary open access archive for the deposit and dissemination of scientific research documents, whether they are published or not. The documents may come from teaching and research institutions in France or abroad, or from public or private research centers.

L'archive ouverte pluridisciplinaire **HAL**, est destinée au dépôt et à la diffusion de documents scientifiques de niveau recherche, publiés ou non, émanant des établissements d'enseignement et de recherche français ou étrangers, des laboratoires publics ou privés.

THÈSE PRÉSENTÉE
POUR OBTENIR LE GRADE DE
DOCTEUR DE
L'UNIVERSITÉ DE BORDEAUX

ÉCOLE DOCTORALE

SPÉCIALITÉ: Polymères

Par Diana KAZARYAN

**SYNTHÈSE DE TERPOLYMÈRES AMPHIPHILES LINÉAIRES ET COMB-
LIKE À DOUBLE LIAISON ÉPOXYDÉE ET LEUR AUTO-ASSEMBLAGE
EN VÉSICULES MAGNÉTIQUES AVEC CAPACITÉ DE FIXATION DE
FORME SOUS RÉTICULATION UV**

**SYNTHESIS OF AMPHIPHILIC LINEAR AND COMB-LIKE TERPOLYMERS WITH
EPOXIDIZED DOUBLE-BOND AND THEIR SELF-ASSEMBLY INTO MAGNETIC
VESICLES WITH SHAPE FIXING ABILITY UNDER UV CROSS-LINKING**

Sous la direction de : Olivier SANDRE et Frédéric PERUCH

Soutenue le 03/10/2023

Membres du jury :

M. SANDRE, Olivier
M. PERUCH, Frédéric
Mme BRULET Annie
Mme MINGOTAUD Anne Françoise
Mme GIGOUX Véronique
M. LECOMMANDOUX Sébastien
M. MORNET Stéphane
Mme MRAKOVIĆ, Ana

Directeur de recherche CNRS, Université de Bordeaux
Directeur de recherche CNRS, Université de Bordeaux
Ingénieure de recherche CNRS, Université Paris Saclay
Chargée de recherche CNRS, Université de Toulouse
Chargée de recherche INSERM Université de Toulouse
Professeur des universités, Université de Bordeaux
Directeur de recherche CNRS, Université de Bordeaux
Senior research associate, University of Belgrade

Directeur de thèse
Directeur de thèse
Rapporteuse
Rapporteuse
Examinatrice
Président
Invité
Invitée

Abstract:

Magnetic polymersomes containing iron oxide magnetic nanoparticles (IONPs) have been studied mainly in the magnetic hyperthermia concept, as potential anticancer treatment. On the other hand, the use of magnetic polymersomes as mechanical actuators capable of inducing cell apoptosis by strong membrane distortion from within has not been investigated.

Herein, the above hypothesis is explored by the synthesis of a new model system. To achieve mechanical destruction, it is imperative that an anisotropic morphology is attained in order to exert a torque on the membranes when applying a rotating magnetic field (RMF). This work reports the synthesis and investigation of ellipsoid like magnetic polymersomes capable of rotating around their axis after the application of a RMF of low frequency (LF). Specifically, hydrophobically modified IONPs are embedded in the hydrophobic membrane of graft and triblock copolymers designed to self-assemble into a vesicular shape. The graft copolymer consists of a poly(ethylene glycol)-block-poly(amino trimethyl carbonate)(PEG-*b*-PATC) diblock copolymer that has been further modified via a “grafting to” process, using reductive amination to attach a carbonyl telechelic 1,4-cis-poly(isoprene) oligomer, resulting in the graft copolymer PEG-*b*-(PTDOC-*g*-PI). While the triblock copolymer consists of a diblock copolymer poly(ethylene glycol)-block-poly(trimethylene carbonate) that further modified via an esterification reaction with a carboxyl modified poly(isoprene). The final copolymers are modified once more by partial epoxidation of the PI block, which allows the further cross-linking step.

After the formation of the vesicles is confirmed, a static magnetic field is applied which aligns the IONPs in linear aggregates in its direction. The alignment of the IONPs prompts a morphological shift of the polymersomes, due to the fluid state of the hydrophobic membrane, resulting in an ellipsoid like morphology. The final morphology is permanently stabilized by photo-crosslinking of the hydrophobic membrane via a ring-opening polymerization of the epoxides.

Résumé:

Les polymersomes magnétiques contenant des nanoparticules magnétiques d'oxyde de fer (IONP) ont été étudiés principalement dans le concept d'hyperthermie magnétique, en tant que traitement anticancéreux potentiel. En revanche, l'utilisation de polymersomes magnétiques comme actionneurs mécaniques capables d'induire l'apoptose cellulaire par une forte distorsion membranaire de l'intérieur n'a pas été étudiée.

Ici, l'hypothèse ci-dessus est explorée par la synthèse d'un nouveau système modèle. Pour parvenir à une destruction mécanique, il est impératif d'atteindre une morphologie anisotrope afin d'exercer un couple sur les membranes lors de l'application d'un champ magnétique tournant (RMF). Ce travail rapporte la synthèse et l'étude de polymersomes magnétiques de type ellipsoïde capables de tourner autour de leur axe après l'application d'un RMF de basse fréquence (LF). Plus précisément, les IONP modifiés de manière hydrophobe sont intégrés dans la membrane hydrophobe des copolymères greffés et triblocs conçus pour s'auto-assembler en une forme vésiculaire. Le copolymère greffé est constitué d'un copolymère dibloc poly(éthylène glycol)-*b*-poly(amino triméthyl carbonate) (PEG-*b*-PATC) qui a été encore modifié via un processus de « greffage sur », en utilisant une amination réductrice pour attacher un carbonyle téléchélique Oligomère 1,4-cis-poly(isoprène), aboutissant au copolymère graft PEG-*b*-(PTDOC-*g*-PI). Alors que le copolymère tribloc est constitué d'un copolymère diblock poly(éthylène glycol)-*b*-poly(triméthylène carbonate) qui est ensuite modifié via une réaction d'estérification avec un poly(isoprène) modifié par carboxyle. Les copolymères finaux sont à nouveau modifiés par époxydation partielle du bloc PI, ce qui permet une nouvelle étape de réticulation.

Une fois la formation des vésicules confirmée, un champ magnétique statique est appliqué qui aligne les agrégats linéaires IONP dans sa direction. L'alignement des IONP provoque un changement morphologique des polymersomes, en raison de l'état fluide de la membrane hydrophobe, résultant en une morphologie de type ellipsoïde. La morphologie finale est définitivement stabilisée par photo-réticulation de la membrane hydrophobe via une polymérisation par ouverture de cycle du bloc poly(isoprène) époxydé.

Acknowledgement:

These past almost four years have been some of the most interesting years of my life and it is all thanks to the opportunities this project has given me. I would like to thank so many people who have contributed either scientifically or personally throughout all this process of the PhD.

First and foremost, I would like to thank the financing of the ANR MAVERICK 2019 project which has allowed this project to be explored. I would also like to thank my jury that has agreed to read my work and attend my presentation, I truly appreciate it.

I would like to focus this part on all the people that I have met in LCPO over these past three and a half years. First, I would like to thank my two supervisors, who entrusted me with their vision. Oliver Sandre, thank you so much, for accepting me to work on this project and for your immense help and support during the thesis and the writing process. Thank you for your optimism, which as you know is not my strong suit, thus it was certainly needed when things seemed difficult. Finally, I would like to thank you for allowing me to explore different pathways during the project and trusting me to figure things out, I learned a lot.

I would like to thank my second supervisor, Frédéric Peruch for trusting me with this project as well. I would like to thank you for all your help during this thesis, you always had the right answer or the right question whenever I was unsure of what went wrong or right. Thank you for your guidance, patience, and support. I learned a lot from you as well and will always appreciate it.

My sincere acknowledgement goes to the staff of the Bordeaux Institute of Imaging (BIC) for teaching me the electron microscope handling, especially Sabrina Lacomme, Melina Petrel and Dr Etienne Gontier, who are also partners of the MAVERICK project.

I would like to thank the permanent people of the LCPO who I may not have worked with directly but got to know in the lab. I would like to first thank Sébastien Lecommandoux as the director of the LCPO who allowed me to work in the group. Colin Bonduelle, Elisabeth Garanger, Christophe Schatz and Angela Mutschler for all the interesting scientific discussions, your insights and help whenever I needed it. Especially Colin and Christophe who were always available when I had questions, thank you so much.

I want to thank Amelie Vax-Webber for all her help with my SEC analysis but also for all her help during my numerous accidents! I would like to thank Anne-Laure Wirotius, Cédric Le Coz, Paul Marque and Sylvain Bourasseau for their help with the characterizations of my work. Dominique Richard, Séverine Saint-Drenant, Corinne Goncalves-de-Carvalho, Claude Le

Pierres and Olivier Fihey for all their help on the administrative side. Finally, I would especially like to thank Léna Alembik who has helped me tremendously with NMR experiments.

I would also like to thank my labmates from the other teams, where I have met some amazing people who I will cherish even after I leave the LCPO. Specifically, Chloé Pascouau, thank you for your support throughout these three years, for your positivity and friendship. Pablo Gómez Argudo thank you for bringing the Mediterranean vibe to the lab and for the incredible sangria that you taught us how to properly make.

I would like to thank my labmates from Team 3 either the ones that are still here or the ones that have already graduated, who really made my PhD years filled with joy, funny moments, and enormous support. Dongxu Zhou, Sifan, Yue Ye, Yue Pei, Sarah, Antoine, Clémence, Julien, Romain, Pierre, Matthiew, Fanny, Hang, Tim, Martin, Esra, Florian, Manon, Yasmina, Safiya, Leslie, Hannah, Marie, Nadia, Johanna and Eloise thank you for all the great memories guys. Specifically, I would like to thank Anouk my “office-mate” for the positive vibe she brought to the office either with her incredible decorating skills or her kind gestures, Elise aka “MIT” thank you for being the best French teacher I could ever ask for (even if I was a terrible student), Mostafa thank you for your snarky comments that made me laugh and for all the support and help you have given me and Rosanna thank you for always affirming that while I am an old lady I am not alone in the struggle!

A special thank you to Megi, my neighbor both in countries but also in the office, who has supported me whenever I needed to share my disappointments or my successes. Thank you for all the great talks we have had. I will cherish them always. I would also like to thank my friends Pedro Salas Ambrosio and Vusala Ibrahimova who became my instant family in the LCPO and shared incredible moments and adventures with.

I would also like to thank my friends and second chosen family from Greece, who might have been away from me but were always there. My dear Lida, Katerina, Niki, Dimitra and Maria, thank you for being in my life. We have managed to have even more adventures while living in different countries and I cannot wait to see what else we will do in the future. I am so proud of all of you and your support has meant a lot for me!

Finally, I want to thank my family, specifically my mother and grand-mother, two of the most incredible and strong women I know. Thank you so much for all that you have done for me and for helping me to achieve whatever I wanted. Thank you for being with me no matter what, I would not have been who I am today without you, your love, and your constant belief in me.

Table of contents:

Abstract:	2
Résumé:	3
Acknowledgement:	4
List of abbreviations:	10
General Introduction:	12
CHAPTER I: BIBLIOGRAPHIC REVIEW	16
Introduction	18
Polymersomes	18
Magnetic polymersomes:	27
How Nanoparticle shape affects its fate in the biological systems:	33
Protein Corona formation:	33
Phagocytes and Target morphology:	34
Circulation time and cellular uptake:	36
Anisotropic morphology and drug delivery	42
Cell disruption via Mechanical force:	49
Theoretical point of view:	49
Experimental literature on magneto-mechanical actuation:	55
Conclusion:	65
References:	66
CHAPTER II: SYNTHESIS OF GRAFT COPOLYMERS	76
Introduction:	78
Experimental Section:	80
Materials:	80
Methods:	80
Synthesis of heterotelechelic poly(isoprene) oligomer via “one-pot” degradation method	80
Synthesis of the <i>tert</i> -butyl-(1,3-dihydroxypropan-2-yl) carbamate (tBS)	81
Synthesis of the <i>tert</i> -butyl (2-oxo-1,3-dioxan-5-yl) carbamate monomer	82
Poly (ethylene glycol)- <i>block</i> -poly(<i>tert</i> -butyl -amino trimethylene carbonate) (PEG ₁₁₄ - <i>b</i> -PATC ₃₀)	82
Deprotection of PEG ₁₁₄ - <i>b</i> -PATC ₃₀	83
Reductive amination resulting into PEG ₁₁₄ - <i>b</i> -PATC ₂₀ - <i>g</i> -PI _x	83
Epoxidation of PEG ₁₁₄ - <i>b</i> -PATC ₂₀ - <i>g</i> -PI _x	84
Methods of characterization:	85

Results and discussion:.....	88
Graft copolymer synthesis and characterization.....	88
Synthesis of poly(isoprene) oligomer <i>via</i> “one-pot” degradation method	90
Poly(ethylene glycol)- <i>block</i> -poly(tert-butyl -amino trimethylene carbonate) (PEG- <i>b</i> -PBATC).....	92
Deprotection of PEG ₁₁₄ - <i>b</i> -PATC ₂₁ amino side-groups.....	97
Reductive amination for the synthesis of PEG- <i>b</i> -(PATC- <i>g</i> -PI)	99
Epoxidation of PEG ₁₁₄ - <i>b</i> -(PATC ₂₀ - <i>g</i> -PI _n) _m	108
Conclusion:.....	110
References:	111
Supplementary Information:.....	113
CHAPTER III: SYNTHESIS OF TRIBLOCK COPOLYMERS	116
Introduction:	118
Experimental Section:	120
Materials:.....	120
Methods:.....	120
PEG ₁₁₄ - <i>b</i> -PTMC _m block copolymer synthesis:.....	120
Synthesis of hetero-bifunctional poly(isoprene) <i>via</i> “one-pot” degradation method	121
Synthesis of carboxylic-ended bifunctional poly(isoprene)	122
Final synthesis of the PEG ₁₁₄ - <i>b</i> -PTMC _m - <i>b</i> -PI _n triblock copolymer	123
Epoxidation of the PEG ₁₁₄ - <i>b</i> -PTMC _m - <i>b</i> -PI _n double bonds.....	123
Methods of characterization:	125
Results and discussion:.....	127
Triblock copolymer synthesis and characterization:	127
Synthesis of PEG ₁₁₄ - <i>b</i> -PTMC _m by ring opening polymerization:	127
Synthesis of carboxylic end-functionalized poly(isoprene):	133
Synthesis of PEG ₁₁₄ - <i>b</i> -PTMC _m - <i>b</i> -PI _n triblock polymer	137
Epoxidation of PEG ₁₁₄ - <i>b</i> -PTMC _m - <i>b</i> -PI _n :.....	145
Conclusions:	148
References:	149
Supplementary information	150
CHAPTER IV: SYNTHESIS OF HYDROPHOBIC IRON OXIDE NANOPARTICLES (IONPs)	155
Introduction:	157
Experimental Section:	159
Materials:.....	159

Methods:.....	159
Synthesis of hydrophobic IONPs functionalized with oleic acid:	159
Synthesis of carbonyl heterotelechelic poly (isoprene):	161
Synthesis of dopamine functionalized poly (isoprene):	161
Methods of characterization of hydrophobically modified IONPs:	162
Results and discussion:	164
Synthesis of IONPs <i>via</i> the polyol method and their hydrophobic functionalization with oleic acid:	164
Synthesis of carbonyl heterotelechelic poly(isoprene):	168
Synthesis of dopamine functionalized poly(isoprene):	170
Grafting of IONPs with dopamine functionalized poly (isoprene)	174
Conclusion:.....	185
References:	186
Supplementary information:	190
CHAPTER V: STUDY OF THE SELF-ASSEMBLY, CROSS-LINKING UNDER UV AND ELONGATION PROCESS OF MAGNETIC POLYMERSOMES	193
Introduction:	195
Experimental Section:	197
Materials:.....	197
Methods:.....	197
Self-assembly of copolymers with IONPs:	197
Methods of characterization:	199
Results and discussion:.....	203
Study of the self-assembly of graft copolymers PEG ₁₁₄ - <i>b</i> -(PATC- <i>g</i> -PI _x) _n - <i>co</i> -PATC _m	203
Self-assembly of graft copolymers PEG ₁₁₄ - <i>b</i> -(PATC- <i>g</i> -PI _x) _n - <i>co</i> -PATC _m a TEM study:	204
Self-assembly of graft copolymers with hydrophobically-coated IONPs:	205
Study of the Cross-linking process of the hydrophobic membrane:.....	214
Study of the behavior of polymersomes under a static magnetic field:.....	222
Triblock copolymers:	233
Study of the self-assembly of the triblock PEO- <i>b</i> -PTMC- <i>b</i> -PI copolymers:	233
Self-assembly of triblock copolymers with IONPs:	235
Study of the cross-linking process of the hydrophobic membrane of vesicles made of the triblock copolymer and their elongation under a static magnetic field:	238
DLS, SAXS and SANS study of magnetic polymersomes, out and in B_{DC} magnetic field	244

Structural study by X-ray (SAXS) and neutron (SANS) small angle scattering of grafted and triblock copolymers self-assemblies, with or without co-assembled IONPs:.....	244
Structural study by DLS, SAXS and SANS of the grafted and triblock copolymers co-assembled with hydrophobically coated IONPs under a static magnetic field:.....	258
References:	266
CONCLUSIONS AND PERSPECTIVES:	270
Conclusions and Perspectives:	272
References:	275

List of abbreviations:

DBU	1,8-diazabicyclo[5.4.0]undec-7-ene
DIC	<i>N,N'</i> -diisopropylcarbodiimide
DLS	Dynamic Light Scattering
DMF	Dimethylformamide
DOP	Dopamine
DOZY	Diffusion-ordered spectroscopy
DPTS	4-(Dimethylamino)pyridinium 4-toluenesulfonate
DMAP	4-(Dimethylamine)pyridine
ETN3	Triethylamine
FWR	Feed weight ratio
FT-IR	Fourier transform infrared spectroscopy
HMBC	Heteronuclear Multiple Bond Correlation
HSQC	Heteronuclear Single Quantum Coherence
IONPs	Iron oxide Nanoparticles
mCBPA	Meta-chloroperbenzoic acid
NMR	Nuclear Magnetic Resonance
OA	Oleic Acid
PAA- <i>b</i> -PS	Poly(acrylic acid)-block-poly(styrene)
PATC	Poly(amino trimethylene carbonate)
PBut- <i>b</i> -PGA	Poly(butadiene)-block-poly(glutamic acid)
PEG	Poly(ethylene) glycol
PEG- <i>b</i> -PATC	Poly(ethylene) glycol-block- Poly(amino trimethylene carbonate)
PEG- <i>b</i> -PBLG	Poly(ethylene) glycol-block

PEG- <i>b</i> -PTMC	Poly(ethylene) glycol-block-poly(trimethylene)carbonate
PEG- <i>b</i> -PTMC- <i>b</i> -PI	Poly(ethylene) glycol-block-poly(trimethylene)carbonate-graft-poly(isoprene)
PhI	Photo-Initiator
PI	Poly(isoprene)
PIDOP	Poly(isoprene) functionalized with Dopamine
PTMC	Poly(trimethylene)carbonate
PTMC- <i>b</i> -PGA	Poly(trimethylene)carbonate-block-Poly(glutamic acid)
ROP	Ring Opening Polymerization
SANS	Small Angle Neutron Scattering
SAXS	Small Angle X-ray Scattering
SEC	Size Exclusion Chromatography
TADC	<i>tert</i> -butyl (2-oxo-1,3-dioxan-5-yl) carbamate monomer
TEM	Transmission electron microscopy
TFA	Trifluoroacetic acid
TGA	Thermogravimetric Analysis
THF	Tetrahydrofuran
TMC	Trimethylene carbonate
TU	<i>N</i> -cyclohexyl- <i>N'</i> -(3,5-bis(trifluoromethyl)phenyl)thiourea

General Introduction:

The world of nanomedicine has been dominated with polymeric materials self-assembled in a variety of morphologies such as vesicles, micelles, rod-like etc. These structures have been studied as drug-delivery agents extensively over the last decades. These structures can be tailor made in order to offer a variety of stimuli responsiveness such as light, pH, temperature, surface charge, enzymes and magnetic field. This variety of characteristics derives from the choice of polymers which determines the properties of the final structure, depending on the type of the chosen polymers, their architecture, i.e., diblock, triblock, graft copolymer, the molecular weight as well as the functional groups attached. All these characteristics determine the final self-assembled morphologies as well as their possible applications.

With all the varieties of possible morphologies which can be produced micelles and vesicles are the two main structures that have been utilized mainly in literature with the latter offering multiple advantages such as that offer high stability, membrane fluidity and the ability to encapsulate cargo in the hydrophobic membrane and inside the hydrophilic core of the structure. Lately, other morphologies have been gaining interest in nanomedicine as possible drug delivery systems and not only that. Elongated structures have demonstrated a variety of exciting properties such as increased circulation time in the blood stream, enhanced biodistribution and targeting capacity as well as increase cell internalization as well as higher toxicity in some cases.

Iron oxide nanoparticles have been studied extensively in nanomedicine, especially in cancer treatment due to their property of heat production when a high frequency alternating field is applied, this concept is known as magnetic hyperthermia. But lately magnetic nanoparticles have been investigated for another purpose and that is the magneto-mechanical destruction of cells from within. This destruction was attributed to the tendency of the nanoparticles to rotate around their axis when exposed to a rotating magnetic field and thus creating a motion inside the cell compartment, they were embedded in. The responsiveness of iron oxide nanoparticles to a rotating magnetic field by a creation of a torque strong enough to create damage in the cells by an application of a lower frequency magnetic field has sparked a lot of interest.

In the context of this PhD project, it was proposed to investigate the synthesis of a magnetic vesicular structure or polymersome which could be elongated in response to a static magnetic field due to the encapsulated iron oxide nanoparticles. The nanoparticles were proposed to be encapsulated in the hydrophobic membrane of the polymersomes in order to induce an elongation once the field was applied. Such elongation would be the cause of the nanoparticles aligning in the direction of the field and creating linear aggregates inside the membrane. The

linear aggregates would in turn force an elongation of the polymersomes in the direction of the magnetic field, granted that the volume of the nanoparticles was enough for them to form long aggregates that would induce a visible elongation. Once the elongation was achieved and an anisotropic polymersome would be created the next step of the project was proposed to be the stabilization of the anisotropic morphology via cross-linking of the hydrophobic membrane under the magnetic field. The concept of the project was born from the magneto-mechanical properties of the iron oxide nanoparticles. The fact that the latter can respond to the magnetic field by rotating around their axis and creating a force strong enough to create disruption of cell membranes was the core of the project. If the anisotropic polymersomes could respond in the same way as individual nanoparticles, but in a global response due to the volume of nanoparticles embedded in the polymersomes that would result in a system which could potentially induce more damage than individual iron oxide nanoparticles can.

Thus, the project was broken into three parts, with part number one being the synthesis of copolymers that have the potential to self-assemble into polymersomes and can produce a membrane with a thickness large enough to accommodate the necessary iron oxide nanoparticles (Chapter II and III). Part two the synthesis and functionalization of hydrophobically coated iron oxide nanoparticles than can be embedded into the hydrophobic membrane and respond to the magnetic field (Chapter IV) and finally part three which included the combination of the two first steps, by assembling the copolymer with the iron oxide nanoparticles and studying the elongation as well as the cross-linking process (Chapter V).

This is exactly the flow of the presented chapters in this dissertation. Chapter I being bibliography chapter presenting the advantages that elongated structures have displayed in literature in the previous year as well as the magneto-mechanical properties of iron oxide nanoparticles. Chapter II, describing the synthesis of one of the copolymers which was chosen to be investigated as the potential polymersome forming copolymer. Specifically, we present the synthesis of a graft copolymer consisting of PEG-*b*-(PATC-*g*- PI) which was synthesized by a combination of ROP and reductive amination. The synthesis of the tert-butyl (2-oxo-1,3-dioxan-5-yl) carbamate monomer is described as well, which was chosen as the foundation block in order to graft the poly(isoprene) block. Graft morphology was chosen in order to provide potentially a better system for a stronger cross-linking which would be capable to stabilize the elongated morphology.

In chapter III, we describe the synthesis of another copolymer that was proposed as vessel for our study, the triblock copolymer PEG-*b*-PTMC-*b*-PI. Once more the copolymer was synthesized by a combination of ROP and another reaction to attach the final block of poly (isoprene) which in this case was a Steglich esterification. The synthesis and characterization

of this copolymer is described as well as the necessary modifications that were performed on the poly(isoprene) block to make it capable of reacting with the hydroxyl group of the PTMC block.

Chapter IV demonstrates the synthesis of iron oxide nanoparticles (IONPs) via a polyol route and their subsequent functionalization with oleic acid or a modified poly(isoprene) with a dopamine group. The characterization of the nanoparticles via a variety of methods is described as well. In both Chapter 2 and 3 as well as Chapter 4 the synthesis of poly(isoprene) is described due to the different needs of functional groups and molar masses.

Finally, Chapter V binds all the components together in order to produce magnetic polymersomes, whose morphology is verified by TEM and SANS analysis and their cross-linking capacities under UV are studied and observed via TEM. Moreover, the polymersomes are exposed to a static magnetic field and their elongation is observed via TEM after the cross-linking of their membranes. Finally, the conclusions and perspectives of the project are discussed.

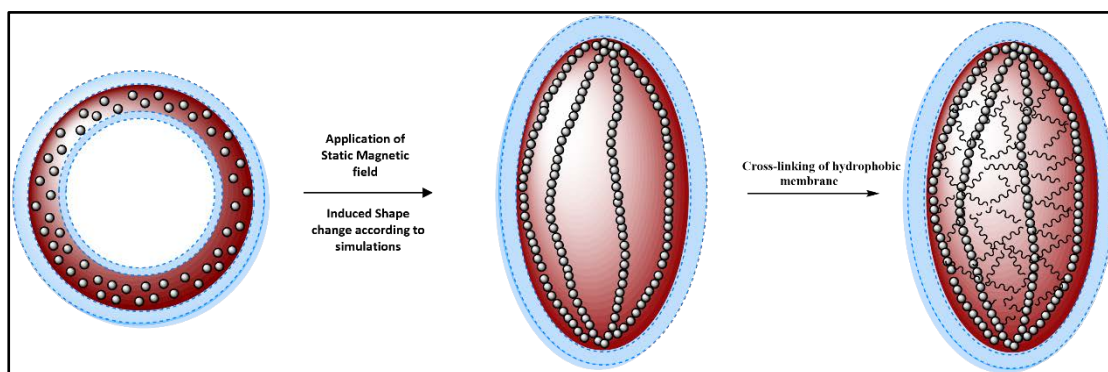


Image 1: Depiction of magnetic polymersomes whose elongation is induced after the application of a static magnetic field and the consequent cross-linking via UV irradiation.

CHAPTER I: BIBLIOGRAPHIC REVIEW

Introduction

The idea of a “Magic bullet” capable of reaching specific places in the human body, releasing the necessary cargo, *i.e.* drug in most of the cases, and cause minimal side effect has existed since the beginning of the 20th century and was introduced by Dr. Paul Ehrlich and his work on targeted medicine.[1] While this idealized version has not yet been achieved, science has gone a long way since then and many approaches and designs have been investigated.

Micelles, spherical structures, have been dominant in the latest decades in hopes of achieving that goal. Lately, focus has shifted on different architectures and the idea of a perfect sphere as the ideal candidate for delivery is no longer the only possibility.[1] The morphology of the “delivery capsule” seems to be playing an important role not only in the encapsulation of a drug, but also in the circulation lifetime in the body [2], the immunological response, site delivery as well as the absorption rate [3]. All the previous points seem to differ between morphologies with some to be presenting advantages over classical spherical morphology. Thus, the choice of the right morphology is one of the key parameters in understanding and perhaps predicting how well a delivery system can work.

Nanorods and elongated ellipsoids present a higher circulation time due to their shape that causes them to flow more easily in the blood stream, mimicking blood cells and their flow process [4]. Furthermore, the resulting delivery site can be tuned by the morphology, with elongated nanoparticles to present higher delivery rates at different organs [5]. Of course, the size is the one parameter that seems to be stable when making the choice of a delivery system, where nanoparticles between 100-200 nm seem to be the better choice to escape the reticuloendothelial system (RES)[6].

Polymersomes

Continuing with the concept of a magic bullet capable of delivering precious cargo into the body, the study of polymersomes emerged. By mimicking nature and looking deeper into the cell morphology it was extracted that cells were already an ideal system which can be studied for drug delivery systems. Ever since then nanomedicine has been striving to provide an ideal system which can come closer to cell morphology [7]. Using the architecture of cells as inspiration, naturally the creation of liposomes was achieved by creating a bilayer of phospholipids that consist of natural or synthetic phospholipids, with a hydrophilic head and a hydrophobic chain (lipid) that assemble into a vesicle. While liposomes are to this day regarded as a prominent drug delivery system with a great example the well-known Doxil, they have

many disadvantages that need to be improved to create a more sustainable system, thus polymersomes emerged.

Polymersomes are widely known as the synthetic equivalents of liposomes, consisting of synthetic amphiphilic copolymers in contrast to natural phospholipids, that due to their properties are self-assembled into a vesicular morphology. For a spherical morphology to be considered vesicular, the structure should consist of a membrane while maintaining an empty core which can be hydrophobic or hydrophilic depending by the nature of the system. Liposomes and polymersomes do exhibit similarities but also many differences and a lot of extensive literature has been published that thoroughly describe their individual characteristics, such as the review by Nsairat *et al.*[8] which in depth described liposomes and the latest publication of Rideau *et al.*[9] a comparison study between liposomes and polymersomes.

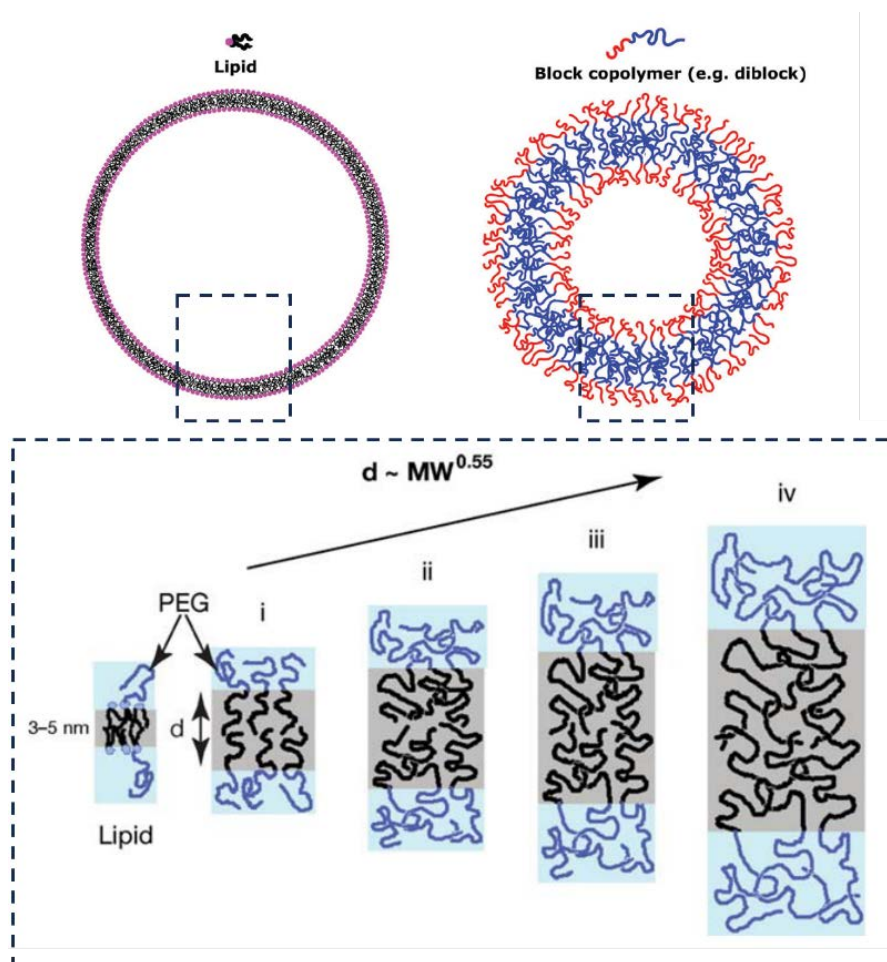


Figure 1: A 2D depiction of liposomes and polymersomes from Rideau *et al.*[9] and the dependance of membrane thickness on the molecular weight of the hydrophobic copolymer as depicted by Discher *et al.*[10].

One of the main advantages of polymersomes as drug-delivery systems is the big range of membrane thickness compared to liposomes. A larger membrane thickness allows the

polymersomes to enclose various cargo both in their membrane as well as the interior simultaneously [11], and their membrane thickness averages between 5 to 50 nm depending on the length of the copolymers chosen [12]. Liposomes tend to present a membrane thickness of 3 to 5 nm (Figure 1).

Membrane permeability is also one of the main differences between liposomes and polymersomes, where the latter exhibit a higher permeability due to the low molar mass. While high permeability can be an asset when a good diffusion is necessary for the enclosed cargo, it is a big disadvantage in terms of release control. In this case, polymersomes present a better alternative and exhibit better retention control. This characteristic is attributed to their high chemical versatility, which allows the formation of polymersomes out of a big library of polymers, as well as higher molar mass in the copolymers that are chosen. Furthermore, it is possible to tune the permeability of the formed membrane by incorporating stimuli which can destabilize their membrane [13], [14] and result to higher permeability (Figure 2).

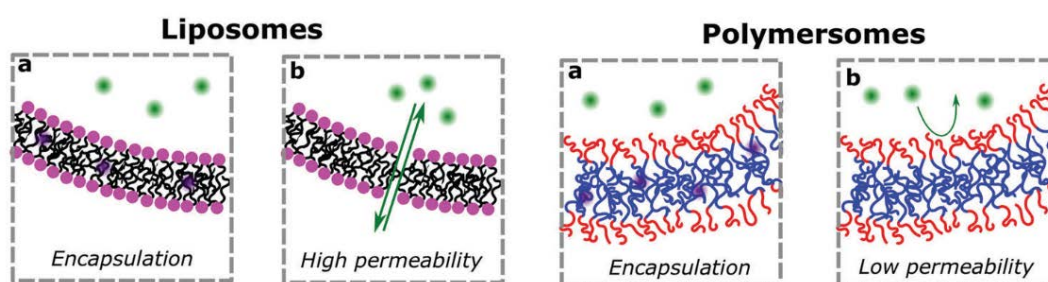


Figure 2: Depiction of the difference between the encapsulation and permeability properties of liposomes and polymersomes as depicted in Rideau *et al.*[9]

Due to their low membrane permeability and high chemical versatility, polymersomes tend to be more thermodynamically stable, resulting in structures that can remain stable over months. On the other hand, liposomes exhibit lower stability due to the instability of the lipids that are utilized for their formation [15]. Of course, this tendency is highly dependent on the chosen method of self-assembly, the size of the liposomes and the conditions of their storage [16]. The same thing could be said for polymersomes, as depending on the copolymers that were chosen, different characteristics of lateral diffusivity, polymersome size and inter-molecular reactions between the polymers, would emerge [17].

All these properties of course are in the end affected by the choice of the building blocks for both liposomes and polymersomes, with the latter being an easier prospective model to control due to the high chemical versatility of the polymers that can be produced. The biocompatibility property of liposomes can be achieved for polymersomes as well, as it depends on the blocks

which are chosen for their formation. Multitude of biocompatible polymersomes examples exist in literature like poly(trimethylene carbonate)-*b*-poly(L-glutamic acid) (PTMC-*b*-PGA) polymersomes [18], poly (ethylene-glycol)-*b*-polylactic acid (PEG-*b*-PLA) [19] and so many more depending on the design of the system and its necessities, such as poly[2-(methacryloyloxy)ethyl phosphorylcholine-*block*-2-(diisopropylamino)ethyl methacrylate] (PMPC-*b*-PDPA) polymersomes [20]. With so many advantages and availability of choice that synthetic polymers offer, polymersomes have been studied thoroughly in many aspects of biomedical applications [21]–[23].

The concept of polymersomes, or polymeric vesicles was first introduced by Disher *et al.* [24] almost 30 years ago when they studied the self-assembly process of poly(ethylene oxide)-*b*-poly(ethyl ethylene) (EO₄₀-EE₃₇) copolymers and over these three decades a big amount of research has already been done to understand their properties and capabilities. A variety of reviews have been published which combine the latest works on polymersome formation, properties and applications, such as by Araste *et al.*[25], Le Meins *et al.*[26] and Leong *et al.* [27]. One of the first publications which had observed polymeric vesicles was by Meijer *et al.*[28] where the self-assembly of polystyrene-dendrimer amphiphilic block copolymers was studied and multiple morphologies were observed including vesicles. Similar observations of the morphology were provided by Zhang & Eisenberg [29] where they studied the self-assembly of polystyrene-*block*-poly(acrylic acid), PS-*b*-PAA diblock copolymers in aqueous solutions. The same group continued on the study of the self-assembly of this diblock copolymer in order to control the final morphology by differentiation of the length of each block [30], [31]. Soon after, a new paper by Discher *et al.*[32] was published in 2000 studying the self-assembly process into vesicles of various diblock copolymers and polymer-lipids.

The self-assembly of well-defined copolymers in aqueous solutions which is reached at equilibrium is dictated mainly by the need for achieving the lowest energy possible between the polymer and water interactions as well as each of the polymer blocks [33]. One parameter that can easily predict the resulting morphology after the spontaneous self-assembly is known as the critical packing parameter p , which is a dimensionless parameter and is defined by the equation: $p = \frac{v}{a_0 l_c}$

where v represents the volume of the hydrophobic chains, a_0 represents the head group area and l_c the length of the hydrophobic tail [34]. This parameter correlates the relationship between the surfactant molecules *i.e.*, the head group (area of the hydrophilic block), volume of the hydrophobic chains and length with the resulting morphology by predicting the most likely morphology of the final structures. This parameter was first introduced by Israelachvili *et al.*[35] who explained the bilayer formation of both lipids and polymers.

This critical parameter ranges between a variety of values which depict the morphologies, *i.e.*, for a p value $p \leq 1/3$ the resulting morphology is a spherical micelle, when the parameter is $1/3 < p \leq 1/2$ the observed morphologies are cylindrical micelles while for $1/2 < p \leq 1$ the observed morphologies are vesicles (Figure 3).

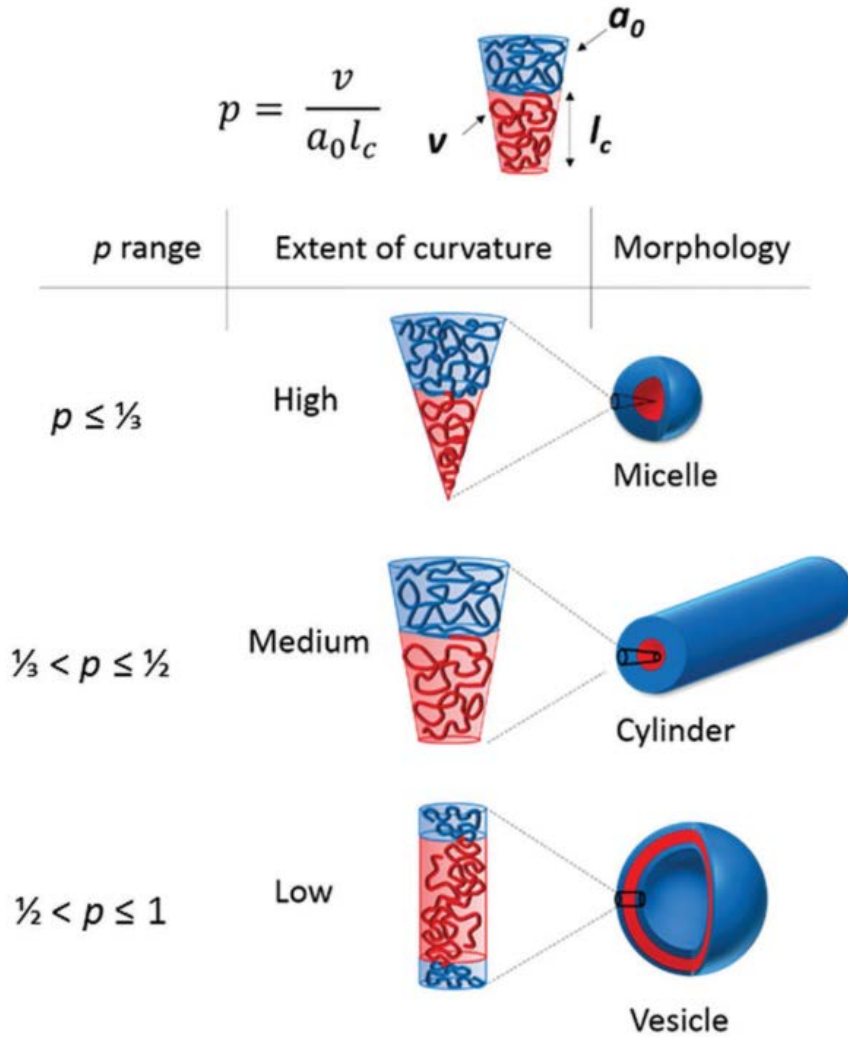


Figure 3: Depiction of the influence of the packing parameter on the final morphology during the self-assembly process from [33].

Another parameter which is frequently used to describe and predict the final morphology of copolymers is the hydrophilic fraction f . This parameter usually reflects the fraction of molar mass of the hydrophilic block divided by the total molar mass of the blocks of the copolymer and is calculated by the equation below:

$$f = \frac{Mn \text{ hydrophilic block}}{Mn \text{ hydrophilic block} + Mn \text{ hydrophobic block}}$$

A general rule of thumb is as follows, where when $40\% < f < 50\%$ then cylindrical morphologies tend to form. If $f > 50\%$ then micelles form while when f is lower than 40% and ranging between $25\% < f < 40\%$ vesicles tend to form (Figure 4). This parameter is not always accurate and depending on the nature of the polymers which were utilized for each system the limits of f may vary [36].

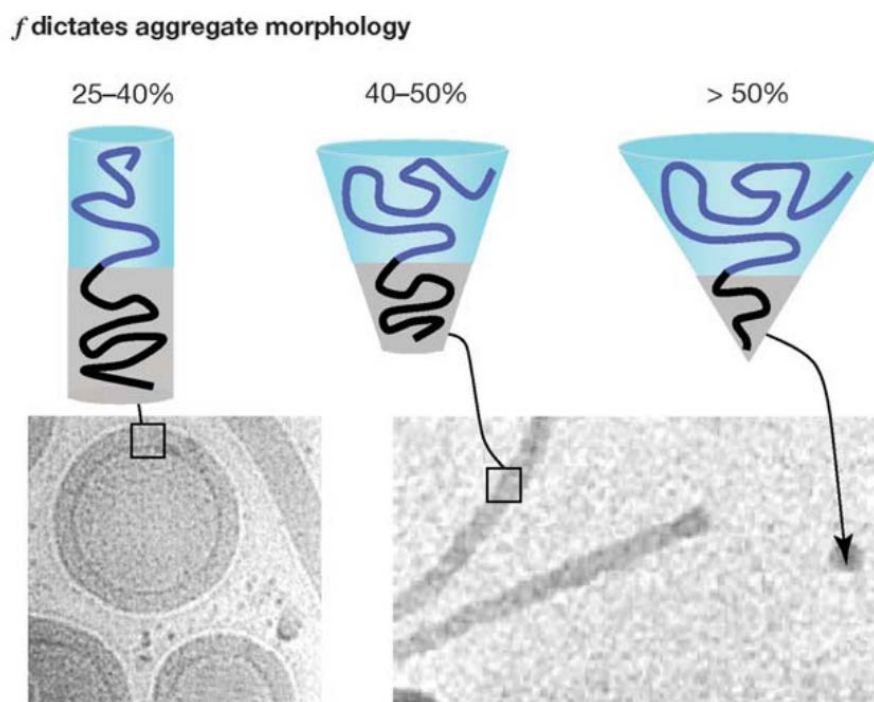


Figure 4: Hydrophilic fraction f as represented for various morphologies accompanied with the subsequent morphologies via cryo-TEM, as depicted by Discher *et al.*[10].

In general, the self-assembly process of copolymers and their final morphology is determined by many parameters, which include the nature of the copolymers, the molecular weight, the interactions between each block as well as the composition of the copolymers *i.e.*, diblock, triblock, graft, brush etc. [37]. For example, many copolymer compositions could result in polymersome formation (Figure 5) [25]. While diblock copolymers AB have been studied more predominantly in the field of polymersome formation [38], [39] there are many examples in the bibliography of other copolymers that can self-assemble resulting in such morphology.

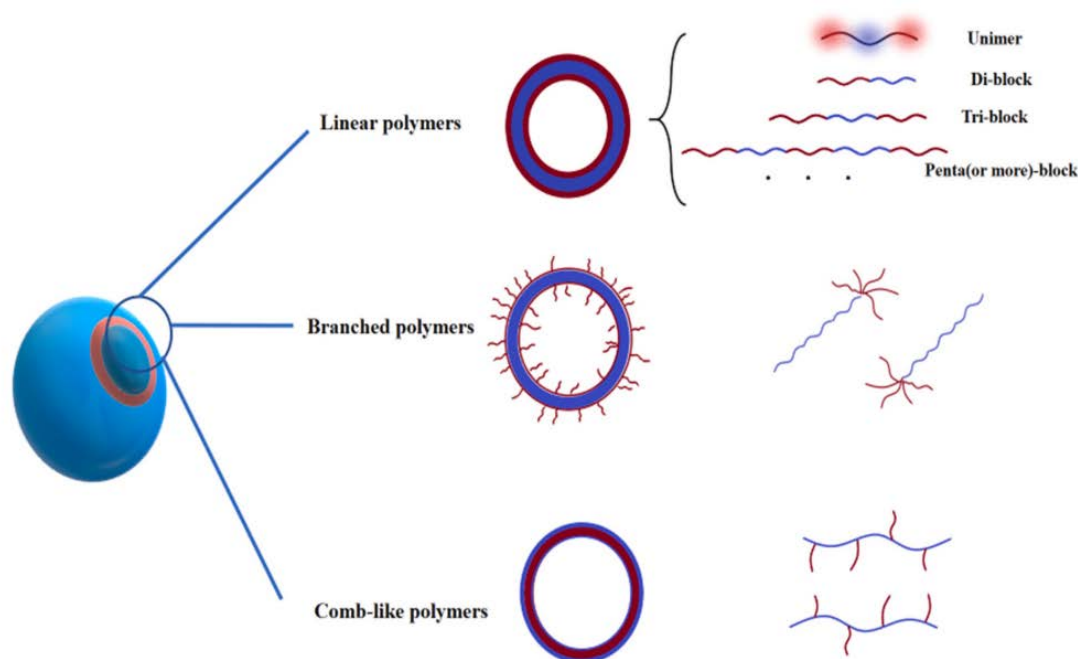


Figure 5: Different copolymer compositions which could result in polymersome formation as depicted in Araste *et al.*[25].

Various examples in the bibliography present examples of triblock ABC copolymers which can result in polymersome formation [40]–[45]. A recent study from 2019 by Konishcheva *et al.*[46], presented the formation of polymersomes by the self-assembly of a triblock copolymer consisted of poly(ethylene oxide)-*block*-polycaprolactone-*block*-poly(2-methyl-2-oxazoline) (PEO₄₅-*b*-PCL₁₁₀-*b*-PMOXA₄). The triblock copolymers could be characterized as ABC, ABA, depending on the hydrophilicity and hydrophobicity of each block. Examples of such copolymers were presented in extensive reviews by Iqbal *et al.*[47] and Wyman *et al.*[48]. More specifically, Zhao *et al.* [49] demonstrated the self-assembly process of an ABC linear copolymer consisting of poly(isoprene-*block*-styrene-*block*-2-vinyl pyridine) (PI-*b*-PS-*b*-P2VP). Another example, was published by Liu and Eisenberg in 2003 [50] where the synthesis of pH triggered vesicles was described. The ABC triblock copolymer poly (acrylic acid)-*block*-polystyrene-*block*-poly (4-vinyl pyridine) (PAA₂₆-*b*-PS₈₉₀-*b*-P4VP₄₀) with an acidic block PAA and a basic block P4VP were self-assembled in acidic or basic conditions resulting in a different block forming the shell of the polymersomes (Figure 6).

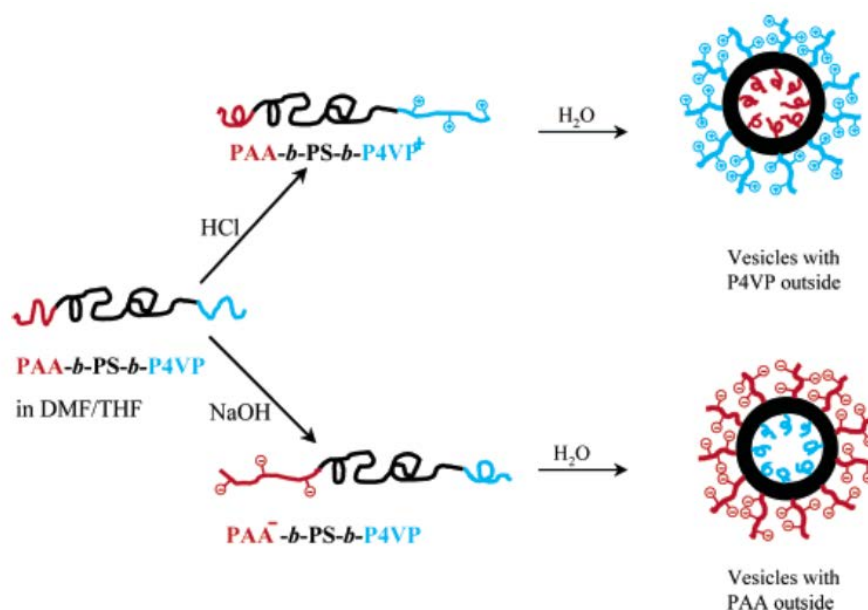


Figure 6: Representation of the pH-triggered self-assembly of the triblock copolymer $\text{PAA}_{26}\text{-}b\text{-PS}_{890}\text{-}b\text{-P4VP}_{40}$.
Figure reproduced from [50].

Other complex copolymer architectures have demonstrated polymersome formation such as brush copolymers and graft copolymers. The difference between these two architectures lies in the grafting density, where brush copolymers exhibit a densely packed nature while graft copolymers have a sparser grafting. Grafting density affects the physical properties of the copolymers as well as their self-assembly properties, as well as the length of the grafted side chain. The synthesis of grafted copolymers is achieved through three possible routes[51] (Figure 7):

- “Grafting to” [52]
- “Grafting through” [53]
- “Grafting from” [54]

Each route depends on the available functional groups on the backbone, the available monomers, and results in different grafting density as some are more favorable than others.

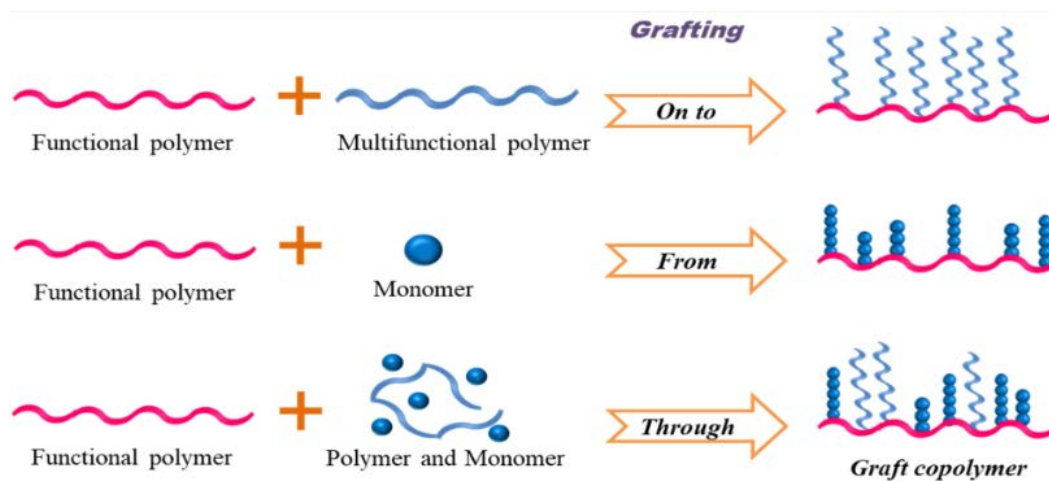


Figure 7: Schematic representation of the chemical routes to synthesize graft copolymers. Figure reproduced from [55].

The study of the self-assembly of graft copolymers in aqueous solutions has not been as extensive as for other types of copolymers so far, but the existing literature demonstrates that graft copolymers exhibit good potential in controlling the self-assembled morphology in order to produce polymersomes [56][57], when the grafting density and length of the side chains is controlled. Li *et al.*[58] described the synthesis and self-assembly properties of the graft copolymer poly(ethylene oxide-co-allyl glycidyl ether)-*graft*-poly(3-caprolactone). In this case the backbone of the copolymer was hydrophilic while the grafted chains hydrophobic. The copolymer was synthesized via a “grafting from” approach in order to ensure the control of the architecture. Following the self-assembly process spherical morphologies were formed, with the copolymer poly(EO₁₂₂-co-AGE₆-g-CL₁₄₂) with the wt% of hydrophobic segments being 73% appeared to form polymersomes with a controlled size. The authors further demonstrated that the increase of the hydrophobic segments resulted in micellar morphology and a potential mechanism was suggested, where the grafted chains were packed closely when forming the hydrophobic membrane.

Wang *et al.*[59] demonstrated the synthesis of another graft copolymer, poly (lactide-co-diazidomethyl trimethylene carbonate)-g-poly(ethylene glycol) [P(LA-co-DAC)-g-PEG] only in this case the hydrophilic block represented the backbone of the copolymer while the grafted chains were hydrophilic. Herein, the authors utilized the “grafting to” process via a click reaction in order to produce the graft copolymer, which allowed them to control the grafting density of PEG. It was reported that the graft copolymers with a hydrophilic ratio $f_{\text{PEG}} = 33\%$ had formed polymersomes while copolymers with a higher grafting density, thus with a higher f_{PEG} , formed micelles when $f_{\text{PEG}} > 50\%$.

Magnetic polymersomes:

Due to the large library of available polymers which can be utilized in order to synthesize polymersomes, it is possible to create polymersomes which are responsive to many stimuli which would enhance their capabilities to act as drug-delivery agents and minimize side-effects [6]. Such stimuli include pH, light, enzymes, temperature, and redox responsiveness (Figure 8). For a more in-depth analysis, extensive reviews have been published [60]–[62]. Lately, magnetic field has been investigated in biomedical applications. A lot of literature is dedicated on to the ability of super paramagnetic iron oxide nanoparticles (SPIONs) to act as MRI contrast agents[63][64] and the combination of such a characteristic along with the ability of polymersomes to encapsulate hydrophilic and hydrophobic cargo has made magnetic polymersomes a great alternative for nanomedicine[65].

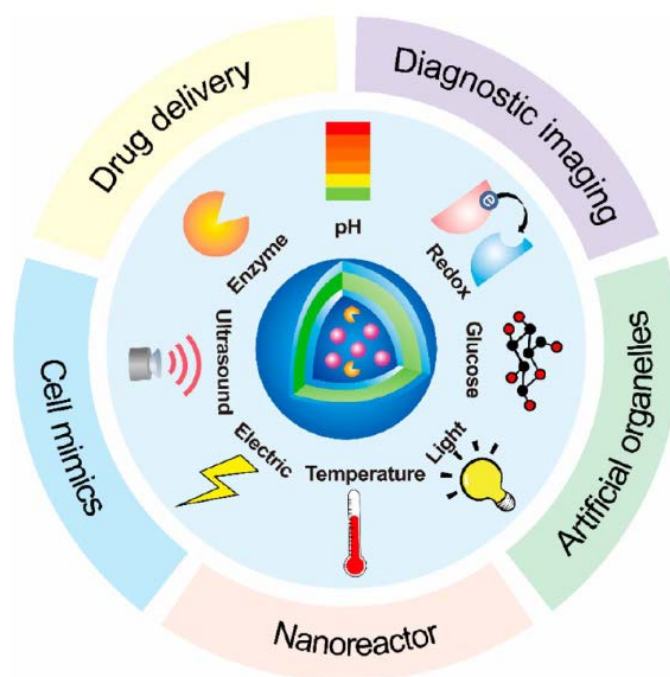


Figure 8: Diagram of the available stimuli for polymeric drug delivery systems. Reproduced by Hu *et al.* [62]

In recent studies where magnetic nanoparticles were incorporated into polymersomes, the systems were able to combine their MRI contrast properties as well as the drug-delivery abilities of polymersomes. Polymersomes can be utilized as a good system to deliver SPIONs for MRI applications as can be seen in a study by Duan *et al.* [66] where cationic polymersomes with encapsulated SPIONs were investigated as a delivery system of iron oxide nanoparticles in order to study via MRI the mesenchymal stem cells (MSCs). Another great example of a system which utilized SPIONs as potential MRI contrast agents was published by Ren *et al.* [67] where the authors synthesized polymersomes consisting of poly(tert-butyl acrylate-stat-acrylic acid)

[PEO-*b*-P(AA-*stat*-tBA)] and deposit superparamagnetic iron oxide nanoparticles directly inside the hydrophobic membrane utilizing the interaction of iron salts with the anionic PAA chains. They were able to produce magnetic polymersomes which exhibited a high T_2 relaxivity, ensuring a good contrast for MRI applications. Finally, the polymersomes were tested as drug-delivery agents in their capability of encapsulating and releasing doxorubicin. The system was revealed to be capable of releasing doxorubicin at pH=7.4 at a good rate (Figure 9).

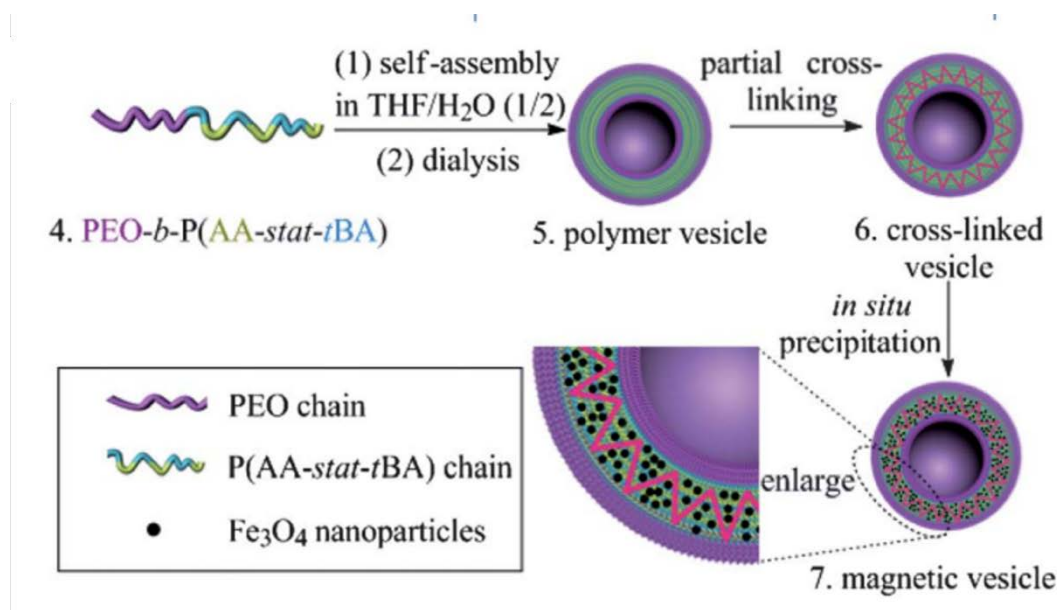


Figure 9: Self-assembly of magnetic polymersomes via a direct deposition of SPIONs into the membrane by in situ precipitation. Figure reproduced from Ren *et al.*[67].

Pourtau *et al.*[68] demonstrated a system of a magnetic polymersome comprised of poly(trimethylene carbonate)-*b*-poly(glutamic acid) (PTMC-*b*-PGA) self-assembled with hydrophobically coated USPIOs in order to enhance MRI contrast of bone metastasis. While Sanson *et al.*[11] utilized a similar system of magnetic polymersomes for MRI contrast as well.

Furthermore, magnetic polymersomes can be applied for more than MRI contrast agent, for example, in the same study by Sanson *et al.*[11] *in vitro* analysis of the release rate of doxorubicin loaded magnetic polymersomes was performed while a high frequency rotating magnetic field was applied. The application of the field induced a faster release of the doxorubicin by a factor of 2, when compared to the system without the magnetic field. This phenomenon was attributed to the ability of SPIONs to produce heat due to Néel's relaxation (as will be further discussed in the cell disruption via mechanical force section). The topical production of heat in the hydrophobic membrane of PTMC induced the increase of fluidity of the membrane, thus increasing the release of doxorubicin.

Similar observations were obtained by Oliveira *et al.*[69] with a similar system as described above. The magnetic polymersomes loaded with doxorubicin were internalized in HeLa cells and the cell viability was studied for a system which had been exposed to high frequency alternating field and one without the field. The system which had been exposed revealed a lower cell viability when compared to the non-exposed one, suggesting that the local heat production of the magnetic nanoparticles had aided in the release of doxorubicin (Figure 10). Such systems relay on the notion of AMF hyperthermia, where iron oxide nanoparticles are utilized for cancer treatment systems due to their ability to release heat under a high frequency alternating field [57-58] but without actually utilizing it as a means to lower cell viability since the heat released by the entrapped USPIOs is local in the polymersomes and not in the cell.

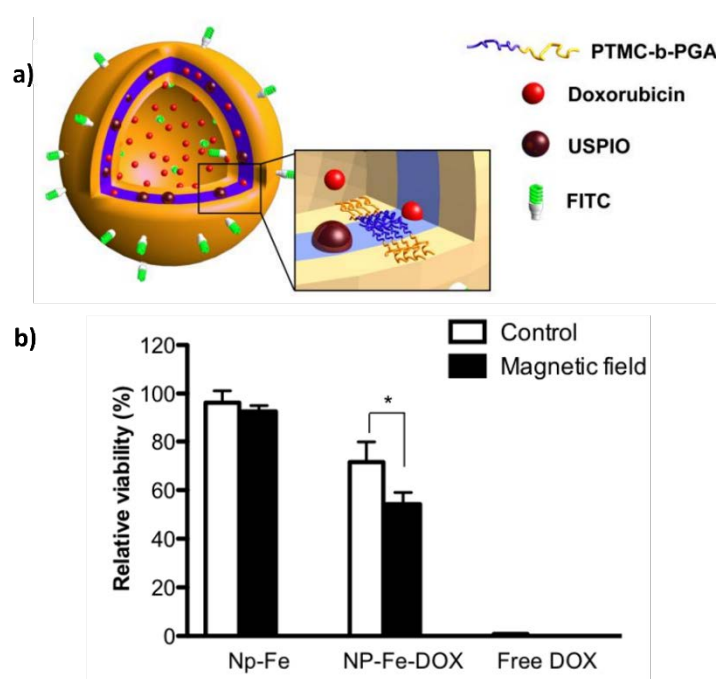


Figure 10: a) Magnetic polymersomes loaded with doxorubicin and b) measured cell viability of HeLa cells for three systems, Np-Fe: control with no doxorubicin, NP-Fe-DOX: magnetic polymersomes loaded with doxorubicin and Free DOX: free doxorubicin at the same concentration as the one in the loaded polymersomes. White bars demonstrate the results obtained by the systems with no application of alternating, black bars demonstrate the results obtained for systems exposed to alternating magnetic field. Reproduced from Oliveira *et al.*[69].

The response of magnetic nanoparticles to a magnetic field, without the contribution of heat release, is gaining momentum lately to be exploited for biomedical applications. Magnetic polymersomes could have the capacity to be utilized as a guiding system as well, as described by Krack *et al.*[72]. Multi-lamellar polymersomes formed by a diblock copolymer of polyisoprene-*block*-poly(ethyleneoxide) (PI₅₃-*b*-PEO₂₈) self-assembled along with hydrophobically modified iron oxide nanoparticles demonstrated a magnetophoretic mobility moving at a speed of 12 $\mu\text{m/s}$ when magnetic field was present (Figure 11).

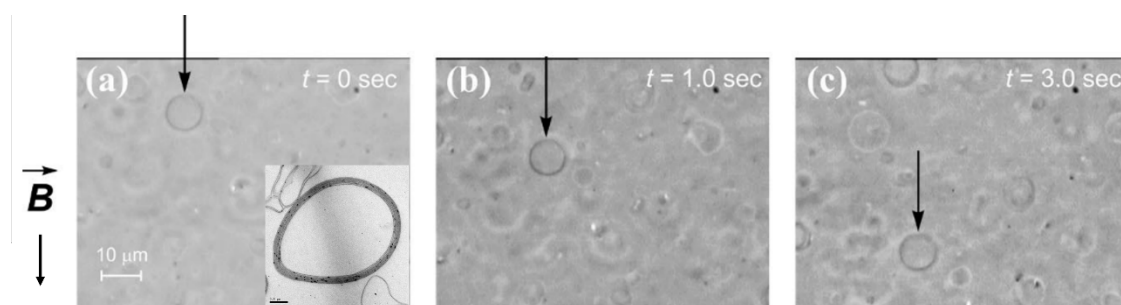


Figure 11: Demonstration of the magnetophoretic mobility of PI-*b*-PEO magnetic polymersomes when an Nd-magnet is present. Reproduced from Krack *et al.*[72].

A fascinating study by Long *et al.*[73] which exploited the mechanical response of magnetic nanoparticles to a magnetic field, studied the release of a drug-like substance fluorescein isothiocyanate (FITC-dextran) while the spherical magnetic colloidosome was exposed to magnetic field periodically. The colloidosome consisted of poly(N-isopropylacrylamide) (PNIPAm) with iron oxide nanoparticles embedded in its outer layer. The resulting microcapsule had a large width of 2 μ m, and the iron oxide nanoparticles were ~600nm. The results of the study demonstrated that once a magnetic field was applied the structure would elongate in its direction resulting in a shift of morphology from spherical to ellipsoid like. The extent of the elongation appeared to be dependent on the intensity of the field (Figure 12a-b). Once it was established that the elongation occurred, the authors proceeded to study the release abilities of the system, where it was derived that the release appeared to be faster for the system which had been exposed to the pulsed magnetic field, with the value reaching 92% while the control group had reached only 23% in the same time period. Finally, the release rate was tested for multiple field intensities, and it was revealed that the release increased along with the intensity of the field, with the release rate to be much faster for the highest field of 1800G, while the control group had not reached even 50% of release at the same time (Figure 12c-d). This study can demonstrate how the elongation of potential drug delivery systems can improve drug release.

Of course, this is not the first time that the elongation properties of magnetic polymersomes under a magnetic field have been demonstrated, as multiple studies have observed this phenomenon. For example, Lecommandoux *et al.*[74] had demonstrated the elongation process of polybutadiene-*block*-poly(glutamic acid) (PBD-*b*-PGA) polymersomes with encapsulated hydrophobically modified iron oxide nanoparticles in the PBD membrane. Via the use of SANS analysis the authors were able to identify the elongation of the polymersomes under a static magnetic field by visualization of the scattering pattern which had become anisotropic once the

field was applied (Figure 13). Furthermore, they were able to detect a shift in membrane thickness in the direction parallel to the field. Similar observation were made by Sanson *et al.*[11] for the PTMC-b-PGA system with 50 and 70% feed weight ratio (FWR%) of SPIONs.

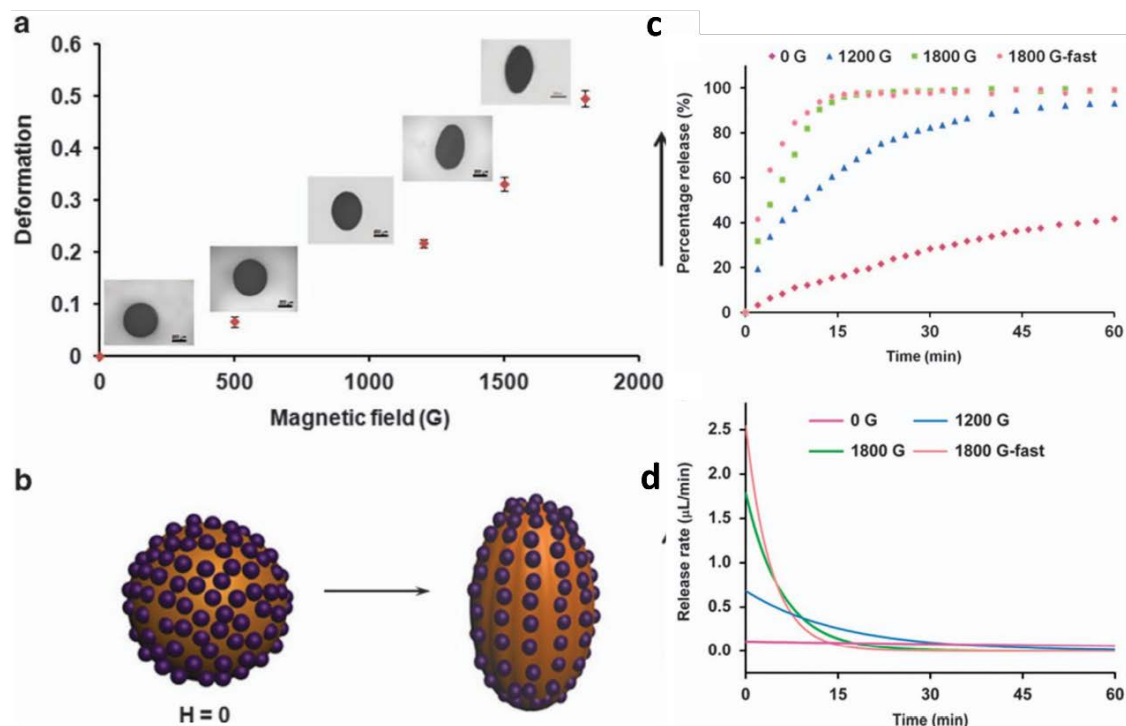


Figure 12: a) Elongation of the magnetic colloidosome in correlation of the intensity of the magnetic field (Scale bar= 500μm) b) Illustrative depiction of the elongation process, c) Release percentage of the FITC-dextran from the magnetic colloidosomes in regards to the intensity of the pulsed magnetic field (OG: No field) and d) release rate of FITC-dextran in regards to the intensity of the pulsed field. Reproduced from Long *et al.*[73].

The deformation of the spherical morphology of polymersomes has been studied theoretically by the use of coarse-grained molecular dynamics Ryzhkov and Raikher quite extensively [75]–[78]. The authors have utilized this method to theoretically predict how magnetic polymersomes would deform under the application of a magnetic field. The authors were able to demonstrate that the elongation is produced due to the alignment of magnetic nanoparticles in the direction of the field. According to the literature, magnetic nanoparticles tend to be in a disorganized state in the absence of the field, but once the field is applied their magnetic moments μ align in its direction. Due to the nanoparticles being restrained in the membrane the aggregation which is induced by the magnetic field leads the nanoparticles to form linear aggregates or chains due to dipole-dipole interactions, which extend parallel to the field. The formed chains spread around the membrane and are not aggregated with each other, these linear chains force the membrane to deform in a direction parallel to the field (Figure 14). Such exact behavior is presented in the studies above.[11], [73], [74] verifying the theoretical studies as well.

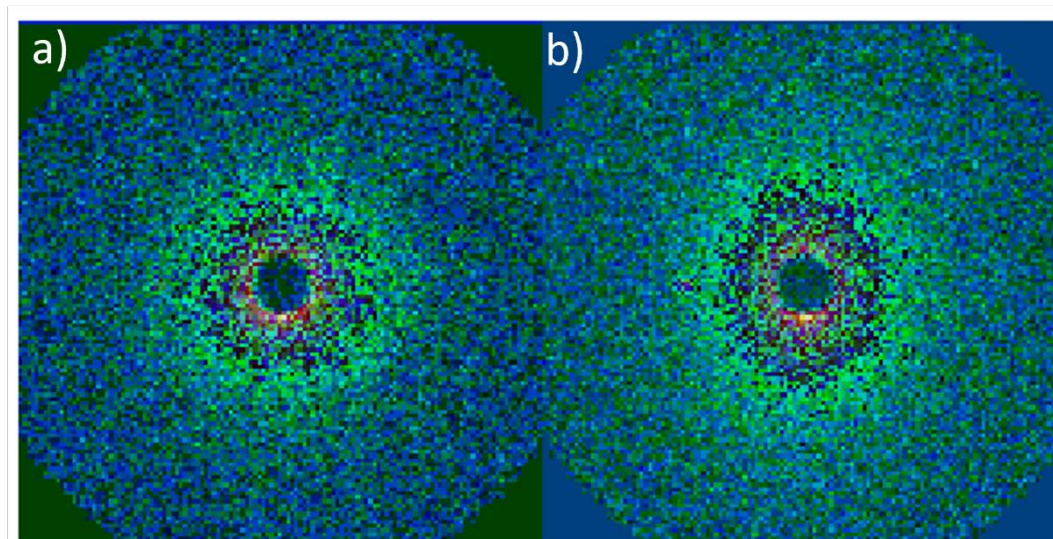


Figure 13: Scattering pattern of AANS analysis of the PBD-*b*-PGA magnetic polymersomes a) zero magnetic field and b) under a horizontal magnetic field with an intensity of $H \sim 0.1$ T. Reproduced from Lecommandoux *et al.* [74].

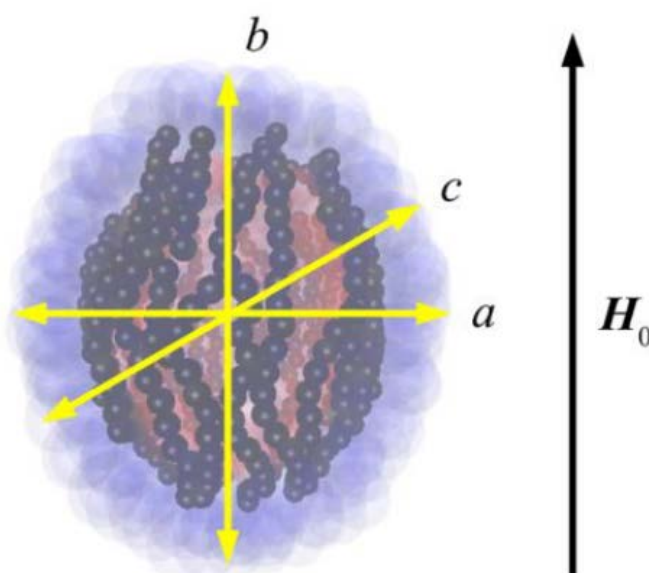


Figure 14: Illustrative scheme of the formation of linear aggregates which force the deformation of the polymersome in the direction of the magnetic field H . Reproduced from [77].

An elongated structure for polymersomes could be deemed beneficial for biomedical applications as lately a lot of literature has demonstrated the advantages that anisotropic morphologies present over the classic spherical system, such as improved circulation time, enhanced internalization, and cellular uptake. Such literature will be presented in the next part of the chapter.

How Nanoparticle shape affects its fate in the biological systems:

Over the past decade the impact of the shape of a drug delivery system in nanomedicine has been studied quite extensively, with many studies observing a vastly different acting mechanisms, internalization times and circulation times depending on the shape of the “object”. Some very extensive reviews have been written on the subject of how the morphology impacts the fate of the delivery systems in biological medium and what advantages each morphology holds over others, great examples are the works published by Kinnear *et al.* [79], Truong *et al.* [80] as well as by William *et al.* [81]. Herein such literature will be explored in order to determine whether non-spherical or anisotropic shapes are capable of offering an advantage in nanomedicine or at the very least whether the difference between spherical and non-spherical systems is important enough.

Protein Corona formation:

To study the immune response that a drug delivery agent is creating as well as the pathway that it will follow when and if it internalizes into the cells, it is important to understand the role of the protein corona formation. Protein corona on nanoparticles is not a new concept, it has been intensely studied throughout the last years. PEG (Polyethylene glycol) has been used, steadily over the past decades in drug delivery formulation as a stealth agent [82]–[84], not only as the hydrophilic block responsible for the self-assembly of various diblock copolymers but also as a key component to avoid non-specific protein interaction with the surface of any given nanoparticle, eliciting an immune response [85]. This is achieved due to the highly hydrated backbone of PEG resulting in repulsive steric hindrance interactions with the proteins in serum or plasma. Interestingly enough, protein corona formation still happens to a certain degree and cannot be fully avoided even by the use of PEG and neither should it be avoided [86]. Schöttler *et al.* [86] showed that it is the “ideal” combination of attached proteins on the surface that helped the internalization of nanoparticles functionalized with poly(ethylene glycol) (PEG) or poly(ethylene phosphate) (PEEP) rather than the lack of. Different protein coronas seem to form around various morphologies, resulting in different signaling pathways of the immune system [86].

Gagner *et al.* [4] demonstrated that the shape influence of the nanoparticles on the protein corona formation was showcased by the synthesis of chemically identical silica nanoparticles, differentiating only in their morphology, with one being a sphere and the other rod-like. A higher packing density was achieved in both serum and plasma proteins onto the rod-like NPs, suggesting that its flat surface offers a better area for the proteins to attach. Gagner *et al.* investigated the packing density capabilities of golden spheres and rods with two different

proteins and comparable results were obtained [87]. An opportunity for targeting capacity was presented for both morphologies. While protein composition seemed similar for both shapes, the rod-like NPs presented a higher absorption of immunoglobulin proteins compared to the spherical ones and may present a possibility for liver or spleen targeting. Furthermore, albumin, quite a detrimental protein, responsible for longer time circulation, presented a low adsorption rate for both morphologies, with a slightly higher percentage of 10% for the spherical morphology. On the other hand, both spheres and rod-like NPs exhibited a high absorption of apolipoprotein B100, crucial for brain targeted delivery (Figure 15).

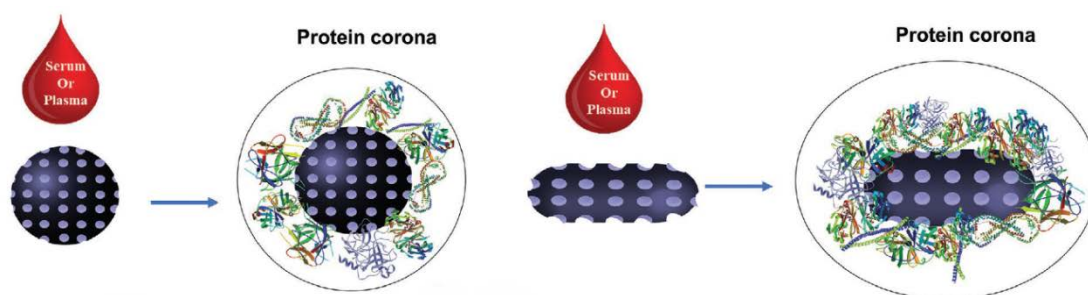


Figure 15: Protein corona formation around different morphologies from [4].

Phagocytes and Target morphology:

Protein corona formation is not the only obstacle drug delivery vectors need to go through to reach their desired targets. Phagocytosis is an elegant immune response that almost all cell types use to clear out pathogens from the system[88]. The main groups of cells that can efficiently phagocytize particles are macrophages[89]. Phagocytosis is an important process for drug delivery thanks to its role to clear out the particles from the system, thus diminishing the circulation time and the uptake efficiency of potential delivery systems. So far, phagocytosis has shown to be affected by a variety of parameters some of which are, the size of the particles, for example big particles immediately get phagocytized[90], their external shell, as discussed above, which when exhibiting different charges on the surface has shown to be responsible for faster clearance[91]. Lately, the shape of a particle and its aspect ratio have been considered as important parameters in this equation and thus have been further studied [92]. Mitragotri investigated the role of different size and shape of core crosslinked polystyrene NPs in the phagocytic process [93].

While the shape of the particle influenced the process; another important parameter was the contact point of the cells and particle. Indeed, if anisotropic ellipsoidal shaped particles were introduced into the cells by their smaller surface, then they would immediately get internalized, while if the contact area was the “long” surface then internalization was harder and slower. The Ω parameter which was attributed as the contact angle revealed that if it was small enough

(<45°) then the cells could internalize particles as big as their size but if the Ω value was within specific limits then particles as small as 0.2% of cell volume did not get internalized. In other words, anisotropic nanoparticles of sizes as big as in this research got either internalized faster or not at all depending on the angle (Figure 16). This study presented an interesting observation where while size of the particles indeed is key, the cell does not detect immediately the volume until the particles were fully internalized thus it is not the first parameter to affect the process of internalization, making the shape of the particle an important parameter, perhaps even the most important in this case.

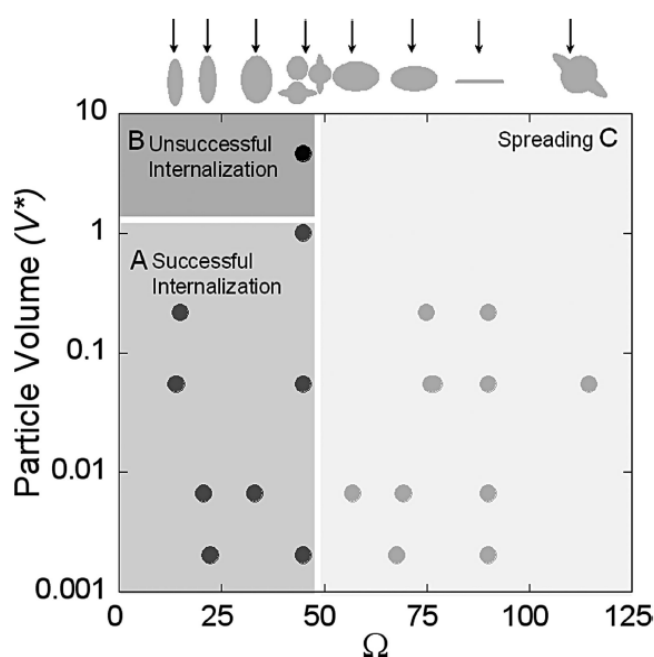


Figure 16: Demonstration of the effect of the relationship between the contact angle and the particle volume on the internalization process. Reproduced from Mitragotri *et al.*[93].

A study that investigated further the shape dependence of macrophage phagocytosis was published by Sharma *et al.*[94]. Herein, the authors used polystyrene NPs consisting of three different shapes *i.e.* Spheres, and ellipsoids that are either prolate (*i.e.* elongated) or oblate (*i.e.* flattened). The two last shapes were derived from spheres of various sizes to consider the size parameter as well in the phagocytosis process. In this case, the results showed shape dependence in the attachment as well as the internalization of particles into macrophages. Specifically, the shape parameter is more prominent with smaller and intermediate sizes compared to bigger sizes where phagocytosis was non-discriminatory towards shape. Oblate particles revealed to be the ones that tended to internalize faster, followed by spheres and finally prolate particles.

On the other hand, prolate particles were better attached on the macrophages followed by oblates and spheres last. As the authors describe both attachment and internalization are key factors in phagocytosis and the fact that oblate internalize faster than the other shapes, sometimes twice as fast, when of a specific size, suggests that there is a clear and definitive distinction between shapes. As a result, at least for smaller particles $<3\mu\text{m}$, it would be fair to suggest that prolate shapes are better at avoiding clearance from the system by having a slower or no phagocytosis and thus offering perhaps a more viable option for drug delivery systems that need a longer blood circulation.

Further verification that morphology affects the phagocytosis process was demonstrated by Paul *et al.*[95] where ellipsoid latex nanoparticles demonstrated a lower phagocytosis rate $\sim 5X$ than spherical latex nanoparticles of almost similar size, once more verifying that morphology is a key parameter (Figure 17).

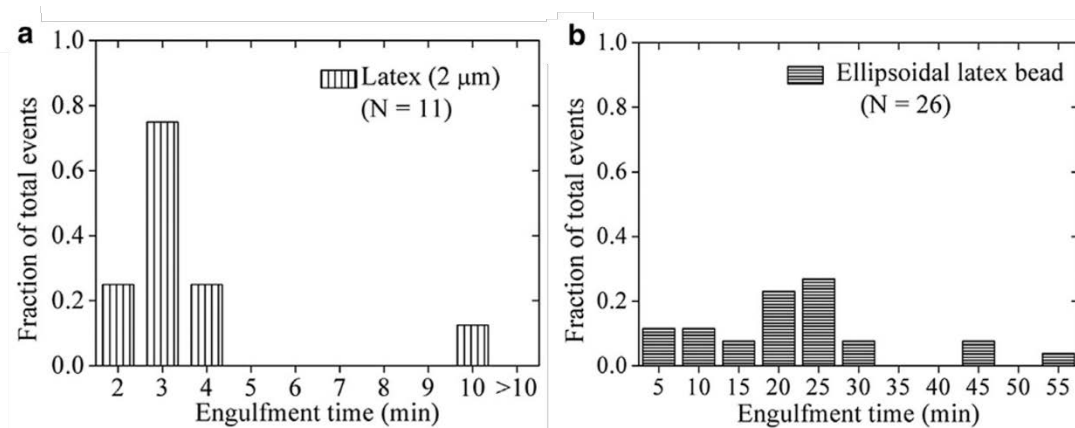


Figure 17: Figure reproduced from Paul *et al.* [95] demonstrating the phagocytosis time of a) spherical latex nanoparticles and b) ellipsoid latex nanoparticles in macrophage-like cell line RAW 264.7.

Circulation time and cellular uptake:

Many new studies have emerged demonstrating the effects of anisotropic morphology on blood circulation and cellular uptake over spherical systems. A prolonged circulation time offers an important advantage for drug delivery systems as well as an increased cellular uptake, which would result in an increased amount of the drug load to be deposited at the target sites.

In another study, filomicelles *i.e.* long cylinders prepared by self-assembly of diblock copolymers of poly(ethylene glycol)-*block*-poly(caprolactone) (PEG-*b*-PCL) or poly(ethylene glycol) *block*-(poly(ethylethylene)) (PEG-*b*-PEE), presented better circulation times when compared to their spherical vesicle counterparts at the same dose, 1 week and 2 days respectively, suggesting that anisotropic particles may offer a better circulation time than

spherical ones [96]. In this case, circulation time was directly and linearly affected by the length of the filomicelles until reaching a critical length resulting in fragmentation. Furthermore, rigidity is an important parameter indicating that filomicelles with a rigid crosslinked core were cleared faster, in a matter of hours, as compared to flexible ones.

The shape of drug delivery agents or vesicles not only affects circulation time but also cell apoptosis percentage, replication activity of cancer cells and their metabolic state [5]. Specifically, Scarpa *et al.* [5] synthesized two polymeric vesicles consisting of the diblock copolymer poly(2-(methacryloyloxy)ethyl phosphocholin)-*block*-poly(2-diisopropylamino)ethyl methacrylate) (PMPC-*b*-PDPA) differentiating only in shape, with one being a sphere and the other a tube in order to investigate their interaction with three different cell lines, two of which being cancerous. Their results suggest that the tube or elongated morphology had a different integration and accumulation rate with the cells compared to the spheres. Spheres were integrated in the cytosol while tubes were both in the cytosol and the cellular membrane, suggesting that elongated morphologies perhaps undergo “*delayed endocytosis*” due to their shape as already discussed above [5]. Furthermore, cell viability was affected by the shape as well, where tube shaped vesicles decreased cell viability by almost 40% after incubation for 48h with cancer cell lines compared to sphere morphology (Figure 18).

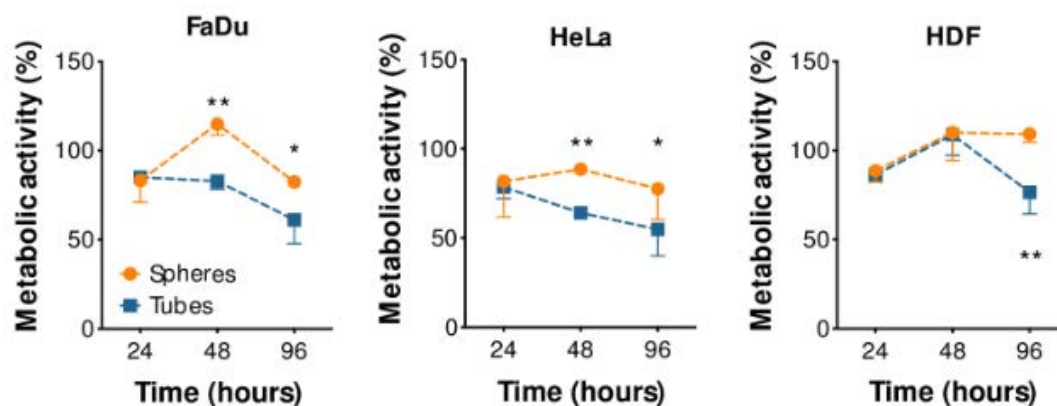


Figure 18: Cell viability of three cell lines after incubation with spheres or tubes. Reproduced from Scarpa *et al.* [5].

Further results on the effect of morphology on cellular uptake were reported by L'Amoreaux *et al.* [97]. Poly(ethylene glycol)-*b*-poly(lactic acid) (PEG_{1kDa}-*b*-PLA_{5kDa}) polymersomes were formed with two distinct morphologies, prolate ellipsoid and spherical, with a similar size of around 190 nm. After incubation in human neural cells (SH-SY5Y), prolate morphology exhibited a higher uptake compared to the spherical one. Specifically, both morphologies were loaded with Nile Red and BSA-Fluorescein (bovine serum albumin) followed by an incubation

with SH-SY5Y. Using fluorescent imaging, the neuroblastoma cells which were incubated with prolate polymersomes presented a higher intensity than the spherical ones, containing either one of the two dyes. Nevertheless, both polymersomes achieved a higher uptake compared to free dye (Figure 19).

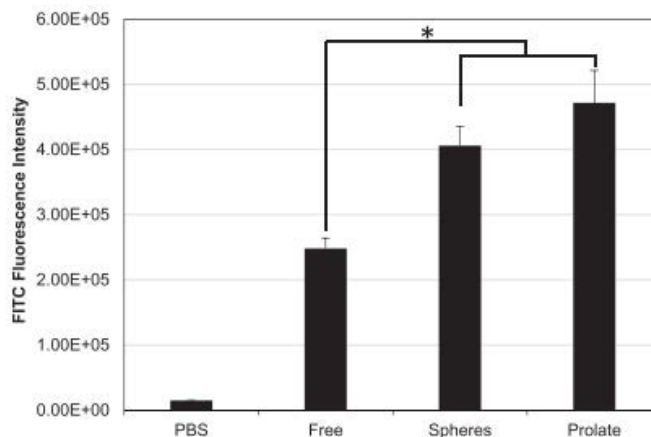


Figure 19: Flow cytometry results comparing the uptake of either free dye or spherical or prolate polymersomes in SH-SY5Y cell line. Reproduced from [97].

A paper published in 2006 by Chithrani *et al.*[98], presented opposite results regarding the uptake of anisotropic gold nanoparticles when compared to spherical ones in mammalian cells. While the study presented results which revealed that spherical nanoparticles demonstrated a higher uptake in HeLa cell line they did note a difference in the uptake of rod-like nanoparticles of a smaller aspect ratio 1:3 (length of 50nm) when compared to rod-like nanoparticles of 1:5 aspect ratio (length of 100nm), result which confirm the difference the aspect ratio plays in the uptake and internalization of nanoparticles (Figure 20).

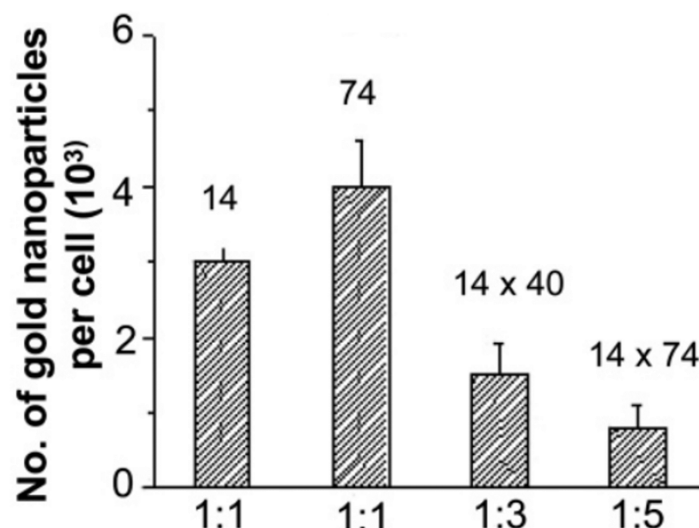


Figure 20: Cellular uptake of gold nanoparticles with two different morphologies, specifically spherical nanoparticles of 14nm and 74nm, as well as two rod-like nanoparticles of distinct aspect ratios 1:3 and 1:5.

Reproduced from Chithrani *et al.* [98].

Similar conclusions regarding the difference in the uptake due to aspect ratio can be found in a study published by Agarwal *et al.* [3]. The study demonstrated the uptake of rod-like and discoidal PEG-functionalized hydrogel nanoparticles by mammalian cells, presenting a higher uptake of the discoidal nanoparticles compared to the rod-like ones. The study presents results for a variety of cell-lines which exhibited similar results in regard to the preference of the discoidal nanoparticles, but the uptake is furthermore cell-specific, as they suggest that each type of cell “senses” the morphology (Figure 21).

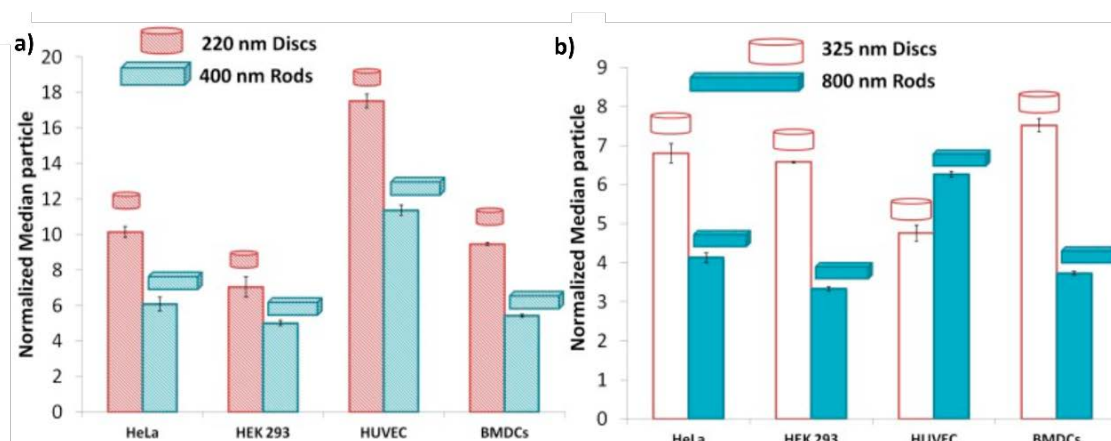


Figure 21: Cellular uptake of four different cell lines, HeLa, HEK 293, HUVEC and BMCs of two different nanoparticle systems with two aspect ratios each a) disks (pink) of 220nm diameter and nanorods (blue) of 400nm and b) disks (white pink) of 325nm diameter and nanorods (dark blue) of 800nm. Figure reproduced from Agarwal *et al.* [3].

Following this study Agarwal *et al.* [99] published another study where they explored the internalization of discoidal nanoparticles into 3D spheroidal models of solid tumors and studied the effect of shape and aspect ratio on the internalization process of a tumor like spheroid. Once more they presented results which indicate discoidal nanoparticles with a low aspect ratio of 0.3 (where aspect ratio was defined as H/D , where H stand for height and D for the diameter of the nanoparticle) had a high internalization into the spheroid. In this study the discs with a lower aspect ratio of 0.3 were internalized in higher degrees than the discs of 0.5 which were internalized in higher ratios in the various cells lines that were presented in the previous study [3]. This result could suggest that in tumor like delivery a lower aspect ratio was preferential for the discoidal moiety. Interestingly, polystyrene spherical nanoparticles which were tested in the study presented a low penetration in the “tumor” when compared to anisotropic shapes (Figure 22).

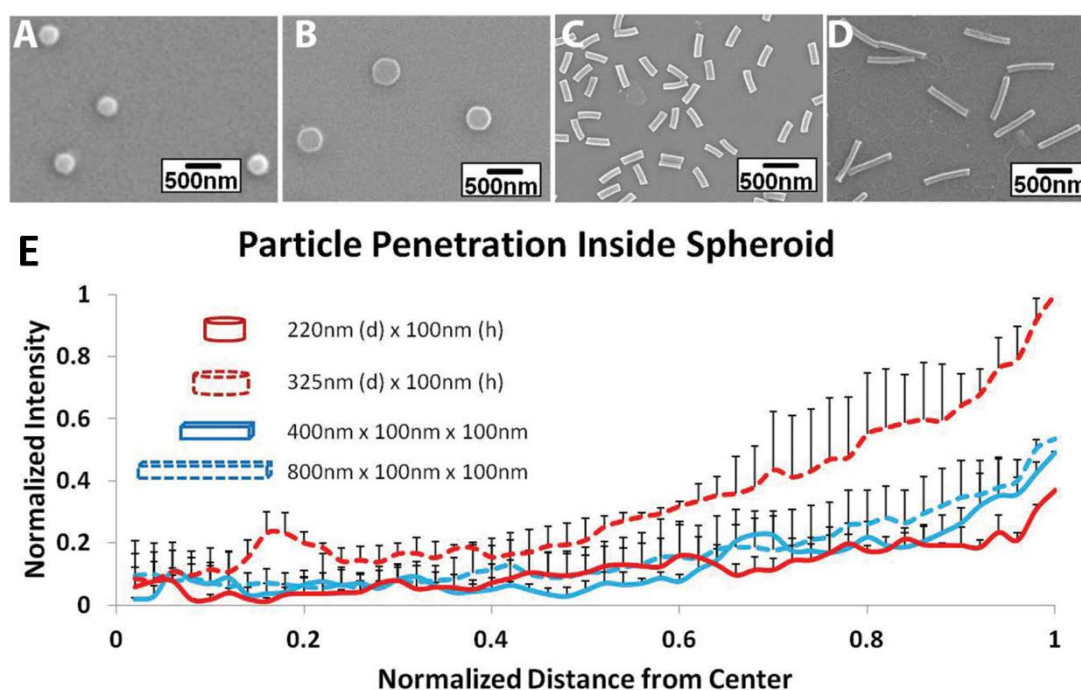


Figure 22: SEM images of two different morphologies discoidal and nanorods with different size, discoidal morphology A) 220 nm diameter, 100 nm height and B) 325 nm diameter, 100 nm height. Nanorods C) 400 nm length, 100 nm height and 100 nm width and D) 800 nm length, 100 nm height and 100 nm width. E) Graph of the internalization of all four systems in the spheroid calculated measuring the distance from the spheroid center.

Figure reproduced from [99].

A study by Gratton *et al.* [100] investigated the cellular uptake and the internalization kinetics of a variety of non-spherical PRINT particles (particles produced by cationic poly(ethylene glycol) cross-linked hydrogels produced by particle replication non-wetting templates). The study revealed differences between the internalization of the morphologies into HeLa cells

concluding that while aspect ratio affected the internalization the volume of the particles played a major role as well.

An interesting study by Barua *et al.*[101] demonstrated a cell-specificity exhibited by rod-like nanoparticles functionalized with a targeting antibody, trastuzumab, towards breast cancer cell lines when compared with spherical nanoparticles. The functionalized rod-like nanoparticles exhibited a higher specificity of almost 1.5 times than spherical ones in all three cell types which were chosen. Furthermore, the author tested whether the system could suppress the inhibition of the BT-474 breast cancer cell line. Indeed, the results suggested that rod-like nanoparticles presented a higher inhibition growth of the cells compared to the sphere systems (Figure 23).

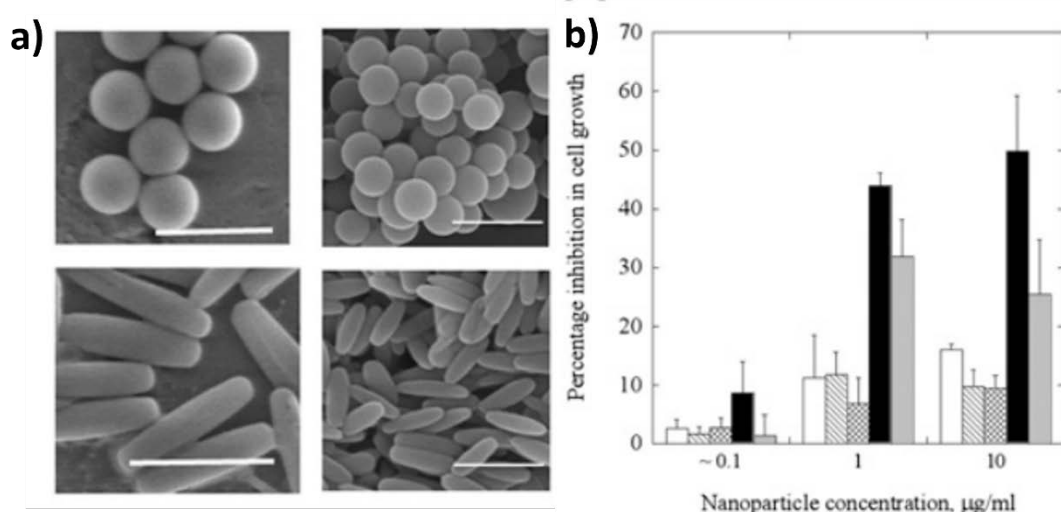


Figure 23: a) SEM images of the spherical and rod-like nanoparticles used in the study (scale bar 500nm) and b) depiction of the inhibition of the BT-474 breast cancer cell line by the antibody coated rod-like nanoparticles (black bar), BSA-coated rod-like nanoparticles (grey line bar), coated spherical nanoparticles (gridded bar), BSA-coated spherical nanoparticles (white bar) and the antibody trastuzumab in solution (gray bar). Figure published by Barua *et al.*[101].

Of course, all these studies take into account other parameters that may affect the internalization process and cellular uptake such as the charge of the nanoparticles, size, dosage concentration and cell types as it would be inaccurate to suggest that the morphology is the only parameter which affects the result each time[3], [99], [100]. Furthermore, the difference in the material which was utilized in the synthesis of the nanoparticles affects each process, as the stiffness of the nanoparticles would play a big role in the interaction with cell membrane and internalization.

Anisotropic morphology and drug delivery

Scarpa *et al.* investigated also the influence of the shape onto drug delivery capacity and efficacy [5]. A combination of doxorubicin loaded tubular and spherical vesicles were integrated in cancer cells and control cells. A different effect was observed for both cell lines. An intense reduction of cell inhibition concentration (IC_{50}) for HeLa cells, almost by 12 times when tubular morphology was involved compared to the spherical ones, was observed. Furthermore, a selectivity index (SI) was reported as well to study the targeting abilities towards cancer cells, which allowed the observation that loaded tubes presented a higher efficiency, almost 10-fold, compared to free doxorubicin or loaded spheres.

Enhanced therapeutic effect has been reported when increased tumor cell apoptosis was achieved with drug loaded filomicelles compared to the free drug [96]. Furthermore, the filomicelle length played an important role as filomicelles of 8 μm present better results than shorter ones of 1 μm . Synergetic effect was achieved when the longest filomicelles of 8 μm were combined with a higher drug dose, leading to increased cell apoptosis and tumor shrinkage (Figure 24).

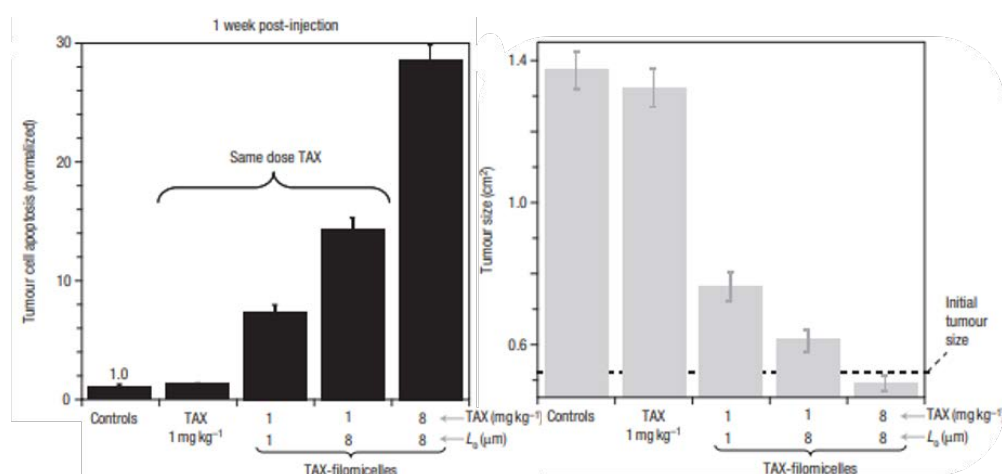


Figure 24: a) Dependence of cell apoptosis on the length of filomicelles and b) tumor shrinkage dependence on size of filomicelles. Reproduced from [96].

A recent study by Bai *et al.* [102] studied the effect of tubular morphology and size on the efficacy of drug delivery and cell apoptosis in cancer treatment. An amphiphilic copolymer of cellulose-*g*-(CPT-*b*-OEGMA) consisting of poly (ethylene glycol), cellulose and 6-hydroxyhexyl methacrylate modified camptothecin, which is glutathione responsive, was self-assembled into prodrug cylindrical polymer brushes (CPBs) with three different lengths of (CCO-1) 186nm, (CCO-2) 40nm and (CCO-3) 21nm respectively. The CPBs were incorporated in three cell lines, two of which were cancerous cell lines HeLa, and MCF-7 while L929 was

tested as control. They were able to demonstrate the differences between the size of the samples and the effect it has on tumor accumulation and penetration, circulation time and finally *in vivo* anticancer activity. While all three samples had a good interaction with the cancer cells, CCO3, the smallest in length sample, presented a higher penetration which was to be expected due to its size and the tendency of smaller particles to enter the cells due to the EPR effect. On the other hand, a higher accumulation on the tumor site after 24 hours was observed for the longest sample CCO-1 but that was attributed to its longer circulation time compared to the other two samples. A longer circulation time for rod-like particles has been already discussed above [96] and while all three of the analyzed samples have a rod-like morphology the length differs as well as the interaction point of the samples. While the smallest particles, CC-O3, had a smaller accumulation it presented the highest permeability between the three samples.

Interestingly, while the above results were expected if we consider the existing studies on rod-like particles and the dependency on size with tumor accumulation and permeability the group presented result on how size of rod-like particles affects tumor tissue shrinkage. When the particles with the prodrug, CPT, were injected into MCF-7 tumor-bearing nude mice they observed a slower tumor growth for the smallest COO-3 particles compared to the longest particles. Specifically, while the control group with no particles injected had a tumor growth by 8 times the original size, the CCO-3 sample had only a 1.7 increase while the CCO-1 and CCO-2 group had an increase of 3.4 and 2.2 respectively. While the CCO-3 group had the smallest increase it is still remarkable that all the rod-like particles had a significant effect on the final size of the tumors (Figure 25).

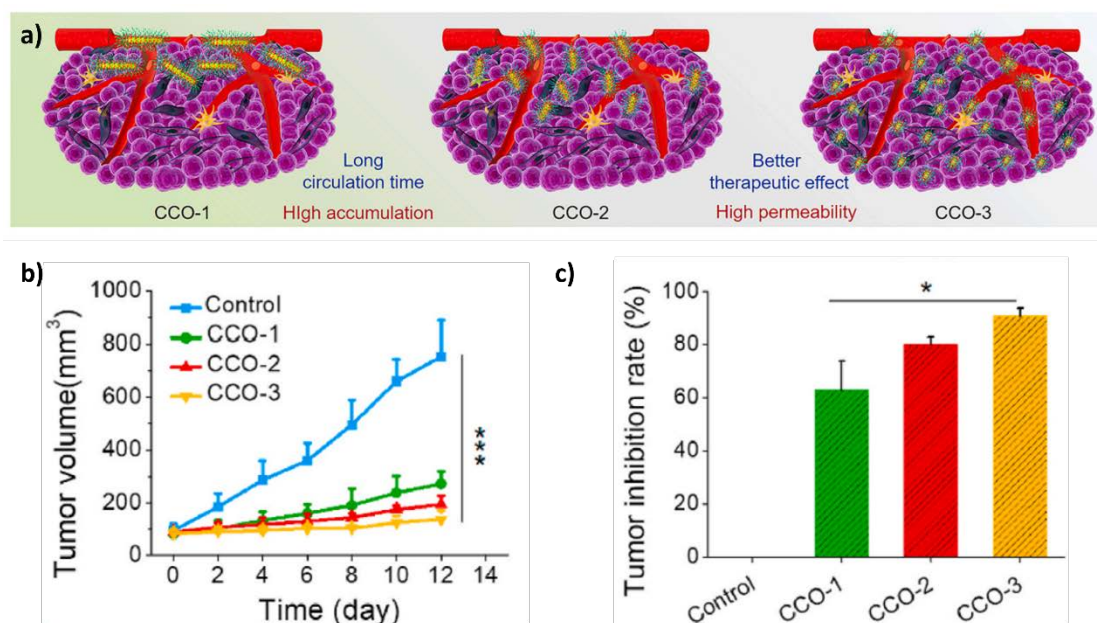


Figure 25: a) Schematic representation of the observed properties of the polymer brushes CCO-1, CCO-2 and CCO-3, b) effect on the tumor volume after 12 days of treatment with no polymer brushes (control), CCO-1, CCO-2 and CCO-3, and c) inhibition of the tumor after 12 days of treatment. Reproduced from [102].

Another study which explored the anticancer activity of rod-like particles was published in 2016 by Li *et al.*[103]. The study included extensive research on the effects of rod-like particles on tumor suppression compared with spherical particles as well as the effects of morphology on internalization and blood circulation. Polymeric nanoparticles (NPs) consisting of PEG-*b*-PCL diblock copolymer loaded with doxorubicin were studied both *in vitro* and *in vivo* either with HeLa and HepG2 cancer cell lines or with mice Belb/c bearing an H22 tumor respectively. Three different samples were prepared, with one of a spherical morphology and two rod-like morphologies differentiating in their diameter and length, 20nm×300nm and 40nm×600nm. The *in vivo* results presented particularly interesting results when it came to the pharmacokinetics of the doxorubicin loaded NPs compared to free doxorubicin in the mice. Specifically, they detected a significant difference between the clearance time of each NP as well as free doxorubicin, with the longest rod-like doxorubicin loaded sample presenting the longest circulation time and the slowest elimination after 24 hours with $30.43 \pm 2.96\%$ of the injected dose to be still present. The elimination half-life ($t_{1/2\beta}$) was the highest between all the all the samples suggesting that there was a difference between morphologies (Figure 26).

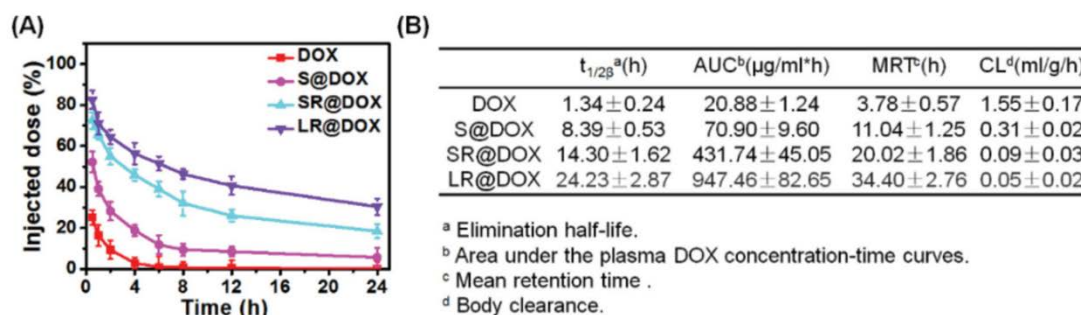


Figure 26: A) Presentation of the pharmacokinetic profile of all samples including free DOX after intravenous injection (S@DOX: spherical micelles, SR@DOX: short rod-like micelle and LR@DOX: long rod-like micelle), B) Table of various pharmacokinetic parameters after injection. Reproduced from Li *et al.*[103].

Furthermore, the study presented results which confirmed how this NPs can increase tumor suppression and how it is differentiated between morphologies. Specifically, while the control group (consisting of 0.9% saline solution and blank micelles groups) demonstrated a fast tumor growth from 25.08 ± 1.85 to $1281.49 \pm 81.2 \text{ mm}^3$ after 21 days the DOX loaded micelles presented a suppressed increase of tumor volume with the LR@DOX i.e., long rod-like micelle, appearing to have the highest suppression of volume increase, only reaching $292.34 \pm 93.02 \text{ mm}^3$ (Figure 26a). Moreover, immunological analysis was performed on tumor sections on the 10th and 21st day post injection and the apoptotic rate was calculated using the results of TUNEL (TdT-mediated dUTP nick end labeling) analysis. Once more the LR@DOX micelles presented an increased apoptotic rate of $86.3 \pm 2.03\%$ which was higher than all the other micelles-DOX formulations (Figure 26b).

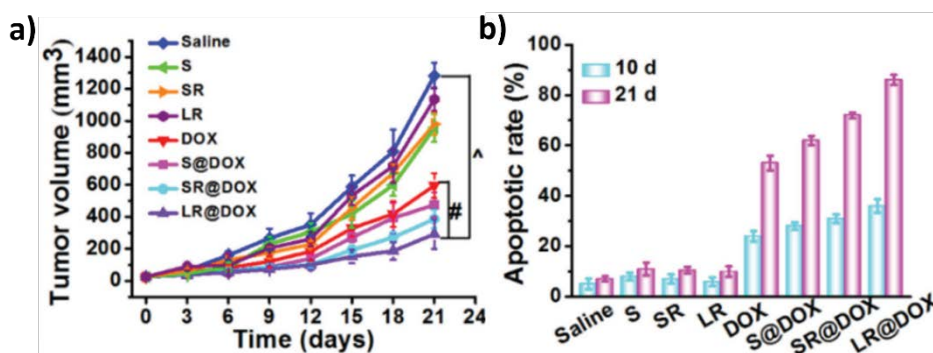


Figure 27: a) Tumor volume change after treatment of the H22 tumor-bearing Balb/c mice with different micelle samples at a dose of $2\text{mg}\cdot\text{kg}^{-1}$ (Saline: control group, S: spherical micelle with no DOX, SP: short rod-like micelle no DOX, LR: long rod-like micelle no DOX, DOX: free doxorubicin, S@DOX: spherical micelles loaded with DOX, SR@DOX: short rod-like micelle and LR@DOX: long rod-like micelle loaded with DOX. b) Apoptotic rate

calculated for all micelle formulation including DOX loaded and non-loaded micelles. Reproduced from Li *et al.*[103].

Such results clearly confirmed both the potential of rod-like systems to act as anticancer systems but once more demonstrated how different morphologies and size affect the final activity.

Another fascinating study conducted by Garbuzenco *et al.*[104] published in 2014 which explored the anti-cancer properties of anisotropic nanoparticles combined with two drugs. More specifically, the study explored the synthesis of Janus nanoparticles comprised of a polymer, poly(lactic-co-glycolic acid) (PLGA) and a lipid, Precirol ATO 5. The resulting nanoparticles were self-assembled with two drugs, one hydrophobic, curcumin and one hydrophilic doxorubicin (DOX). The efficacy of the anisotropic nanoparticles against lung cancer was tested on mice which exhibited lung cancer, due to the transfer of a human cancer cell line A549. The combination of the anisotropic particles along with the two drugs was the most successful treatment in suppressing, almost completely, the growth of the tumors which remained in the original size of $\sim 50 \text{ mm}^3$ when the treatment was administered via inhalation. While treatment with just doxorubicin or the nanoparticles alone or containing only one of the two drugs did not allow for similar results (Figure 28a-c).

Interestingly, when studying the distribution of the loaded nanoparticles via the inhalation method, they were able to detect that the nanoparticles of a larger size, 450nm, were more apparent in lungs after 1 hour of treatment and were still present after 24hours compared to smaller ones of 150nm, suggesting that the anisotropic nanoparticles had a good accumulation at the target site with the larger ones presenting better results (Figure 28d-h). Finally, cellular internalization was studied on the cancer line A-549 and the anisotropic nanoparticles were mainly present in the cytoplasm and the nuclei, suggesting a good internalization process as well.

While these results can not only be attributed to the morphology since the main component of the anti-cancer activity in this case was the combination of the two drugs, but it is also important to acknowledge it as a key parameter. The presence of the nanoparticles in the system was important enough to affect the shrinkage of the tumor even when only one drug was involved and to a higher degree than just the drug alone, for example free DOX (Figure 28c).

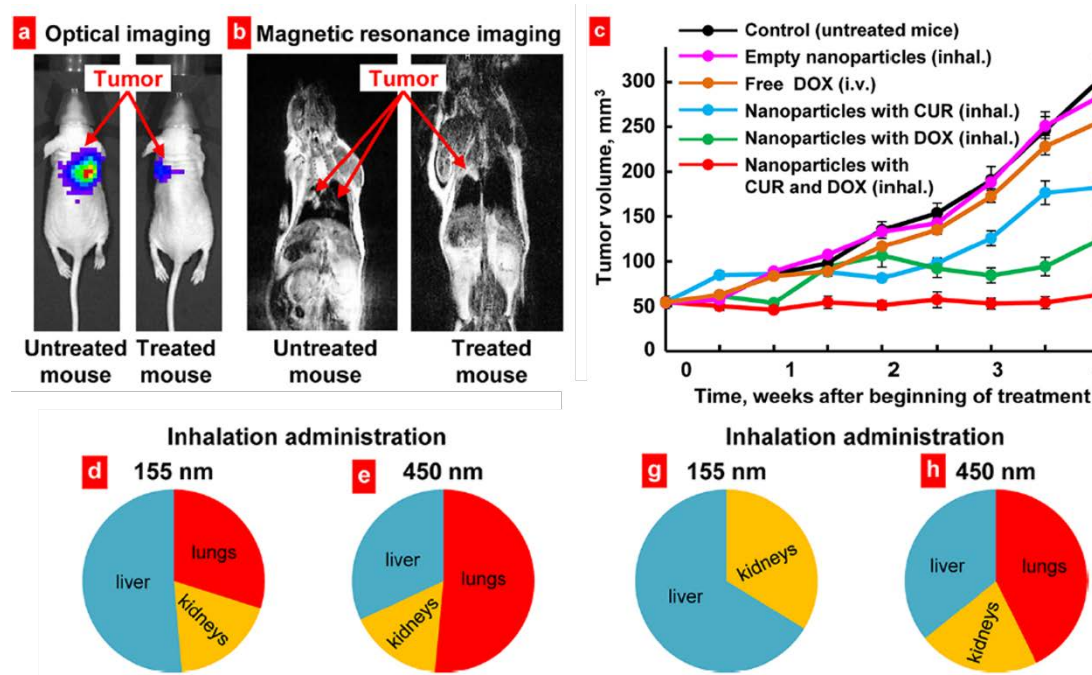


Figure 28: Figure reproduced from [104]. a) Depicting the tumor growth on the mice before and after treatment with the Janus nanoparticles loaded with DOX and curcumin via optical imaging and b) via magnetic resonance imaging. c) Figure depicting the tumor growth suppression after treatment with various systems and d-h) figures of the biodistribution of two sizes Janus loaded nanoparticles in various organ sites of mice via inhalation d-e) after one hour of treatment for 150nm and 450nm nanoparticles respectively and g-h) after 24 hours of treatment.

A study published in 2017 by Debele *et al.* [105] demonstrated the effects of rod-like micelles as potential colon cancer treatment. Specifically, a drug combination of doxorubicin and α -Tos (α -tocopheryl succinate) was formulated with micelles which were self-assembled from a copolymer of poly(ethylene glycol)-b-poly(hydroxypropyl methacrylamide-g- α -tocopheryl succinate-g-histidine). The complexation of doxorubicin with histidine forced the spherical micelles to rearrange into rod-like micelles resulting in an anisotropic system. Herein the researchers were able to detect that the system had a good accumulation for the human colon cancer cell line HCT116 and a low macrophage uptake, at least in the first 6 hours post treatment, suggesting a good circulation time. While the study does not attribute the mechanism of action to the morphology it is interesting to note that the rod-like micelles had a good targeting towards the tumor cite (Figure 29) and doxorubicin was able to be released into the cytosol in vitro in the HCT116 cell line, suggesting a good internalization of the rod-like micelles.

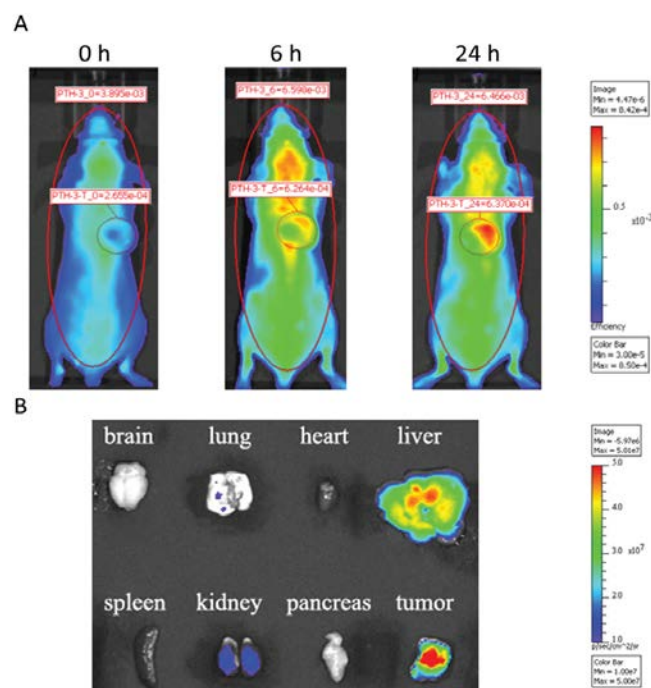


Figure 29: Figure from [105] displaying the biodistribution in the organs of HCT116 colon cancer-bearing mice 24 hours post-treatment with the drug-loaded rod-like micelles.

Finally, some studies have suggested that ellipsoid polymersomes exhibit an enhanced cell-targeting ability when compared to their spherical counterparts. For example Lai *et al.* [106] presented ellipsoidal polymersomes consisting of poly(2-hydroxyethyl aspartamide) which was substituted with octadecyl chains (PHEA-*g*-C₁₈) and functionalized to various degrees with PEG. The self-assembled polymersomes were functionalized with an RGD peptide in order to add a targeting moiety. The study was able to demonstrate that the ellipsoidal polymersomes had a higher affinity on a model tissue than spherical polymersomes, a characteristic which was attributed to the longer axis of the ellipsoidal morphology which allowed for a better adhesion.

From this part of the chapter, it has been demonstrated that a lot of research has been navigated towards the properties of non-spherical nanoparticles in nanomedicine over the last decades. It has been exhibited that some anisotropic morphologies bear advantages in increased circulation times, cell internalization and enhanced drug delivery. Of course, many parameters are at large and each system should be tailored for the delivery site and cell type [107]. Nonetheless, there seems to be an interest in anisotropic morphologies due to the advantages that they offer.

Cell disruption via Mechanical force:

Theoretical point of view:

Nanomedicine has been focusing mostly on systems that can transport active substances to a targeting area, either by drug encapsulation into a self-assembled nanocarrier, such as micelles, but also polymersomes which are the polymeric analogues of liposomes, and controlled release by a local trigger in the tumor environment (lower pH, oxidative stress or enzymes) or by utilizing an alternating magnetic field (AMF) combined with the heating capacity of magnetic nanoparticles. All these methods, although successful, tend to provide a more passive approach on cell apoptosis. Interestingly, a new approach has been emerging over the latest years, which offers a more “practical” and targeted solution. The main theme consists of applying mechanical forces onto the membranes of cell compartments that when strong enough could create a disruption of said membranes. This disruption will then initiate a chain of events, most likely a cellular pathway for membrane repair, but powerful enough to destroy directly or disrupt the membrane in a fashion that can possibly lead to cell apoptosis.

To achieve such mechanical force from the inside of the cells, particles capable of reacting to external stimuli need to be incorporated. Thus, the idea of magnetic nanoparticles that can react to an outside magnetic field to yield a response has started to gain momentum. Since decades, magnetic nanoparticles have been investigated for magnetic hyperthermia, a technique in which cancer cell apoptosis is achieved after an alternating magnetic field (AMF) with high frequencies, usually ranging between 100 to 700 kHz, is applied on iron oxide magnetic nanoparticles accumulated at a tumor place, which in turn produce heat in response with the temperature ranging between 43 and 46 °C [108], [109], [110]. While AMF can enter deep tissue, the disadvantage of the technique lies on the lack of temperature control and consequently of uncontrolled necrosis of tissue. On another hand, when a magnetic field with low frequencies, usually less than 1000 Hz (Figure 30), is applied, iron oxide nanoparticles present a different response and are able to produce a mechanical force or torque without producing heat [111].

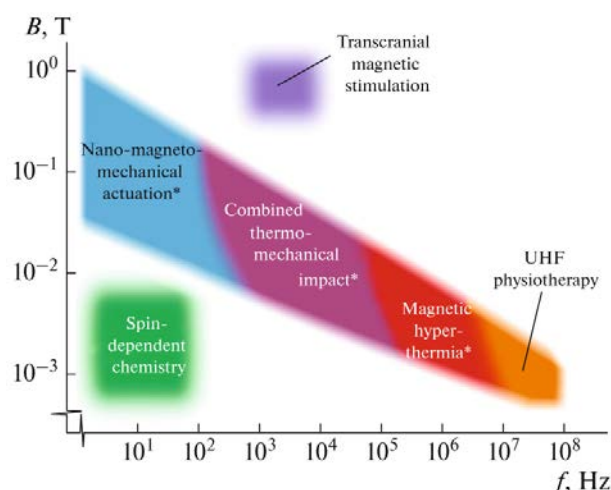


Figure 30: A schematic depiction of the frequencies and amplitude required for various techniques involving MNPs. Reproduced from Golovin *et al.*[112].

As described by Golovin *et al.*[113], when such low frequencies are applied, MNPs undergo mechanical rotational oscillations, a process that is named nanomagnetic mechanical activation (NMMA) and has been reported already in a multitude of studies as described below. The mechanical torque or rotation moment L ($L = \mu \cdot B$) with μ the magnetic moment of the nanoparticles and B the magnetic field amplitude imposed on the MNPs under a uniform AMF is responsible for forcing the MNPs in a rotational vibrational motion. When the MNPs are put under a non-homogeneous magnetic field, forces F are produced that can be utilized to create change and initiate a variety of responses. The later can be exploited for many purposes, such as targeted cell apoptosis but also other for other applications [114]. For instance, various studies have explored this motion to know whether it could activate ion channels in cells, control enzyme catalytic activity, change mechanical properties of cells to detect early stages of various diseases as well as achieve target drug delivery to cells simply by inducing a force strong enough to activate specific pathways. It is important to note that to induce any of the processes above it is imperative to achieve enough force by the MNPs. For example, ion channel activation dictates forces between 0.2 and 10 pN, activation of cellular membrane receptors requires 10 to 50 pN while the destruction of cellular membranes requires higher forces from 60 to 150 pN as tested by single-molecule force spectroscopy techniques [115].

To understand why the MNPs undergo oscillations that can force any type of mechanical change in a system, it is important to understand how the magnetic field acts on them and their magnetic moments. When single-domain superparamagnetic MNPs are dispersed in a medium, their magnetic moments μ are randomly oriented but when external AMF is applied, MNPs begin to perform rotational oscillations to achieve a magnetic ordering. Néel relaxation and

Brownian relaxation are two competing relaxation pathways for the magnetic moments μ when an AMF is applied [70]. Both produce a different effect on the MNPs and their magnetic moments. More specifically when the magnetic moment of the nanoparticle rotates without full rotation of the nanoparticle itself, then Néel relaxation takes place and heat is produced. This mechanism is the one aimed for magnetic hyperthermia.

On another hand, when the magnetic moment of the nanoparticle remains frozen but the particle itself rotates, Brownian relaxation takes place, resulting in no heat production and shear stress in the medium [71]. Both relaxations can occur simultaneously, and their appearance depends on the size of the MNPs, the viscosity of the dispersed liquid and the frequency of the magnetic field, due to the relaxation time τ favored for each frequency. The relaxation time [28, 29] for Néel relaxation is stated as $\tau_N = \frac{\tau_0}{2} \sqrt{\pi \frac{kT}{KV}} e^{KV/kT}$ with K being the anisotropy constant of the particle and V its volume. While Brownian relaxation time [117] is dependent on the hydrodynamic volume V_H of the particle and the viscosity of the liquid η with the Brownian relaxation time τ_B being: $\frac{3\eta V_H}{kT}$.

From Figure 31, it can be seen that Brownian motion favors nanoparticles with larger hydrodynamic volume while Néel relaxation smaller ones, in constant conditions at room temperature. As already said, the mechanisms can appear simultaneously and thus the effective relaxation time of the system τ is stated as: $\frac{1}{\tau} = \frac{1}{\tau_N} + \frac{1}{\tau_B}$

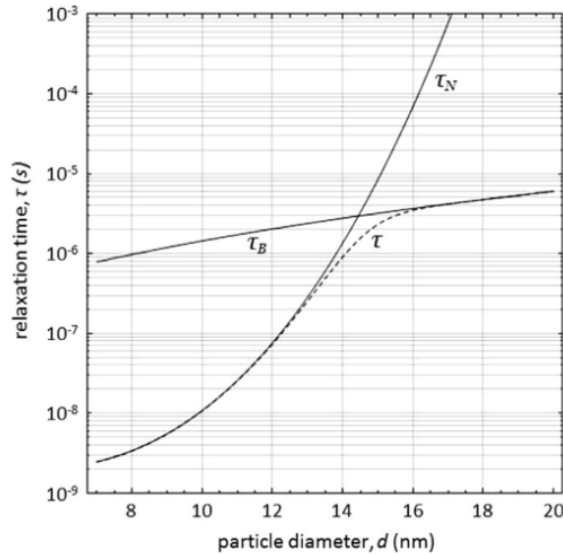


Figure 31: Relation between the effective relaxation time of single-domain magnetite MNPs and their diameter.

Reproduced from [71].

While Figure 31 demonstrates that smaller MNPs tend to favor Néel relaxation it is counterintuitive that smaller sizes are mostly utilized in literature for nanomagnetic mechanical activation, and the opposite would be favorable. But it is important to remember that MNP relaxation is also dependent on the frequency of the magnetic field. Specifically, for NMMA the frequencies are much lower, as already discussed above, lower than 1000 Hz and since the typically Brownian systems are in the order of 10^{-5} s for a frequency of 15 kHz it would be natural to assume that for even lower frequencies as the ones utilized in the NMMA systems this relaxation motion would be dominant. For example, free MNPs with a radius of 5-7 nm exhibit Brownian relaxation faster than Néel relaxation in lower frequency AMF [118].

Various parameters play a role when it comes to cell apoptosis due to magneto-mechanical response such as the type of magnetic field, *i.e.* alternating (AMF) or rotating magnetic field (RMF), the magnitude of the magnetic field (expressed as H_{ac} in $\text{kA}\cdot\text{m}^{-1}$ or B_{ac} in mT) as well as frequency (in Hz) and time of exposure [119], [120]. Moreover, concentration, size and shape of the nanoparticles play also a major role. Spherical, rod like, anisotropic or more complex morphologies [33–35] (Figure 32) result in different outcomes. Whether the nanoparticles are functionalized with target specific moieties that can offer them better internalization or even attachment to the cell membrane, such as anchoring to the plasma membrane or cytoskeleton, could yield better cell apoptosis results due to higher affinity and stronger interactions.[124], [125].

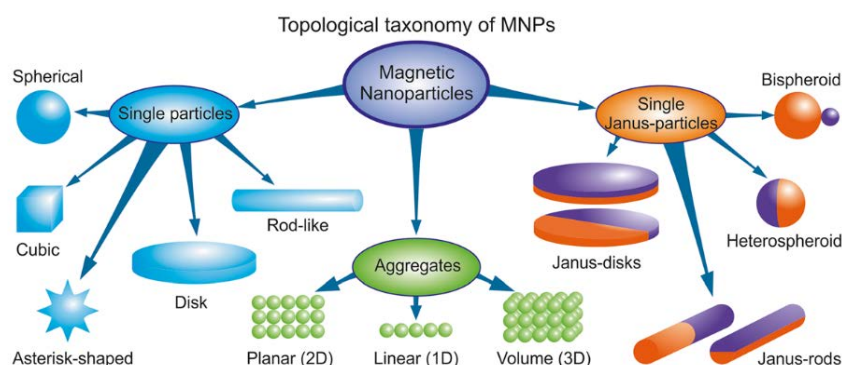


Figure 32: Demonstration of the variety of shapes for MNPs that can be used for magneto-mechanical actuation from Golovin *et al.*[115].

The physicochemical interactions of the MNPs must be also considered, such as Van der Waals interactions or hydrogen and electrostatic bonding. Besides, dipole-dipole moments between MNPs closely packed in a medium will inevitably affect their acting mechanism and can only be ignored when the MNPs are coated with a nonmagnetic shell, for example gold shell [126]. It is important to consider the viscosity of the liquid which embeds the MNPs and offers an

additional viscous resistance. The ways the nanoparticles respond to the field crucially impacts the outcome, for example, whether the NPs respond in an individual way to the field or aggregate and give a group reaction would result in a different mechanism of action [39-40]. Finally, the internalization and final placement of NPs in the cells will inevitably affect their mechanism of reaction [129].

Golovin *et al.* have published a variety of studies on how magnetic nanoparticles act under an alternating magnetic field and what are the theoretical forces that can potentially be produced by a variety of morphologies and conformations [23–25,30,38,42]. The authors have presented comprehensive explanations and calculations for each morphology. For example, single nanoparticles with a core size of 10 nm can produce a small force F of around 0.1 pN when under a non-uniform magnetic field of 0.1 T, which may not be enough for membrane destruction but can be exploited for other purposes. Of course, it is important to consider here whether the MNPs are attached to a targeted macromolecule or protein, enzyme etc. and how this attachment may affect the resulting force. As they suggest, the theoretical contact point would produce a force with higher magnitudes such as 100-400 pN for same size MNPs and a magnetic field of 1T. Such an increase is due to the support that the attachment of the MNPs onto the macromolecule offered, or as the author writes, counter-body.

The forces produced by each morphology differ with each other as can be expected since the contact points each morphology can offer differ as well. For example, a rod like magnetic nanoparticle, with a length L and a magnetic moment μ along its long axis, when attached to a membrane can produce forces from its tips [23,25]. The authors describe the motion of the MNP when a non-homogeneous AMF is applied, as a kayak paddle. Such oscillation will produce forces on the tips of the particle which will affect the membrane they are in contact with (Figure 33).

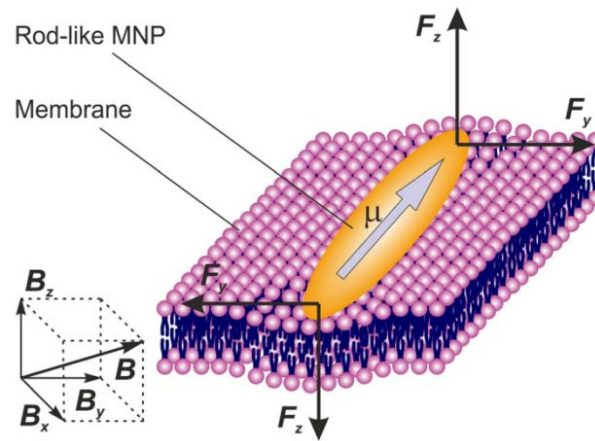


Figure 33: Rod like MNP attached to a membrane and the forces F produced from [115].

Interestingly according to the equation $F_z = J_s \rho V B_z / L$ the force F_z does not depend on the length of the MNP, with $V = D^2 \cdot L$ with D being the diameter of MNP. Here the calculated pressure $P = F_z / D^2$ that was found to be produced by the tips of the MNPs was found to be 40 kPa which is a lot higher than the stiffness of a cytoskeleton's membrane, deeming these MNPs capable to ensue possible damage on attached cells, based on these theoretical values.

To increase the forces produced by magnetic nanoparticles the use of aggregates instead of rod-like nanoparticles would be better. In this case, the aggregation of MNPs due to the application of a magnetic field would increase the total magnetic moment of the system when compared to a single MNP. Through theoretical calculations by Golovin et al. [115] closely positioned MNPs whose magnetic moments are aligned under the AMF will form a worm-like structure due to their attraction to each other in order to achieve a minimal magnetostatic interaction energy U_D . Thus, if the aggregates are stable enough, they could be exploited in order to create a system that has more potential as mechanical actuators.

Experimental literature on magneto-mechanical actuation:

From a theoretical standpoint, MNPs can be used as actuators that can cause a variety of possible mechanical changes or deformations in a system, by the shear strain that is produced after a magnetic field with low frequencies is applied as already mentioned in many studies. For instance, ultra small iron oxide magnetic nanoparticles (USPIONS) small as 6 nm were combined with a rotating magnetic field (RMF) and were able to cause cell apoptosis up to 34% rate of cell viability of a specific pancreatic cancer cell line [131]. A low amplitude magnetic field of 40 mT with 1 Hz frequency was found to offer the best results while higher amplitudes did not help to increase cell apoptosis. Furthermore, the authors investigated the mechanism responsible for the observed apoptosis by the mechanical forces produced. Specifically, after staining cells loaded with USPIONS with Lysotracker, a fluorescent dye which specifically labels the lysosomal compartments, and applying a RMF, they discovered that a lysosomal rupture is visible (Figure 34).

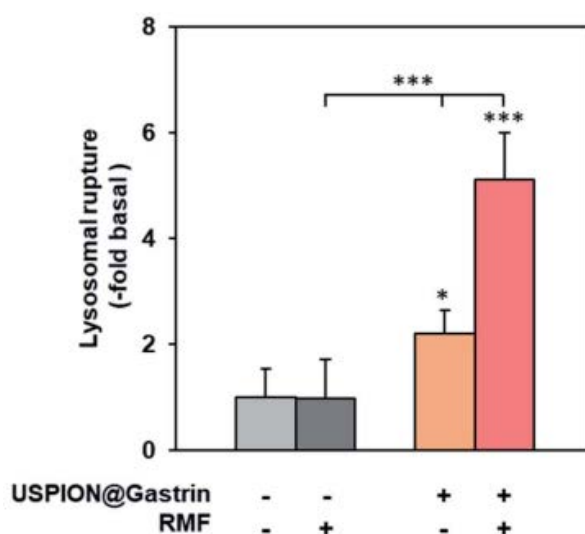


Figure 34: Flow cytometry result quantifying the lysosomal rupture with and without the application of RMF and USPIONS. Reproduced from [131].

Following the lysosomal rupture, they investigated which enzymes of the inflammatory cascade were, at least partially, responsible for cell apoptosis and concluded that cathepsin-B plays a major role. Specifically, they incubated USPIONS functionalized by a targeting ligand (gastrin) with cells which had an inhibitor for cathepsin-B or not, as well as an inhibitor or not for cathepsin-D. The results suggested that in the absence of a cathepsin-B inhibitor and the presence of a RMF, the USPIONS were able to cause cell apoptosis with the produced torque, whereas when the inhibitor was present, cell apoptosis was prevented (Figure 35).

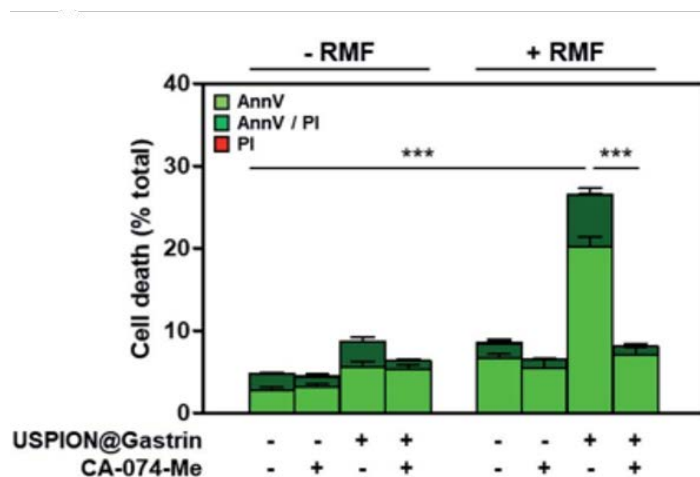


Figure 35: Effect of cathepsin-B activity on cell death percentage. Reproduced from [131].

In another study, anisotropic disk-shaped NiFe vortex particles (1 μm diameter) were utilized as mechanical actuators in order to cause cell apoptosis of a human renal cancer cell line *in vitro* [122]. Specifically, the main focus was to cause membrane disruption but not destruction, by attaching the particles onto cancer cell membranes. It was made possible by functionalizing the particles with an antibody; anti hCA9 rabbit polyclonal IgG, in order to target one of the common hypoxia cell markers called Carbonic anhydrase CA9 which has been shown to over express in tumors but not in healthy cells [44,45]. The disks were incubated with SKRC-59 hCA9 cells and an amount of 30 disks was found to be bound per cell. An alternating magnetic field of 30 mT was applied onto the cells, with a frequency of 20 Hz for 1 h, and finally the cells were incubated for another 6 h. After the previously described process, renal cell viability was checked and a decrease by almost 70% of viable cells was observed, when compared to control cells with no magneto-mechanical treatment (Figure 36).

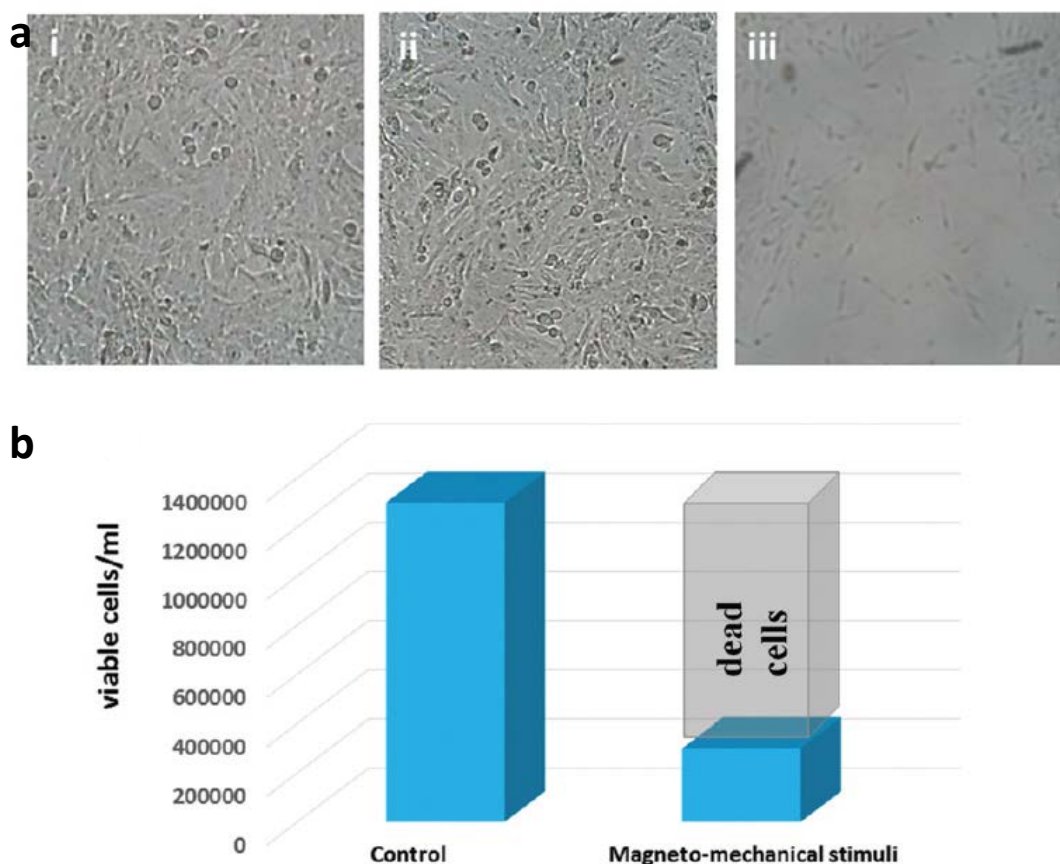


Figure 36: a) Optical microscopy results comparing control cells (i), control cells incubated with the functionalized disks (ii) and cells after the alternating magnetic field treatment (iii). b) Cell counting on control cells and after the treatment of cells incubated with functionalized disks. Reproduced from [122].

Further confirmation on the apoptosis was observed by flow cytometry where the treated cells were stained with Alexa Fluor 488 annexin V to target the necrotic as well as the apoptotic cells and propidium iodide which targets the nucleus region of necrotic cells. Herein, it was observed an increase of the apoptotic cells while also a visible decrease of viable cells and cell population in general, confirming the original optical microscopy results. The mechanism of the magneto-mechanical caused apoptosis was investigated as well and was ascribed to the activation of an intracellular biochemical response which was triggered by the extracellular membrane vibrations. The authors suggest that ion Ca channels were activated and resulted in a caspase activation, which leads to cellular apoptosis.[134]

In another study, a combination of antibody functionalized spherical nanoparticles with a dynamic field (DMF), which forces the MNPs to rotate around their axes, were utilized in order to study how DMF affects internalization of MNPs into cells as well as cell apoptosis and their effect on lysosomes [124]. More specifically, spherical nanoparticles with a size of 100 nm were divided in two groups with one being functionalized with an antibody specific to the

membrane of lysosomes, LAMP1 and the second one was left non-functionalized. Both MNPs were incubated with rat insulinoma cells (INS-1) and studied for the effect of the DMF on their internalization. LAMP1-MNPs provided a higher internalization, 21.2% compared to non-functionalized MNPs, 13.3% after an application of DMF with 20 Hz frequency.

Further, Zhang *et al.* studied the effect of the MNPs and DMF on lysosomes and whether this combination is capable of their disruption. Indeed, after following up with the fluorescent intensity of LysoTracker Green, a lysosomal compartment tracker, they observed a decrease of intensity after another 20 min treatment with DMF in the cells that contained LAMP1-MNPs compared to non-functionalized MNPs where the intensity drop was not substantial (Figure 13). Such an interesting distinctive behavior between the MNPs effect may be explained by the fact that the LAMP1-MNPs are attached onto the membrane and thus when rotating under the DMF the destruction of the membrane is more probable while during the rotation of the unattached MNPs, the disturbance of the membrane is not as intense. Such a hypothesis is proven in the same study after testing the pH change of cell compartments. Specifically, after lysosomal destruction, the acidic compartments in the cell would decrease in volume and to test such a thing an acidotropic probe was employed to measure the intensity decrease of LysoSensor green DND 189. Herein, the intensity decreased significantly more with the combination of LAMP1-MNPs and DMF when compared to bare MNPs and DMF, 368 AU/cell compared to 769.5 AU/cell (Figure 37).

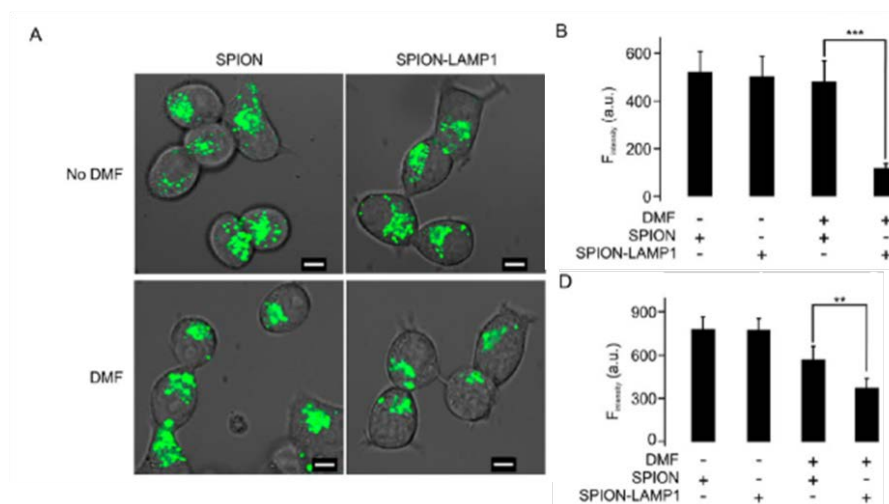


Figure 37: a) Cells embedded with MNPs stained with LysoTracker Green with and without DMF treatment, b) fluorescence intensity decrease of LysoTracker Green and c) fluorescence intensity decrease of LysoSensor green.

Reproduced from [124].

Another study, demonstrating magneto-mechanical actuation, employed small superparamagnetic iron oxide nanoparticles (SPIONs) in order to create disruption of cell membrane facilitated by an AC alternating magnetic field (AMF) with a rather low radio-frequency of 50 kHz [130]. SPIONs with a size ranging from 7 to 8 nm were functionalized with a variety of copolymers, with specific emphasis given on PAA-P85-SMNPs Poly(acrylic acid)-Pluronic P85. They were incorporated in two carcinogenic, MDA-MB-231 and BT474 cell lines as well as a non-carcinogenic cell line MCF10A. Application of a low frequency pulsed or continuous AMF resulted in a reduction of cell viability for the carcinogenic cell lines while on the other hand the non-carcinogenic line presented no significant change suggesting specificity in this method for cancerous cells. Specifically, at a concentration of 0.05 mg/mL of PAA-P85-SMNPs, both cancerous cell lines presented a reduction in cell viability but reacted differently depending on the regime that was used. For example, MDA-MB-231 presented 50% cell viability in the pulsed regime, and no cell viability reduction for the continuous one, while BT474 presented 25% reduction of cell viability compared to 50% reduction in continuous flow, suggesting that the pulsed regime yielded better results. On another hand, MCF10A presented no response to neither pulsed nor continuous regime (Figure 38).

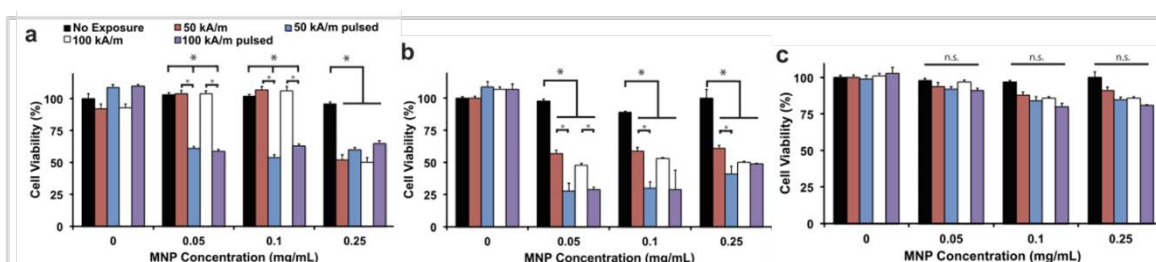


Figure 38: Cell viability and effect of exposure to alternating magnetic fields with different values and regimes for a)MDA-MB-231, b)BT474 and c)MCF10A. Reproduced from[130].

The mechanism of cell apoptosis was also investigated. It appeared to be different for the mechanism described above [124], more specifically no lysosomal rupture was observed, with the lysosomes remaining intact and no leakage of their acidic compartments to the cytosol. The reduction of cell viability was attributed to the disruption of actin skeleton, a key element in the cytoskeleton which is highly intertwined with the lysosomal system of the cells and has been shown already as an important parameter that could lead to cell apoptosis [135]. It was confirmed by confocal microscopy which showed a disruption of the actin cytoskeleton of the cancerous cell lines but not for the control cell line due to the higher fragility of the cytoskeleton of cancerous cells when magneto-mechanical forces were applied, leading to cell apoptosis (Figure 39).

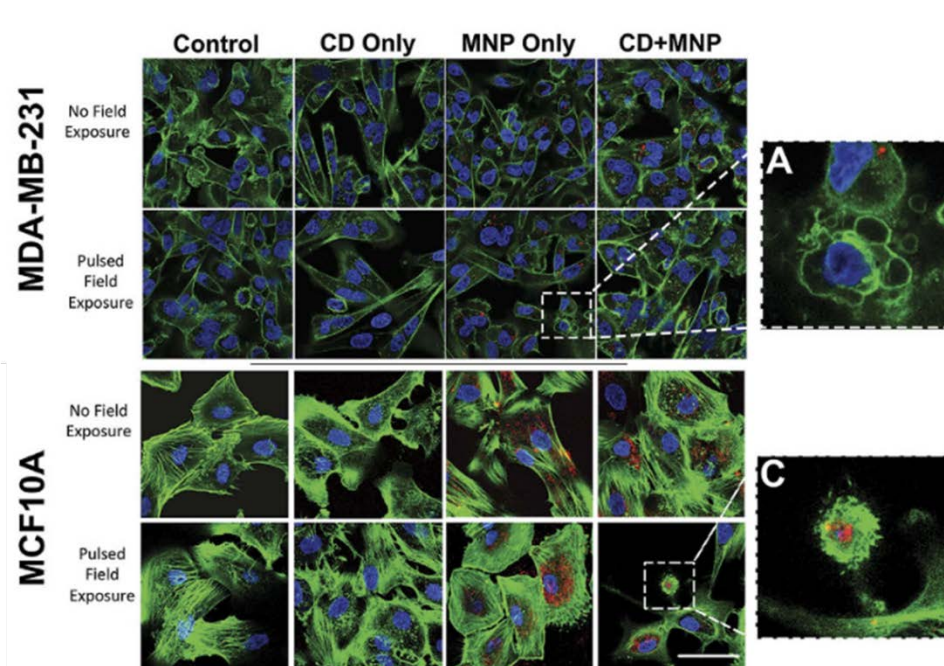


Figure 39: Confocal images of actin (green) disruption before and after the application of alternating magnetic field. Reproduced from [130].

Another study utilized a low frequency magnetic field (LF RMF) to induce glioblastoma cell apoptosis both *in vitro* and *in vivo* [136]. Disk-shaped microparticles (MP) of 2 μm diameter ($\text{Ni}_{80}\text{Fe}_{20}/5\text{ nm Au}$) were incubated *in vitro* in human glioblastoma cell line U87 followed by a treatment with a rotating magnetic field of 1T magnitude and 20 Hz frequency. After 30 min of treatment, the cells presented evident disruption of their cellular compartments. The internalization mechanism of the disks which was studied by TEM, suggested that they were accumulated near the nuclear membrane of the cells yet did not cause any cellular destruction without any LFMF treatment. After 1 min of treatment, cells exhibited an immediate shape change and beginning of destruction (Figure 40a). To study whether these MPs can cause cell apoptosis and tumor growth inhibition *in vivo*, U87 cells already incubated with MPs were injected into athymic nude mice. The mice were treated with RMF for 1 h per day for 7 days. 21 days after the treatment, 60% of the treated group appeared to have a controlled tumor size while 28 days after the treatment, 40% had no tumor signal, as followed by bioluminescence imaging (BLI) of a luciferase gene capable of tracking tumor growth. On the other hand, the control group that had not undergone LFRMF treatment but was injected with the U87MPs showed a little tumor decrease after 50 days (Figure 40b). Such results indicated that that a combination of the disks with LF RMF treatment could succeed in controlling the growth of the tumor.

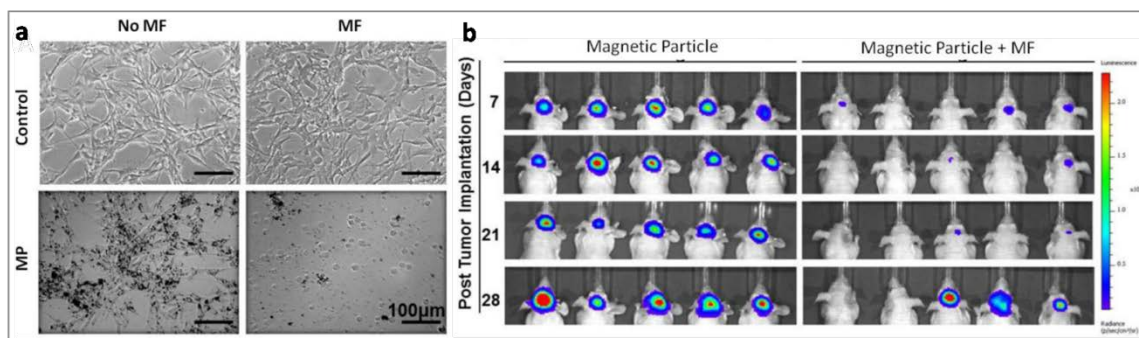


Figure 40: a) TEM images of U87 cells with or without MPs before and after treatment with LFMF and b) Bioluminescence imaging of *in vivo* implantation of MPs in mice and the progress of tumor growth during and after the LF RLF treatment. Reproduced from [136].

A more recent study also investigated the possible damaging effects of a LF RMF on glioblastoma cancer cells due to lysosomal membrane disruption [127]. In this case, 62 nm size cube shaped iron oxide magnetic nanoparticles, doped with zinc, did not cause disruption by rotation around their axes as in previous studies but formed anisotropic linear aggregates during the application of the field. These chains subsequently rotated, creating enough movement that produced strong enough forces in response to the field causing a disruption of the lysosomal membrane, leading to cell apoptosis.

The same cancer glioma cell line as discussed above, U87, was utilized to embed nanoparticles functionalized with the EGF peptide, which made them target specifically the tumor cell membrane. The nanoparticles were rendered non-toxic up to 200 mg/mL and were found to accumulate mostly in the lysosomes of the cells. ARMF at low frequency of 15 Hz was found to be enough to cause aggregation of the nanoparticles inside the lysosomes and damage their membranes, resulting in a change of cell morphology and in some cases membrane destruction, with the treated cells to present almost 58% membrane destruction. The process was visualized via PI staining, a dye staining cells with compromised membranes [137]. Finally, cell viability was investigated by staining cells with Annexin V, a protein involved in cell membrane repair, in order to follow the apoptotic cells, [138] and after a three day treatment of RMF, 90% of the cells appeared to be damaged (Figure 41).

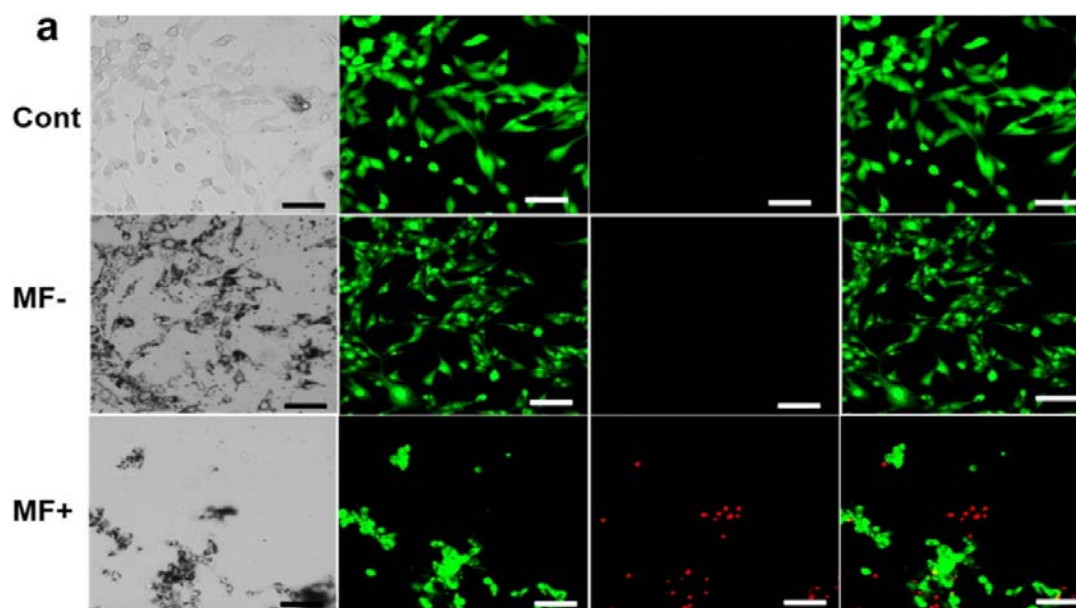


Figure 41: Fluorescence micrographs of cells embedded with EGF-MNPs before and after RMF treatment, stained with Calcein AM for alive cells (green fluorescence) and PI for dead cells (red fluorescence). Reproduced from [127].

A similar study depicting cell apoptosis *via* formation of elongated iron oxide nanoparticles aggregates under the application of an alternating magnetic field was published [128]. An AMF was applied on breast cancer MDA-MB-231 cells embedding 80 nm diameter superparamagnetic iron oxide nanoparticles, resulting in linear aggregate formation of the NPs inside the cells in the direction of the field. The aggregate formation caused significant movement capable of achieving cell apoptosis in the range of 26% 1 day after treatment with a very high amplitude (4.7 T) magnetic field at a low frequency of 5.4 kHz (Figure 42).

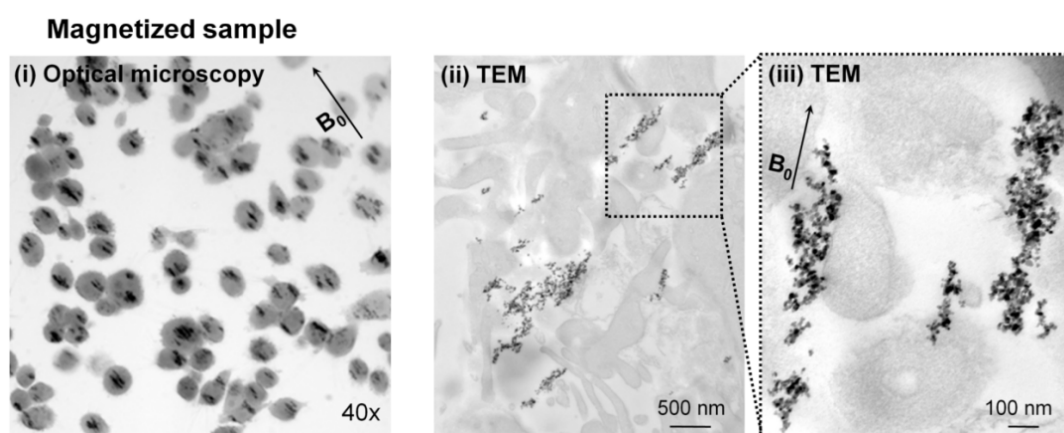


Figure 42: TEM images of MDA-MB-231 cells embedded with MNPs after the application of 4.7 T magnetic field. Reproduced from [128].

Glioblastoma cell membrane destruction was also investigated by utilizing iron-nickel disks and their response to an AMF [125]. A specific target biofunctionalization of the disks with anti-human-IL13 α 2R antibody was performed to specifically target the cells. The anisotropic disk shape morphology aided the membrane destruction after the application of the field. Specifically, when a field is applied, the torque created aligned the disks in the field direction causing rotation of the disks which were anchored onto the membrane. Interestingly, the authors found that smaller frequencies of 10 and 20 Hz were able to induce higher cell apoptosis results compared to higher frequencies, 90% compared to 75% and lower. Evident morphological change, loss of structural integrity as well as “edges” on the cell surface were some of the observed phenomena.

Multiwalled carbon nanotubes (MWCNTs) exhibiting magnetic properties were also reported to induce cell apoptosis after an application of a rotating magnetic field to breast cancer cells MCF-7 [139]. The nanotubes were observed to cause membrane permeabilization and structural changes after RMF application of minimum 40 mT due to their magnetic nature, which allowed them to rotate or create aggregates that responded to the field with movement. Such response was able to cause cell membrane damage and surface roughness, specifically when magnetic fields higher than 40 mT were applied, together with leakage of lactate dehydrogenase (LDH) enzyme, which was observed, thereby verifying cell membrane damage [140] (Figure 43).

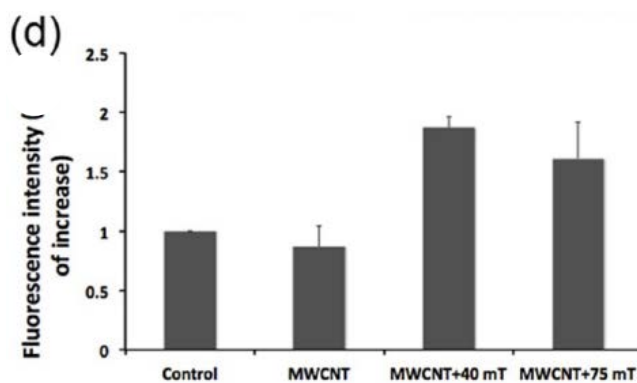


Figure 43: LDH leakage from cells. Reproduced from [139].

A more recent study employed anisotropic rectangular Fe-Cr-Nb-B microparticles (MPs) as magneto-mechanical actuators to cause cell apoptosis to MG-63 human osteosarcoma (HOS) and Normal Human Dermal Fibroblasts (NHDF), while applying a low frequency rotating magnetic field [123]. The authors investigated the correlation between concentration, frequency, and magnitude of magnetic field on cell viability. The highest concentration of 5 mg/mL of MPs presented the highest apoptosis value, while when keeping the concentration at 2 mg/mL and changing frequencies, it was found that above 50 Hz, cell viability increased, a

phenomenon which was explained by the MPs inability to react anymore to the rotating field efficiently (asynchronous rotation). Time of exposure exhibited linear correlation with cell viability decrease, accordingly. Interestingly, when stable parameters were chosen for cancer cells and non-cancerous cells, cell viability decreased by 40% for MG-63 while NHDF showed no decrease, suggesting a difference in the structure between cancerous and healthy cells, which affects the stability of the membranes a phenomenon which was already discussed above [130] suggesting the structural weakness of the cytoskeleton of cancer cells to be a possible explanation. Finally, while investigating the mechanism by which the MPs cause cell apoptosis, it was observed that the nanoparticles were located mainly on the cell membrane and in the cytosol, thus when rotating field was applied, their mechanism of rotation impacted cellular outer membranes and did not involve lysosomal damage as in the studies presented above [124].

As can be seen from the above studies, magneto-mechanical actuation can indeed be achieved via the utilization of iron oxide nanoparticles and various architectures of magnetic nanoparticles can be employed to achieve possible cell apoptosis such as spheres, disks, cube and rods. Smaller frequencies are utilized for magneto-mechanical actuation in order to ensure heat production but also to induce Brownian relaxation which forces the nanoparticles to produce a mechanical force which in turn can be utilized. Both rotating magnetic field (RMF) and alternating magnetic field (AMF) seem to be able to produce the desired torque from nanoparticles while low frequencies are applied. Via magneto-mechanical actuation, cell apoptosis was indeed possible but the biological pathways which are followed need further investigation.

Conclusion:

In this chapter we have explored the difference between polymersomes and why they are considered a good alternative to liposomes as to act as drug delivery agents. Mainly polymersomes exhibit an extraordinary capacity in enclosing both hydrophilic and hydrophobic cargo simultaneously. It is possible to synthesize polymersomes by utilizing a big range of polymers thus the final characteristics are easily tunable, such as size, length of membrane and responsiveness to various stimuli. Furthermore, polymersomes are able to be formed from a variety of copolymers such as diblock, triblock, brush, graft etc. Further on, stimuli-responsive polymersomes were discussed with a particular interest in magnetic polymersomes and their ability in deforming under a magnetic field. To study the advantages of elongated structures we discussed how various anisotropic morphologies compare to classical spherical morphologies which are usually chosen as drug-delivery agents. Their advantages are discussed, such as a longer circulation time, better internalization, and cell uptake. As well as better drug delivery capabilities due to those advantages. Finally, magneto-mechanical actuation of iron oxide nanoparticles (IONPs) is discussed as a possible route to cause cell disruption that may lead to cell death. In this context, the behavior of IONPs under rotating magnetic field is described and various literature is reported which proves the concept of magneto-mechanical actuation.

The goal of this thesis was to synthesize magnetic polymersomes whose morphology would be able to shift from spherical to an elongated one under a static magnetic field. Furthermore, the elongated morphology would be stabilized via cross-linking to ensure its anisotropy once the field would no longer be applied. The point of creating an anisotropic morphology was based on the idea of magneto-mechanical destruction, meaning that our system could act as an actuator of cell destruction once it was internalized and the static magnetic field was applied. In this context we first studied the synthesis of two copolymeric systems which could be utilized in the polymersome formation. A graft copolymer PEG-*b*-TDOC-*g*-PI and a triblock copolymer PEG-*b*-PTMC-*b*-PI were chosen as the two systems whose synthesis and self-assembly behavior were studied. Furthermore, we synthesized hydrophobically coated iron oxide nanoparticles and studied the self-assembly behavior of the polymeric system along with the IONPs, where the polymersome morphology was confirmed. The final magnetic polymersomes were studied under a static magnetic field of 0.4T where the elongation of the polymersomes was stabilized via a UV cross-linking of the hydrophobic membrane. The elongated morphologies were also studied via TEM and SANS analysis where their formation was verified.

References:

- [1] D. S. Williams, I. A. B. Pijpers, R. Ridolfo, and J. C. M. van Hest, "Controlling the morphology of copolymeric vectors for next generation nanomedicine," *J. Control. Release*, vol. 259, pp. 29–39, 2017.
- [2] M. Müllner *et al.*, "Size and rigidity of cylindrical polymer brushes dictate long circulating properties in vivo," *ACS Nano*, vol. 9, no. 2, pp. 1294–1304, 2015.
- [3] R. Agarwal, V. Singh, P. Journey, L. Shi, S. V. Sreenivasan, and K. Roy, "Mammalian cells preferentially internalize hydrogel nanodiscs over nanorods and use shape-specific uptake mechanisms," *Proc. Natl. Acad. Sci. U. S. A.*, vol. 110, no. 43, pp. 17247–17252, 2013.
- [4] R. Madathiparambil Visalakshan *et al.*, "The Influence of Nanoparticle Shape on Protein Corona Formation," *Small*, vol. 16, no. 25, 2020.
- [5] E. Scarpa *et al.*, "Tuning cell behavior with nanoparticle shape," *PLoS One*, vol. 15, no. 11 November, pp. 1–16, 2020.
- [6] T. Anajafi and S. Mallik, "Polymersome-based drug-delivery strategies for cancer therapeutics.," *Ther. Deliv.*, vol. 6, no. 4, pp. 521–534, 2015.
- [7] W. K. Spoelstra, S. Deshpande, and C. Dekker, "Tailoring the appearance: what will synthetic cells look like?," *Curr. Opin. Biotechnol.*, vol. 51, pp. 47–56, 2018.
- [8] H. Nsairat, D. Khater, U. Sayed, F. Odeh, A. Al Bawab, and W. Alshaer, "Liposomes: structure, composition, types, and clinical applications.," *Heliyon*, vol. 8, no. 5, p. e09394, May 2022.
- [9] E. Rideau, R. Dimova, P. Schwille, F. R. Wurm, and K. Landfester, "Liposomes and polymersomes: a comparative review towards cell mimicking," *Chem. Soc. Rev.*, vol. 47, no. 23, pp. 8572–8610, 2018.
- [10] D. E. Discher and F. Ahmed, "Polymersomes," *Annu. Rev. Biomed. Eng.*, vol. 8, pp. 323–341, 2006.
- [11] C. Sanson *et al.*, "Doxorubicin loaded magnetic polymersomes: Theranostic nanocarriers for MR imaging and magneto-chemotherapy," *ACS Nano*, vol. 5, no. 2, pp. 1122–1140, 2011.
- [12] I. Meerovich and A. K. Dash, "Polymersomes for drug delivery and other biomedical applications," in *Materials for biomedical engineering*, Elsevier, 2019, pp. 269–309.
- [13] M.-H. Li and P. Keller, "Stimuli-responsive polymer vesicles," *Soft Matter*, vol. 5, no. 5, pp. 927–937, 2009.
- [14] K. T. Kim, J. J. L. M. Cornelissen, R. J. M. Nolte, and J. C. M. van Hest, "A Polymersome Nanoreactor with Controllable Permeability Induced by Stimuli-Responsive Block Copolymers," *Adv. Mater.*, vol. 21, no. 27, pp. 2787–2791, Jul. 2009.
- [15] D. D. Lasic and D. Papahadjopoulos, *Medical applications of liposomes*. Elsevier, 1998.
- [16] L. Sercombe, T. Veerati, F. Moheimani, S. Y. Wu, A. K. Sood, and S. Hua, "Advances and challenges of liposome assisted drug delivery," *Front. Pharmacol.*, vol. 6, p. 286, 2015.

- [17] M. C. Branco and J. P. Schneider, "Self-assembling materials for therapeutic delivery," *Acta Biomater.*, vol. 5, no. 3, pp. 817–831, 2009.
- [18] C. Sanson, C. Schatz, J. F. Le Meins, A. Brûlet, A. Soum, and S. Lecommandoux, "Biocompatible and biodegradable poly(trimethylene carbonate)-b-Poly (L-glutamic acid) polymersomes: Size control and stability," *Langmuir*, vol. 26, no. 4, pp. 2751–2760, 2010.
- [19] H. C. Shum, J.-W. Kim, and D. A. Weitz, "Microfluidic Fabrication of Monodisperse Biocompatible and Biodegradable Polymersomes with Controlled Permeability," *J. Am. Chem. Soc.*, vol. 130, no. 29, pp. 9543–9549, Jul. 2008.
- [20] J. Du, Y. Tang, A. L. Lewis, and S. P. Armes, "pH-Sensitive Vesicles Based on a Biocompatible Zwitterionic Diblock Copolymer," *J. Am. Chem. Soc.*, vol. 127, no. 51, pp. 17982–17983, Dec. 2005.
- [21] D. E. Discher *et al.*, "Emerging applications of polymersomes in delivery: From molecular dynamics to shrinkage of tumors," *Prog. Polym. Sci.*, vol. 32, no. 8, pp. 838–857, 2007.
- [22] L. Messenger, J. Gaitzsch, L. Chierico, and G. Battaglia, "Novel aspects of encapsulation and delivery using polymersomes," *Curr. Opin. Pharmacol.*, vol. 18, pp. 104–111, 2014.
- [23] D. H. Levine *et al.*, "Polymersomes: A new multi-functional tool for cancer diagnosis and therapy," vol. 46, no. 1, pp. 25–32, 2009.
- [24] B. M. Discher *et al.*, "Polymersomes: Tough vesicles made from diblock copolymers," *Science (80-.)*, vol. 284, no. 5417, pp. 1143–1146, 1999.
- [25] F. Araste, A. Aliabadi, K. Abnous, S. M. Taghdisi, M. Ramezani, and M. Alibolandi, "Self-assembled polymeric vesicles: Focus on polymersomes in cancer treatment," *J. Control. Release*, vol. 330, no. October 2020, pp. 502–528, 2021.
- [26] J. F. Le Meins, O. Sandre, and S. Lecommandoux, "Recent trends in the tuning of polymersomes' membrane properties," *Eur. Phys. J. E*, vol. 34, no. 2, 2011.
- [27] J. Leong, J. Y. Teo, V. K. Aakalu, Y. Y. Yang, and H. Kong, "Engineering Polymersomes for Diagnostics and Therapy," *Adv. Healthc. Mater.*, vol. 7, no. 8, p. 1701276, Apr. 2018.
- [28] J. C. M. Van Hest, D. A. P. Delnoye, M. W. P. L. Baars, M. H. P. Van Genderen, and E. W. Meijer, "Polystyrene-dendrimer amphiphilic block copolymers with a generation-dependent aggregation," *Science (80-.)*, vol. 268, no. 5217, pp. 1592–1595, 1995.
- [29] L. Zhang and A. Eisenberg, "Multiple morphologies and characteristics of 'crew-cut' micelle-like aggregates of polystyrene-b-poly(acrylic acid) diblock copolymers in aqueous solutions," *J. Am. Chem. Soc.*, vol. 118, no. 13, pp. 3168–3181, 1996.
- [30] K. Yu, L. Zhang, and A. Eisenberg, "Novel morphologies of 'crew-cut' aggregates of amphiphilic diblock copolymers in dilute solution," *Langmuir*, vol. 12, no. 25, pp. 5980–5984, 1996.
- [31] L. Zhang and A. Eisenberg, "Formation of crew-cut aggregates of various morphologies from amphiphilic block copolymers in solution," *Polym. Adv. Technol.*, vol. 9, no. 10–11, pp. 677–699, 1998.
- [32] B. M. Discher, D. A. Hammer, F. S. Bates, and D. E. Discher, "Polymer vesicles in

- various media,” *Curr. Opin. Colloid Interface Sci.*, vol. 5, no. 1–2, pp. 125–131, 2000.
- [33] K. E. B. Doncom, L. D. Blackman, D. B. Wright, M. I. Gibson, and R. K. O’Reilly, “Dispersity effects in polymer self-assemblies: A matter of hierarchical control,” *Chem. Soc. Rev.*, vol. 46, no. 14, pp. 4119–4134, 2017.
- [34] A. Blanazs, S. P. Armes, and A. J. Ryan, “Self-assembled block copolymer aggregates: From micelles to vesicles and their biological applications,” *Macromol. Rapid Commun.*, vol. 30, no. 4–5, pp. 267–277, 2009.
- [35] J. N. Israelachvili, D. J. Mitchell, and B. W. Ninham, “Theory of self-assembly of lipid bilayers and vesicles,” *Biochim. Biophys. Acta - Biomembr.*, vol. 470, no. 2, pp. 185–201, 1977.
- [36] Y.-Y. Won, A. K. Brannan, H. T. Davis, and F. S. Bates, “Cryogenic Transmission Electron Microscopy (Cryo-TEM) of Micelles and Vesicles Formed in Water by Poly(ethylene oxide)-Based Block Copolymers,” *J. Phys. Chem. B*, vol. 106, no. 13, pp. 3354–3364, Apr. 2002.
- [37] G. Riess, “Micellization of block copolymers,” *Prog. Polym. Sci.*, vol. 28, no. 7, pp. 1107–1170, 2003.
- [38] S. Y. Kim, H. J. Kim, K. E. Lee, S. S. Han, Y. S. Sohn, and B. Jeong, “Reverse thermal gelling PEG - PTMC diblock copolymer aqueous solution,” *Macromolecules*, vol. 40, no. 15, pp. 5519–5525, 2007.
- [39] J. C.-M. Lee *et al.*, “Preparation, stability, and in vitro performance of vesicles made with diblock copolymers,” *Biotechnol. Bioeng.*, vol. 73, no. 2, pp. 135–145, Apr. 2001.
- [40] H. Sun, F. Meng, R. Cheng, C. Deng, and Z. Zhong, “Reduction and pH dual-bioresponsive crosslinked polymersomes for efficient intracellular delivery of proteins and potent induction of cancer cell apoptosis,” *Acta Biomater.*, vol. 10, no. 5, pp. 2159–2168, 2014.
- [41] G. Yu and A. Eisenberg, “Multiple Morphologies Formed from an Amphiphilic ABC Triblock Copolymer in Solution,” *Macromolecules*, vol. 31, no. 16, pp. 5546–5549, Aug. 1998.
- [42] A. Blanazs, M. Massignani, G. Battaglia, S. P. Armes, and A. J. Ryan, “Tailoring Macromolecular Expression at Polymersome Surfaces,” *Adv. Funct. Mater.*, vol. 19, no. 18, pp. 2906–2914, Sep. 2009.
- [43] R. Stoenescu and W. Meier, “Vesicles with asymmetric membranes from amphiphilic ABC triblock copolymers,” *Chem. Commun.*, no. 24, pp. 3016–3017, 2002.
- [44] A. Wittemann, T. Azzam, and A. Eisenberg, “Biocompatible polymer vesicles from biamphiphilic triblock copolymers and their interaction with bovine serum albumin,” *Langmuir*, vol. 23, no. 4, pp. 2224–2230, 2007.
- [45] R. Takahashi *et al.*, “Polymersome formation induced by encapsulation of water-insoluble molecules within ABC triblock terpolymers,” *Polym. Chem.*, vol. 11, no. 20, pp. 3446–3452, 2020.
- [46] E. V. Konishcheva, D. Daubian, S. Rigo, and W. P. Meier, “Probing membrane asymmetry of ABC polymersomes,” *Chem. Commun.*, vol. 55, no. 8, pp. 1148–1151, 2019.
- [47] S. Iqbal, M. Blenner, A. Alexander-Bryant, and J. Larsen, “Polymersomes for

- Therapeutic Delivery of Protein and Nucleic Acid Macromolecules: From Design to Therapeutic Applications,” *Biomacromolecules*, vol. 21, no. 4, pp. 1327–1350, 2020.
- [48] I. W. Wyman and G. Liu, “Micellar structures of linear triblock terpolymers: Three blocks but many possibilities,” *Polymer (Guildf)*, vol. 54, no. 8, pp. 1950–1978, 2013.
- [49] W. Zhao, D. Chen, Y. Hu, G. M. Grason, and T. P. Russell, “ABC triblock copolymer vesicles with mesh-like morphology,” *ACS Nano*, vol. 5, no. 1, pp. 486–492, 2011.
- [50] F. Liu and A. Eisenberg, “Preparation and pH Triggered Inversion of Vesicles from Poly(acrylic Acid)-block-Polystyrene-block-Poly(4-vinyl Pyridine),” *J. Am. Chem. Soc.*, vol. 125, no. 49, pp. 15059–15064, 2003.
- [51] A. Bhattacharya and B. N. Misra, “Grafting: a versatile means to modify polymers: Techniques, factors and applications,” *Prog. Polym. Sci.*, vol. 29, no. 8, pp. 767–814, 2004.
- [52] H. Gao and K. Matyjaszewski, “Synthesis of Molecular Brushes by ‘Grafting onto’ Method: Combination of ATRP and Click Reactions,” *J. Am. Chem. Soc.*, vol. 129, no. 20, pp. 6633–6639, May 2007.
- [53] D. Neugebauer, Y. Zhang, T. Pakula, S. S. Sheiko, and K. Matyjaszewski, “Densely-Grafted and Double-Grafted PEO Brushes via ATRP. A Route to Soft Elastomers,” *Macromolecules*, vol. 36, no. 18, pp. 6746–6755, Sep. 2003.
- [54] K. Matyjaszewski, “Bulk Atom Transfer Radical Polymerization,” *ACS Symp. Ser.*, vol. 713, pp. 96–112, 1998.
- [55] K. Kuperkar, D. Patel, L. I. Atanase, and P. Bahadur, “Amphiphilic Block Copolymers: Their Structures, and Self-Assembly to Polymeric Micelles and Polymersomes as Drug Delivery Vehicles,” *Polymers (Basel)*, vol. 14, no. 21, 2022.
- [56] T. Naolou, A. Meister, R. Schöps, M. Pietzsch, and J. Kressler, “Synthesis and characterization of graft copolymers able to form polymersomes and worm-like aggregates,” *Soft Matter*, vol. 9, no. 43, pp. 10364–10372, 2013.
- [57] A. P. Martinez, Z. Cui, C. Hire, T. A. P. Seery, and D. H. Adamson, “Synthesis and Self-Assembly of Toothbrush-like Block Copolymers,” *Macromolecules*, vol. 48, no. 13, pp. 4250–4255, 2015.
- [58] B. Li *et al.*, “A novel amphiphilic copolymer poly(ethylene oxide-co-allyl glycidyl ether)-graft-poly(ϵ -caprolactone): Synthesis, self-assembly, and protein encapsulation behavior,” *Polym. Chem.*, vol. 3, no. 9, pp. 2421–2429, 2012.
- [59] Y. Wang *et al.*, “Protein-Resistant Biodegradable Amphiphilic Graft Copolymer Vesicles as Protein Carriers,” *Macromol. Biosci.*, vol. 15, no. 9, pp. 1304–1313, 2015.
- [60] O. Onaca, R. Enea, D. W. Hughes, and W. Meier, “Stimuli-responsive polymersomes as nanocarriers for drug and gene delivery,” *Macromol. Biosci.*, vol. 9, no. 2, pp. 129–139, 2009.
- [61] F. Meng, Z. Zhong, and J. Feijen, “Stimuli-responsive polymersomes for programmed drug delivery,” *Biomacromolecules*, vol. 10, no. 2, pp. 197–209, 2009.
- [62] X. Hu, Y. Zhang, Z. Xie, X. Jing, A. Bellotti, and Z. Gu, “Stimuli-Responsive Polymersomes for Biomedical Applications,” *Biomacromolecules*, vol. 18, no. 3, pp. 649–673, 2017.

- [63] S. M. M. Moghadam, M. Alibolandi, M. Babaei, J. Mosafer, A. S. Saljooghi, and M. Ramezani, "Fabrication of deferasirox-decorated aptamer-targeted superparamagnetic iron oxide nanoparticles (SPION) as a therapeutic and magnetic resonance imaging agent in cancer therapy," *JBIC J. Biol. Inorg. Chem.*, vol. 26, no. 1, pp. 29–41, 2021.
- [64] L. Li *et al.*, "Superparamagnetic iron oxide nanoparticles as MRI contrast agents for non-invasive stem cell labeling and tracking," *Theranostics*, vol. 3, no. 8, p. 595, 2013.
- [65] S. Lecommandoux, O. Sandre, F. Chécot, J. Rodriguez-Hernandez, and R. Perzynski, "Magnetic Nanocomposite Micelles and Vesicles," *Adv. Mater.*, vol. 17, no. 6, pp. 712–718, Mar. 2005.
- [66] X. Duan *et al.*, "The long-term fate of mesenchymal stem cells labeled with magnetic resonance imaging-visible polymersomes in cerebral ischemia," *Int. J. Nanomedicine*, vol. 12, pp. 6705–6719, Dec. 2017.
- [67] T. Ren, Q. Liu, H. Lu, H. Liu, X. Zhang, and J. Du, "Multifunctional polymer vesicles for ultrasensitive magnetic resonance imaging and drug delivery," *J. Mater. Chem.*, vol. 22, no. 24, pp. 12329–12338, 2012.
- [68] L. Pourtau *et al.*, "Antibody-functionalized magnetic polymersomes: In vivo targeting and imaging of bone metastases using high resolution MRI," *Adv. Healthc. Mater.*, vol. 2, no. 11, pp. 1420–1424, 2013.
- [69] H. Oliveira, E. Pérez-Andrés, J. Thevenot, O. Sandre, E. Berra, and S. Lecommandoux, "Magnetic field triggered drug release from polymersomes for cancer therapeutics," *J. Control. Release*, vol. 169, no. 3, pp. 165–170, 2013.
- [70] B. Jeyadevan, "Present status and prospects of magnetite nanoparticles-based hyperthermia," *J. Ceram. Soc. Japan*, vol. 118, no. 1378, pp. 391–401, 2010.
- [71] A. E. Deatsch and B. A. Evans, "Heating efficiency in magnetic nanoparticle hyperthermia," *J. Magn. Magn. Mater.*, vol. 354, pp. 163–172, 2014.
- [72] M. Krack, H. Hohenberg, A. Kornowski, P. Lindner, H. Weller, and S. Förster, "Nanoparticle-Loaded Magnetophoretic Vesicles," *J. Am. Chem. Soc.*, vol. 130, no. 23, pp. 7315–7320, Jun. 2008.
- [73] Y. Long, C. Liu, B. Zhao, K. Song, G. Yang, and C. H. Tung, "Bio-inspired controlled release through compression-relaxation cycles of microcapsules," *NPG Asia Mater.*, vol. 7, no. 1, p. e148, 2015.
- [74] S. Lecommandoux, O. Sandre, F. Chécot, J. Rodriguez-Hernandez, and R. Perzynski, "Self-assemblies of magnetic nanoparticles and di-block copolymers: Magnetic micelles and vesicles," *J. Magn. Magn. Mater.*, vol. 300, no. 1, pp. 71–74, 2006.
- [75] A. Ryzhkov and Y. Raikher, "Size-dependent properties of magnetosensitive polymersomes: Computer modelling," *Sensors (Switzerland)*, vol. 19, no. 23, pp. 1–10, 2019.
- [76] A. V. Ryzhkov, P. V. Melenev, M. Balasoiu, and Y. L. Raikher, "The effect of magnetic nanoparticle concentration on the structure organisation of a microferrogel," *J. Phys. Conf. Ser.*, vol. 994, no. 1, 2018.
- [77] A. V. Ryzhkov and Y. L. Raikher, "Field-Induced Deformation and Structure Changes in a Magnetic Polymersome: Many-Particle Simulation," *IOP Conf. Ser. Mater. Sci. Eng.*, vol. 581, no. 1, 2019.

- [78] A. Ryzhkov and Y. Raikher, “Coarse-grained molecular dynamics modelling of a magnetic polymersome,” *Nanomaterials*, vol. 8, no. 10, pp. 1–12, 2018.
- [79] C. Kinnear, T. L. Moore, L. Rodriguez-lorenzo, B. Rothen-rutishauser, and A. Petrifink, “Form Follows Function: Nanoparticle Shape and Its Implications for Nanomedicine,” 2017.
- [80] N. P. Truong, M. R. Whittaker, C. W. Mak, and T. P. Davis, “The importance of nanoparticle shape in cancer drug delivery,” no. October 2018, 2015.
- [81] D. S. Williams, I. A. B. Pijpers, R. Ridolfo, and J. C. M. van Hest, “Controlling the morphology of copolymeric vectors for next generation nanomedicine,” *J. Control. Release*, vol. 259, pp. 29–39, 2017.
- [82] S. Palchetti *et al.*, “The protein corona of circulating PEGylated liposomes,” *Biochim. Biophys. Acta - Biomembr.*, vol. 1858, no. 2, pp. 189–196, 2016.
- [83] F. Liu, Y. Sun, C. Kang, and H. Zhu, “Pegylated Drug Delivery Systems: From Design to Biomedical Applications,” *Nano Life*, vol. 06, no. 03n04, p. 1642002, 2016.
- [84] K. C. Tjandra *et al.*, “Modulating the Selectivity and Stealth Properties of Ellipsoidal Polymersomes through a Multivalent Peptide Ligand Display.,” *Adv. Healthc. Mater.*, vol. 9, no. 13, p. e2000261, Jul. 2020.
- [85] B. Kang *et al.*, “Tailoring the stealth properties of biocompatible polysaccharide nanocontainers,” *Biomaterials*, vol. 49, pp. 125–134, 2015.
- [86] S. Schöttler *et al.*, “Protein adsorption is required for stealth effect of poly(ethylene glycol)- and poly(phosphoester)-coated nanocarriers,” *Nat. Nanotechnol.*, vol. 11, no. 4, pp. 372–377, 2016.
- [87] J. E. Gagner, M. D. Lopez, J. S. Dordick, and R. W. Siegel, “Effect of gold nanoparticle morphology on adsorbed protein structure and function,” *Biomaterials*, vol. 32, no. 29, pp. 7241–7252, 2011.
- [88] A. Aderem and D. M. Underhill., “Mechanisms of phagocytosis in macrophages.,” *Annu. Rev. Immunol.*, vol. 17, no. 3, pp. 593–623, 1999.
- [89] B. Burke and C. E. Lewis, “The Macrophage,” *Oxford Univ. Press. New York*, 2002.
- [90] M. K. Pratten and J. B. Lloyd., “Pinocytosis and phagocytosis: the effect of size of a particulate substrate on its mode of capture by rat peritoneal macrophages cultured in vitro.,” *Biochim. Biophys. Acta.*, vol. 881, pp. 307–313, 1986.
- [91] Y. Tabata and Y. Ikada., “Effect of the size and surface charge of polymer microspheres on their phagocytosis by macrophage.,” *Biomaterials*, vol. 9, pp. 356–362, 1988.
- [92] W. Wang, K. Gaus, R. D. Tilley, and J. J. Gooding, “The impact of nanoparticle shape on cellular internalisation and transport: What do the different analysis methods tell us?,” *Mater. Horizons*, vol. 6, no. 8, pp. 1538–1547, 2019.
- [93] J. A. Champion and S. Mitragotri, “Role of target geometry in phagocytosis.,” *Proc. Natl. Acad. Sci. U. S. A.*, vol. 103, no. 13, pp. 4930–4934, Mar. 2006.
- [94] G. Sharma *et al.*, “Polymer Particle Shape Independently Influences Binding and Internalization by Macrophages,” *J Control Release*, vol. 147, no. 3, pp. 408–412, 2010.
- [95] D. Paul, S. Achouri, Y. Z. Yoon, J. Herre, C. E. Bryant, and P. Cicuta, “Phagocytosis

- dynamics depends on target shape,” *Biophys. J.*, vol. 105, no. 5, pp. 1143–1150, 2013.
- [96] Y. Geng *et al.*, “Shape effects of filaments versus spherical particles in flow and drug delivery,” *Nat. Nanotechnol.*, vol. 2, no. 4, pp. 249–255, 2007.
- [97] N. L’Amoreaux, A. Ali, S. Iqbal, and J. Larsen, “Persistent prolate polymersomes for enhanced co-delivery of hydrophilic and hydrophobic drugs,” *Nanotechnology*, vol. 31, no. 17, p. 175103, 2020.
- [98] B. Devika Chithrani, A. A. Ghazani, and W. C. W. Chan, “Determining the Size and Shape Dependence of Gold Nanoparticle Uptake into Mammalian Cells,” vol. 6, no. 4, pp. 662–668, 2006.
- [99] R. Agarwal *et al.*, “Effect of shape, size, and aspect ratio on nanoparticle penetration and distribution inside solid tissues using 3D spheroid models,” *Adv. Healthc. Mater.*, vol. 4, no. 15, pp. 2269–2280, Oct. 2015.
- [100] S. E. A. Gratton *et al.*, “The effect of particle design on cellular internalization pathways,” no. January 2014, 2008.
- [101] S. Barua, J. W. Yoo, P. Kolhar, A. Wakankar, Y. R. Gokarn, and S. Mitragotri, “Particle shape enhances specificity of antibody-displaying nanoparticles,” *Proc. Natl. Acad. Sci. U. S. A.*, vol. 110, no. 9, pp. 3270–3275, 2013.
- [102] S. Bai *et al.*, “Cylindrical polymer brushes-anisotropic unimolecular micelle drug delivery system for enhancing the effectiveness of chemotherapy,” *Bioact. Mater.*, vol. 6, no. 9, pp. 2894–2904, 2021.
- [103] D. Li, Z. Tang, Y. Gao, H. Sun, and S. Zhou, “A Bio-Inspired Rod-Shaped Nanoplatfrom for Strongly Infecting Tumor Cells and Enhancing the Delivery Efficiency of Anticancer Drugs,” *Adv. Funct. Mater.*, vol. 26, no. 1, pp. 66–79, 2016.
- [104] O. B. Garbuzenko, J. Winkler, M. S. Tomassone, and T. Minko, “Biodegradable Janus nanoparticles for local pulmonary delivery of hydrophilic and hydrophobic molecules to the lungs,” *Langmuir*, vol. 30, no. 43, pp. 12941–12949, 2014.
- [105] T. A. Debele *et al.*, “A pH sensitive polymeric micelle for co-delivery of doxorubicin and α -TOS for colon cancer therapy,” *J. Mater. Chem. B*, vol. 5, no. 29, pp. 5870–5880, 2017.
- [106] M.-H. Lai, J. H. Jeong, R. J. Devolder, C. Brockman, C. Schroeder, and H. Kong, “Ellipsoidal Polyaspartamide Polymersomes with Enhanced Cell-Targeting Ability,” *Adv. Funct. Mater.*, vol. 22, no. 15, pp. 3239–3246, Aug. 2012.
- [107] Z. W, F. NA, and H. AMR, “In vitro uptake of polystyrene microspheres: Effect of particle size, cell line and cell density,” *J Control. Release*, vol. 71, pp. 39–51., 2001.
- [108] B. Samanta, H. Yan, N. O. Fischer, J. Shi, D. J. Jerry, and V. M. Rotello, “Protein-passivated Fe₃O₄ nanoparticles: low toxicity and rapid heating for thermal therapy,” *J. Mater. Chem.*, vol. 18, no. 11, pp. 1204–1208, 2008.
- [109] J. P. Fortin, C. Wilhelm, J. Servais, C. Ménager, J. C. Bacri, and F. Gazeau, “Size-sorted anionic iron oxide nanomagnets as colloidal mediators for magnetic hyperthermia,” *J. Am. Chem. Soc.*, vol. 129, no. 9, pp. 2628–2635, 2007.
- [110] M. Bañobre-López, A. Teijeiro, and J. Rivas, “Magnetic nanoparticle-based hyperthermia for cancer treatment,” *Reports Pract. Oncol. Radiother.*, vol. 18, no. 6, pp. 397–400, 2013.

- [111] M. F. Contreras, R. Sougrat, A. Zaher, T. Ravasi, and J. Kosel, “Non-chemotoxic induction of cancer cell death using magnetic nanowires,” *Int. J. Nanomedicine*, vol. 10, pp. 2141–2153, 2015.
- [112] Y. I. Golovin, A. O. Zhigachev, D. Y. Golovin, S. L. Gribanovsky, A. V. Kabanov, and N. L. Klyachko, “Straintronics for Nanomedicine: Manipulating Biochemical Systems via Controllable Macromolecular Nanodeformation,” *Bull. Russ. Acad. Sci. Phys.*, vol. 84, no. 7, pp. 815–819, 2020.
- [113] Y. I. Golovin, A. O. Zhigachev, N. L. Klyachko, and A. V. Kabanov, “Localizing the Nanodeformation Impact of Magnetic Nanoparticles on Macromolecular Objects by Physical and Biochemical Means,” *Bull. Russ. Acad. Sci. Phys.*, vol. 82, no. 9, pp. 1073–1078, 2018.
- [114] Y. I. Golovin *et al.*, “Selective Deformation of Single Macromolecules and Biomolecular Structures as a Method for Remote Control of Their Properties and Functions for Next-Generation Medicine,” *Russ. Metall.*, vol. 2019, no. 4, pp. 374–384, 2019.
- [115] Y. I. Golovin *et al.*, “The dynamics of magnetic nanoparticles exposed to non-heating alternating magnetic field in biochemical applications: theoretical study,” *J. Nanoparticle Res.*, vol. 19, no. 2, 2017.
- [116] Louis Néel, “Théorie du traînage magnétique des ferromagnétiques en grains fins avec application aux terres cuites.,” *Ann. géophysique*, vol. 5, pp. 99–136, 1949.
- [117] W.F. Brown, “Thermal fluctuations of a single-domain particle,” *Phys. Rev.*, vol. 130, pp. 1677–1686, 1963.
- [118] Y. I. Golovin, S. L. Gribanovskii, D. Y. Golovin, N. L. Klyachko, and A. V. Kabanov, “Single-domain magnetic nanoparticles in an alternating magnetic field as mediators of local deformation of the surrounding macromolecules,” *Phys. Solid State*, vol. 56, no. 7, pp. 1342–1351, 2014.
- [119] A. R. Tsiapla *et al.*, “Cell Behavioral Changes after the Application of Magneto-Mechanical Activation to Normal and Cancer Cells,” *Magnetochemistry*, vol. 8, no. 2, 2022.
- [120] K. Spyridopoulou *et al.*, “Effect of low frequency magnetic fields on the growth of MNP-treated HT29 colon cancer cells,” *Nanotechnology*, vol. 29, no. 17, 2018.
- [121] D. Cheng, X. Li, G. Zhang, and H. Shi, “Morphological effect of oscillating magnetic nanoparticles in killing tumor cells,” pp. 1–8, 2014.
- [122] S. Leulmi *et al.*, “Triggering the apoptosis of targeted human renal cancer cells by the vibration of anisotropic magnetic particles attached to the cell membrane,” *Nanoscale*, vol. 7, no. 38, pp. 15904–15914, 2015.
- [123] H. Chiriac *et al.*, “Fe-Cr-Nb-B ferromagnetic particles with shape anisotropy for cancer cell destruction by magneto-mechanical actuation,” *Sci. Rep.*, vol. 8, no. 1, pp. 2–10, 2018.
- [124] C. Apoptosis, E. Zhang, M. F. Kircher, X. M. Koch, L. Eliasson, and S. N. Goldberg, “Dynamic Magnetic Fields Remote- Rotation,” *ACS Nano*, vol. 8, no. 4, pp. 3192–3201, 2014.
- [125] D. H. Kim *et al.*, “Biofunctionalized magnetic-vortex microdiscs for targeted cancer-cell destruction,” *Nat. Mater.*, vol. 9, no. 2, pp. 165–171, 2010.

- [126] Y. I. Golovin, N. L. Klyachko, M. Sokolsky-Papkov, and A. V Kabanov, "Single-domain magnetic nanoparticles as force generators for the nanomechanical control of biochemical reactions by low-frequency magnetic fields," *Bull. Russ. Acad. Sci. Phys.*, vol. 77, no. 11, pp. 1350–1359, 2013.
- [127] Y. Shen *et al.*, "Elongated nanoparticle aggregates in cancer cells for mechanical destruction with low frequency rotating magnetic field," *Theranostics*, vol. 7, no. 6, pp. 1735–1748, 2017.
- [128] S. Hapuarachchige, Y. Kato, E. J. Ngen, B. Smith, M. Delannoy, and D. Artemov, "Non-temperature induced effects of magnetized iron oxide nanoparticles in alternating magnetic field in cancer cells," *PLoS One*, vol. 11, no. 5, pp. 1–12, 2016.
- [129] D. W. Wong, W. L. Gan, Y. K. Teo, and W. S. Lew, "Interplay of cell death signaling pathways mediated by alternating magnetic field gradient," *Cell Death Discov.*, vol. 4, no. 1, 2018.
- [130] A. M. Master *et al.*, "Remote actuation of magnetic nanoparticles for cancer cell selective treatment through cytoskeletal disruption," *Sci. Rep.*, vol. 6, no. April, pp. 1–13, 2016.
- [131] S. Lopez *et al.*, "Magneto-mechanical destruction of cancer-associated fibroblasts using ultra-small iron oxide nanoparticles and low frequency rotating magnetic fields," *Nanoscale Adv.*, vol. 4, no. 2, pp. 421–436, 2022.
- [132] P. Swietach, S. Wigfield, P. Cobden, C. T. Supuran, A. L. Harris, and R. D. Vaughan-Jones, "Tumor-associated carbonic anhydrase 9 spatially coordinates intracellular pH in three-dimensional multicellular growths," *J. Biol. Chem.*, vol. 283, no. 29, pp. 20473–20483, 2008.
- [133] C. Potter and A. L. Harris, "Hypoxia inducible carbonic anhydrase IX, marker of tumor hypoxia, survival pathway and therapy target," *Cell Cycle*, vol. 3, no. 2, pp. 164–167, 2004.
- [134] M. P. Mattson and S. L. Chan, "Calcium orchestrates apoptosis," *Nat. Cell Biol.*, vol. 5, no. 12, pp. 1041–1043, 2003.
- [135] D. Kulms, H. Düßmann, B. Pöppelmann, S. Ständer, A. Schwarz, and T. Schwarz, "Apoptosis induced by disruption of the actin cytoskeleton is mediated via activation of CD95 (Fas/APO-1)," *Cell Death Differ.*, vol. 9, no. 6, pp. 598–608, 2002.
- [136] Y. Cheng *et al.*, "Rotating Magnetic Field Induced Oscillation of Magnetic Particles for in vivo Mechanical Destruction of Malignant Glioma," *Control Release*, pp. 75–84, 2017.
- [137] C. Riccardi and I. Nicoletti, "Analysis of apoptosis by propidium iodide staining and flow cytometry," *Nat. Protoc.*, vol. 1, no. 3, pp. 1458–1461, 2006.
- [138] M. van Engeland, L. J. Nieland, F. C. Ramaekers, B. Schutte, and C. P. Reutelingsperger, "Annexin V-affinity assay: a review on an apoptosis detection system based on phosphatidylserine exposure," *Cytometry*, vol. 31, no. 1, pp. 1–9, Jan. 1998.
- [139] D. Liu, L. Wang, Z. Wang, and A. Cuschieri, "Magnetoporation and magnetolysis of cancer cells via carbon nanotubes induced by rotating magnetic fields," *Nano Lett.*, vol. 12, no. 10, pp. 5117–5121, 2012.
- [140] F. K.-M. Chan, K. Moriwaki, and M. J. De Rosa, "Detection of Necrosis by Release of Lactate Dehydrogenase Activity BT - Immune Homeostasis: Methods and Protocols,"

Chapter I

A. L. Snow and M. J. Lenardo, Eds. Totowa, NJ: Humana Press, 2013, pp. 65–70.

CHAPTER II: SYNTHESIS OF GRAFT COPOLYMERS

Introduction:

One of the main challenges in our study of elongated magnetic polymersomes was to achieve an adequate cross-linking of the hydrophobic membrane, capable of keeping the elongation even after the magnetic field was removed. Many possible solutions were investigated throughout this PhD project, one of those being the synthesis of a graft copolymer, which would present a hydrophobic side chain bearing groups with cross-linking potential. This side chain would act as an element of the hydrophobic membrane of the polymersome system, and due to the arborescent nature of a graft copolymer, the chains would theoretically intertwine with one another resulting in a stronger contact after cross-linking and allow a better network formation than for example a linear block copolymer would offer.

In order to produce polymersomes that were flexible enough to induce elongation when a magnetic field was applied, elastomeric polymers were chosen. In our case, poly(isoprene) (PI) was chosen due to its rubbery state (*i.e.* of low T_g) allowing thus elongation when a magnetic field of sufficient intensity would be applied and a functionalized PTMC-like polymer with amine pendant groups, later called poly(amino trimethylene carbonate) (PATC), due to its similarity to poly(trimethylene) carbonate (PTMC), a polymer very well known for its elastomeric properties. Thus, this chapter is dedicated to explore the synthesis and characterization of a variety of graft copolymers, more precisely amphiphilic block-brush copolymers which self-assembly has been studied, in literature [1]. Under certain circumstances, comb-like polymers with grafted hydrophobic chains can self-assemble into vesicular structures, as evidenced by Ibrahimova *et al.* [2] with fatty chains grafted along the polypeptide backbone of elastin-like peptides (ELPs). In this work, MeO-PEG₁₁₄-OH ($M_n = 5000 \text{ g}\cdot\text{mol}^{-1}$) was chosen as the macroinitiator of the ring opening polymerization (ROP) to serve as the hydrophilic block of the graft copolymer due to its known and well-studied biocompatible properties and stealth effect in biological media (*i.e.* repelling blood serum proteins).

In this research project (ANR MAVERICK), the controlled degradation of commercially *cis* 1,4-polyisoprene resulting in carbonyl ended heterotelechelic poly(isoprene) with a controlled molar mass has been studied and further verified from previous work in the laboratory [3-5]. This carbonyl end heterotelechelic feature was utilized for the post-polymerization functionalization of the diblock copolymer *via* the use of reductive amination reaction, which includes the formation of an imine between the amine and an aldehyde group and its further reduction by the use of a reducing agent, which in this case was chosen to be sodium triacetoxyborohydride (NaBH(OAc)₃) [6-8]. This reducing agent offers a less toxic effect when

compared to sodium cyanoborohydride (NaBH_3CN) and is also capable to selectively reduce aldehydes and not ketone groups [9]. This specific selectivity was crucial for this synthetic route since the carbonyl ended heterotelechelic poly(isoprene) presents both groups on its end, an aldehyde and a ketone.

To produce copolymers that would be able to self-assemble into polymersomes, various studies have concluded that the hydrophilic weight fraction is a key parameter. For example, for PEG-*b*-PTMC, the ideal hydrophilic fraction (f_{PEG}) should be less than 20%, with latest study by Lebleu *et al.* [10] presenting a system of PEG₄₅-*b*-PTMC₉₆ that formed vesicles with a f_{PEG} =17%. There is thus a discrepancy with the case of PEG-polydiene block copolymers, for which Discher & Eisenberg have proven that a hydrophilic weight fraction in the range $0.25 < f_{\text{PEG}} < 0.45$ is capable of producing vesicles [11],[12].

In this work, a variety of copolymers were synthesized while keeping the hydrophilic PEG block length at a steady length and varying the degree of polymerization of the PATC block.

Experimental Section:

Materials:

Tetrahydrofuran (THF), diethylether (Et₂O), dichloromethane (DCM), chloroform (CHCl₃), methanol (MeOH), heptane, and dimethylformamide (DMF) were purchased from Sigma-Aldrich. THF, DMF and DCM were dried by a solvent purification system. Chloroform was dried with CaH₂ and distilled under vacuum. Triethylamine (Et₃N) was purchased from Sigma-Aldrich and was dried by CaH₂ and distilled under vacuum. Meta-chloroperbenzoic acid (m-CBPA), periodic acid (H₅IO₆), sodium carbonate (Na₂CO₃) were purchased from Alfa Aesar (Thermo Fisher). Celite™ (natural diatomaceous earth), serinol (2-amino-1,3-propanediol), di-*tert*-butyldicarbonate, ethylchloroformate, *tert*-Butyl (1,3-dihydroxypropan-2-yl), MeO-PEG₁₁₄-OH ($M_n = 5000 \text{ g}\cdot\text{mol}^{-1}$) was purchased from Alfa Aesar (Thermo Fisher), 1,8-diazabicyclo[5.4.0]undec-7-ene (DBU) was purchased from Alfa Aesar (Thermo Fisher) and dried with CaH₂ and distilled under vacuum. *N*-cyclohexyl-*N'*-(3,5-bis(trifluoromethyl)phenyl)thiourea (TU), molecular sieves (4Å) were activated by flame drying and left under vacuum overnight and were purchased from Sigma-Aldrich. Sodium triacetoxyborohydride (NaBH(AcO)₃) 97% was purchased from Sigma-Aldrich.

Methods:

Synthesis of heterotelechelic poly(isoprene) oligomer via “one-pot” degradation method

The following procedure describes the synthesis of a poly(isoprene) oligomer with a DP of 5-6 units ($M_n = 340 \text{ g}\cdot\text{mol}^{-1}$). Such a small DP resulted in a different cleaning process than the one that was followed for higher molar mass, 1000-35000 $\text{g}\cdot\text{mol}^{-1}$. The reaction was performed at room temperature, not under inert conditions.

In a 500 mL round-bottom flask, 5 g of commercial *cis*-1,4-poly(isoprene) 800000 $\text{g}\cdot\text{mol}^{-1}$ were left under stirring overnight in 250 mL THF. The following day, 5.4 g (0.03 mol) of mCBPA was solubilized in 50 mL THF and added dropwise to the poly(isoprene) solution. The mixture was left to stir for 2 h before a dropwise addition 7 g (0.03 mol) of periodic acid solubilized in 50 mL of THF, and the mixture was left to stir for another 2 h. Finally, 14 g of sodium carbonate was added in the reaction to react with the produced acids and the mixture was left to stir for 30 min before filtration through Celite™. The filtrated solution was concentrated under vacuum

until THF was fully evaporated. The dry product was re-solubilized in heptane, forming a yellow solution and white precipitate which was filtered off through Celite once more. The solution was dried again under vacuum before re-solubilizing in heptane and filtering through Celite™. The previous process was repeated 3 times before the yellow solution was finally left to dry under vacuum overnight in order to recover the product. The final product had a honey-like consistency and color with a resulting yield in the range of 60-70%.

Calculations that were followed in order to measure the necessary amount of mCPBA and periodic acid following existing measurement in literature by Berto *et al.*: [4]

For example, if the desired final molar mass of poly(isoprene) is $41000 \text{ g}\cdot\text{mol}^{-1}$, the theoretical molar mass is $19430 \text{ g}\cdot\text{mol}^{-1}$ with an epoxidation rate of 35%. Keeping in mind the correlation between the final M_n and the epoxidation rate, it is possible to calculate values that are outside of the provided values in Table S1. In our case, we aimed small oligomer with $M_n = 340 \text{ g}\cdot\text{mol}^{-1}$, thus we calculated the targeted epoxidation rate as so:

If $M_n^{\text{th}} = 2120 \text{ g}\cdot\text{mol}^{-1}$ leads to $M_n^{\text{exp}} = 3600 \text{ g}\cdot\text{mol}^{-1}$, then our targeted $M_n^{\text{exp}} = 340 \text{ g}\cdot\text{mol}^{-1}$ corresponds to $M_n^{\text{th}} = 2120 \times 340/3600 = 200 \text{ g}\cdot\text{mol}^{-1}$. Thus we can calculate the necessary Epoxy_{theor}(%) by the following equation:

$$M_n^{\text{th}} = \frac{100}{\text{Epoxy}_{\text{theor}}} \times 68, \text{ where } 68 \text{ g}\cdot\text{mol}^{-1} \text{ is the molar mass of the molar unit of PI.}$$

¹H NMR (400 MHz, CDCl₃), δ(ppm): 9.74 (t, 1H, $-\text{CH}_2\text{CHO}$), 5.14 (t (broad), 5H $-\text{CH}_2\text{CHv}$), 2.47 (t, 2H, $-\text{CH}_2\text{CHO}$), 2.42 (t, 2H, $-\text{CH}_2\text{COCH}_3$), 2.33 (t, 2H, $-\text{CH}_2\text{CH}_2\text{CHO}$), 2.00–2.12 (m (broad), 20H, $-\text{CH}_2\text{CHv}$ and $-\text{CH}_2\text{C}(\text{CH}_3)\text{v}$), 1.68 (s (broad), 15H $-(\text{CH}_3)\text{CvCH}-$).

Synthesis of the *tert*-butyl-(1,3-dihydroxypropan-2-yl) carbamate (tBS)

The synthesis of the *tert*-butyl-(1,3-dihydroxypropan-2-yl) carbamate (tBS) was performed according to literature with minor modifications. [13] First, in round-bottom flask 5 g (0.055 mol) of serinol were solubilized in a 500 mL mixture of Milli-Q and THF (40:10 v/v) respectively. The solution was cooled down to 0 °C and 11.25 mL (0.0825 mol, 1.5 eq) of triethylamine (Et₃N) was added. Finally, 14.5 g of di-*tert*-butyl dicarbonate (0.066 mol, 1.2 eq) solubilized in THF was added dropwise over 1 h under stirring. The reaction was left to stir for another 16 h at room temperature before distilling the THF under vacuum. Furthermore, an extraction with ethyl acetate (4 times, 50 mL) was performed on the remaining solution and the organic phase was dried with MgSO₄ before filtration through a fritted filter funnel and concentration under vacuum. Finally, to isolate the final product a recrystallization was

performed with ethyl acetate resulting in a white crystalline solid product with a yield in the range 60-70% (3.5 g).

^1H NMR (400 MHz, CDCl_3), δ ppm: 5.18 (s, $-\text{CH}-\text{NH}-\text{CO}-\text{C}-(\text{CH}_3)_3$), 3.77–3.86 (dq, $\text{OH}-\text{CH}_2-\text{CH}(\text{NHCO}-\text{C}-(\text{CH}_3)_3)-\text{CH}_2-\text{OH}$), 3.69 (s, $\text{OH}-\text{CH}_2-\text{CH}(\text{NH}-\text{CO}-\text{C}-(\text{CH}_3)_3)-\text{CH}_2-\text{OH}$), 1.45 (s, $-\text{C}-(\text{CH}_3)_3$).

Synthesis of the *tert*-butyl (2-oxo-1,3-dioxan-5-yl) carbamate monomer

The synthesis of *tert*-butyl (2-oxo-1,3-dioxan-5-yl) carbamate monomer was adapted from literature with minor modifications.[13] In a round-bottom flask, 3 g (15.6 mmol) of *tert*-butyl-(1,3-dihydroxypropan-2-yl) carbamate and 3.73 g of ethyl chloroformate (2.2 eq, 34.4 mmol, 3.29 mL) were solubilized in 30 mL of THF and the solution was cooled down to 0°C. Then 5.44 mL of triethylamine (2.5 eq, 39 mmol) were added dropwise to the solution over a period of 1 h and the reaction was left to stir for another 16 h at room temperature. The next day, white salts were produced, and the reaction was filtered off leaving behind a beige solution which was dried under vacuum resulting in a beige powder which was dried under vacuum overnight. The solid was washed with a cold mixture of THF:diethyl ether (2:8) respectively, resulting in the final white powder of *tert*-butyl (2-oxo-1,3-dioxan-5-yl) carbamate monomer (yield: 66%, 2 g).

^1H NMR (400 MHz, CDCl_3): δ (ppm): 5.38 (s, $-\text{CH}-\text{NH}-\text{CO}-\text{C}-(\text{CH}_3)_3$), 4.37–4.57 (dd, $\text{OH}-\text{CH}_2-\text{CH}(\text{NH}-\text{CO}-\text{C}(\text{CH}_3)_3)-\text{CH}_2-\text{OH}$), 4.12 (s, $\text{OH}-\text{CH}_2-\text{CH}(\text{NH}-\text{CO}-\text{C}(\text{CH}_3)_3)-\text{CH}_2-\text{OH}$), 1.44 (s, $-\text{C}-(\text{CH}_3)_3$)

Poly (ethylene glycol)-*block*-poly(*tert*-butyl -amino trimethylene carbonate)

(PEG₁₁₄-*b*-PATC₃₀)

The synthesis of the poly(ethylene glycol)-*block*-poly(*tert*-butyl-amino trimethylene carbonate) (PEG₁₁₄-*b*-PBATC₃₀) diblock was achieved *via* a ring opening polymerization (ROP) of the *tert*-butyl (2-oxo-1,3-dioxan-5-yl) carbamate monomer by initiation with the $\text{CH}_3\text{-PEG}_{114}\text{-OH}$ macromonomer. In a Schlenk tube, 0.17 g (1 eq, $3.45 \cdot 10^{-5}$ mol) of $\text{CH}_3\text{-PEG}_{114}\text{-OH}$ were solubilized in dry toluene to remove moisture *via* the formation of an azeotropic solution. The solution was left to stir at 40 °C for 1 h before subsequent distillation of toluene and drying overnight under vacuum. In a vial, 0.3 g (1.38 mmol, 40 eq) of *tert*-butyl (2-oxo-1,3-dioxan-5-yl) and 0.015 g ($4.14 \cdot 10^{-5}$ mol, 1.2 eq) of TU co-catalyst were solubilized in 2 mL of dry THF

while at 40 °C to aid the solubilization of the monomer, while 1 mL of THF was added to solubilize CH₃-PEG₁₁₄-OH. Once both reactants were solubilized, the monomer solution was added into the CH₃-PEG₁₁₄-OH solution. The temperature was lowered and set to 36 °C. 0.0062 mL of DBU ($4.14 \cdot 10^{-5}$ mol, 1.2 eq) was solubilized in 0.2 mL of THF and added to the reaction. The reaction was terminated after 2.5 h of reaction at 80% conversion by addition of 0.2 mL of acetic acid and precipitation in 40 mL cold diethyl ether. The mixture was centrifuged at 4 °C (10 min, 4000 g) and the precipitate was washed another 2 times to remove the unreacted monomer and other impurities. The final product was dried under vacuum. The resulting diblock copolymer was a white powder with a yield of 70% (0.3 g).

¹H NMR (400 MHz, CDCl₃): δ (ppm): 5.2 (s, -CH-NH-C-CO-C-(CH₃)₃), 4.2(m,-CO-OCH₂-CH-(NH-CO-C(CH₃)₃)-CH₂-), 3.6 (m broad, CH₃-O-CH₂-CH₂-O-), 3.3 (s,CH₃-O-CH₂-CH₂-O-), 1.4 (m broad,-CH-NH-C-CO-C-(CH₃)₃)

Deprotection of PEG₁₁₄-*b*-PATC₃₀

The deprotection of the amino groups in the diblock copolymer was adapted from literature[13]. 100 mg of the diblock copolymer were solubilized in 10 mL of dry chloroform (or dichloromethane) and the temperature was dropped to 0 °C. 5 eq of trifluoroacetic acid (3.2 mL) was added dropwise and the reaction was allowed to proceed for 1 h to achieve full deprotection, before termination by precipitation in 40 mL of cold diethyl ether and centrifugation at 4 °C (10 min, 4000 g). The precipitate was washed another 2 times resulting in a colorless viscous product, which was dried under vacuum overnight with a yield of 99% for this deprotection step.

¹H NMR (400 MHz, DMSO-d₇): δ (ppm): 8.2 (s, -CH-NH₃⁺TFA⁻), 4.15(d broad,-CO-OCH₂-CH-(NH₃⁺)-CH₂-), 3.37 (s,-CO-OCH₂-CH-(NH₃⁺)-CH₂-),3.5 (m broad, CH₃-O-CH₂-CH₂-O-), 3.3 (s,CH₃-O-CH₂-CH₂-O-)

Reductive amination resulting into PEG₁₁₄-*b*-PATC₂₀-*g*-PI_x

The synthetic route described herein is the one of the graft copolymers PEG₁₁₄-*b*-PATC₂₀-*g*-PI_x that was achieved *via* a reductive amination process between the aldehyde groups of the heterotelechelic poly(isoprene) PI₅(5) and the free amines of the diblock copolymer PEG₁₁₄-*b*-PAC₂₀(8). In a Schlenk tube, 0.06 g (1 eq, 0.178 mmol) of PEG₁₁₄-*b*-PAC₂₀(8) and 0.49 g (7 eq, 1.44 mmol) of PI₅(5) were solubilized in 3 mL of dry toluene and left to stir for 1 h under 40 °C to remove moisture from the system through an azeotrope. Subsequently, the toluene was

distilled under vacuum and the reactants were left to dry under vacuum overnight. The following day, 1.2 mL of dry THF and 1.2 mL of dry DMF as well as 0.2 mL (8 eq, 1.44 mmol) of triethylamine were added to the Schlenk to keep the concentration of the solution at 200 mg/mL. Then molecular sieves 4 Å were added to half the volume of the solvents and the reaction was left to stir for 24 h under 40 °C under stirring, with the aim to eliminate the water molecules formed by the condensation reaction between the amino and aldehyde groups. Finally, 0.78 g (5eq) of sodium triacetoxyborohydride were added in 3 doses of 0.26 g/hour and the reaction was left to proceed for another day (24 h) before termination by precipitation in 40 mL of cold heptane. The product was centrifuged for 10 min (4 °C, 4000 g) followed by removal of the supernatant. The precipitate was re-solubilized in a small volume of dichloromethane (3mL) and the solution was filtered through 0.45 µm pore size PTFE filter while being precipitated in 40 mL of cold heptane again. Further centrifugation (10 min, 4 °C, 4000 g), separation of the precipitate, re-solubilization in dichloromethane, re-filtration and re-precipitation in heptane and final centrifugation and solid pellet separation from the liquid phase before letting the product dry overnight under vacuum overnight. The resulting graft copolymer was a viscous orange product with a yield of 54% (0.06 g).

¹H NMR (400 MHz, CDCl₃): δ (ppm): 5.2 (m, broad -CH₂-CH-CCH₃-CH₂), 4.2 (m, broad), 3.5 (m, broad CH₃-O-CH₂-CH₂-O-), 3.3 (s, CH₃-O-CH₂-CH₂-O-), 2.4 (t, CH₃-CO-CH₂-), 2.1 (t, -CH₂-CH₂-NH-), 2 (m broad, -CH₂-CH-CCH₃-CH₂-), 1.5 (s, -CH₂-CH-CCH₃-CH₂-)

Epoxidation of PEG₁₁₄-*b*-PATC₂₀-*g*-PI_x

In a vial, 50 mg of the graft copolymer PEG₁₁₄-*b*-(PATC-*g*-PI₅)₁₅-*co*-PATC₅ was solubilized in 2 mL of THF at room temperature. The calculations that took place for the amount of the epoxidizing agent are described below, so 20 mg of mCBPA was added to the solution in order to achieve 40% of epoxidation and the reaction was left to stir for 2h before precipitation in 40mL of cold heptane (10 min, 4 °C, 4000 g). Following the separation of the solid from the supernatant, heptane was added again, and the precipitate was washed another 2 times before drying under vacuum overnight. The final product was a dry orange solid with a yield of 94% (0.05 g).

$$\% \text{PI in } ^1\text{HNMR} = \frac{I_{5.2} \times 68}{(I_{5.2}) \times 68 + \left(\frac{I_{3.6}}{4}\right) \times 44 + \left(\frac{I_{4.2}}{4}\right) \times 118.1} = \frac{2040}{10420} = 0.196, \text{ i.e } 19.6\% \text{ of poly(isoprene)}$$

Thus, %PI × m_{polymer} = m_{PI} , for 50 mg of polymer, m_{PI} = 9.8 mg

$$n_{\text{PI}} = \frac{m_{\text{PI}}}{68} = 0.144 \text{ mmol}$$

$$n_{\text{mCPBA}} = \text{Epoxid\%}_{\text{Theor.}} \times n_{\text{PI}} = 40\% \times 0.144 \text{ mmol} = 0.0576 \text{ mmol}$$

$$m_{\text{mCPBA}} = n_{\text{mCPBA}} \times 172.57 \text{ g/mol} = 0.009 \text{ g or 9 mg of mCPBA}$$

¹H NMR (400 MHz, CDCl₃): δ (ppm): 5.2 (m, broad -CH₂-CH-CCH₃-CH₂), 4.2 (m, broad), 3.5 (m, broad CH₃-O-CH₂-CH₂-O-), 3.3 (s, CH₃-O-CH₂-CH₂-O-), 2.69 (CH₂-CHO-CCH₃-CH₂-), 2.4 (t, CH₃-CO-CH₂-), 2.1 (t, -CH₂-CH₂-NH-), 2 (m broad, -CH₂-CH-CCH₃-CH₂-), 1.5 (s, -CH₂-CH-CCH₃-CH₂-), 1.2 (d broad, CH₂-CHO-CCH₃-CH₂-).

Methods of characterization:

Nuclear Magnetic Resonance (NMR):

¹H NMR experiments were performed in deuterated chloroform CDCl₃ in room temperature (296K) on a NMR BRUKER AVANCE I spectrometer which was operating at a frequency of 400 MHz. The instrument was equipped with a BBFO probe capable of producing Z-gradient at all frequencies with strength 50 G·cm⁻¹. The spectra were acquired with an acquisition time of 4 seconds and 32 scans. The concentration of each sample was 10 mg/ml. The NMR spectra were acquired by Topspin software from BRUKER.

Diffusion-ordered spectroscopy (DOSY):

Diffusion-ordered spectroscopy (DOSY) was performed at room temperature (296K) on a BRUKER Ascend 400 NMR spectrometer. The spectrometer was equipped with a cryo-Probe Prodigy. The concentration of the sample was 15mg/ml. The pulse program which was utilized to acquire the spectra was dstebpgp3s. The spectra were recorded with 16K time domain data points in the t₂ dimension and 16 t₁ increments. The compromise diffusion Δ was set at 100ms while the gradient pulse length δ was set at 2.3ms.

Size exclusion chromatography (SEC):

Size exclusion chromatography (SEC) analysis to determine the molar mass *M_n* and dispersity *D* was performed in THF on an UltiMate™ 3000 Standard (SD) HPLC/UHPLC system produced by Thermoscientific. The system was equipped with a multi angle light scattering probe (MALS) (Wyatt Technologies), a differential refractive index detector (dRI) (Wyatt Technologies) and a UV-Vis diode array detector (Thermoscientific). Polymer separation was performed by a three-column set of TOSOH TSK HXL gel (G2000, G3000 and G4000) the exclusion limits which were from 200 to 400000 g·mol⁻¹. The calibration of the column was

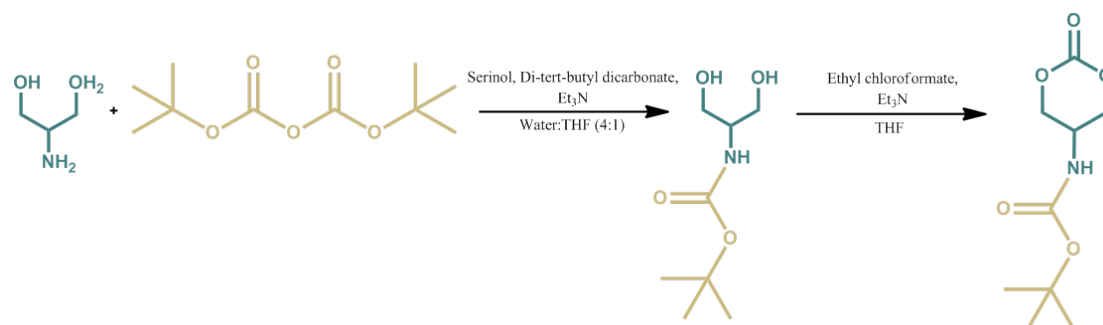
performed with polystyrene standards of an EasiVial kit of polystyrenes (PS) from Agilent. The medium molecular weight range was in the range of 162 to 364000 g·mol⁻¹. Finally, the analysis of the chromatograms was performed with Astra software by Wyatt Technologies.

Size exclusion chromatography (SEC) in DMF was performed as well in a similar system as described for SEC THF. An UltiMate™ 3000 Standard (SD) HPLC/UHPLC system produced by Thermoscientific was utilized. The solvent solution was DMF+ LiBr 1g·L⁻¹. The system was equipped with a multi angle light scattering probe (MALS) (Wyatt Technologies), a differential refractive index detector (dRI) (Wyatt Technologies) and a UV-Vis diode array detector (Thermoscientific). The separation of polymers was performed by a three-set column system, consisting of Shodex Asahipack columns (GF-1G 7B, GF310 AND GF510). Column calibration was performed with polystyrene standards as described above and the analysis of chromatograms was once more performed with Astra software.

Results and discussion:

Graft copolymer synthesis and characterization

The first step for the synthesis of the graft copolymer was to synthesize a functionalized monomer capable of post-polymerization modifications. While many trials were performed in order to synthesize a monomer which was already modified by including a poly(isoprene) side chain, unfortunately this goal was not achieved. Thus, the idea of synthesizing a monomer which would still be polymerized *via* controlled ring opening polymerization, like trimethylene carbonate (TMC), but which includes a functional group to attach the poly(isoprene) post-polymerization, was conceived. This thought process concluded in the synthesis of *tert*-butyl (2-oxo-1,3-dioxan-5-yl) carbamate (TBDOC) cyclic monomer, which has already been synthesized and characterized quite well in literature (Scheme 1) [13]. This 6-carbon cyclic monomer, capable of being polymerized by a macroinitiator bearing an –OH moiety was ideal in this case due to its amine bearing group which could be further exploited for “grafting to” reactions. Moreover, one of the reactants to prepare TBDOC is serinol (2-amino-1,3-propanediol), a molecule potentially derived from glycerol, by chemical or enzymatic reaction (thus bio-sourced) [14].



Scheme 1: Schematic representation of the synthetic route of *tert*-butyl (2-oxo-1,3-dioxan-5-yl) carbamate cyclic carbonate monomer (TBDOC).

The first step of the synthetic route was the protection of the amine group of bio-sourced reagent serinol by attaching a BOC protecting group through reaction with di-*tert*-butyl dicarbonate (Scheme 1). Further on, the cyclization process was performed by slow addition of ethyl chloroformate at 0 °C. Both reactions were characterized by proton nuclear magnetic resonance (¹HNMR) in both deuterated chloroform (CDCl₃) and deuterated water (D₂O), depending on the solubility of each product. As depicted in Figure 44, after the first step, one can see the total disappearance of the signal at 2.9 ppm and the appearance of a signal at 1.4 ppm for the *tert*-butyl group. For the second step, one can see in Figure 45, the shift of the signals at 3.7 and 3.8 ppm towards 4.1 and 4.5 ppm respectively due to the formation of the carbonate monomer. The overall reaction yield is similar to the one described in the literature, *i.e.* about ~70%.

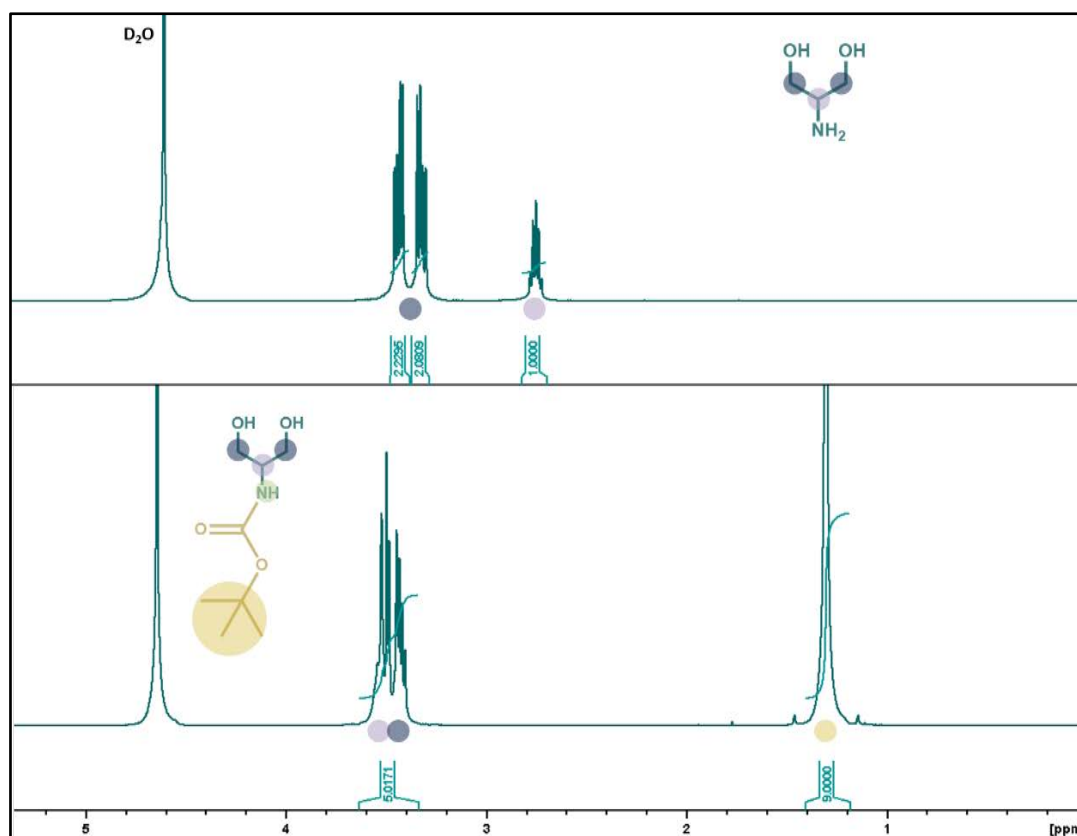


Figure 44: ^1H NMR spectra in D_2O of serinol and *tert*-butyl-(1,3-dihydroxypropan-2-yl) carbamate.

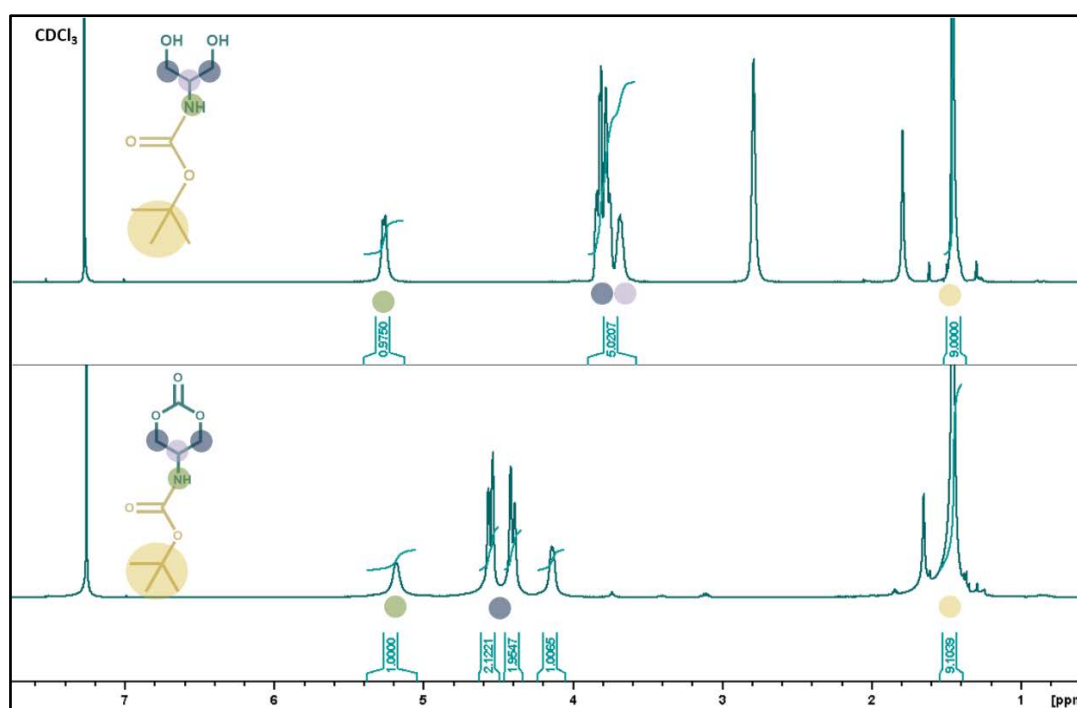
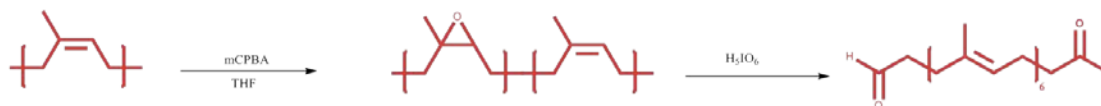


Figure 45: ^1H NMR spectra in CDCl_3 of *tert*-butyl-(1,3-dihydroxypropan-2-yl) carbamate and *tert*-butyl (2-oxo-1,3-dioxan-5-yl) carbamate monomer.

Synthesis of poly(isoprene) oligomer *via* “one-pot” degradation method

The chosen method to synthesize the poly(isoprene) block followed previous procedures from literature [3-5, 15], (Scheme 2). The determination of the final M_n was achieved by ^1H NMR spectroscopy and SEC in THF or DMF.



Scheme 2: “one-pot” degradation of polyisoprene to yield a carbonyl heterotelechelic PI.

A library of poly(isoprene) blocks was synthesized with targeted molar masses ranging from $M_n = 300$ to $1000 \text{ g}\cdot\text{mol}^{-1}$ to be utilized in accordance to the need of further reactions. In the literature,[4] it was confirmed a linear variation between the theoretical and the experimental epoxidation rates of polydienes, resulting in a slope of 0.96 suggesting that the reaction between the double bonds and mCBPA happens almost equimolarly. Furthermore, it was also proved a linear correlation between the M_n by ^1H NMR or by SEC and $1/\text{Epoxy}_{\text{theo}}(\%)$ ratio, suggesting that it is possible to have a controlled final molar mass of heterotelechelic polydienes (Figure 46).

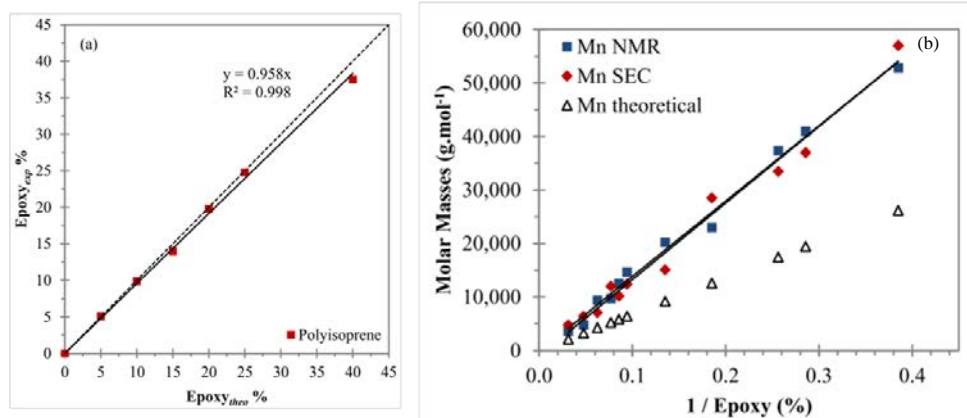


Figure 46: a) the correlation between the theoretical epoxidation rate ($\text{Epoxy}_{\text{theo}}(\%)$) and experimental epoxidation rate ($\text{Epoxy}_{\text{exp}}(\%)$) using mCBPA and b) the correlation between the resulting molar M_n determined by NMR or by SEC and the parameter $1/\text{Epoxy}_{\text{theo}}(\%)$ from Berto et al.[4].

Thus, following the experimental values of M_n that the authors have provided it is quite easy to calculate the desired epoxidation degree necessary to achieve the final M_n that is targeted for each case (Table S 1).

So, in the case of $M_{n\text{ th}}=200\text{ g}\cdot\text{mol}^{-1}$, $\text{Epoxy}_{\text{theor}}=34\%$ and once this value is known it is possible to calculate the amount of mCBPA needed to achieve the final desired molar mass very simply by multiplying $\text{Epoxy}_{\text{theor}}\% \times n_{\text{PI}}$ and utilizing this value to calculate both the amount of mCBPA and periodic acid since both reagents required the same equivalents. This method indeed manages to provide the desired M_n with slight discrepancies as can be seen in Table 2 and Figure 47 which illustrate the molar masses of a library of PI chains that was synthesized throughout.

Table 1: Molecular characteristics of synthesized poly(isoprene)(PI) chains obtained by SEC and ^1H NMR.

PI (97% <i>cis</i> -1,4, $M_n=800\text{ kg}\cdot\text{mol}^{-1}$)	$M_n^{\text{Theor.}}$ ($\text{g}\cdot\text{mol}^{-1}$)	$M_n^{\text{1H NMR}}$ ($\text{g}\cdot\text{mol}^{-1}$)*	DP_{1HNMR}	M_n^{SEC} ($\text{g}\cdot\text{mol}^{-1}$)**	\mathcal{D}^{**}
PI ₆ (1)	340	410	6	780	1.4
PI ₅ (2)	340	340	5	660	1.4
PI ₈ (3)	340	540	8	780	1.9
PI ₅ (4)	340	340	5	310	2.4
PI ₅ (5)	340	340	5	460	1.9

*Number-average molar mass (M_n) calculated by ^1H NMR spectroscopy in CDCl_3 using $M_n = I_{5.14\text{ppm}} \times 68\text{ g}\cdot\text{mol}^{-1}$,

**Number-average molar mass (M_n) and dispersity (\mathcal{D}) obtained by SEC in DMF, column calibration by polystyrene standards (PS)

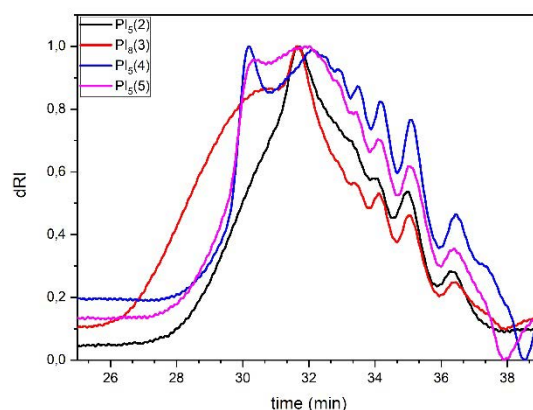


Figure 47: Normalized SEC chromatograms in DMF of poly(isoprene) oligomer chains: PI₅ (2) (black), PI₈ (red) (3), PI₅(4) (blue) and PI₅ (5) (pink).

As can be seen by the chromatograph in Figure 47 multiple length fractions are visible due to the low average molar mass of the polymers, which correspond to dimers, trimers etc. This is

an important note for the following reaction of “grafting to”, which will be exploited via reductive amination, were the smaller fraction will prove to be more reactive and end up being the ones attached. Nonetheless the polymer synthesis was successful and the ^1H NMR in CDCl_3 (Figure 48) confirmed the presence of both heterotelechelic groups, aldehyde and ketone, and the main number-average M_n of the polymer was easily calculated as well by integrating the aldehyde proton as 1, at 9.74 ppm.

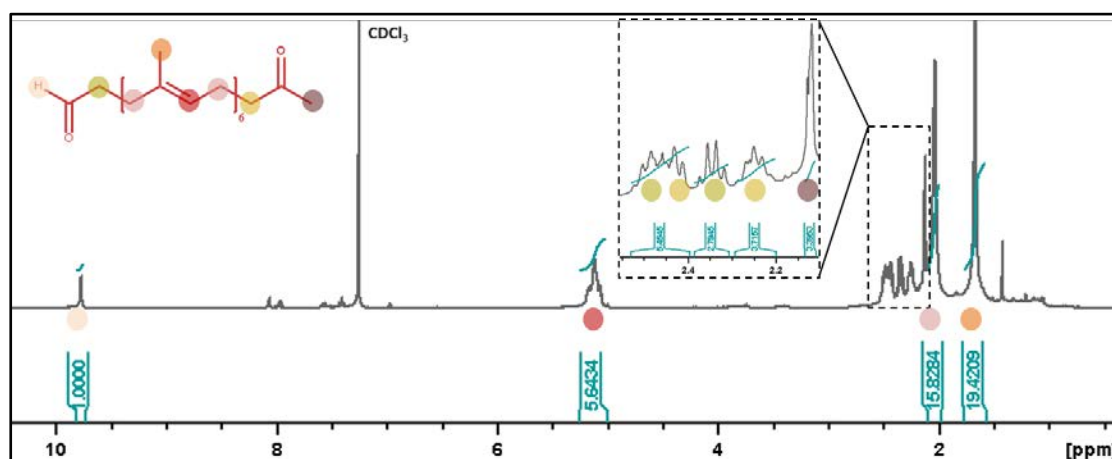
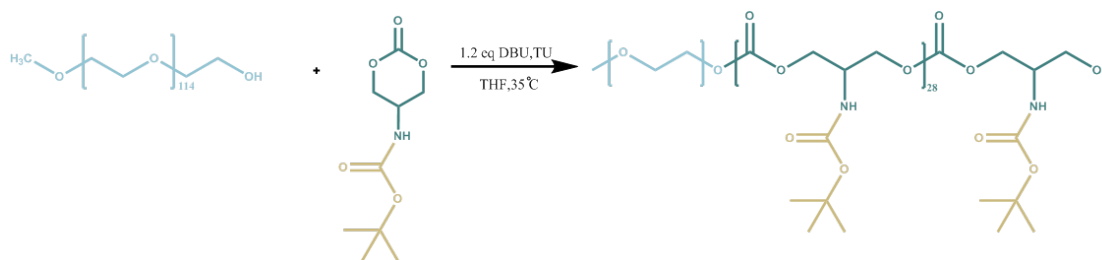


Figure 48: ^1H NMR spectra in CDCl_3 of poly(isoprene) oligomer PI_6 (1) prepared with the depolymerization method using mCPBA as epoxidizing agent of double bonds and H_5IO_6 for oxidative bond cleavage.

The ^1H NMR revealed that the cleaning process of the polymer was not enough to remove the byproduct of the reaction visible at 7.5-8 ppm, specifically benzoic acid which is being produced during the degradation reaction, even after multiple re-solubilizations in heptane and filtering. Although this byproduct could possibly slow down the following reactions due to its acidic nature, it was decided to use the polymers regardless of this potential issue and modification in the “grafting to” reaction were made in order to accommodate this presence of acid in the system by increasing the equivalents of triethylamine.

Poly(ethylene glycol)-*block*-poly(*tert*-butyl -amino trimethylene carbonate) (PEG-*b*-PBATC)

The synthesis of poly(ethylene glycol)-*block*-poly(*tert*-butyl-amino trimethylene carbonate) (PEG-*b*-PBATC) copolymers proceeded via the ring opening polymerization (ROP) of the *tert*-butyl (2-oxo-1,3-dioxan-5-yl) carbamate monomer TBDOC, which was previously synthesized. $\text{MeO-PEG}_{5\text{kDa}}\text{-OH}$ was utilized as a macroinitiator of the polymerization reaction, 1,8-diazabicyclo[5.4.0]undec-7-ene (DBU) and *N*-cyclohexyl-*N'*-(3,5-bis(trifluoromethyl)phenyl)thiourea (TU) as the organic catalytic system (Scheme 3).



Scheme 3: Synthesis of PEG-*b*-PBATC in THF with a DBU/TU catalytic system.

In this study, several PEG₁₁₄-*b*-PBATC_m copolymers were synthesized to study the rate of polymerization of the synthesized monomer and its limits. Finally, the diblock with a specific degree of polymerization (DP) of 20 was chosen to proceed with the “grafting to” to produce the graft copolymers which will be utilized to further self-assemble into magnetic polymersomes. MeO-PEG₁₁₄-OH ($M_n = 5000 \text{ g}\cdot\text{mol}^{-1}$) was the only macroinitiator which was used for the synthetic process and its purity was verified both by ^1H NMR in CDCl_3 (Figure 49) and SEC in THF (Figure 51) showing a molar mass of $M_n = 5000 \text{ g}\cdot\text{mol}^{-1}$ with no other visible populations.

The polymerization of the monomer was performed using an organic catalytic system DBU/TU with 1.2 eq each according to the molar ratio of MeO-PEG₁₁₄-OH. This equivalent was chosen from literature by Lebleu *et al.*[10] where the ROP of TMC was achieved using the same catalytic system much faster than just the DBU alone. In our case, 1.2 eq resulted in nice and controlled polymerizations which lead to very low dispersity, but minor adjustments had to be made to accommodate to this functional monomer. Firstly, the monomer appeared to be insoluble in THF in the concentration that was chosen for the TMC system, 230 g/L thus an increase of solvent was necessary, resulting in a lower concentration of monomer in the system, of 80 g/L. Moreover, a temperature increase from room temperature to 36°C appeared to allow a better solubilization of the monomer as well as of the macroinitiator. Under these conditions, the polymerization reaction reached 80% conversion after 2.5 h for a targeted DP of 30, with a low molar mass dispersity ranging between 1.02 and 1.10.

The kinetics of the reaction was followed by ^1H NMR spectroscopy, with aliquots taken every hour, each aliquot being terminated with acetic acid to stop the reaction. The progression of the reaction was observed by the decrease of the characteristic peaks of the monomer at 4.37–4.57 ppm and the gradual appearance of the peak at 4.2 ppm corresponding to the peak of the 5 protons of the PBATC block. The degree of polymerization and molar mass can be easily calculated while calibrating the peak at 3.3 ppm ($\text{CH}_3\text{-PEG-}$) as 3 protons each time (Figure 49).

The equation for the calculation of the molar mass of the diblock copolymer via ^1H NMR was then:

$$M_n = \frac{I_{4.26\text{ppm}}}{5} \times 217.22 + \frac{I_{3.65\text{ppm}}}{4} \times 44$$

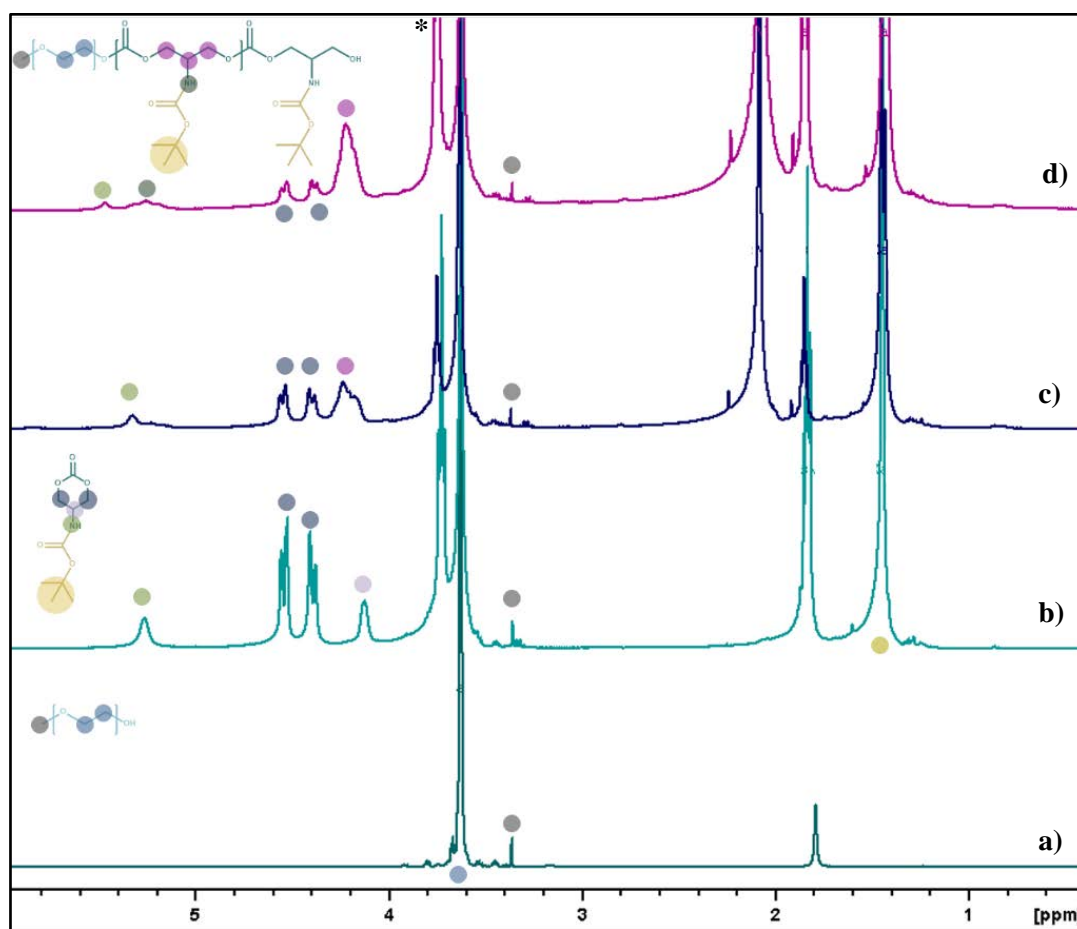


Figure 49: ^1H NMR spectra in CDCl_3 of the kinetics of diblock synthesis a) macroinitiator $\text{MeO-PEG}_{114}\text{-OH}$, b) reaction mixture before DBU addition, c) aliquot after 1h reaction, d) aliquot after 2h reaction. *THF solvent peak present at 3.8ppm.

While the reaction reached 80% conversion after 2.5 h of reaction, it was terminated by quenching with acetic acid, followed by the purification of the polymer by precipitation in cold diethyl ether. The reaction was chosen to be terminated at 80% conversion to avoid possible side reactions, such as the ones that were observed for the TMC monomer in literature, where after 80% a coupling reaction was observed. Finally at this stage, the reaction was washed 3 times by re-precipitation in diethyl ether to remove unreacted monomer and the catalysts DBU/TU. The final product was analyzed by ^1H NMR and SEC in DMF. An example of such diblock copolymer is presented in Figure 50 ($\text{PEG}_{114}\text{-}b\text{-PBATC}_{20}$ (7)). The obtained diblocks are listed in Table 2.

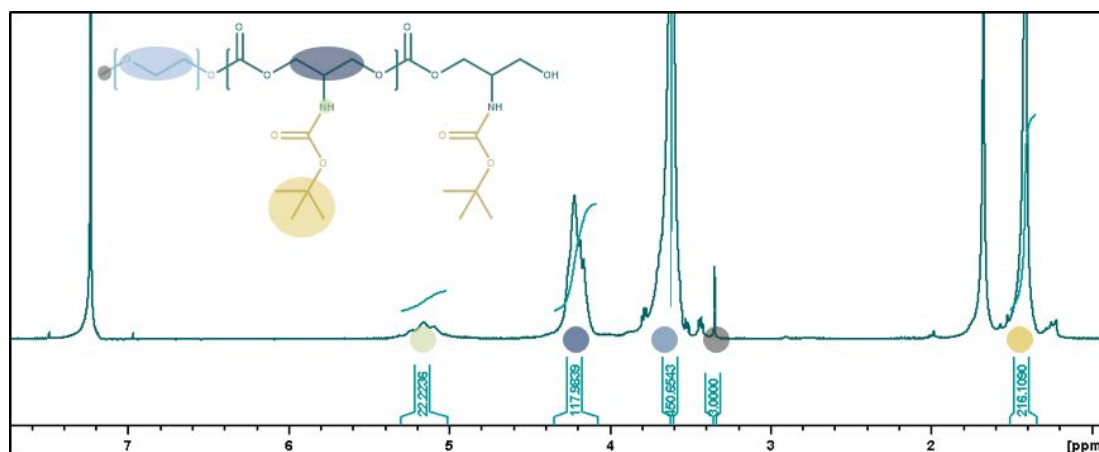


Figure 50: ^1H NMR spectrum in CDCl_3 of $\text{PEG}_{114}\text{-}b\text{-PBATC}_{28}$ (7) in Table 3 after purification.

The targeted DP for diblock $\text{PEG}_{114}\text{-}b\text{-PBATC}_{23}$ (1) was 24 for 80% conversion ^1H NMR analysis (Table 2) suggested that the resulting DP after 2.5h of reaction resulted to a DP was very close to the targeted one. For $\text{PEG}_{114}\text{-}b\text{-PBATC}_m$ (3), the targeted DP was 32 for 80% conversion the resulting DP ended up being 36 *i.e.*, close to the targeted DP (reaction time 3.5 hours), but the SEC chromatograms revealed a higher dispersity and a shoulder on the right indicating smaller populations present. While this could indicate that for higher DPs the control of the polymerization is lost in these conditions, it was eventually attributed to bad solubilization of the terminating agent, acetic acid in this particular reaction. To prove this point $\text{PEG}_{114}\text{-}b\text{-PBATC}_m$ (4 and 5) were synthesized with the same targeted DP as $\text{PEG}_{114}\text{-}b\text{-PBATC}_{39}$ (3) in the same conditions, while making sure that the acetic acid had enough time to properly terminate the reaction. The polymers resulted in high DPs and lower polydispersity in SEC.

Table 2: Characteristics of PEG₁₁₄-*b*-PBATC_m

	M_n^{SEC} (g·mol ⁻¹)*	\bar{D} *	M_n^{HNMR} PB ATC (g·mol ⁻¹)**	M_n^{HNMR} PE G ₁₁₄ - <i>b</i> - PBATC _m (g·mol ⁻¹)	Targete dDP PBATC	DP PBATC ***	CV ^{final}
PEG ₁₁₄ - <i>b</i> -PBATC ₂₃ (1)	8103	1.04	5040	10040	24	23	95%
PEG ₁₁₄ - <i>b</i> -PBATC ₂₈ (2)	7130	1.03	4950	9950	32	28	88%
PEG ₁₁₄ - <i>b</i> -PBATC ₃₉ (3)	10440	1.11	8550	13550	32	39	100%
PEG ₁₁₄ - <i>b</i> -PBATC ₃₄ (4)	12500	1.09	7380	12380	39	34	87%
PEG ₁₁₄ - <i>b</i> -PBATC ₂₈ (5)	12700	1.05	6080	11080	32	28	88%
PEG ₁₁₄ - <i>b</i> -PBATC ₂₁ (6)	12460	1.02	4650	9650	32	21	66%
PEG ₁₁₄ - <i>b</i> -PBATC ₁₉ (7)	12360	1.07	4170	9170	32	19	60%
PEG ₁₁₄ - <i>b</i> -PBATC ₂₈ (8)	11710	1.09	6080	11080	32	28	88%

*Number-average molar mass (M_n) and dispersity (\bar{D}) measured by SEC chromatography in DMF solvent with PS calibration; ** Number-average molar mass (M_n), degree of polymerization (DP) and final conversion calculated by ¹H NMR spectroscopy in CDCl₃.

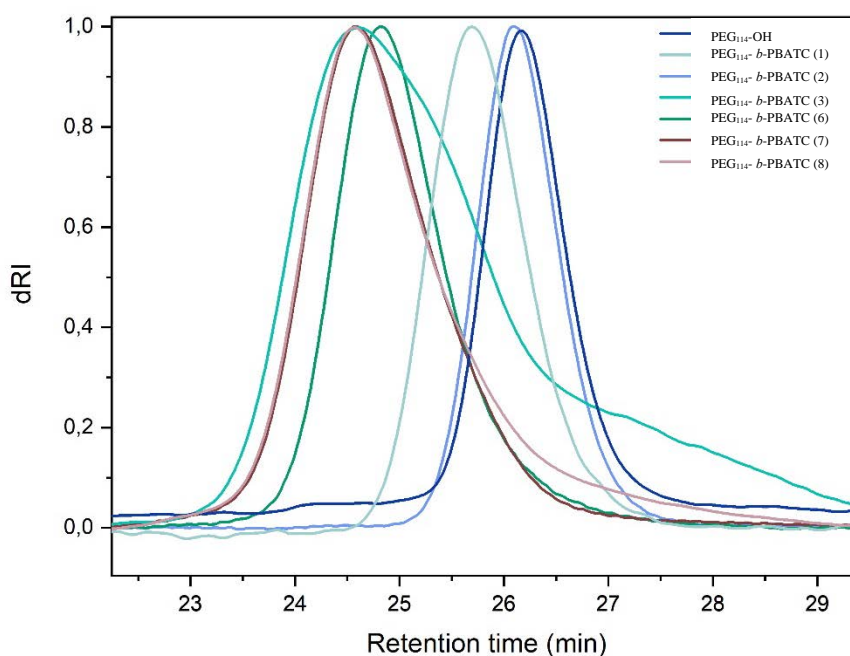
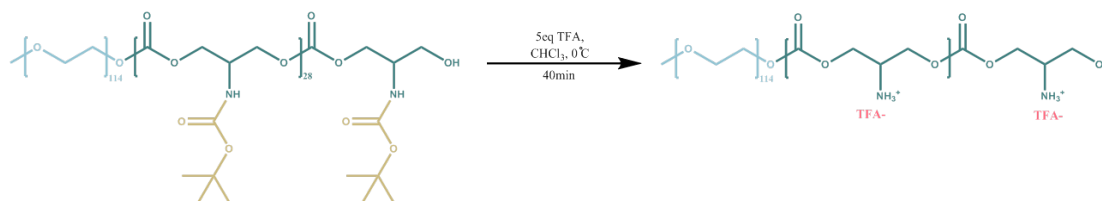


Figure 51: SEC chromatographs in DMF of the PEG₁₁₄-*b*-PBATC_m diblock copolymers with protected amino groups of a variety of M_n values.

Deprotection of PEG₁₁₄-*b*-PATC₂₁ amino side-groups

Following the synthesis of the PEG₁₄₄-*b*-PATC_m diblock, the next step was the deprotection of amines on the poly(amino trimethylene carbonate) block (Scheme 4). The deprotection process was adapted from literature in order to avoid polymer degradation by the acidic medium as much as possible. Specifically, the protected diblock copolymers were solubilized in a dry solvent, either dry chloroform or dry dichloromethane, both performing the reaction with acceptable results. Trifluoroacetic acid (TFA) was utilized as deprotecting agent, in same amount whatever the DP. The time of reaction was dependent on the DP. For instance, for a DP of 30, a reaction time of 40 min was necessary. To purify the deprotected polymer, the solution was precipitated in cold diethyl ether and washed three more times to eliminate the traces of the protecting BOC group. While degradation and non-full deprotection was observed in some cases, it was concluded that the quality of TFA was a major component for the resulting polymer.



Scheme 4: Deprotection of PEG-*b*-PATC with TFA.

For example, PEG₁₁₄-*b*-PBATC₂₁ (6) with a DP 21 was solubilized in dry chloroform at 0°C. The volume of added TFA was adjusted accordingly in order to achieve a dilution of 1:3 (v/v) TFA:CHCl₃. The reaction time was 40 min to achieve full deprotection. After deprotection, the reaction was terminated by precipitation in cold diethyl ether. After deprotection the polymers become insoluble in deuterated chloroform and their analysis by ¹H NMR was performed in deuterated DMSO. The disappearance of the –BOC peak at 1.5 ppm is visible, allowing to assume the full deprotection and the adequate purification of the polymers. Moreover, a visible difference appeared between the peak of the protected amine group at 7 ppm and the deprotected protonated amine at 8.5 ppm (Figure 52).

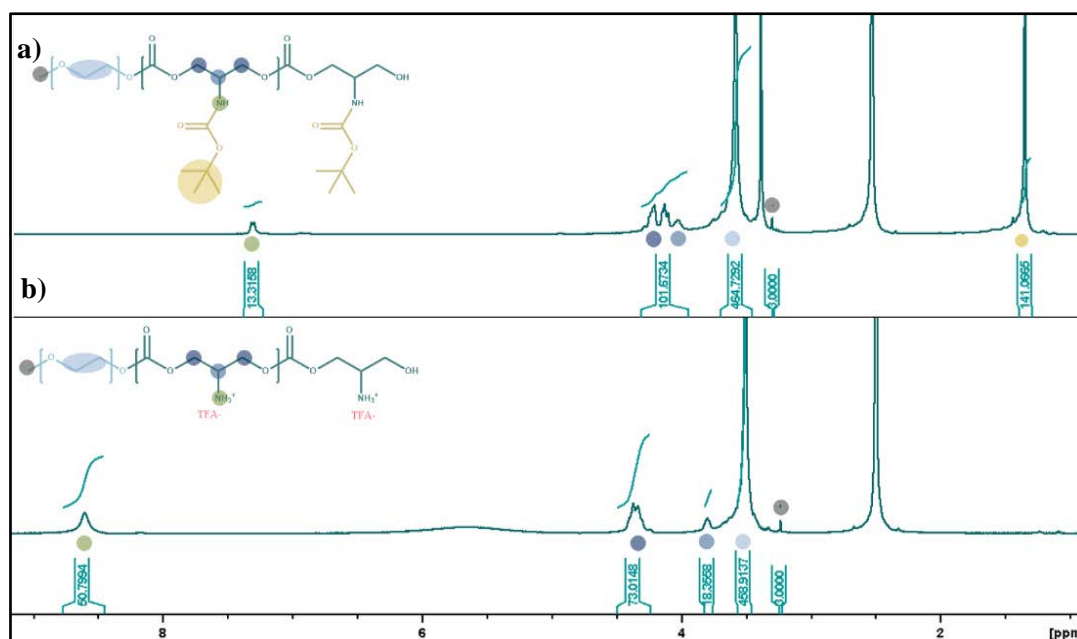


Figure 52: ¹H NMR spectra in (CD₃)₂SO of a) the protected PEG₁₁₄-b-PBATC₂₁ and b) the deprotected PEG₁₁₄-b-PATC₁₈ (PPATC3).

The calculation of the final DP was done by integrating the methyl peak of poly (ethylene glycol) as 3 and integrating the peak at 3.8 ppm which has been assigned to the methine proton in each molecular unit in the PATC. While the polymer appeared fully deprotected, some degradation did take place with the final DP of the being lower after deprotection. This behavior was observed for all the deprotection reactions were the degradation of the diblock to some extent could not be avoided (Table 3).

Table 3: Degree of polymerization of the final PEG₁₁₄-b-PATC_n diblocks and the reaction time of the deprotection

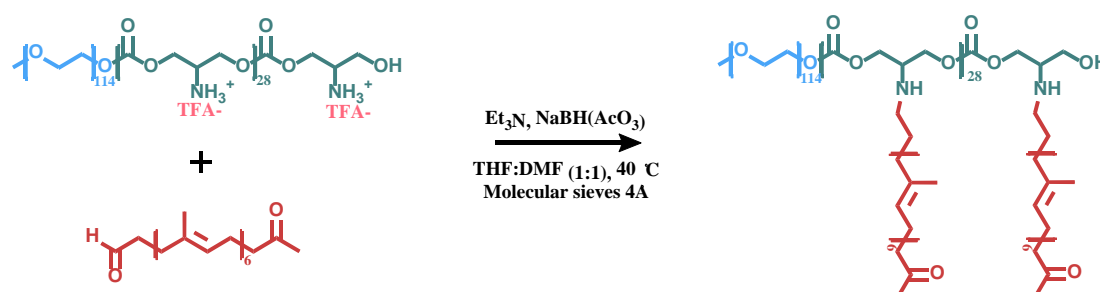
	DP PBATC*	DP PATC**	Reaction time (min)
PEG ₁₁₄ -b-PATC ₂₂ (PPATC1)	28	22	40
PEG ₁₁₄ -b-PATC ₃₁ (PPATC2)	36	31	50
PEG ₁₁₄ -b-PATC ₁₈ (PPATC3)	21	18	40
PEG ₁₁₄ -b-PATC ₁₇ (PPATC4)	19	17	40
PEG ₁₁₄ -b-PATC ₂₀ (PPATC5)	28	20	40

*Degree of polymerization (DP) calculated by ¹H NMR spectroscopy in CDCl₃, **Degree of polymerization (DP) calculated by ¹H NMR spectroscopy in (CD₃)SO.

Reductive amination for the synthesis of PEG-*b*-(PATC-*g*-PI)

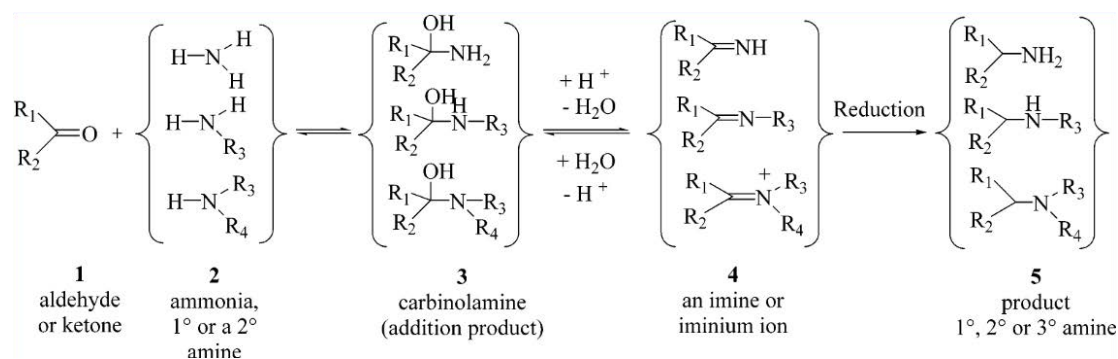
The synthesis of the graft copolymer was achieved *via* a reductive amination reaction between the primary amine groups of the PEG₁₁₄-*b*-PATC₂₀ diblock and the aldehyde end-group of the poly(isoprene) block (Scheme 5). Various conditions were implemented for the reaction in order to increase the grafting density of the copolymer, ideally 100 % of the amine functions should have reacted at the exception of the temperature that remained the same (40 °C) and the solvent mixture THF/DMF (1:1 v/v). Both solvents had to be used to allow the solubility of the diblock, which after the deprotection process was no longer soluble in THF. Moreover, even if the oligomer of PI was soluble in DMF, when the reaction was performed strictly in DMF the functionalization did not seem to improve, thus a mixture of 1:1 in volume was decided as the most appropriate solvent in order to ensure the best solubility possible for both components.

It is well known that “grafting to” reactions, when it comes to coupling reactions, are not widely accepted as the best method to achieve high functionalization, and “grafting through” or “grafting from” are generally accepted as better methods. “Grafting to” has gained popularity with the introduction of click reactions that allowed for better control in the addition of side chains [16]. In our case, the reaction utilized, while not being a click reaction, allowed for a high functionalization due to the nature of the poly(isoprene) that was utilized. Specifically, the DP of poly(isoprene) is low which increased its reactivity and limited steric repulsions between the chains when those were close to the backbone site of attachment.



Scheme 5: Reductive amination between the diblock PEG₁₁₄-*b*-PATC₂₈ and the aldehyde group of the PI.

The reductive amination between an aldehyde group and an amine is a very well-known reaction and has been exploited in this study where various conditions were tested. Furthermore, a reductive amination consists of an intermediate state which includes the transient formation of an imine before it is reduced by a reducing agent into a secondary amine (Scheme 6).



Scheme 6: Reproduced from [7] depicting the step, including the intermediate formation of an imine, in the reductive amination reaction.

While, literature suggest that with the use of an adequate reducing agent, this step can be avoided by directly reducing the final product without the formation of the imine step, in our case it was found that the aldehyde group of the poly(isoprene) would be reduced into an alcohol only after 2 h of stirring with sodium triacetoxyborohydride, thus the risk of actually losing one of our reactants was great, if we added the reducing agent to the reaction immediately. As already discussed above, the ketone group of the poly(isoprene) is not reduced by our chosen selective reducing agent, which was one of the reasons why it was specifically chosen, including its reduced toxicity. To return to the point of imine formation, water is being produced during this intermediate state and the reaction can shift back while the water is still present in the medium. To limit this possibility, molecular sieves were implemented in the reaction as well. Their addition limited the moisture presence that could react with the reducing agent and render it inactive, but also allowed the reaction to go faster. In our case, the reaction time was reduced to 24 h instead of 6 days without molecular sieves. Furthermore, all reactions were performed under inert atmosphere (nitrogen gas flow) and all reagents were dried as well.

Triethylamine was added to the reaction as a deprotonating agent of the amines on the backbone of the diblock copolymer. An excess of triethylamine was found to be necessary (8 eq relative to the amine moieties was found to be an adequate amount). Such a high amount of triethylamine was necessary due to the presence of benzoic acid in the poly(isoprene) block and allowed a higher functionalization by eliminating the acid from the reaction by the formation of a salt which was precipitated during the reaction.

The kinetics of the functionalization was followed by ^1H NMR in CDCl_3 by the decrease of the peak of the aldehyde proton at 9.74 ppm keeping the integration of the peak at 5.14 ppm at 5, *i.e.*, the DP of the poly(isoprene). The integration did not change significantly after 4 h suggesting that the highest functionalization was achieved after that period (Figure 53).

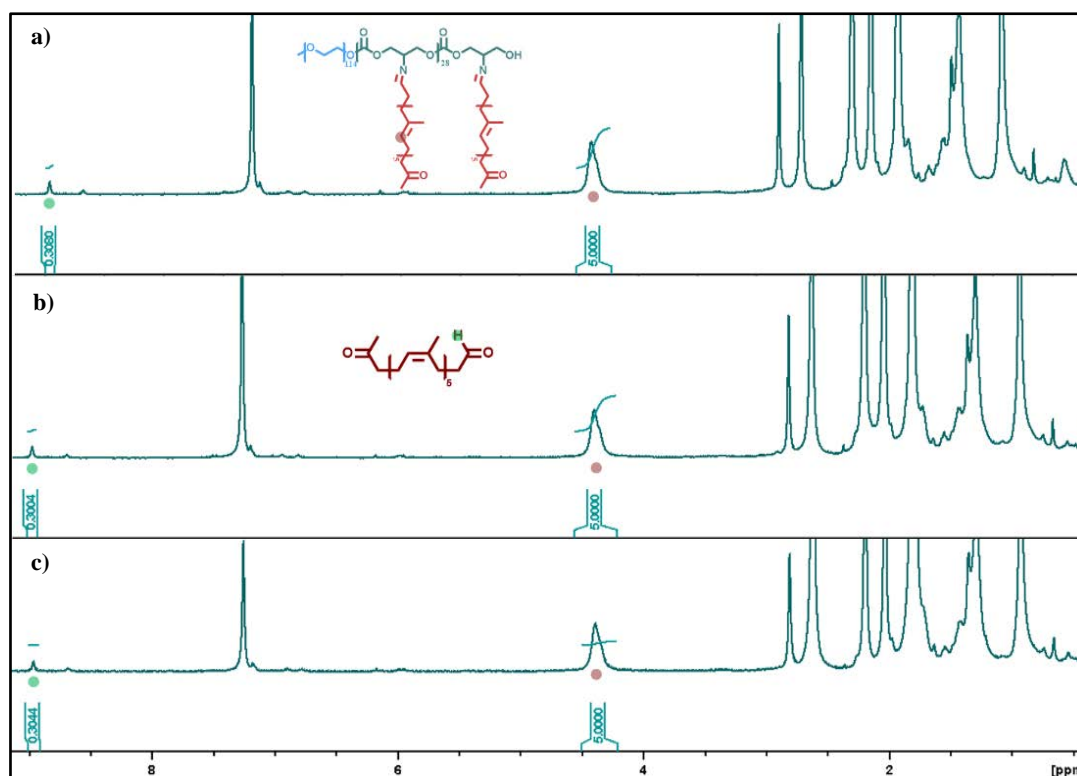


Figure 53: ^1H NMR spectra in CDCl_3 of graft copolymer (G1) at different reaction times a) 4 h, b) 6 h, c) 24 h.

Several tests were performed to know whether the reaction time before the addition of the reducing agent would change the outcome. Five reactions, with the same conditions were performed by changing only the time at which the reducing agent was added (2, 4, 6, 8 or 24 h) for a 24 h reaction. The final products were filtered and precipitated in cold heptane before being analyzed by ^1H NMR and SEC in DMF. All reactions produced the same conversion (74 %), thus 2 h is enough for the imine formation (Figure 54).

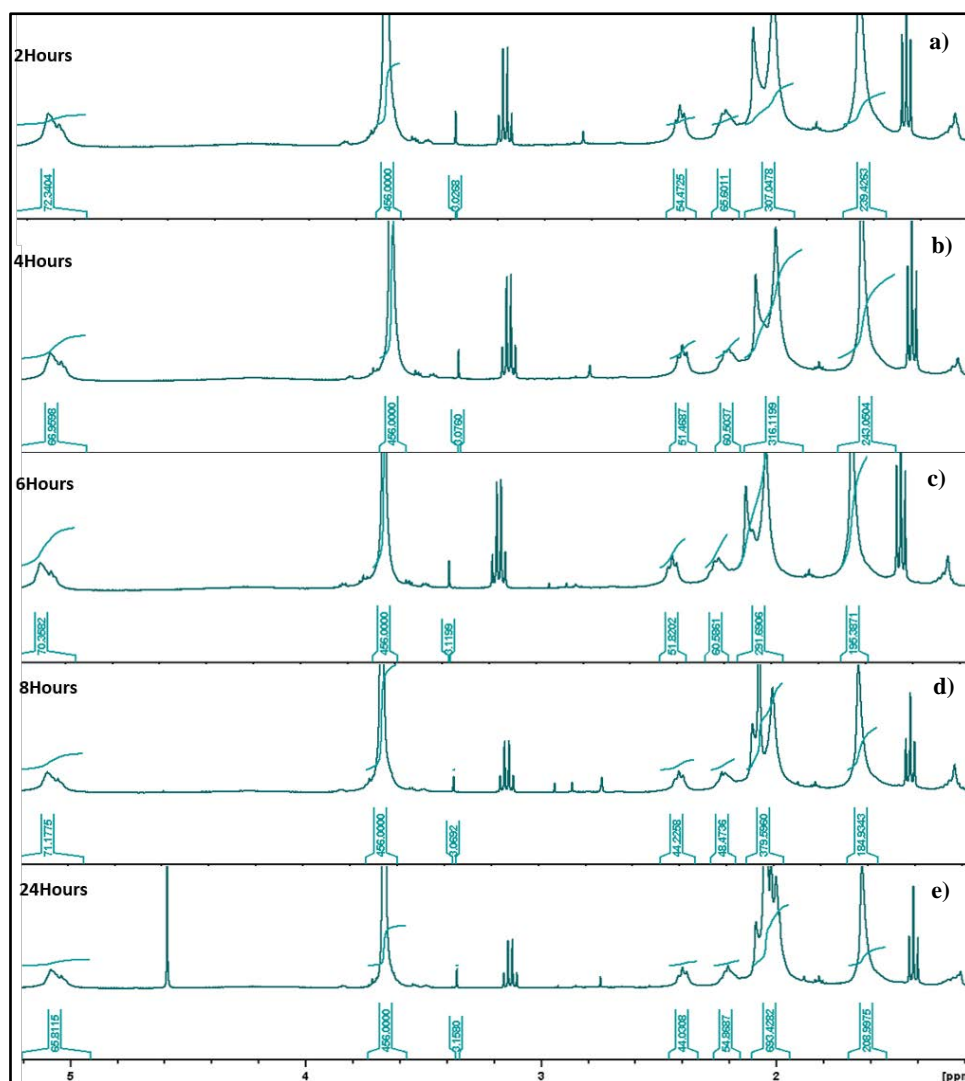


Figure 54: ^1H NMR spectra in CDCl_3 of 5 graft copolymers (G2) with different times of imine formation steps before the addition of reducing agent a) 2 h, b) 4 h, c) 6 h, d) 8 h and d) 24 h.

Table 4: Reaction conditions for the graft copolymer $\text{PEG}_{114}\text{-}b\text{-(PATC}_n\text{-}g\text{-PI}_m)$ (G1) and $\text{PEG}_{114}\text{-}b\text{-(PATC}_n\text{-}g\text{-PI}_m)$ (G2)

Graft	$\text{PEG}_{114}\text{-}b\text{-PTDOC}_n$ (nDP)	PI_m (mDP)	eq PI	C ($\text{mg}\cdot\text{mL}^{-1}$)	THF (mL)	DMF (mL)	ET_3N (mL)	Eq $\text{NaBH}(\text{AcO})_3$
G1	18	5	7	400	0.6	0.8	0.2	5
G2	19	5	7	200	0.3	0.3	0.1	5

After concluding that the imine formation step remains stable between 2 and 24 h and no further addition of poly(isoprene) is achieved after that period of time the following reactions were performed with a 24 h step of imine formation before adding the reducing agent into the reaction to perform the reduction. The reduction step seemed to be working well after 24 h passed as can be seen in Figure 55 where the reaction time was 24 h and no aldehyde group was present in the final ^1H NMR spectra as can be detected by the lack of the characteristic aldehyde peak of poly(isoprene) at 9.8 ppm in the final graft copolymer when compared to the poly(isoprene) carbonyl telechelic poly(isoprene). The lack of the peak at 2.5 ppm could also be observed after the completion of the reaction, which also confirms the lack of any aldehyde groups present in the final system, as this peak represents the protons on the carbon that is next to the aldehyde group.

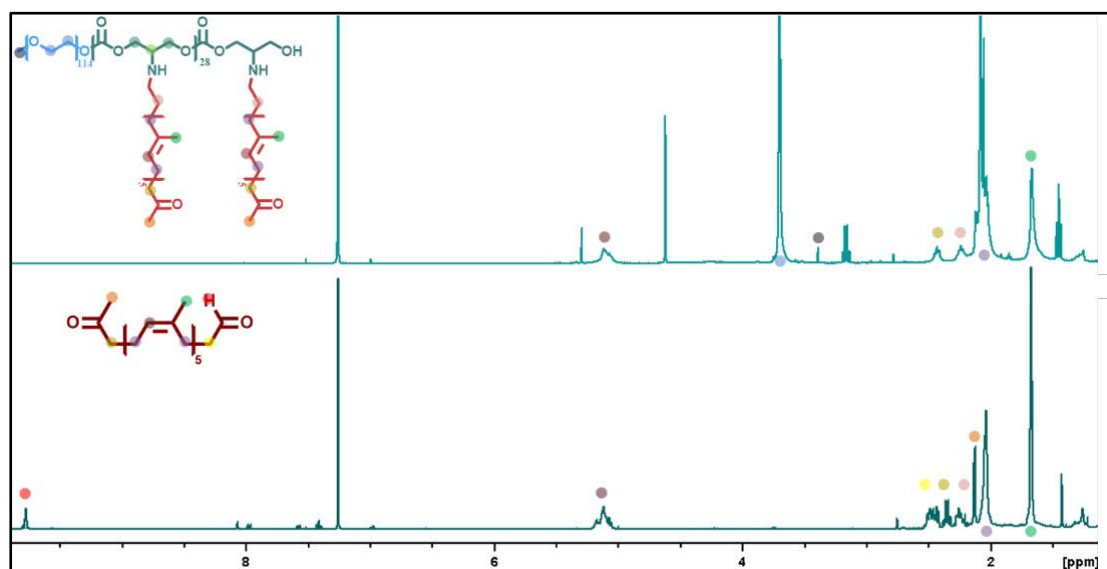


Figure 55: ^1H NMR spectra in CDCl_3 of a) graft copolymer $\text{PEG}_{114}\text{-}b\text{-(PATC}_n\text{-}g\text{-PI)}_m$ (G2) after 24 h and b) carbonyl heterotelechelic poly(isoprene) $\text{PI}_5(4)$.

The influence of the concentration was also studied. First, reactions were performed at a concentration of $400 \text{ mg}\cdot\text{mL}^{-1}$ which lead to a high viscosity issue. Thus, reactions were also tested at $200 \text{ mg}\cdot\text{mL}^{-1}$. The final polymers exhibited a high functionalization rate similar to the polymers obtained at a concentration of $400 \text{ mg}\cdot\text{mL}^{-1}$. It is important to acknowledge again the fact that the integration of poly(isoprene) at 5.2 ppm cannot be taken into account to calculate the functionalization, since in reality it seems that the functionalization happens by a variety of distinct fractions that exist in the produced poly(isoprene) and it is quite possible that the smaller oligomers of the population are kinetically faster to react than for example the average molar mass that has a DP of 5. Indeed, in the case of these reaction the poly(isoprene) that was

used was PI₅ (5) with a DP 5 and $D=1.93$ which indeed is a high dispersity and thus provides the possibility of a non-controlled functionalization.

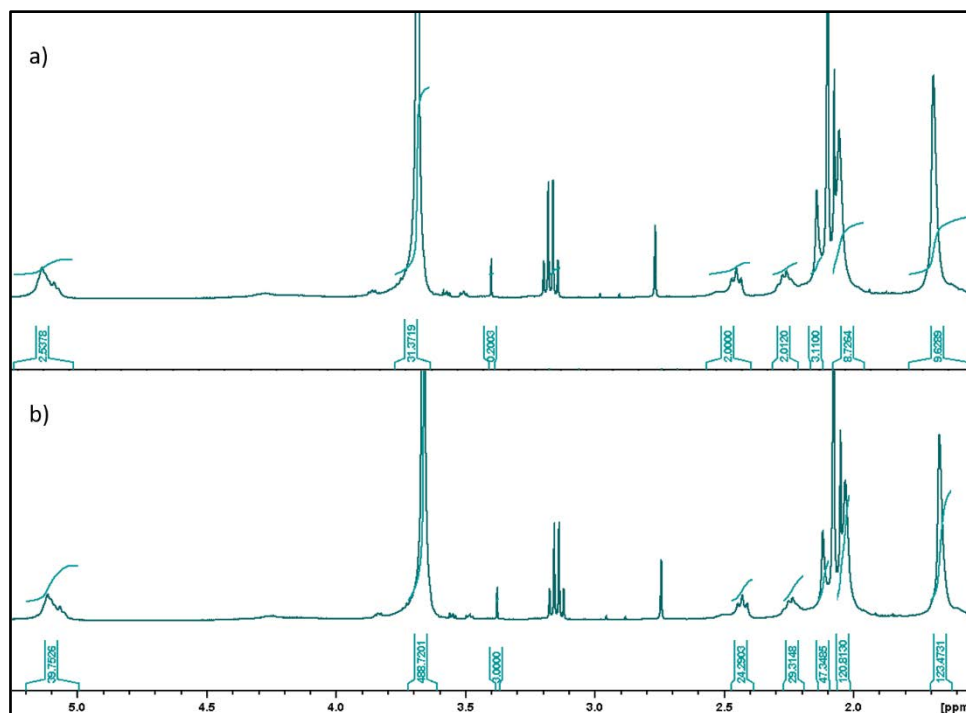


Figure 56: ¹H NMR spectra in CDCl₃ of the graft copolymer PEG₁₁₄-*b*-(PATC-*g*-PI₃)₁₅-*co*-PATC₁₅ (G3) a) integrating the peak at 2.4 ppm as 2H and b) the final polymer integrating the peak of PEG₁₁₄ at 3.6ppm as 489H.

Thus, a different peak is used to calculate the functionalization, which is the peak at 2.4 ppm which represents the 2H on the carbon that is next to the ketone which remains stable throughout the reaction since the ketone does not react in these conditions. Indeed, when integrating the peak at 2.4 ppm as 2 protons, it is possible to see the actual DP of the attached poly(isoprene) sidechains both for the peak at 5.2 ppm and the peak at 1.65 ppm which represents the methylene protons that each molecular unit of poly(isoprene) is bearing. For example, for the graft copolymer PEG₁₁₄-*b*-(PATC-*g*-PI₃)₁₅-*co*-PATC₁₅ (G3), the original DP of poly(isoprene) was 5 while in ¹H NMR, after integration of the peak at 2.4 ppm, it was found that the attached PI had a DP of almost 3, which indeed suggests that the smallest chains of the population were attached. This can be corroborated by the peak of methylene protons, which appear to be almost 10 concluding to a DP close to 3 (Figure 56). Through this process, it was found that the functionalization of this graft was 67%, the poly(isoprene) chains attached being of 204 g/mol, and the total molar mass of PI being 3060 g/mol.

The calculation of the degree of functionalization (*D.F.*) was done via the equation:

$$D.F.\% = \frac{I_{5.2ppm}}{DP_{PI} \times DP_{PAC}} \times 100$$

Similar conditions were used for the graft copolymer PEG₁₁₄-*b*-PATC₂₀-*g*-PI₅ (G4) with a slight increase of poly(isoprene) to 8 equivalents. The resulting copolymer exhibited in this case a 100% functionalization (Figure S7). *Via* the calculations performed in ¹H NMR it was found the poly(isoprene) attached had a DP of 5, *i.e.* 340 g·mol⁻¹ and a total molar mass of 7990 g·mol⁻¹. Furthermore, the SEC analysis (Figure S8) offered further verification of the functionalization, both by the shift from the original diblock PEG₁₁₄-*b*-PAC₂₀ and by the appearance of a UV peak in both graft copolymers due to the attached poly(isoprene). But it is important to note that free poly(isoprene) was still present in the systems as can be seen in SEC for the graft copolymer G3 and G4 which could suggest that the calculated via ¹H NMR degree of functionalization is not 100% accurate and the actual functionalization is less (Figure S4).

Another graft copolymer which will be studied in the self-assembly process in Chapter V is graft PEG₁₁₄-*b*-(PATC-*g*-PI₄)₂₀-*co*-PATC₁₁ (G5). This copolymer had a higher molar mass for the PATC block, more specifically PEG₁₁₄-*b*-PATC₃₁ (PPTAC2) was utilized for the graft to reductive amination, with a DP of 30. The conditions of the reaction were the initial conditions with a polymer concentration of close to 400 mg·mL⁻¹ and the time before reduction was just 2 hours. This polymer was synthesized before changing the concentration to 200 mg·mL⁻¹, nevertheless the polymer was utilized for many self-assembly procedures in the subsequent chapter thus it is mentioned as well. The degree of functionalization was calculated to be 67% from ¹H NMR (Figure S2) and had a low polydispersity in SEC THF (Figure S3). The reaction conditions of the three main graft copolymers which are utilized in this study are depicted in Table 5.

Table 5: Reaction conditions for the graft copolymers PEG₁₁₄-*b*-(PATC-*g*-PI₃)₁₅-*co*-PATC₅ (G3), PEG₁₁₄-*b*-PATC₂₀-*g*-PI₅ (G4) and PEG₁₁₄-*b*-(PATC-*g*-PI₄)₂₀-*co*-PATC₁₁(G5).

Graft copolymer	PEG ₁₁₄ - <i>b</i> -PAC ₂₀ mg·mL ⁻¹	PI ₅ mg·mL ⁻¹	eq PI	C mg·mL ⁻¹	THF mL	DMF mL	Et ₃ N mL	Eq NaBH(AcO) ₃
G3	60	490	7	200	1.2	1.2	0.2	5
G4	60	520	8	200	1.25	1.25	0.5	5
G5	60	400	7	380	0.5	0.5	0.15	5

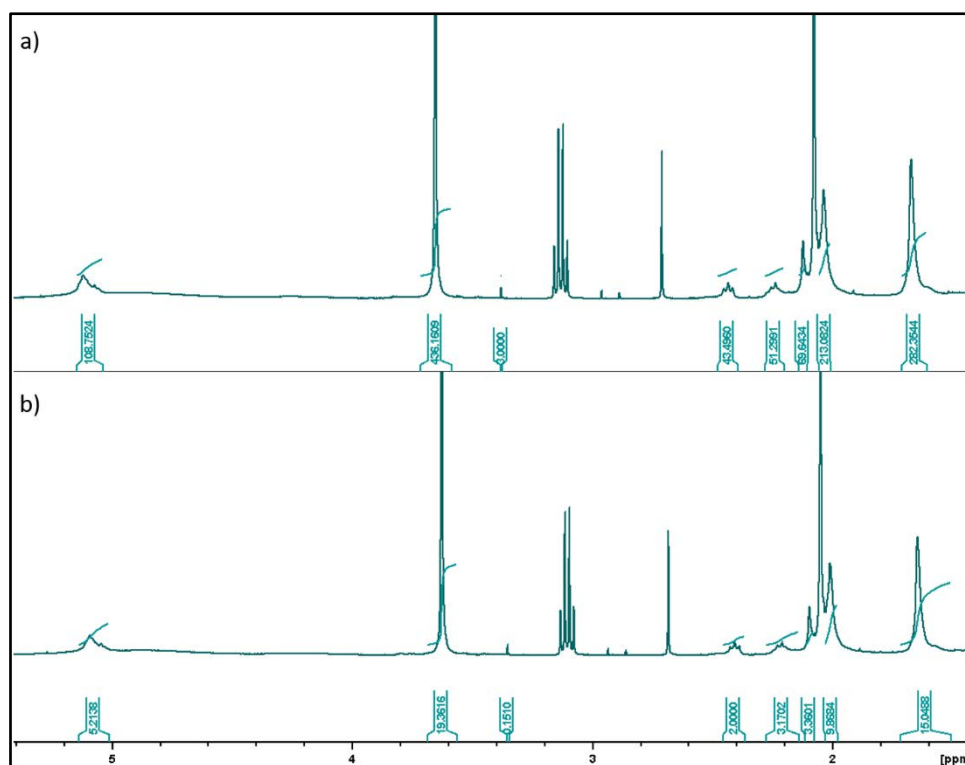


Figure 57: ^1H NMR spectra in CDCl_3 of the graft copolymer $\text{PEG}_{114}\text{-}b\text{-PATC}_{20}\text{-}g\text{-PI}_5$ (G4) a) the final polymer integrating the peak of PEG_{114} at 3.6ppm as 456H and b) integrating the peak at 2.4 ppm as 2H.

Table 6: Characteristics obtained for the $\text{PEG}_{114}\text{-}b\text{-(PATC-}g\text{-PI}_x\text{)}_n\text{-}co\text{-PATC}_m$ copolymers.

Graft	$M_n^{1\text{H NMR}}$ ($\text{g}\cdot\text{mol}^{-1}$)*	Poly(isoprene) $\text{DP}^{1\text{H NMR}}$	$M_{n\text{SEC}}$ ($\text{g}\cdot\text{mol}^{-1}$)**	D^{**}
G3	10420	3	11080	1.2
G4	15350	5	10300	1.6
G5	13980	4	10520	1.4

Finally, DOSY NMR analysis was performed for the graft copolymer $\text{PEG}_{114}\text{-}b\text{-PATC}_{20}\text{-}g\text{-PI}_5$ (G4) to verify that only one diffusion coefficient is present thus confirming that only one kind of copolymer is present and that it is different from the original diblock and or the poly(isoprene) homopolymer. Indeed, in we can verify that the graft copolymer G4 has only once diffusion coefficient $D=9.3\times 10^{-11}\text{ m}^2/\text{s}$, which is smaller than the one of the free diblock or PI homopolymer. Thus, confirming once more the success of the grafting reaction (Figure S 1).

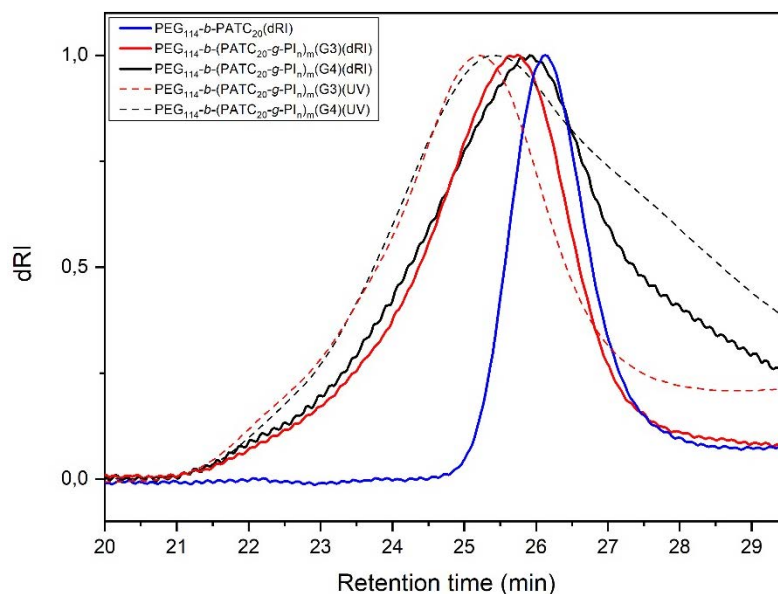


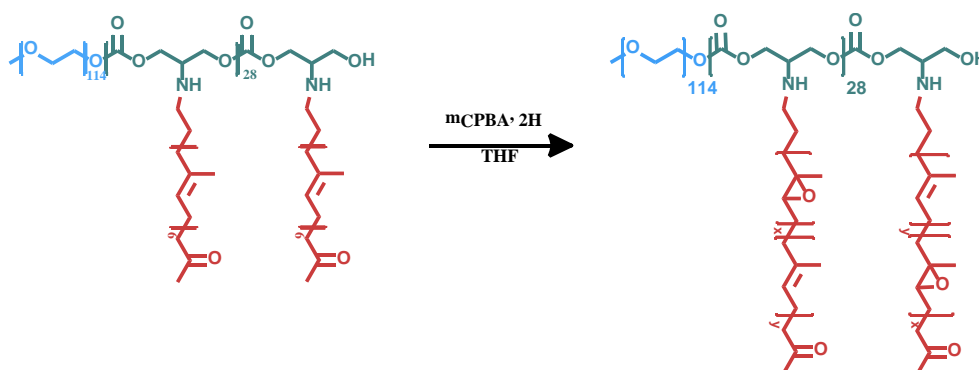
Figure 58: SEC in THF dRI signal of the initial diblock copolymer PEG₁₁₄-*b*-PATC₂₀ and the graft copolymers PEG₁₁₄-*b*-(PATC-*g*-PI₃)₁₅-*co*-PATC₅ (G3) and PEG₁₁₄-*b*-PATC₂₀-*g*-PI₅ (G4) and UV signal of the initial diblock copolymer PEG₁₁₄-*b*-PATC₂₀ and the graft copolymers PEG₁₁₄-*b*-(PATC-*g*-PI₃)₁₅-*co*-PATC₅ (G3) and PEG₁₁₄-*b*-PATC₂₀-*g*-PI₅ (G4).

The final copolymers that were described above, such as the graft copolymers PEG₁₁₄-*b*-(PATC-*g*-PI₃)₁₅-*co*-PATC₅ (G3) and PEG₁₁₄-*b*-PATC₂₀-*g*-PI₅ (G4) exhibited a good functionalization as can be seen both by ¹H NMR and SEC analysis, whose characteristics are demonstrated in Table 6. The most important parameter though was the hydrophilic ratio f_{PEG} which determines the self-assembly behavior of the polymer. In this case f_{PEG} was found to be 48% for PEG₁₁₄-*b*-(PATC-*g*-PI₃)₁₅-*co*-PATC₅ (G3), 33% for PEG₁₁₄-*b*-PATC₂₀-*g*-PI₅ (G4) and 36% for PEG₁₁₄-*b*-(PATC-*g*-PI₄)₂₀-*co*-PATC₁₁ (G5) respectively.

All ratios are quite high if we consider the necessary f_{PEG} for diblock copolymers such as PEG-*b*-PTMC which requires the hydrophilic ratio to be lower than 20% to self-assemble into vesicles but the grafts G4 and G5 fall into the general parameter for f_{PEG} that have been set for vesicle formation [17]. An important parameter in our system is the fact that the second hydrophobic block is poly(isoprene) and taking this into account, the necessary hydrophilic ratio for the copolymers to self-assemble into vesicles increases dramatically [18]. Specifically, as already mentioned in the introduction following the literature published by Discher & Eisenberg [19] the necessary hydrophilic ratio for PEO-polydienes to form vesicular self-assemblies is in the range $0.25 < f_{\text{PEG}} < 0.45$. Following this, we can expect that our polymers can indeed form vesicles, which will be studied in Chapter V.

Epoxidation of PEG₁₁₄-*b*-(PATC₂₀-*g*-PI)_n_m

In order to achieve the step involving the permanent deformation of the polymersomes after the application of a magnetic field, the hydrophobic membrane had to be modified in order to allow cross-linking which would enable a network formation causing a physical change in the properties of the membrane, from fluid to solid, elastomeric state. In order to perform the cross-linking of the PI chains, we decided to use the high reactivity of epoxides. To this end, the partial epoxidation of the double bonds of the poly(isoprene) blocks was achieved in THF at room temperature with mCPBA, its amount being calculated to achieve a predetermined epoxide percentage (Scheme 7).



Scheme 7: Representation of the epoxidation reaction for the graft copolymer PI side chains.

The percentage of epoxidation was targeted to be around 30-40 % to avoid changing the hydrophobic nature of poly(isoprene) sidechains. The epoxidized polymer was characterized by ¹H NMR to determine the degree of epoxidation. Two new peaks appeared in ¹H NMR, which were attributed to the epoxidized units of poly (isoprene): the triplet at 2.69 ppm (proton on the carbon bearing the epoxide group) and a doublet at 1.28 ppm (protons of the methyl group of the epoxide) (Figure 59). It was thus possible to calculate the epoxidation rate with the following equation:

$$\%Epoxidation = \frac{I_{2.69}}{I_{2.69} + I_{5.2}}$$

Thus, the final epoxidation of the graft copolymer PEG₁₁₄-*b*-(PATC-*g*-PI₃)₁₅-*co*-PATC₅ (G3) was 40% (Figure 59), 30% for the graft copolymer PEG₁₁₄-*b*-PAC₂₀-*g*-PI₅ (G4) (Figure 60) and 40 % for PEG₁₁₄-*b*-(PATC-*g*-PI₄)₂₀-*co*-PATC₁₁ (G5) (Figure S 2b).

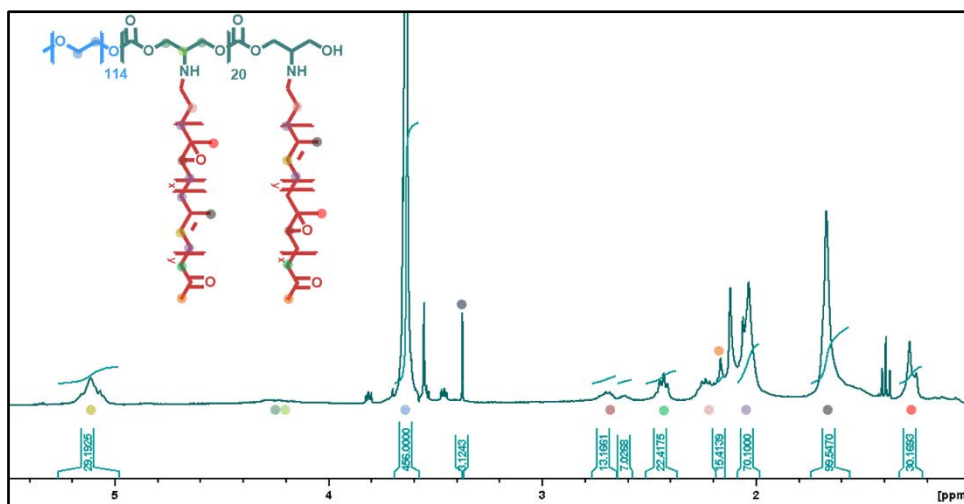


Figure 59: ^1H NMR spectra in CDCl_3 of the epoxidized graft copolymer $\text{PEG}_{114}\text{-}b\text{-(PATC-g-PI}_3\text{)}_{15}\text{-co-PATC}_5$ (G3).

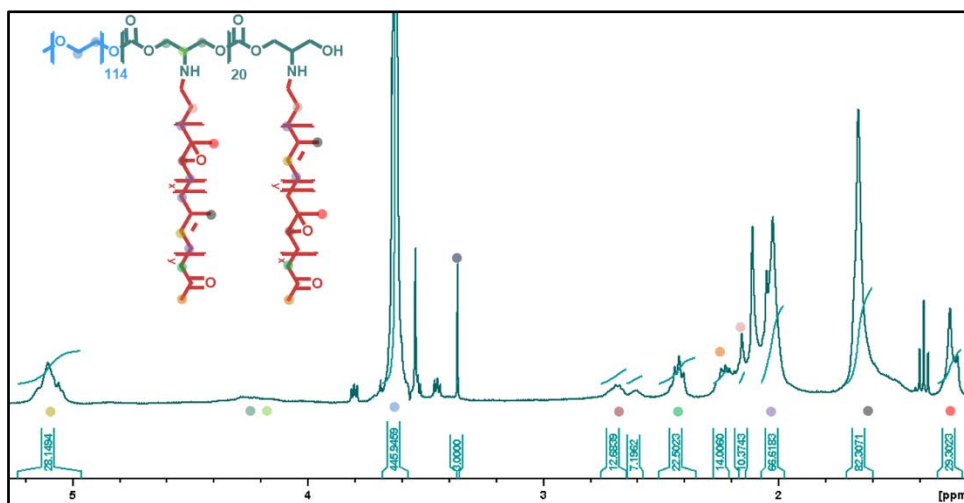


Figure 60: ^1H NMR spectra in CDCl_3 of the epoxidized graft copolymer $\text{PEG}_{114}\text{-}b\text{-PAC}_{20}\text{-g-PI}_5$ (G4).

Conclusion:

In conclusion, this chapter described the synthesis and characterization of graft copolymers $\text{PEG}_{114}\text{-}b\text{-(PATC}_{20}\text{-}g\text{-PI}_x)_m$ *via*: (i) the synthesis of diblock copolymers by ring-opening polymerization (ROP) of the *tert*-butyl (2-oxo-1,3-dioxan-5-yl) carbamate monomer TBDOC, (ii) deprotection of the amino groups, (iii) reductive amination between the aldehyde groups of a carbonyl heterotelechelic poly(isoprene) and the amine groups of the diblock copolymer $\text{PEG}_{114}\text{-}b\text{-PATC}_n$ and (iv) partial epoxidation of PI pendant chains.

The ROP proceeded by using $\text{CH}_3\text{-PEG}_{114}\text{-OH}$ as a macroinitiator in THF using DBU/TU as an organic catalytic system. A range of diblock copolymers were synthesized with a variety of polymerization degrees and low molar mass dispersity values. Following the synthesis of the diblock copolymers, their deprotection was also described using trifluoroacetic acid as a deprotection agent. The best conditions, *i.e.* right amount of TFA and time, to result in a deprotected copolymer without major degradation were described as well. Furthermore, the synthesis of a poly(isoprene) with a low DP was described *via* a “one-pot degradation” of a high molar mass industrial *cis*-1,4-poly(isoprene) $800000\text{ g}\cdot\text{mol}^{-1}$ using mCBPA and periodic acid as oxidative double-bond cleavage agents.

The final poly(isoprene) exhibited a small average DP ranging from 5 to 8 but with a “broad” dispersion of oligomer sizes, which affected the final functionalization of the graft copolymers. Consequently, various conditions were studied for the synthesis of the graft copolymers, using reductive amination as the “coupling” reaction with sodium triacetoxyborohydride ($\text{NaBH}(\text{AcO})_3$) as the reducing agent in order to find the best conditions. Finally, graft copolymers such as $\text{PEG}_{114}\text{-}b\text{-(PATC-}g\text{-PI}_3)_{15}\text{-}co\text{-PATC}_{15}$ (G3) and $\text{PEG}_{114}\text{-}b\text{-PATC}_{20}\text{-}g\text{-PI}_5$ (G4) were epoxidized to produce polymers that could be cross-linked in further reactions with an epoxidation of 40% and 30% respectively.

Three of the synthesized herein copolymers G3, G4 and G5, while exhibiting a $f_{\text{PEG}} > 20\%$, will be further studied for their self-assembly properties, in presence of hydrophobically coated magnetic iron oxide nanoparticles (IONPs) in order to observe their reaction to magnetic field as well as their cross-linking properties (Chapter V).

References:

- [1] E. B. Zhulina, S. S. Sheiko, and O. V Borisov, "Theoretical advances in molecular bottlebrushes and comblike (co)polymers: solutions{,} gels{,} and self-assembly," *Soft Matter*, vol. 18, no. 46, pp. 8714–8732, 2022.
- [2] V. Ibrahimova, H. Zhao, E. Ibarboure, E. Garanger, and S. Lecommandoux, "Thermosensitive Vesicles from Chemically Encoded Lipid-Grafted Elastin-like Polypeptides," *Angew. Chemie Int. Ed.*, vol. 60, no. 27, pp. 15036–15040, 2021.
- [3] A. V. Radchenko *et al.*, "Facile synthesis of 1,4-: Cis -polyisoprene-polypeptide hybrids with different architectures," *Polym. Chem.*, vol. 10, no. 19, pp. 2456–2468, 2019.
- [4] P. Berto, S. Grelier, and F. Peruch, "Controlled degradation of polyisoprene and polybutadiene: A comparative study of two methods," *Polym. Degrad. Stab.*, vol. 154, pp. 295–303, 2018.
- [5] P. Berto, S. Grelier, and F. Peruch, "Telechelic Polybutadienes or Polyisoprenes Precursors for Recyclable Elastomeric Networks," *Macromol. Rapid Commun.*, vol. 38, no. 22, pp. 2–7, 2017.
- [6] A. F. Abdel-Magid, K. G. Carson, B. D. Harris, C. A. Maryanoff, and R. D. Shah, "Reductive amination of aldehydes and ketones with sodium triacetoxyborohydride. Studies on direct and indirect reductive amination procedures," *J. Org. Chem.*, vol. 61, no. 11, pp. 3849–3862, 1996.
- [7] A. F. Abdel-Magid and S. J. Mehrman, "A review on the use of sodium triacetoxyborohydride in the reductive amination of ketones and aldehydes," *Org. Process Res. Dev.*, vol. 10, no. 5, pp. 971–1031, 2006.
- [8] S. Sato, T. Sakamoto, E. Miyazawa, and Y. Kikugawa, "One-pot reductive amination of aldehydes and ketones with α -picoline-borane in methanol, in water, and in neat conditions," *Tetrahedron*, vol. 60, no. 36, pp. 7899–7906, 2004.
- [9] A. F. Abdel-Magid, C. A. Maryanoff, and K. G. Carson, "Reductive amination of aldehydes and ketones by using sodium triacetoxyborohydride," *Tetrahedron Lett.*, vol. 31, no. 39, pp. 5595–5598, 1990.
- [10] C. Lebleu, L. Rodrigues, J. M. Guigner, A. Brûlet, E. Garanger, and S. Lecommandoux, "Self-Assembly of PEG-b-PTMC Copolymers: Micelles and Polymersomes Size Control," *Langmuir*, vol. 35, no. 41, pp. 13364–13374, 2019.
- [11] J. Du, "Polymer Vesicles," *Adv. Hierarchical Nanostructured Mater.*, vol. 9783527333, no. August, pp. 177–192, 2014.
- [12] H. Aranda-Espinoza, H. Bermudez, F. S. Bates, and D. E. Discher, "Electromechanical limits of polymersomes," *Phys. Rev. Lett.*, vol. 87, no. 20, pp. 208301-1-208301-4, 2001.
- [13] M. Rauschenbach, S. B. Lawrenson, V. Taresco, A. K. Pearce, and R. K. O'Reilly, "Antimicrobial Hyperbranched Polymer–Usnic Acid Complexes through a Combined ROP-RAFT Strategy," *Macromol. Rapid Commun.*, vol. 41, no. 18, 2020.
- [14] U. Jost, B. Andreeßen, D. Michalik, A. Steinbüchel, and U. Kragl, "Downstream processing of serinol from a glycerol-based fermentation broth and transfer to other amine containing molecules," *Eng. Life Sci.*, vol. 17, no. 5, pp. 479–488, 2017.

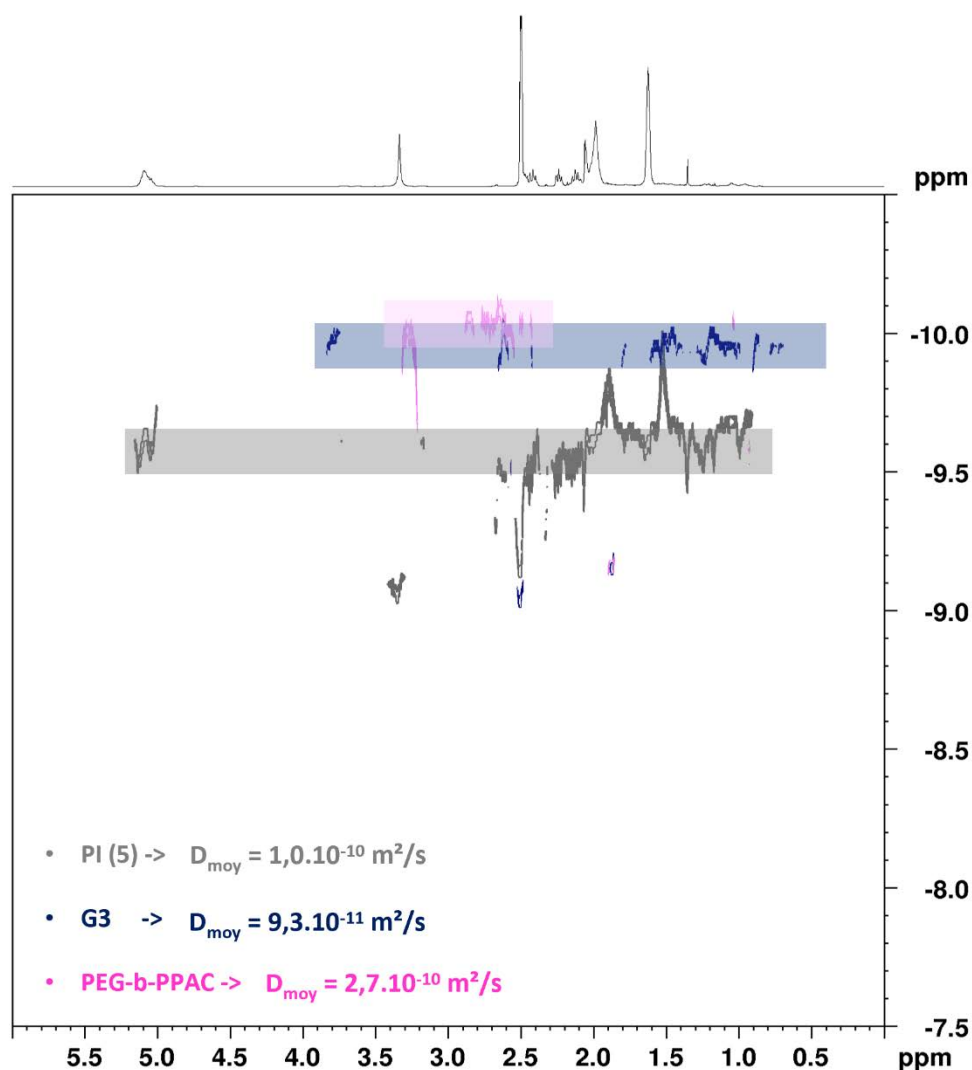
- [15] S. Gillier-Ritoit, D. Reyx, I. Campistron, A. Laguerre, and R. P. Singh, "Telechelic cis-1,4-oligoisoprenes through the selective oxidolysis of epoxidized monomer units and polyisoprenic monomer units in cis-1,4-polyisoprenes," *J. Appl. Polym. Sci.*, vol. 87, no. 1 SPEC., pp. 42–46, 2003.
- [16] A. Bhattacharya and B. N. Misra, "Grafting: a versatile means to modify polymers: Techniques, factors and applications," *Prog. Polym. Sci.*, vol. 29, no. 8, pp. 767–814, 2004.
- [17] B. M. Discher *et al.*, "Polymersomes: Tough vesicles made from diblock copolymers," *Science (80-.)*, vol. 284, no. 5417, pp. 1143–1146, 1999.
- [18] J. Ding and G. Liu, "Polyisoprene-block-poly(2-cinnamoylethyl methacrylate) Vesicles and Their Aggregates," *Macromolecules*, vol. 30, no. 3, pp. 655–657, Feb. 1997.
- [19] D. E. Discher and A. Eisenberg, "Polymer Vesicles," *Science (80-.)*, vol. 297, no. 5583, pp. 967–973, 2002.

Supplementary Information:

Table S 1: Theoretical and experimental M_n values for each epoxidation condition from [5]

One-pot degradation results for the synthesis of CTPI (EPI cleaved by periodic acid).

entry	Epoxy _{th} %	$M_{n\ th}^a$ (g.mol ⁻¹)	$M_{n\ NMR}^b$ (g.mol ⁻¹)	$M_{n\ SEC}^c$ (g.mol ⁻¹)	\bar{D}^d	Calculated Functionality ^e
27	0.26	26 150	52 800	57 000	1.5	1.82
28	0.35	19 430	41 000	37 000	1.5	1.88
29	0.39	17 440	37 400	33 500	1.5	1.89
30	0.54	12 590	23 000	28 500	1.5	1.91
31	0.74	9190	20 200	15 100	1.5	1.95
32	1.06	6410	14 700	12 400	1.4	1.96
33	1.17	5810	12 500	10 200	1.4	1.97
34	1.30	5230	9700	12 000	1.3	1.96
35	1.60	4250	9400	7100	1.5	1.98
36	2.10	3240	4800	6400	1.5	1.98
37	3.20	2120	3600	4800	1.3	1.98

**Figure S 1:** DOSY NMR spectra of poly(isoprene) (gray), graft copolymer G3 (blue) and the diblock copolymer (pink) along with their measured diffusion coefficients.

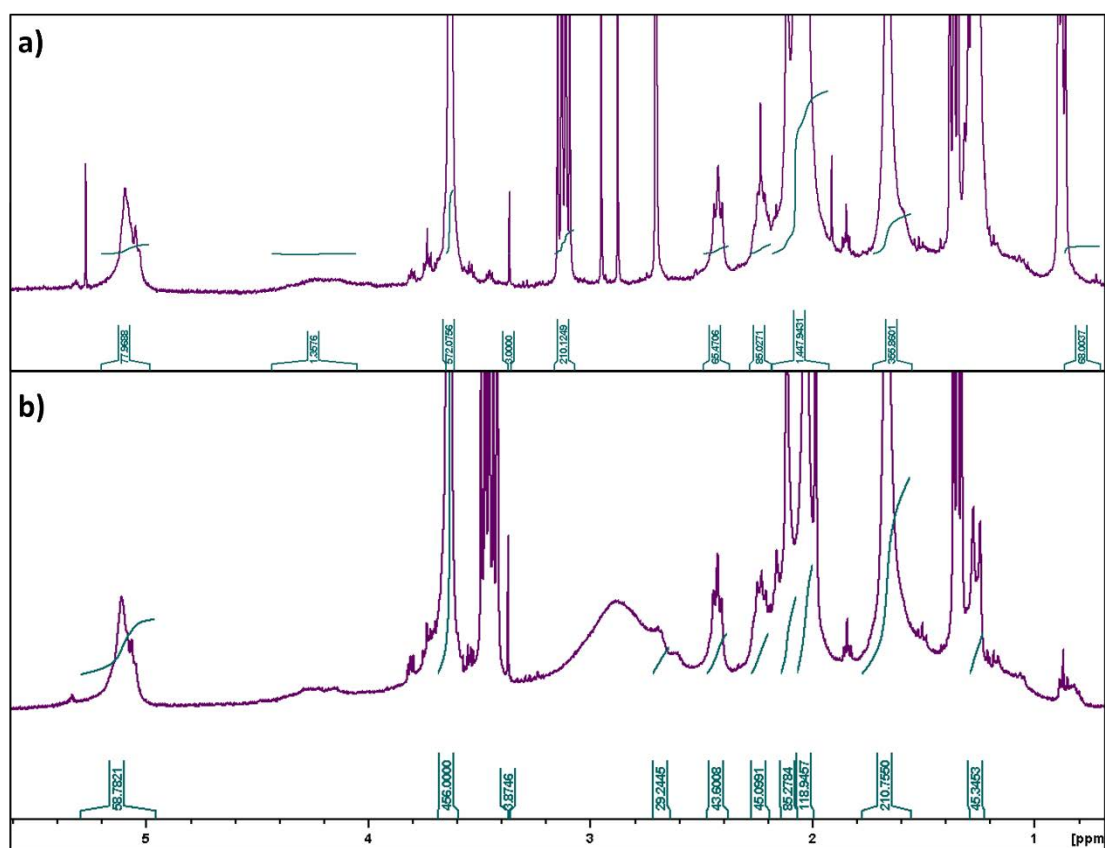


Figure S 2: a) ^1H NMR graft copolymer $\text{PEG}_{114}\text{-}b\text{-(PATC-g-PI}_4\text{)}_{20}\text{-co-PATC}_{11}$ (G5) and b) the epoxidized graft copolymer G5, $\text{Ep}\%=40$.

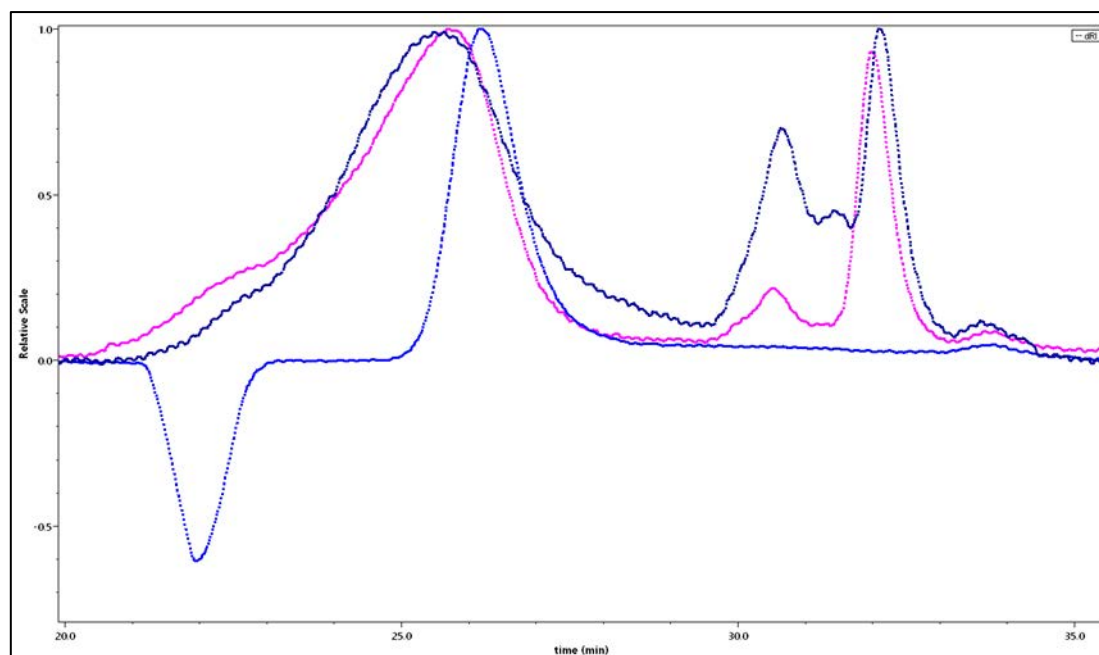


Figure S 3: SEC chromatogram in THF of the diblock copolymer PPTDOC (3) (light blue), graft copolymer G1 (pink) and graft copolymer G5 (dark blue).

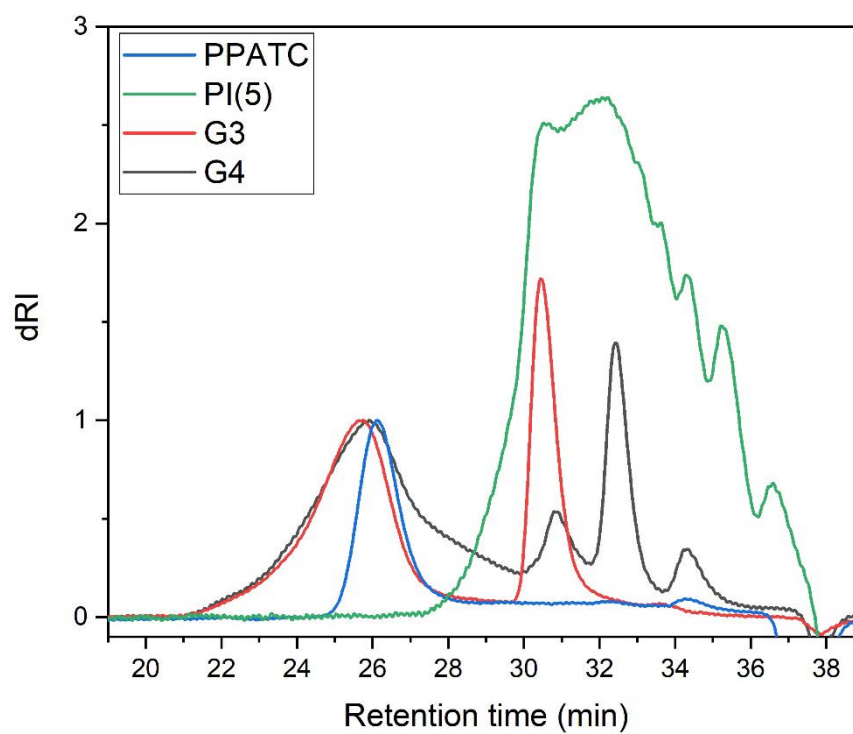


Figure S 4: SEC in THF of the diblock copolymer PPATC1 (blue), poly(isoprene) PI (5) (green), the graft copolymer G3 (red) and the graft copolymer G4(black).

CHAPTER III: SYNTESIS OF TRIBLOCK COPOLYMERS

Introduction:

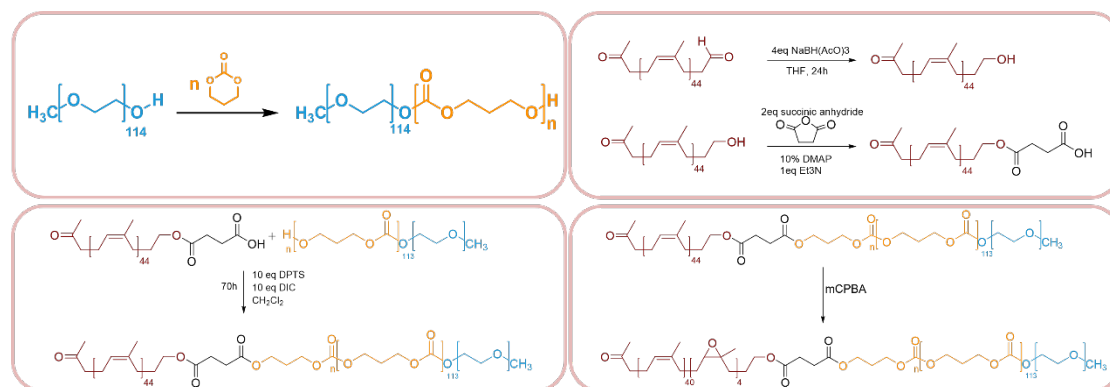
This chapter describes the synthesis and characterization of the triblock copolymer PEG₁₁₄-*b*-PTMC₂₀₀-*b*-PI₄₀, which was chosen as a possible component to be later self-assembled into magnetic polymersomes capable to be elongated under the magnetic field and sustain an anisotropic morphology by cross-linking even after the removal of the field. The PI block was attached onto the initial diblock copolymer of PEG₁₁₄-*b*-PTMC₂₀₀ in order to introduce a cross-linkable moiety into the system, specifically the double bonds of the PI that were transformed into epoxides capable to undergo cross-linking with a cationic photoinitiator or via diamine cross-linking. Both ideas were investigated, yet the cationic initiator path was the most utilized as it can be delayed until UV illumination at a controlled dose.

Poly(ethylene glycol) (MeO-PEG₁₁₄-OH of $M_n = 5000 \text{ g}\cdot\text{mol}^{-1}$) was chosen as the hydrophilic block due to its biocompatible and stealth properties and was used as a macroinitiator for the polymerization of trimethylene carbonate monomer (TMC) *via* ring opening polymerization (ROP). PTMC, a biocompatible and biodegradable polymer, was chosen as one of the hydrophobic blocks due to its rubbery state that would allow the magnetic nanoparticles to move with no restraint when the magnetic field is applied resulting in an elongation of the vesicles. The controlled polymerization of TMC, with the use of DBU as an organic catalyst and TU as a co-catalyst, has already been studied extensively and the reaction conditions were adapted in this synthesis in order to reach the desired molar mass faster with low dispersity of the resulting copolymer.[1]

In order to produce polymers that can be self-assembled into vesicles, the hydrophilic fraction f_{PEG} needs to be in a specific range [2,3]. Indeed, following various publications in particular the ones by Lebleu *et al.*[1,4], it was found that PEG-*b*-PTMC diblock copolymer with a fraction as low as 17% is requested to self-assemble into vesicles. Since our system has PTMC as the main hydrophobic block and the poly(isoprene) block was a secondary component, we aimed to produce polymers with a hydrophilic fraction ranging between 15 and 17% rather than following the publications by Discher & Eisenberg suggesting the hydrophilic fraction to be in the range $0.25 < f_{\text{PEG}} < 0.45$ to produce polymersomes for polydiene based copolymer systems [5,6].

A heterotelechelic poly(isoprene) with a small molar mass $2000 \text{ g}\cdot\text{mol}^{-1} < M_n < 4000 \text{ g}\cdot\text{mol}^{-1}$ was synthesized *via* a “one pot” degradation of a high molar mass PI $800 \text{ kg}\cdot\text{mol}^{-1}$ [7, 8]. The reaction is well documented in the literature *via* the use of mCBPA as an epoxidation agent and periodic acid as the ring opening agent in order to result in a well-controlled molar mass of the final polymer. Finally, one of the carbonyl end-groups of the poly(isoprene), specifically the aldehyde group, was transformed into a carboxylic group for further functionalization.[9] The

reaction utilized to yield the final triblock was a Steglich esterification between the hydroxyl end-group of PEG₁₁₄-*b*-PTMC₂₀₀-OH and the carboxylic group of the low molar mass PI [10-12]. As final step in order to produce a polymer capable of being cross-linked, epoxide groups were introduced onto the chain of PI with mCPBA in a controlled manner to result in an epoxidation rate ranging from 7 to 20% (Scheme 8).



Scheme 8: Visual representation of all the reactions which are explored in this chapter in order to synthesize the final epoxidized triblock copolymer PEG₁₁₄-*b*-PTMC_n-*b*-PI_m.

Experimental Section:

Materials:

Tetrahydrofuran (THF), dichloromethane (DCM), methanol (MeOH), toluene and heptane were purchased from Sigma-Aldrich. THF, toluene and DCM were dried by a solvent purification system. Meta-chloroperbenzoic acid (m-CPBA), Periodic acid (H_5IO_6), sodium carbonate (Na_2CO_3) and CeliteTM (natural diatomaceous earth) were purchased from Alfa Aesar, Thermo Fisher. MeO-PEG₁₁₄-OH ($M_n = 5000 \text{ g}\cdot\text{mol}^{-1}$) was purchased from Sigma-Aldrich. 1,8-diazabicyclo[5.4.0]undec-7-ene (DBU) was purchased from Sigma-Aldrich and distilled under vacuum before use. Trimethylene carbonate (1,3-dioxane-2-one, TMC) was purchased from TCI Europe and was purified by three successive recrystallizations in ethyl acetate. Commercial *cis*-1,4-poly(isoprene) 800000 $\text{g}\cdot\text{mol}^{-1}$ was purchased from Scientific Polymer products, *N*-cyclohexyl-*N'*-(3,5-bis(trifluoromethyl)phenyl)thiourea (TU) was synthesized previously in the laboratory [4]. 4-(Dimethylamino)pyridinium 4-toluenesulfonate (DPTS), *N,N'*-diisopropylcarbodiimide (DIC), *N,N',N''*-triethylamine (Et_3N), 4-(Dimethylamino)pyridine (DMAP) was purchased from Sigma Aldrich, 1,4-dioxane. Et_3N was dried with CaH_2 and distilled under vacuum before use.

Methods:

PEG₁₁₄-*b*-PTMC_m block copolymer synthesis:

The reactions were performed under inert atmosphere (nitrogen flow) and the trimethylene carbonate monomer was stored in a glove box before, to avoid degradation. The syntheses of the PEG₁₁₄-*b*-PTMC_m diblock copolymers were achieved by ring-opening polymerization (ROP) using MeO-PEG₁₁₄-OH ($M_n = 5000 \text{ g}\cdot\text{mol}^{-1}$) as macroinitiator. The aimed degree of polymerization (DP) for the TMC block was 196 at a conversion of 80%. In a Schlenk tube, 0.1 g (1 eq, 0.02 mmol) of MeO-PEG₁₁₄-OH was dried *via* the formation of an azeotropic solution using dry toluene and left to stir for 1 h at 40 °C before the distillation of toluene under reduced pressure. The polymeric initiator was left to fully dry overnight under dynamic vacuum before proceeding with the polymerization. In a separate vial, 0.5 g (196 eq, 4.89 mmol) of previously recrystallized TMC monomer was weighted in the glovebox together with 0.022 g (3 eq, 0.06 mmol) of *N*-cyclohexyl-*N'*-(3,5-bis(trifluoromethyl)phenyl)thiourea (TU) and the vial was sealed with a septum. In another vial, 8.9 μL (3 eq, 0.06 mmol) of 1,8-diazabicyclo[5.4.0]undec-7-ene (DBU) was added and the vial was sealed with a septum as well.

The reagents were taken out of the glovebox. In the Schlenk containing the macroinitiator, almost half of the dry THF volume (1 mL) was added to pre-solubilize it while another 1 mL of THF was added *via* a flushed syringe through the septum to the vial containing the monomer and TU mixture. Once both reactants were solubilized, the monomer/TU solution was added to the macroinitiator solution. A small amount of 0.1 mL of THF was added into the DBU vial before aspirating the solution of the catalyst with a syringe and adding it into the Schlenk, marking this moment as the beginning of the reaction. The reaction proceeded at 30°C for 5 h under magnetic stirring before termination by addition of an excess of acetic acid (0.02 mL). The polymer mixture was precipitated into cold methanol and centrifuged at 4 °C (10 min, 4000 g) resulting in a white precipitate. The polymer was washed with methanol and centrifuged 3 more times to remove unreacted monomer and impurities. The product was left to dry overnight under vacuum. The final polymer was a white product, with a weight yield of around 60-70%.

^1H NMR (400 MHz, CDCl_3): δ (ppm): 4.25 (t, -PTMC-CO-O- CH_2 - CH_2 - CH_2 -OH), 4.2 (m broad, -CO-O- CH_2 - CH_2 - CH_2 -O-), 3.15 (-PTMC-CO-O- CH_2 - CH_2 - CH_2 -OH), 3.6 (m broad, CH_3 -O- CH_2 - CH_2 -O-), 3.3 (s, CH_3 -O- CH_2 - CH_2 -O-), 2.0 (m broad, -CO-O- CH_2 - CH_2 - CH_2 -O-), 1.8 (quint, -PTMC-CO-O- CH_2 - CH_2 - CH_2 -OH)

Synthesis of hetero-bifunctional poly(isoprene) *via* “one-pot” degradation method

The following procedure was utilized to synthesize a small molar mass poly(isoprene) as described in the literature [8,13,14]. The targeted DP for this poly(isoprene) was 40. In a round bottom flask of 0.5 L, 5 g of a commercial high molar mass 1,4-*cis*-poly(isoprene) ($800000 \text{ g}\cdot\text{mol}^{-1}$) was left to solubilize in 250 mL THF overnight under stirring. 1.06 g (6.13 mmol) of mCBPA was solubilized in 50 mL of THF and added dropwise over a period of 15 min onto the poly(isoprene) solution. The mixture was let to react for 2 h before 1.67 g (7.36 mmol) of periodic acid which was pre-solubilized in 50 mL of THF was added dropwise in the solution, and the reaction was left to stir for another 2 h. Finally, 5 g of sodium carbonate was added into the reaction in order to react with the produced acids and left to stir for 20 min before the solution was filtered through CeliteTM. Next, the THF was distilled under vacuum to a smaller volume ~10 mL, which was precipitated in 100 mL of cold methanol under vigorous stirring. A viscous precipitate was formed, which was solubilized in diethylether and filtered through CeliteTM. Excess diethylether was distilled again under vacuum and the remaining solution was precipitated again in cold methanol. The precipitate was solubilized again in THF, the THF was distilled, and the final product was dried under vacuum overnight. The final product was a viscous polymer, with the reaction weight yield of ~70%.

^1H NMR (400 MHz, CDCl_3): δ (ppm): 9.74 (t, 1H, $-\text{CH}_2\text{CHO}$), 5.14 (t (broad), 5H $-\text{CH}_2\text{CHv}$), 2.47 (t, 2H, $-\text{CH}_2\text{CHO}$), 2.42 (t, 2H, $-\text{CH}_2\text{COCH}_3$), 2.33 (t, 2H, $-\text{CH}_2\text{CH}_2\text{CHO}$), 2.00–2.12 (m (broad), 20H, $-\text{CH}_2\text{CHv}$ and $-\text{CH}_2\text{C}(\text{CH}_3)\text{v}$), 1.68 (s (broad), 15H $-(\text{CH}_3)\text{CvCH}-$).

Synthesis of carboxylic-ended bifunctional poly(isoprene)

The first step for the synthesis of carboxylic-ended poly(isoprene) is to convert the aldehyde group of the carbonyl-ended poly(isoprene) by reducing the aldehyde group into a hydroxyl group. This step was done according to literature [8]. In a 250 mL round bottom flask, 1.1 g of carbonyl poly(isoprene) was solubilized in 50 mL of THF, followed by the addition of 4 eq of reducing agent $\text{NaBH}(\text{AcO})_3$ (0.57 g, 2.68 mmol) and 1.2 eq of acetic acid (0.87 mmol, 50 μL). An excess of acid should absolutely be avoided to preserve the double bonds of PI. The reaction was left to stir overnight at room temperature. The reaction was then precipitated in cold methanol, re-solubilized in diethylether and filtered through CeliteTM. The diethylether was distilled under vacuum until final volume ~ 10 mL followed by precipitation in cold methanol. The final polymer was solubilized in THF and dried under vacuum overnight. The final product was a viscous polymer with a weight yield of $\sim 80\%$.

^1H NMR (400 MHz, CDCl_3): δ (ppm): 5.14 (t (broad), 1H $-\text{CH}_2\text{CHv}$), 3.64 (t, 2H, $-\text{CH}_2\text{COH}$), 2.42 (t, 2H, $-\text{CH}_2\text{COCH}_3$), 2.44 (t, 2H, $-\text{CH}_2\text{CH}_2\text{COH}$), 2.00–2.12 (m (broad), 4H, $-\text{CH}_2\text{CHv}$ and $-\text{CH}_2\text{C}(\text{CH}_3)\text{v}$), 1.68 (s (broad), 3H $-(\text{CH}_3)\text{CvCH}-$).

The next step is the conversion of the hydroxyl moiety into a carboxylic group adapted from literature [9]. 0.13 g (0.045 mmol, $2900 \text{ g}\cdot\text{mol}^{-1}$) of $-\text{OH}$ terminated poly(isoprene) was solubilized with dry toluene to be dried via an azeotropic solution. The toluene was distilled, and the polymer was dried overnight under vacuum overnight. The same procedure was performed for 0.0089 g (2 eq, 0.089 mmol) of succinic anhydride in a different Schlenk tube. The following day, 0.4 mL of dry 1,4-dioxane was added under nitrogen flow into the polymer together with 6.2 μL (1 eq, 0.045 mmol) of dry trimethylamine. The mixture is then added into the succinic anhydride. Finally, 5.5 mg (1 eq, 0.045 mmol) DMAP was added into the reaction. The reaction was left to stir under room temperature overnight before precipitation in cold methanol. The reaction was centrifuged at 4°C (10 min, 4000 g) and the precipitate was washed another 4 times to remove the excess of succinic anhydride and other impurities. The final yield was $\sim 50\%$ in weight, with a conversion rate of the carboxylic group $\sim 80\%$.

^1H NMR (400 MHz, CDCl_3): δ (ppm): 5.14 (t (broad), 1H $-\text{CH}_2\text{CHv}$), 4.07 (t, 2H, $-\text{CH}_2\text{CO}-\text{CO}-\text{CH}_2\text{CH}_2\text{COOH}$), 3.64 (t, 2H, $-\text{CH}_2\text{COH}$), 2.65 (m, 4H, $-\text{CO}-\text{CH}_2\text{CH}_2\text{COOH}$), 2.42 (t, 2H,

$-CH_2COCH_3$), 2.44 (t, 2H, $-CH_2CH_2-CO-CH_2CH_2COOH$), 2.00–2.12 (m (broad), 4H, $-CH_2CHv$ and $-CH_2C(CH_3)v$), 1.68 (s (broad), 3H $-(CH_3)CvCH-$).

Final synthesis of the PEG₁₁₄-*b*-PTMC_m-*b*-PI_n triblock copolymer

The synthesis of the triblock copolymer was adapted from literature[11]. The reaction utilized for the synthesis of the triblock was a Steglich esterification between the carboxylic end-group of the poly(isoprene) chain and the hydroxyl end-group of the diblock copolymer PEG₁₁₄-*b*-PTMC_m-OH. The procedure was the following: in a Schlenk tube, 0.1 g (1 eq, 0.0059 mmol) of the diblock copolymer was solubilized in dry toluene in order to remove moisture from the system through an azeotrope solution formation. The solvent was then distilled under vacuum, and the diblock copolymer was dried overnight. A similar procedure was followed for 50 mg (3 eq, 0.0176 mmol) of polyisoprene and 17.3 mg (10 eq, 0.0588 mmol) of DPTS in a different Schlenk. The following day, both mixtures were solubilized in 2 mL of dry DCM, equally, and the solutions were combined. After 15 min of stirring at 40°C, 9.1 µL (10 eq, 7.4 mg, 0.0588 mmol) DIC was added into the reaction. After 48 h stirring at room temperature, the reaction was terminated by precipitation in cold heptane to remove the excess of poly(isoprene) and centrifuged at 4°C (10 min, 4000 g). The precipitate was re-solubilized in a small amount of THF (~2 mL) and filtered through a 0.45 µm pore size PTFE filter in order to remove the DPTS solid and re-precipitated in cold heptane again. The product was separated, solubilized, centrifuged 2 more times before finally being dried under vacuum overnight. The final product had a white powder solid-like consistency.

¹H NMR (400 MHz, CDCl₃): δ (ppm): 5.14 (t (broad), 5H $-CH_2CHv$), 4.25 (t, -PTMC-CO-O-CH₂-CH₂-CH₂-OH), 4.2 (m broad, -CO-O-CH₂-CH₂-CH₂-O-), 3.15 (-PTMC-CO-O-CH₂-CH₂-CH₂-OH), 3.6 (m broad, CH₃-O-CH₂-CH₂-O-), 3.3 (s, CH₃-O-CH₂-CH₂-O-), 2 (m broad, -CO-O-CH₂-CH₂-CH₂-O-), 2.00–2.12 (m (broad), 4H, $-CH_2CHv$ and $-CH_2C(CH_3)v$), 1.8 (quint, -PTMC-CO-O-CH₂-CH₂-CH₂-OH), 1.68 (s (broad), 3H $-(CH_3)CvCH-$)

Epoxidation of the PEG₁₁₄-*b*-PTMC_m-*b*-PI_n double bonds

In a vial, 100 mg of the triblock copolymer PEG₁₁₄-*b*-PTMC_m-*b*-PI_n were solubilized in 3 mL of THF. The epoxidation reactant was mCBPA and its amount was calculated for each epoxidation percentage targeted. For example, for an 20% epoxidation rate of a triblock copolymer containing a poly(isoprene) block of DP=44, the amount of mCBPA used was 0.6 mg (0.00347 mmol). The reaction was left to stir at room temperature for 2 h before precipitation in cold heptane and centrifuged at 4°C (10 min, 4000 g). The precipitate was washed 3 more times with heptane and centrifuged.

For example, for the triblock copolymer PEG₁₁₄-*b*-PTMC₂₀₀-*b*-PI₅₀ (PP14PI7) the calculations were as such:

$$\%PI \text{ by } ^1\text{HNMR} = \frac{I_{5.2} \times 68}{(I_{5.2}) \times 68 + \left(\frac{I_{3.6}}{4}\right) \times 44 + \left(\frac{I_{4.2}}{4}\right) \times 102} = \frac{3400}{28800} = 0.118, \text{ i.e. } 11.8 \% \text{ of poly(isoprene)}$$

where the I values are peak integrations at 5.2, 3.6 and 4.2 ppm respectively, corresponding to characteristic protons of PI, PEG and PTMC. Thus, $\%PI \times m_{\text{polymer}} = m_{PI}$, for example 0.1g of polymer results into $m_{PI} = 0.0118$ g.

$$n_{PI} = \frac{m_{PI}}{68} = 0.173 \text{ mmol}$$

$$n_{mCPBA} = \% \text{ Theor. epoxidation} \times n_{PI} = 20 \% \times 0.173 \text{ mmol} = 0.00347 \text{ mmol}$$

$$m_{mCPBA} = n_{mCPBA} \times 172.57 \text{ g/mol} = 0.0006 \text{ g or } 0.6 \text{ mg of mCPBA}$$

^1H NMR (400 MHz, CDCl_3): δ (ppm): 5.14 (t (broad), 5H $-\text{CH}_2\text{CHv}$), 4.25 (t, -PTMC-CO-O- $\text{CH}_2\text{-CH}_2\text{-CH}_2\text{-OH}$), 4.2 (m broad, -CO-O- $\text{CH}_2\text{-CH}_2\text{-CH}_2\text{-O-}$), 3.15 (-PTMC-CO-O- $\text{CH}_2\text{-CH}_2\text{-CH}_2\text{-OH}$), 3.6 (m broad, $\text{CH}_3\text{-O-CH}_2\text{-CH}_2\text{-O-}$), 3.3 (s, $\text{CH}_3\text{-O-CH}_2\text{-CH}_2\text{-O-}$), 2.68 (t, 1H, - $\text{CH}_2\text{-CHO-CCH}_3\text{-CH}_2\text{-}$), 2 (m broad, -CO-O- $\text{CH}_2\text{-CH}_2\text{-CH}_2\text{-O-}$), 2.00–2.12 (m (broad), 4H, $-\text{CH}_2\text{CHv}$ and $-\text{CH}_2\text{C}(\text{CH}_3)\text{v}$), 1.8 (quint, -PTMC-CO-O- $\text{CH}_2\text{-CH}_2\text{-CH}_2\text{-OH}$), 1.68 (s (broad), 3H $-(\text{CH}_3)\text{CvCH-}$), 1.28 (d broad, $\text{CH}_2\text{-CHO-CCH}_3\text{-CH}_2\text{-}$).

Methods of characterization:

Nuclear Magnetic Resonance (NMR):

¹H NMR experiments were performed in deuterated chloroform CDCl₃ in room temperature on a NMR BRUKER AVANCE I spectrometer which was operating at a frequency of 400 MHz. The instrument was equipped with a BBFO probe capable of producing Z-gradient at all frequencies. The spectra were acquired with an acquisition time of 4 seconds and 32 scans. The concentration of each sample was 10 mg/ml. The NMR spectra were acquired by Topspin software from BRUKER.

Diffusion-ordered spectroscopy (DOSY):

Diffusion-ordered spectroscopy (DOSY) was performed in room temperature on a BRUKER Ascend 400 NMR spectrometer. The spectrometer was equipped with a cryo-Probe Prodigy. A relaxation delay D1 of 5 sec was set and the number of scans NS was 16. The acquisition of the spectra was done with the dstebpgp3s pulse program. The time domain points in the t2 were 16K and 16 t1 increments. A compromise diffusion Δ of 100ms was set for all measurements. 95% of the maximum gradient strength was linearly incremented in 16 steps from 5%. Finally, δ , *i.e.*, the gradient pulse length was 2.3ms. The concentration of the sample was 15mg/ml.

Heteronuclear Single Quantum Coherence (HSQC) and Heteronuclear Multiple Bond Correlation (HMBC):

HMBC and HSQC experiments were performed in deuterated chloroform CDCl₃ in room temperature on an NMR BRUKER AVANCE I spectrometer which was operating at a frequency of 400 MHz. The instrument was equipped with a BBFO probe capable of producing Z-gradient at all frequencies. The NMR spectra were acquired by Topspin software from BRUKER.

Size exclusion chromatography (SEC):

Size exclusion chromatography (SEC) analysis to determine the molar mass M_n and dispersity \bar{D} was performed in THF on an UltiMate™ 3000 Standard (SD) HPLC/UHPLC system produced by Thermoscientific. The system was equipped with a multi angle light scattering probe (MALS) (Wyatt Technologies), a differential refractive index detector (dRI) (Wyatt Technologies) and a UV-Vis diode array detector (Thermoscientific). Polymer separation was performed by a three-column set of TOSOH TSK HXL gel (G2000, G3000 and G4000) the exclusion limits of which were from 200 to 400000 g·mol⁻¹. The calibration of the column

was performed with polystyrene standards of an EasiVial kit of polystyrenes (PS) from Agilent. The medium molecular weight range was in the range of 162 to 364000 g·mol⁻¹. Finally, the analysis of the chromatograms was performed with Astra software by Wyatt Technologies.

Fourier transform infrared spectroscopy (FTIR):

FTIR was performed in order to determine the successful grafting of IONPs either by oleic acid or by poly(isoprene). The absorbance spectra were performed with a Bruker Vertex 70 FT-IR spectrometer by addition of a droplet of the IONPs solution on the crystal plate and evaporation of the solvent.

Results and discussion:

Triblock copolymer synthesis and characterization:

The first step for the synthesis of the triblock copolymer was to synthesize a diblock copolymer with a specific hydrophilic weight ratio f_{PEG} that would result in vesicle formation post self-assembly. Following previous publications in the group, PEG-*b*-PTMC tends to form vesicles when f_{PEG} is less than 20%, for example in Lebleu *et al.* [1] a diblock system of PEG₄₅-*b*-PTMC₉₆ formed vesicles when $f_{\text{PEG}}=17\%$. Due to the size of the PEG block ($5000 \text{ g}\cdot\text{mol}^{-1}$) and of the poly(isoprene) chain that would be attached onto the diblock, which was chosen to be $2900 \text{ g}\cdot\text{mol}^{-1}$ (DP=44), the poly(trimethylene carbonate) block of the initial diblock had to be around 20000 g/mol in size in order to achieve the low hydrophilic ratio needed ($f_{\text{PEG}} < 20\%$) once the third block, *i.e.* poly(isoprene) would be attached. The ring opening polymerization (ROP) of TMC monomer had already been studied in the laboratory and specific conditions were already known. But in this case a change in the equivalent of the catalysts was performed in order to increase the rate of reaction and achieve the desired molar mass faster than before.

Synthesis of PEG₁₁₄-*b*-PTMC_n by ring opening polymerization:

The synthesis of the poly(ethylene glycol)-*block*-poly (trimethylene carbonate) PEG₁₁₄-*b*-PTMC was achieved *via* ring-opening polymerization (ROP) with the use of MeO-PEG₁₁₄-OH ($M_n = 5000 \text{ g}\cdot\text{mol}^{-1}$) as a macroinitiator, 1,8-diazabicyclo[5.4.0]undec-7-ene (DBU) as catalyst and *N*-cyclohexyl-*N'*-(3,5-bis(trifluoromethyl)phenyl)thiourea (TU) as co-catalyst (Figure 61, Table 7).

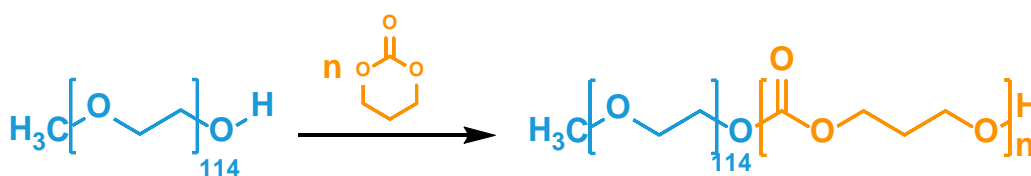


Figure 61: Schematic representation of the ROP of the diblock PEG₁₁₄-*b*-PTMC_n.

Table 7: Reaction conditions and reagents used for the synthesis of PEG₁₁₄-*b*-PTMC_mdiblock before improving the reaction conditions.

Reagent	mmol	eq	g	THF (mL)
MeO-PEG ₁₁₄ -OH (M_n 5.000g/mol)	0.05	1	0.25	1.34
TMC	9.80	196	1	3
TU	0.065	1.3	0.024	-
DBU	0.065	1.3	0.0099 (9.9 μ L)	-

The only macroinitiator that was used for all the reactions was MeO-PEG₁₁₄-OH, with a M_n =5000 g·mol⁻¹. Two different conditions regarding the catalytic system were utilized, specifically the second conditions were modified in order to decrease the reaction time. The initial synthetic route utilized 1.3 eq of the catalyst/co-catalyst system of (DBU/TU)/initiator ratio to achieve the targeted DP=196 of the trimethylene carbonate block.

The kinetics of the reaction were investigated and followed by proton nuclear magnetic resonance (¹H NMR) in deuterated chloroform (CDCl₃) through the decrease of the peak at 4.43 ppm of the 4H of the monomer and the appearance of the triplet at 4.2 ppm which was attributed to the 4H of the PTMC block. By integrating steadily the peak at 3.3 ppm of the methyl end-group (CH₃-) of poly(ethylene glycol) (MeO-PEG₁₁₄-OH) as 3H, it was possible to directly calculate the conversion and the degree of polymerization at each step of the reaction (Figure 62, Figure 63).

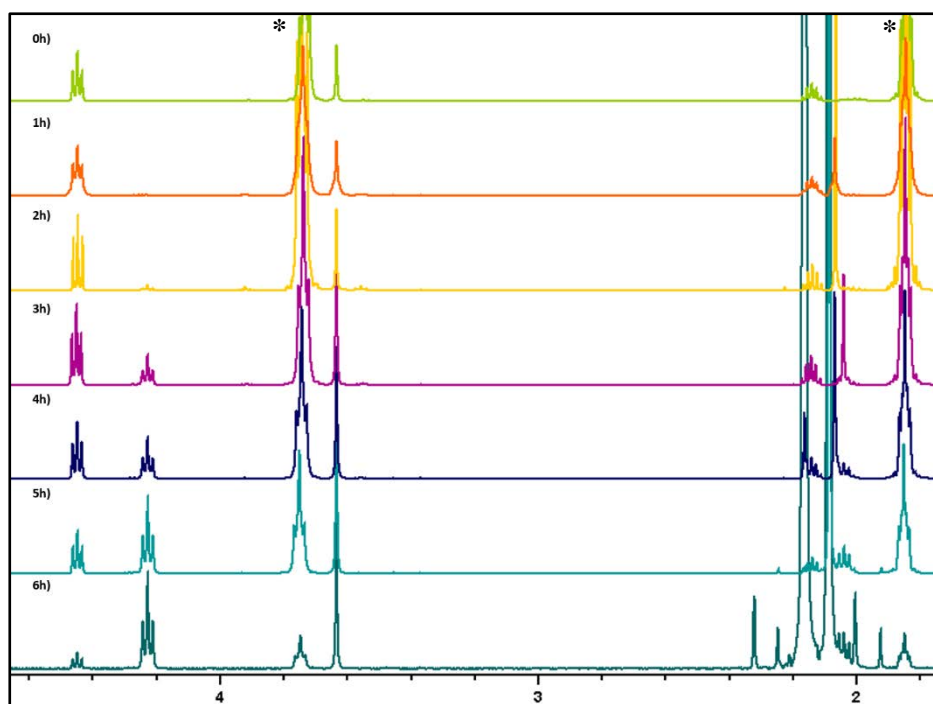


Figure 62: ^1H NMR kinetics in CDCl_3 of the diblock $\text{PEG}_{114}\text{-}b\text{-PTMC}_m$ in the initial conditions (*i.e.* 1.3 eq. catalysts). (*THF solvent peak is present at 1.8 and 3.8ppm).

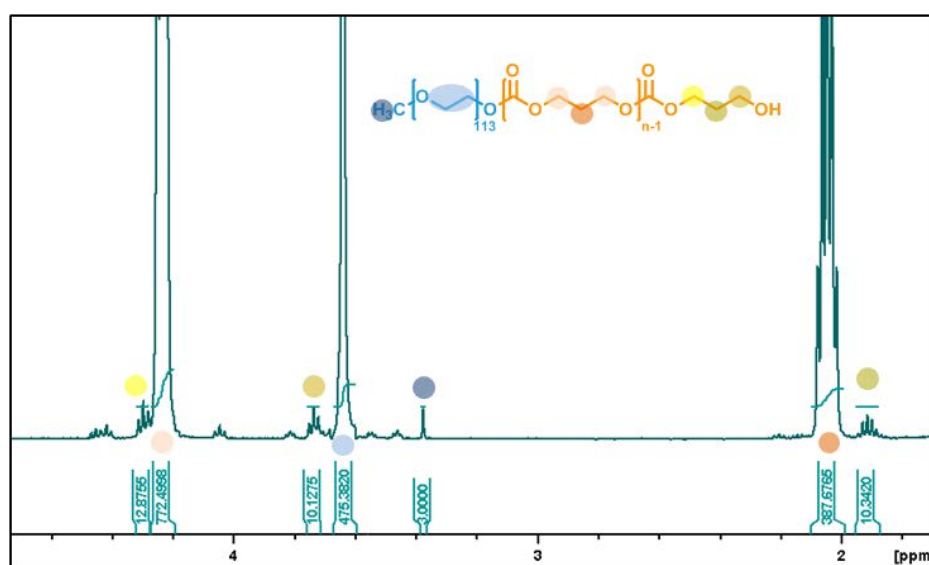


Figure 63: ^1H NMR in CDCl_3 of the final diblock $\text{PEG}_{114}\text{-}b\text{-PTMC}_{193}$ (1).

Previous reports on the synthesis of this diblock copolymer have suggested that at a conversion higher than 80% the reaction produced side reactions that were attributed to intermolecular reaction that resulted to triblock of $\text{PEG-}b\text{-PTMC-}b\text{-PEG}$ [4]. Thus, molar mass increase was followed by size exclusion chromatography (SEC) in THF (Figure 64 and Table 8). It is worth mentioning that after almost 60% conversion, a tail had started to appear in the SEC

chromatograms but on the left side, suggesting smaller mass chains were present in the reaction. Nevertheless, when the reaction was analyzed by ^1H NMR at 6 h of reaction having reached an experimental conversion of 85% and the final SEC results at that time resulted in a low D of 1.14 suggesting that the reaction can reach over 80% conversion without major side reactions. The reaction was terminated after 8.5h by addition of an excess of acetic acid and precipitation in cold methanol, followed by centrifugation.

The precipitate was washed with methanol 3 times to remove the unreacted monomer and other impurities. For these conditions, the reaction lasted 8.5 h with a targeted conversion of 100% (Table 9). The final DP for these conditions was 193 with an experimental conversion of 95% for the poly(trimethylene carbonate) block and the final hydrophilic ratio of the diblock copolymer $f_{\text{PEG}}=20\%$ (Figure 63).

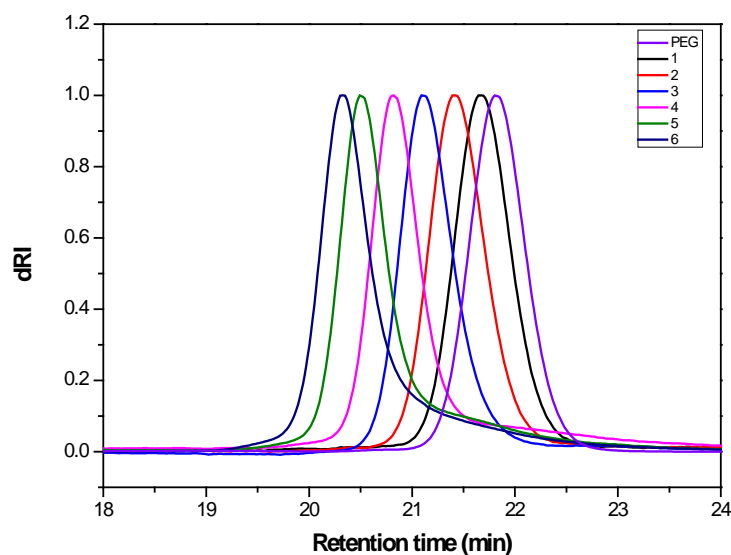


Figure 64: Kinetics of the $\text{PEG}_{114}\text{-}b\text{-PTMC}_m$ diblock copolymer in SEC THF throughout different times from 1 to 6 h.

The final conversion was approximately 100% and yet the final diblock $\text{PEG}_{114}\text{-}b\text{-PTMC}_{193}$ (1) did not present any side reactions as already mentioned which concluded that this conversion was reachable and could produce a well-defined polymer (Figure 63, Figure S 5 and Table 9).

Table 8: Characteristics obtained by SEC THF during the kinetics reaction of diblock formation.

Time of reaction (h)	M_n SEC (g/mol)*	\bar{D} *	Conversion (%) **
1	7290	1.02	11
2	8300	1.02	12
3	9740	1.03	40
4	10020	1.10	59
5	12530	1.09	69
6	13280	1.14	89

*Number-average molar mass (M_n) and dispersity (\bar{D}) obtained by SEC in THF; **Conversion calculated via ^1H NMR in CDCl_3

While the resulted diblock $\text{PEG}_{114}\text{-}b\text{-PTMC}_{193}$ (1) had good characteristics in both ^1H NMR and SEC and the reaction had reproducibility as can be seen in Figures S1 and S2 which represent the ^1H NMR and SEC of another diblock with the same conditions and reaction time $\text{PEG}_{114}\text{-}b\text{-PTMC}_{191}$ (2), an effort to optimize the reaction time was done by increasing the amount of catalysts in the system. Thus, the same reaction conditions remained while the amount of the catalyst/co-catalyst changed from 1.3 to 3 eq. This resulted in a shorter reaction time, which decreased from 8.5h to 5h for a targeted conversion of 100%. Furthermore, to create a diblock with a lower f_{PEG} the targeted DP increased to 245, which would result in an $f_{\text{PEG}}=16.6\%$, a lot closer to the necessary hydrophilic fraction for vesicle formation. Both ^1H NMR (Figure 65) and SEC analyses (Figure 66) suggested that this change in the system did not cause any side reactions and the control of the polymerization remained, resulting in a low dispersity diblock copolymer, with a higher DP of 200 as calculated by ^1H NMR in CDCl_3 (Figure 65).

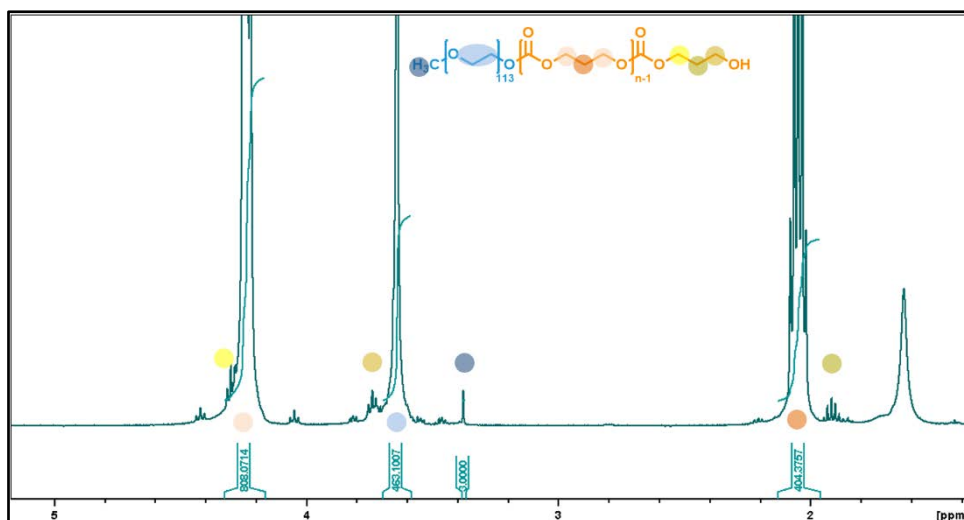


Figure 65: ^1H NMR in CDCl_3 of the final diblock $\text{PEG}_{114}\text{-}b\text{-PTMC}_{200}$ (3).

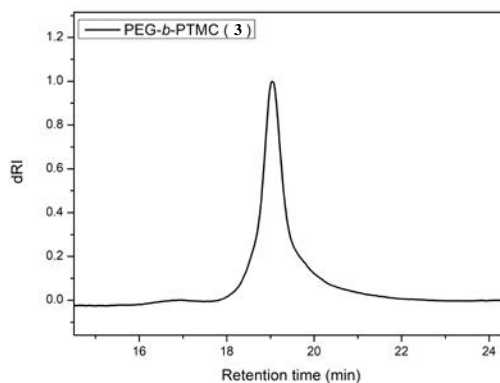


Figure 66: SEC in THF of diblock PEG₁₁₄-*b*-PTMC₂₀₀ (3).

Table 9: Characteristics obtained by SEC and ^1H NMR for the three versions of diblock copolymer.

	M_n SEC (g/mol)*	\bar{D}^*	$M_n^1\text{HNMR(g/mol)}^*$	DP
PEG ₁₁₄ - <i>b</i> -PTMC ₁₉₃ (1)	13500	1.13	22850	193
PEG ₁₁₄ - <i>b</i> -PTMC ₁₉₆ (2)	15400	1.11	24300	196
PEG ₁₁₄ - <i>b</i> -PTMC ₂₀₀ (3)	18550	1.05	25400	200

The final hydrophilic ratio of the PEG₁₁₄-*b*-PTMC₂₀₀ (3) diblock copolymer was $f_{\text{PEG}}=19\%$, similar to the diblock copolymers that were synthesized previously with a final conversion of 82%. In conclusion, in this study, the synthesis of the diblock copolymer PEG₁₁₄-*b*-PTMC_m it was possible to achieve a high conversion of the PTMC block with a good polymerization control and well-defined characteristics. The reactions that were done with a smaller amount of the catalytic system DBU/TU reached high conversions close to 100% without losing the control of the polymerizations but the reaction time appeared to be long, 8.5 h. After changing

the conditions of the reaction by increasing both the targeted DP as well as the amount of the catalyst in the system to 3 eq the reaction was able to reach 82% experimental conversion resulting in polymers with similar characteristics as the original ones but with the reaction taking 5 h. Thus, it was possible to achieve a controlled polymerization for both systems but obviously the system with a higher equivalent of DBU/TU was preferable due to the reduced time of reaction.

Synthesis of carboxylic end-functionalized poly(isoprene):

The synthesis of a small molar mass poly(isoprene) was already discussed in detail in Chapter 2 and the experimental procedure remained almost unchanged with small modifications in the cleaning process of the final polymer. In this case the targeted DP of poly(isoprene) was 40 in order to achieve a final triblock that would result with a $f_{\text{PEG}} \leq 20\%$.

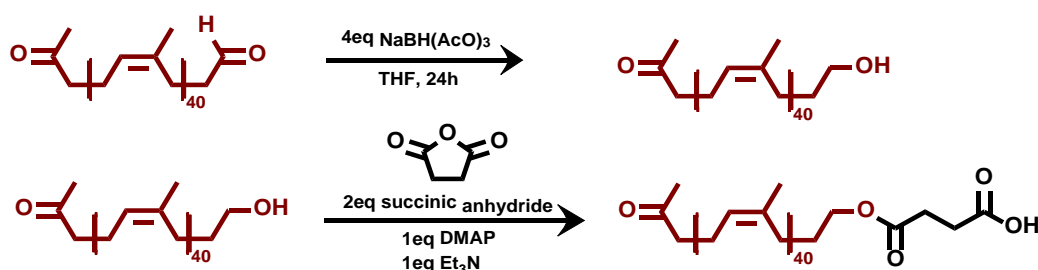


Figure 67: Synthetic route of the carbonyl functionalization of poly(isoprene).

The first step was to retrieve the carbonyl telechelic poly(isoprene), the characteristics of which were determined by ^1H NMR and SEC analyses (Figure 68, Figure 71). The following was to reduce one of the carbonyl groups selectively, *i.e.* the aldehyde only into a hydroxyl group *via* the use of sodium triacetoxyborohydride ($\text{NaBH}(\text{AcO})_3$) [8]. This reducing agent was specifically chosen due to its selectivity in reducing only the aldehyde groups and not the ketones, thus ensuring that only one chain end could be further functionalized. The reaction was already studied and described in literature and was followed accordingly [9]. The transition from an aldehyde group into a hydroxyl group was determined by the disappearance of the characteristic aldehyde proton at 9.7 ppm and the appearance of a triple peak at 3.64 ppm attributed to the 2H residing on the carbon which bears the hydroxyl group. The conversion of the aldehyde into the hydroxyl group was always 100% and the ketone moiety was still present and non-modified (Figure 69).

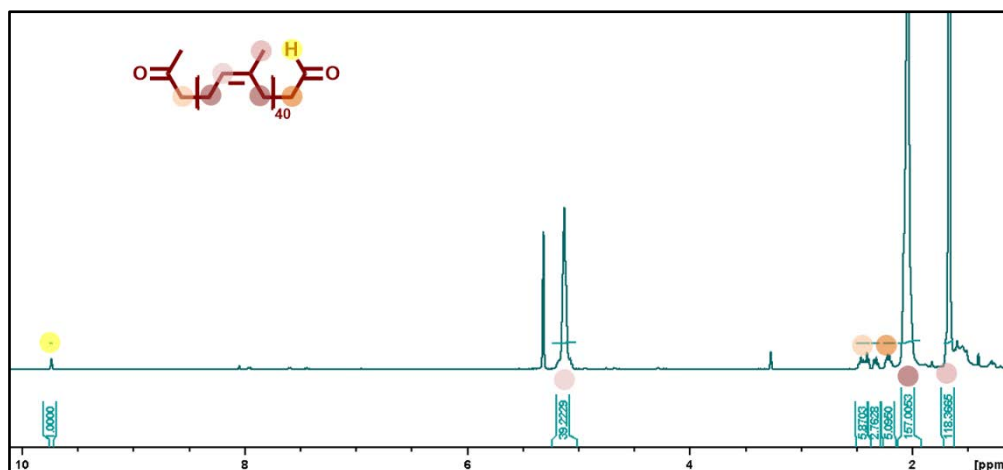


Figure 68: ^1H NMR in CD_2Cl_2 of the carbonyl telechelic poly(isoprene).

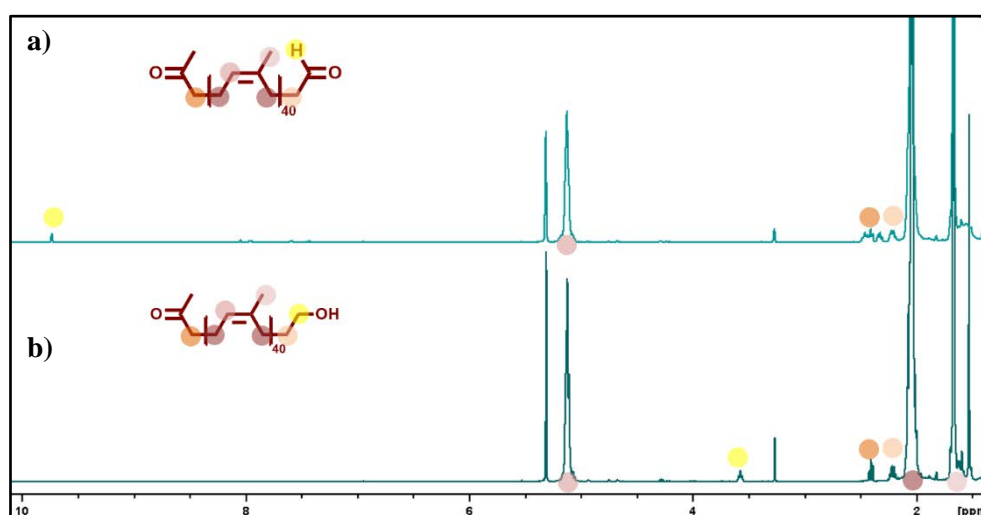


Figure 69: ^1H NMR in CD_2Cl_2 of a) carbonyl telechelic poly(isoprene) and b) hydroxyl-ended poly(isoprene).

The third and final step to create a poly(isoprene) block capable of being coupled with the diblock $\text{PEG}_{114}\text{-}b\text{-PTMC}_{193}$ was to modify the hydroxyl moiety into a carboxylic moiety which would be able to react with the already existing terminating hydroxyl group of the diblock $\text{PEG}_{114}\text{-}b\text{-PTMC}_{193}\text{-OH}$ via a Steglich esterification reaction which will be described further on. The synthesis of the carboxylic-ended poly(isoprene) was done by following existing literature with slight adaptations [10,11,13]. Succinic anhydride was utilized as the coupling agent which after its ring-opening by the hydroxyl group would produce a carboxylic group on the poly(isoprene) (Figure 70). The reaction was terminated after 22 h because, when monitored by ^1H NMR, it was found that even if the reaction was left for 48 h the reaction remained unchanged and 100% conversion was not possible to be reached. Thus, it was concluded that the reaction was not necessary to continue further than 22 h.

The attribution of the proton was further verified with HSQC and HMBC NMR analyses (Figure S 8). In the ^1H NMR spectrum (Figure 70), it is possible to determine that the conversion from a hydroxyl group to carboxylic group was not 100% due to the presence of the triple peak at 3.64 ppm which remained there even after a longer reaction time. Due to the integration of the peak at 3.64 ppm being 0.3, it was possible to determine that the final conversion rate of the carboxylic functionalization by determining how much of the non-functionalized poly(isoprene) was still in the system. If the PI had not been functionalized at all this peak would be integrated as 2, thus after functionalization with carboxylic acid we had 15% of PI-OH left in the system, *i.e.*, the carboxylic functionalization was 85%.

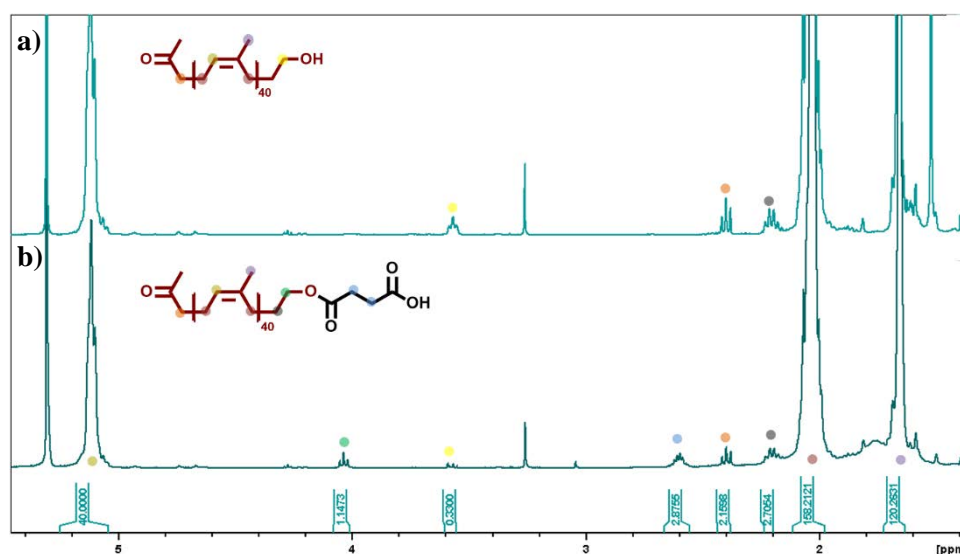


Figure 70: ^1H NMR in CD_2Cl_2 of a) hydroxyl-ended poly(isoprene) and b) carboxylic-ended poly (isoprene) after 22 h reaction.

The final polymer was analyzed by SEC in THF and compared to the poly (isoprene) prior to the functionalization (Figure 71). It was possible to see a shift in the carboxyl functionalized poly(isoprene) when compared to the PI-OH and can be attributed to the difference in the interaction of each functional group with the column. The resulted molar mass was higher by $1000 \text{ g}\cdot\text{mol}^{-1}$, but the measurement of the molar mass in SEC cannot be taken as conclusive due to the use of polystyrene standards and ^1H NMR produced more accurate results as can be seen in Table 10.

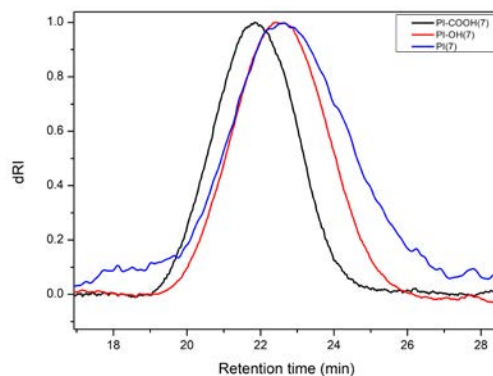


Figure 71: SEC in THF of three different versions of end-functionalized poly(isoprene) chains.

Further verification of the functionalization was provided by FT-IR where the appearance of a classic C=O stretch at 1750 cm^{-1} was observed for PI-COOH as well as the decrease of the O-H stretch was visible (Figure 72). While the lack of the C=O stretch and the presence of the O-H stretch is visible for the PI-OH spectra.

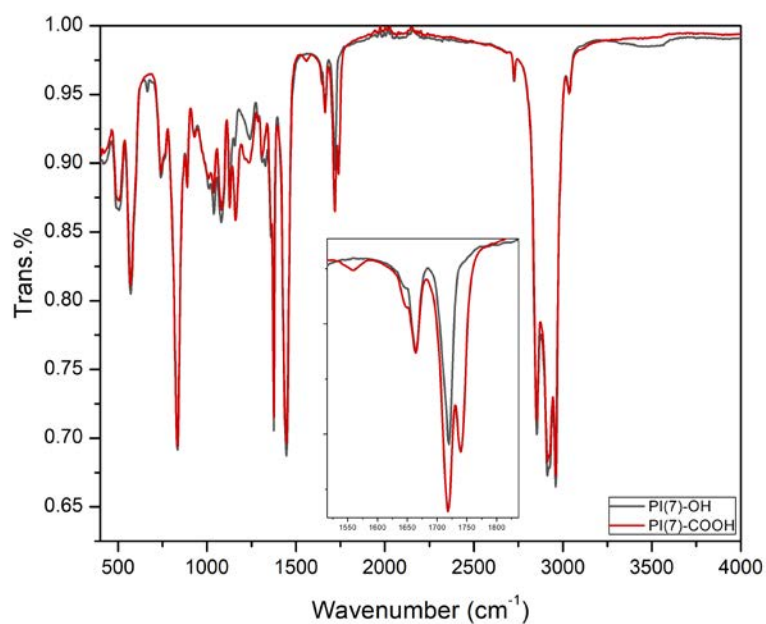


Figure 72: FT-IR spectra of PI-COOH and PI-OH.

Table 10: Characteristics obtained by SEC and ^1H NMR for the three versions of functionalized poly(isoprene).

	M_n SEC (g/mol)*	\bar{D}^*	M_n ^1H NMR(g/mol)*	DP
PI (7)	2800	1.45	2720	40
PI-OH (7)	3430	1.31	2720	40
PI-COOH (7)	4250	1.23	2420	40

Synthesis of PEG₁₁₄-*b*-PTMC_m-*b*-PI_n triblock polymer

The final synthetic step in order to obtain the triblock copolymer is a Steglich esterification between the hydroxyl group of the diblock copolymer PEG₁₁₄-*b*-PTMC₂₀₀ and the carboxylic-functionalized poly(isoprene) PI-COOH chains with the use of DPTS and DIC as the catalytic system. PI₄₀-COOH(7) was utilized as the second hydrophobic block, which if attached properly would result in a triblock with a hydrophilic ratio $f_{\text{PEG}} = 17.8\%$, which falls into the limits of necessary ratio to form vesicles [5, 6].

Usually, Steglich esterification requires DMAP and DCC [12] but after various attempts, the system DMAP/DCC revealed unsuccessful. Therefore, following published literature which already showcased a successful system for coupling poly(isoprene), the choice to change the catalytic system to DPTS/DIC was made. In the referred literature work by Antoine *et al.* [10,11,13], the reaction required 3 days but in our case, such long time produced a side reaction, which was attributed to the presence of free non-functionalized PI-OH, thus the reaction time was decreased to 48 h, which produced better results (Figure 73).

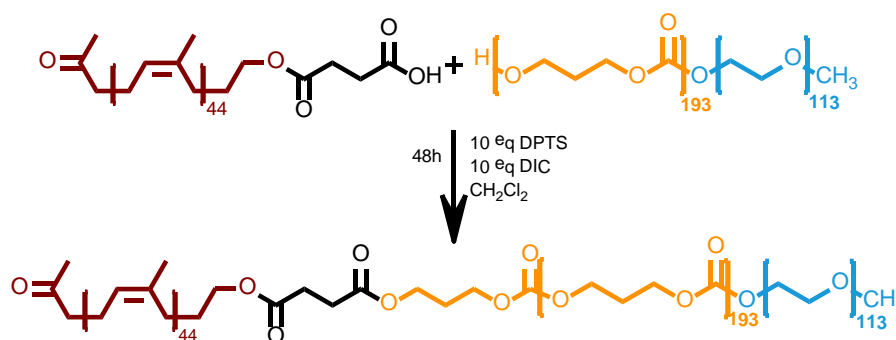


Figure 73: Schematic representation of the Steglich esterification to produce the triblock.

The reaction was done in moisture-free conditions by first drying all the reactants with dry toluene and further drying under vacuum overnight. Both the diblock and poly(isoprene)/DPTS systems were then solubilized in dry dichloromethane, due to the limited solubility of DPTS in THF, and then combined. The reaction temperature was chosen to be 40°C following literature, and after 15 min of stirring, DIC was added. DIC reacts with the carboxylic acid moiety by forming an O-acylisourea intermediate which increases its reactivity.

During this step, DPTS reacts with the intermediate, due to it being a stronger nucleophile, which results in the formation of a reactive amide. This reactive species can then react with the alcohol bearing diblock copolymer, resulting in an ester bond formation. The mechanism described is a standard mechanism of Steglich esterification modified due to the change of the catalytic system from DMAP/DCC to DPTS/DIC (Figure 74).

Multiple attempts to synthesize the triblock were achieved, first by following the reaction time described in literature, *i.e.*, 3 days. These conditions did successfully produce the triblock but due to the presence of the non-functionalized PI-OH in the system, a shoulder at shorter elution times was observed, which suggested a side reaction which was attributed to a reaction between the ketone group of the attached poly(isoprene) and the alcohol group of the non-functionalized PI-OH, forming an intermediate acetal, which would double the amount of PI units incorporated in the copolymer chain (Figure 75).

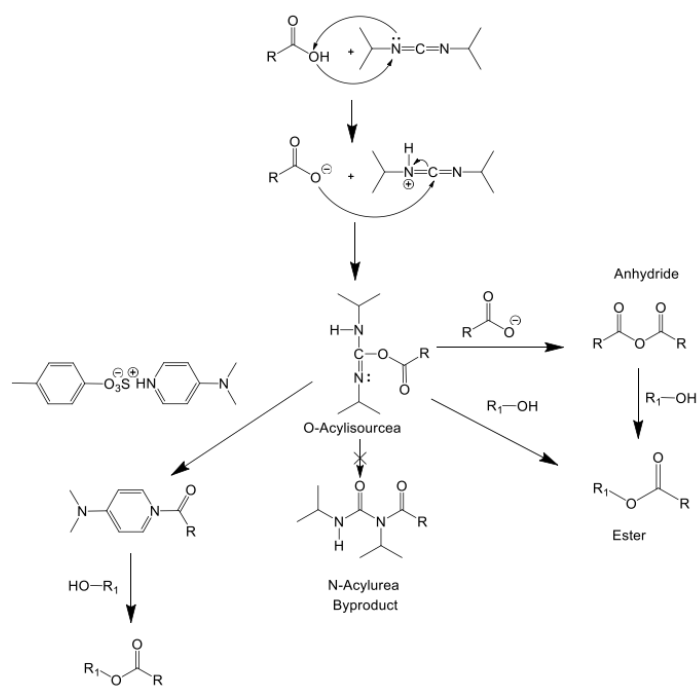


Figure 74: Scheme of the Steglich esterification reaction mechanism from S. Antoine, PhD thesis, U. Bordeaux[15].

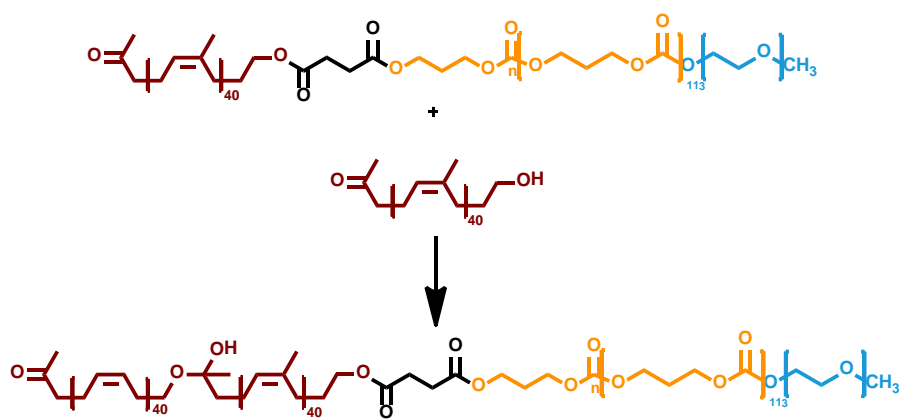


Figure 75: Possible side reaction during the esterification.

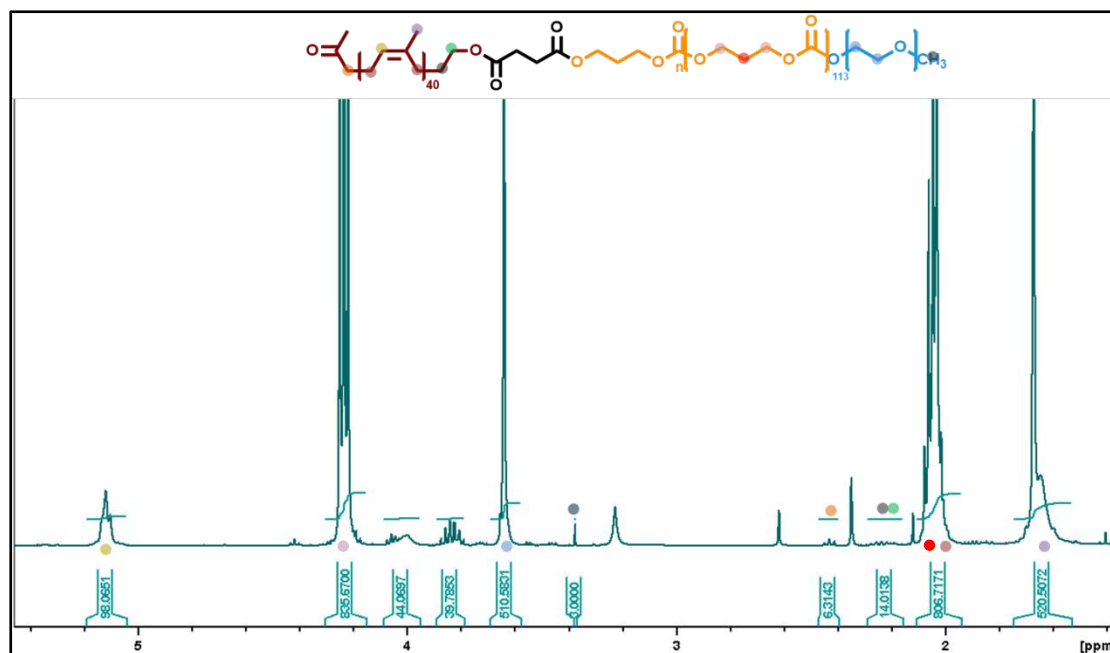


Figure 76: ^1H NMR in CDCl_3 of $\text{PEG}_{114}\text{-}b\text{-PTMC}_{193}\text{-}b\text{-PI}_{98}$ (PP3PI7(4)).

Limiting the reaction time to 48 h still led to the success of the coupling without, as verified by ^1H NMR in CDCl_3 (Figure 76) and SEC in THF (Figure 77) as well as HSQC and HMBC analysis (Figure S 9). Specifically in SEC, it was possible to observe the shift to shorter elution times for the triblock when compared to the diblock $\text{PEG}_{114}\text{-}b\text{-PTMC}_{196}$. Furthermore, the triblock presented a UV response while the diblock did not, which was attributed to the presence of the poly(isoprene) block which exhibits such characteristics that neither PEG nor PTMC do as can be observed in Figure 77b were the triblock copolymer exhibits a UV response while the diblock $\text{PEG-}b\text{-PTMC}$ does not.

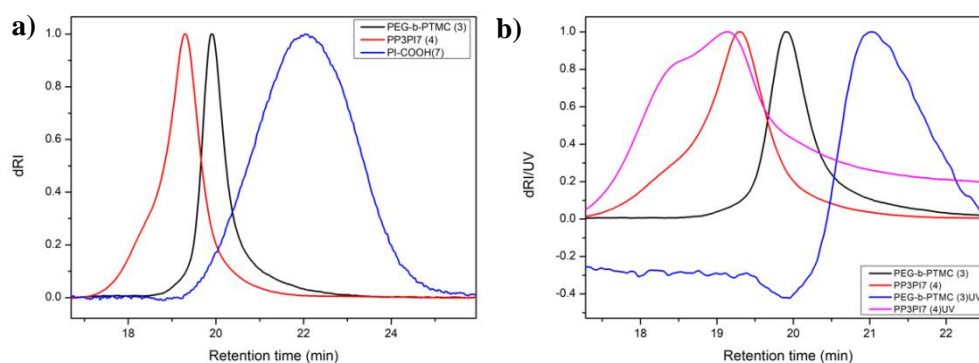


Figure 77: SEC elution curves in THF of a) $\text{PEG-}b\text{-PTMC}$ (3), $\text{PEG}_{114}\text{-}b\text{-PTMC}_{196}\text{-}b\text{-PI}_{98}$ (PP3PI7(4)), and PI-COOH (7) according to the dRI detector and b) of $\text{PEG}_{114}\text{-}b\text{-PTMC}_{196}$ (3) and $\text{PEG}_{114}\text{-}b\text{-PTMC}_{196}\text{-}b\text{-PI}_{98}$ (4) (PP3PI7) according to both the dRI and UV detectors.

As it is visible in both ^1H NMR and SEC analyses, the esterification coupling reaction did work. In SEC, the elution appears at shorter elution times suggesting a higher molar mass when compared to the diblock PEG-*b*-PTMC (3), but a shoulder is visible, which in turn suggests that a side reaction occurred. This can further be verified by the ^1H NMR spectrum where the molar mass of the poly(isoprene) after proton integration seems higher than that of the original block of poly(isoprene), which had a $M_n=2900$ g/mol and $\text{DP}=40$. In this case the DP seems to be 80 when integrating the peak characteristic for poly(isoprene) at 5.2 ppm, which is the double of the original. In the SEC chromatograms (Figure 77), it is visible that there is no free poly(isoprene) remaining in the system, thus we can conclude that double of the poly(isoprene) chains has been attached.

This side reaction was confirmed by addition of acetic acid to the final polymer and was observed by ^1H NMR with the disappearance of the peak at 4 ppm. It was further verified by SEC, after addition of acetic acid to the solution it was visible that free poly(isoprene) appeared in the system without shifting the main peak of the triblock to the original diblock (Figure 78).

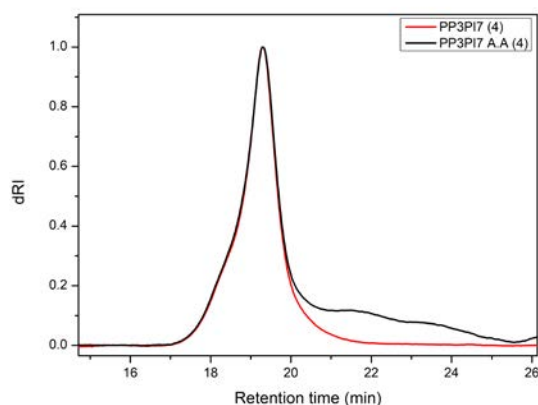


Figure 78: SEC in THF after the addition of acetic acid in the vial of the original triblock PEG₁₁₄-*b*-PTMC₁₉₃-*b*-PI₉₈ (PP3PI7(4)).

To try to eliminate the side reaction various attempts were made by adjusting parameters of the reaction. First, a decrease of the equivalent of poly(isoprene) was attempted, from 3 to 1.5 and 1.2. In ^1H NMR spectra of the final triblock copolymers with lower equivalents of PI₄₀-COOH (7) (Figure 79), it is visible by the integration of poly(isoprene) peak that its molar mass is closer to the actual M_n of the poly(isoprene) block, with a DP 40. This result is better visible for PP1PI7 (7), while PP3PI7 (5) has still a small peak of the characteristic side reaction at 4 ppm. To further confirm how the decrease of equivalents affected the reaction, SEC analysis in THF was performed. The shoulder on the SEC chromatogram remained (Figure 80).

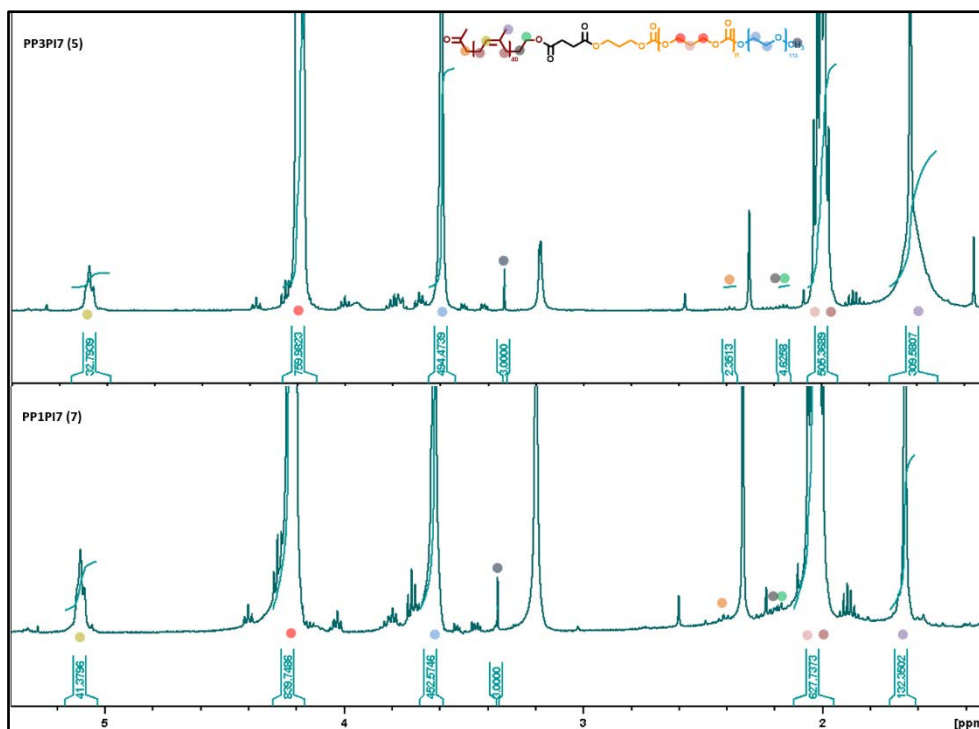


Figure 79: ^1H NMR in CDCl_3 of the triblock copolymers with lower equivalents of poly(isoprene).

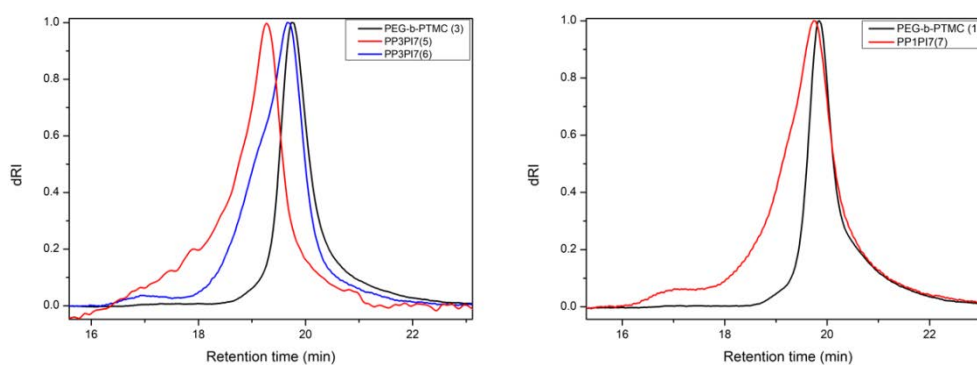


Figure 80: SEC in THF of the triblocks with lower equivalents of poly(isoprene).

All the SEC traces appear to have shifted from the original diblock $\text{PEG}_{114}\text{-}b\text{-PTMC}_n$ while a shoulder on the left is still present in all of them. $\text{PEG}_{114}\text{-}b\text{-PTMC}_{193}\text{-}b\text{-PI}_{33}$ (PP3PI7 (5)) and $\text{PEG}_{114}\text{-}b\text{-PTMC}_{195}\text{-}b\text{-PI}_{40}$ (PP1PI7) with 1.5 and 1.1 eq. respectively, presented better results in SEC. In total, PP3PI7 (5) with 1.5 eq. of poly(isoprene) appears to have the best results while the side reaction still occurred. This brings us to conclude that the decrease of equivalents did not help to completely eliminate the side reaction, but it was helpful to minimize it for the final polymer.

After trying to reduce the equivalents of poly(isoprene), a final attempt to eliminate the side reaction was done by simply decreasing the reaction time. Following the reaction by SEC, it was observed that after 2 days of reaction the elution trace did not appear to have a shoulder (Figure 82) but the side reaction was still present in ^1H NMR, yet decreased compared to the 3 days (Figure 81). The ^1H NMR spectrum reveals that the integration of poly(isoprene) at 5.2 ppm is slightly higher than the original DP by 10 molecular units, resulting in a DP of 50 instead of the original DP of 40. This is confirmed by the appearance of the peak at 4 ppm, characteristic peak of the side reaction. While the DP of PEG and PTMC remain as they were originally in the diblock. Indeed, the side reaction was not able to be eliminated but it was again minimized compared to the original 3 days reaction. Since the side reaction could be reversed by a simple addition of acetic acid and re-precipitation in heptane, these copolymers were utilized as such for the following reactions.

Finally, DOSY NMR analysis was performed in order to verify that the triblock has indeed been formed. The triblock copolymer $\text{PEG}_{114}\text{-}b\text{-PTMC}_{193}\text{-}b\text{-PI}_{33}$ (PP3PI7 (5)) was analyzed against the diblock copolymer $\text{PEG}_{114}\text{-}b\text{-PTMC}_{200}$ and the carboxylated poly(isoprene). It was found that the triblock exhibited only one diffusion coefficient $D = 8,5 \cdot 10^{-11} \text{ m}^2/\text{s}$ lower than the diffusion coefficient of the original diblock $D = 9,9 \cdot 10^{-11} \text{ m}^2/\text{s}$, verifying the integrity of the triblock (Figure S 10).

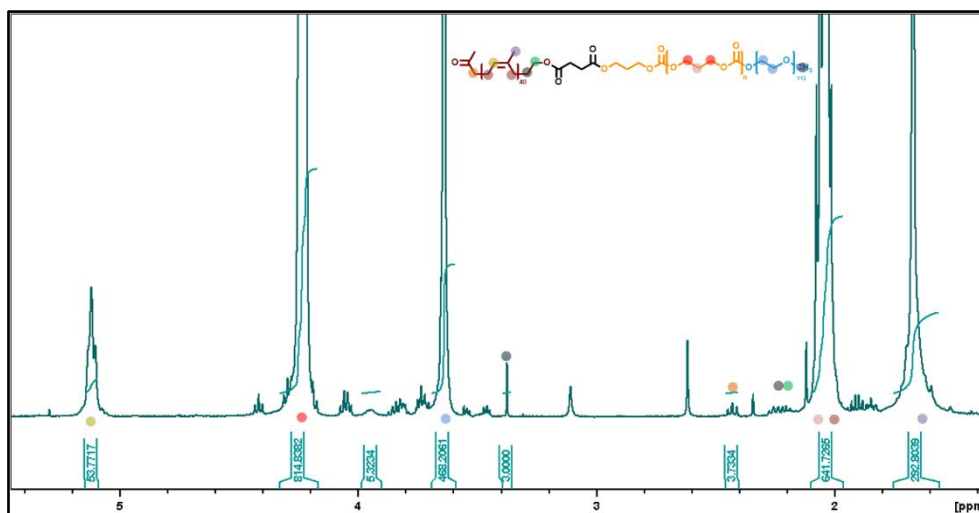


Figure 81: ^1H NMR spectrum in CDCl_3 of the triblock copolymer $\text{PEG}_{114}\text{-}b\text{-PTMC}_{200}\text{-}b\text{-PI}_{33}$ (PP14PI7) with reduced reaction time.

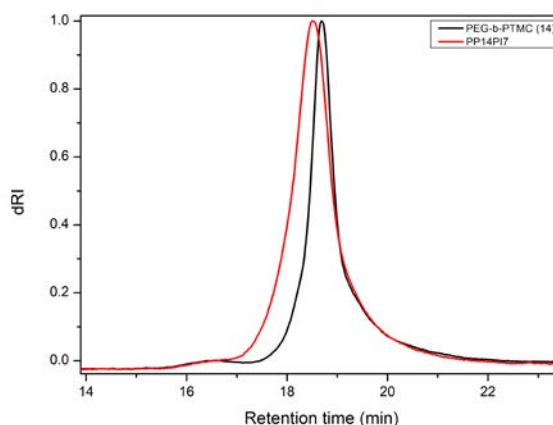


Figure 82: SEC trace in THF of the triblock PEG₁₁₄-*b*-PTMC₂₀₀-*b*-PI₃₃ (PP14PI7) and the diblock PEG₁₁₄-*b*-PTMC₂₀₀ (3).

In conclusion, it was possible to synthesize a triblock copolymer PEG₁₁₄-*b*-PTMC₂₀₀-*b*-PI₄₀ *via* a Steglich esterification which exhibited low dispersity and controllable characteristics in ¹H NMR as well. While some side reactions did occur, it was possible to minimize them and control the outcome. The molecular characteristics of the produced triblock copolymers are depicted in Table 11. Finally, when discussing the synthesis of the triblock copolymers one should not forget the end goal of the project, which was the synthesis of copolymers that could self-assemble in polymersomes. In this case, the diblock copolymers PEG₁₁₄-*b*-PTMC₂₀₀ that were synthesized in the above section had already a hydrophilic weight ration $f_{\text{PEG}} \leq 20$, which was already low enough but with the addition of the poly(isoprene) of a DP=40, with a molar mass $M_n = 2900 \text{ g} \cdot \text{mol}^{-1}$ lowered the f_{PEG} even more and if it is calculated for a functionalization of one poly(isoprene) block and no side reaction occurred it would be $f_{\text{PEG}} = 17.8\%$. Such a hydrophilic ratio is closer to the f_{PEG} that was found necessary for the PEG-*b*-PTMC copolymer to self-assemble into vesicles.

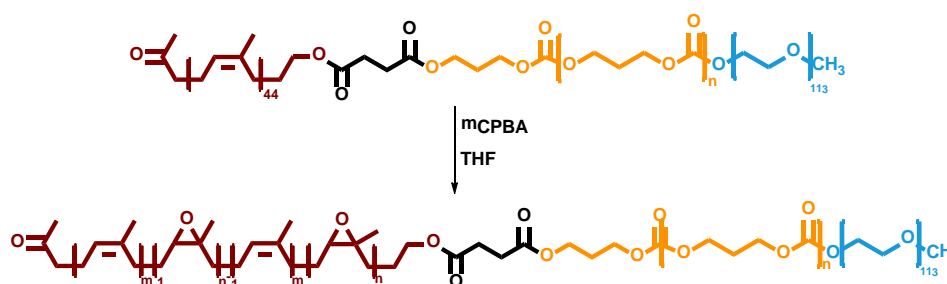
Table 11: Table of molecular characteristics of the four triblock copolymers synthesized.

	eq of PI ₄₀ -COOH(7)	M_n SEC (g·mol ⁻¹)*	\bar{D}^*	M_n ¹ HNMR (g·mol ⁻¹)**	DP of PI-COOH(7)**
PEG ₁₁₄ - <i>b</i> -PTMC ₁₉₃ - <i>b</i> -PI ₉₈ (PP3PI7(4))	3	20980	1.2	32000	98
PEG ₁₁₄ - <i>b</i> -PTMC ₁₉₃ - <i>b</i> -PI ₃₃ (PP3PI7 (5))	1.5	20770	1.18	27600	33
PEG ₁₁₄ - <i>b</i> -PTMC ₂₀₀ - <i>b</i> -PI ₃₃ (PP14PI7)	3	21140	1.1	29000	52
PEG ₁₁₄ - <i>b</i> -PTMC ₁₉₅ - <i>b</i> -PI ₄₀ (PP1PI7)	1.1	14500	1.2	28100	41

*Obtained by SEC characterization in THF**obtained by ¹HNMR measurements in CDCl₃

Epoxidation of PEG₁₁₄-*b*-PTMC_m-*b*-PI_n:

In order to render the triblock copolymer capable of being cross-linked it was imperative to add a cross-linkable moiety, which was chosen to be epoxides. The reaction is easy to handle and is easily reproducible (Figure 83). The amount of epoxidized double bonds on the poly(isoprene) block was chosen to remain low to not alter the hydrophobicity of the block, which would result in affecting the self-assembly process by perhaps changing the hydrophilic ratio. Thus, the targeted range of epoxidation degree was between 7 % and 20%.

**Figure 83:** Representation of the epoxidation reaction of the triblock copolymer via mCPBA.

The epoxidizing agent was mCPBA as previously used for poly(isoprene) during the degradation process. The calculation of the theoretical epoxidation is described in the methods section, and it includes first the determination of the amount of poly(isoprene) in each system and then the calculation of epoxidation percentage.

The occurrence of the epoxidation can be observed in ¹H NMR spectroscopy with the appearance of two characteristic peaks attributed to the molecular units that were bearing the

epoxides at 2.68 ppm and 1.27 ppm (Figure 84). The characteristic peak at 2.68 ppm is used to calculate the epoxidation rate (% Ep) *via* the following equation:

$$\% \text{ Epoxidation} = \frac{I_{2.68}}{I_{2.68} + I_{5.2}}$$

And in the case below the % Ep= 9%

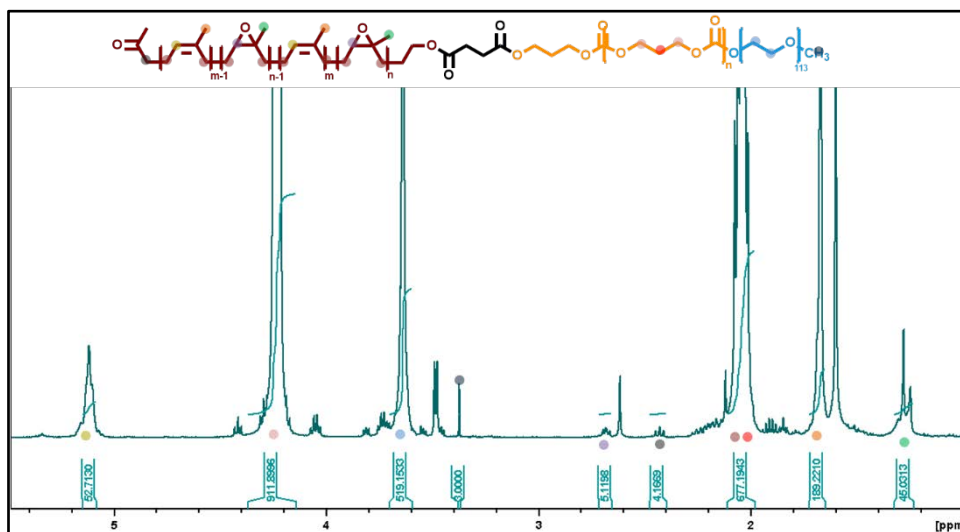


Figure 84: ^1H NMR in CDCl_3 of the epoxidized triblock copolymer $\text{PEG}_{114}\text{-}b\text{-PTMC}_{200}\text{-}b\text{-PI}_{50}$.

A variety of different experimental epoxidations were achieved for different triblock copolymers can be seen in Table 12. In most of the cases the experimental epoxidation was close to the theoretical epoxidation while other times, for example for a theoretical epoxidation 50% the resulting amount was a lot lower, in the range of 20%, this was not expected and can be attributed either to an inadequate reaction time or miscalculation of the amount of poly(isoprene) in the system.

Table 12: Theoretical and experimental values of the epoxidation rate for the triblock copolymers synthesized.

Sample	Theor. % Epoxidation			mCBPA mg			Exper. % Epoxidation*		
PEG₁₁₄-<i>b</i>-PTMC₁₉₃-<i>b</i>-PI₉₈ (PP3PI7(4))	8			0.7			10		
PEG₁₁₄-<i>b</i>-PTMC₁₉₃-<i>b</i>-PI₃₃ (PP3PI7 (5))	20	50	50	0.6	3.8	3.8	7	16	23
PEG₁₁₄-<i>b</i>-PTMC₂₀₀-<i>b</i>-PI₃₃ (PP14PI7)	20			0.6			9		
PEG₁₁₄-<i>b</i>-PTMC₁₉₅-<i>b</i>-PI₄₀ (PP1PI7)	20			0.6			15		

*Calculated via ¹HNMR in CDCl₃ according to the equation: % Epoxidation = $\frac{I_{2.68}}{I_{2.68} + I_{5.2}}$

Conclusions:

In conclusion, this chapter described the synthesis of a series of amphiphilic ABC triblock copolymers $\text{PEG}_{114}\text{-}b\text{-PTMC}_m\text{-}b\text{-PI}_n$. The first step in the synthetic process was to synthesize diblock copolymers of $\text{PEG}_{114}\text{-}b\text{-PTMC}_{200}$ by ring-opening polymerization of TMC monomer using $\text{MeO-PEG}_{114}\text{-OH}$ ($M_n = 5000 \text{ g}\cdot\text{mol}^{-1}$) as a macroinitiator. DBU/TU were used as an organic catalytic system with an equivalent of 1.3/1.3 respectively which resulted in polymers with low dispersity and a desirable DP close to 200 in 8.5h at a conversion of almost 100%. An increase to 3 equivalents of the catalytic system was utilized in order to decrease the reaction time. This resulted in diblock copolymers that had also low dispersity and the desired DP of 200 in 5 h with a lower experimental conversion, 82% conversion.

Further on, the third block of the ABC terpolymers was a poly(isoprene) block with a targeted DP of 40 which was synthesized *via* a one pot degradation process of a high molar mass “industrial grade” 1,4-*cis*-poly(isoprene) $M_n \sim 800000 \text{ g}\cdot\text{mol}^{-1}$. The obtained carbonyl telechelic poly(isoprene) was modified further, by reducing its aldehyde end-group into a hydroxyl group, and finally into a carboxylic group that was used for the final esterification coupling reaction. The modification reaction was made at a high conversion of carboxylic group of 85%, consistently.

Finally, the triblock formation was investigated and characterized by ^1H NMR and SEC. The synthesis of the triblock copolymers proceeded *via* a Steglich esterification between the terminal hydroxyl group of the diblock copolymers $\text{PEG}_{114}\text{-}b\text{-PTMC}_{200}$ and the carboxylic group of $\text{PI}_{40}\text{-COOH}$, by utilizing DPTS and DIC as the catalytic system. A variety of conditions were investigated in order to improve the characteristics of the final copolymers, such as change of the equivalents of the carboxylic group in the reactions from 3 to 1.5 and 1.1. The lowering of the equivalents resulted in better control of functionalization with less side-reactions. The time of the reaction also was modified from 3 days to 2 days. It resulted in an amphiphilic triblock copolymer that has a hydrophilic ratio $f_{\text{PEG}} \leq 20\%$, and which self-assembly in water will be studied in the next chapter.

References:

- [1] C. Lebleu, L. Rodrigues, J. M. Guigner, A. Brûlet, E. Garanger, and S. Lecommandoux, "Self-Assembly of PEG-b-PTMC Copolymers: Micelles and Polymersomes Size Control," *Langmuir*, vol. 35, no. 41, pp. 13364–13374, 2019.
- [2] F. Meng, C. Hiemstra, G. H. M. Engbers, and J. Feijen, "Biodegradable polymersomes," *Macromolecules*, vol. 36, no. 9, pp. 3004–3006, 2003.
- [3] C. Sanson, C. Schatz, J. F. Le Meins, A. Brûlet, A. Soum, and S. Lecommandoux, "Biocompatible and biodegradable poly(trimethylene carbonate)-b-Poly (L-glutamic acid) polymersomes: Size control and stability," *Langmuir*, vol. 26, no. 4, pp. 2751–2760, 2010.
- [4] P. Obtenir and L. E. Grade, "DOCTEUR DE L ' UNIVERSITÉ DE BORDEAUX Par Coralie LEBLEU Polymersomes based on PEG- b -PTMC towards cell-mediated delivery of nanomedicines."
- [5] B. M. Discher *et al.*, "Polymersomes: Tough vesicles made from diblock copolymers," *Science (80-.)*, vol. 284, no. 5417, pp. 1143–1146, 1999.
- [6] J. Du, "Polymer Vesicles," *Adv. Hierarchical Nanostructured Mater.*, vol. 9783527333, no. August, pp. 177–192, 2014.
- [7] P. Berto, S. Grelier, and F. Peruch, "Controlled degradation of polyisoprene and polybutadiene: A comparative study of two methods," *Polym. Degrad. Stab.*, vol. 154, pp. 295–303, 2018.
- [8] A. V. Radchenko *et al.*, "Facile synthesis of 1,4-: Cis -polyisoprene-polypeptide hybrids with different architectures," *Polym. Chem.*, vol. 10, no. 19, pp. 2456–2468, 2019.
- [9] M. Helou, J. F. Carpentier, and S. M. Guillaume, "Poly(Carbonate-urethane): An isocyanate-free procedure from α,ω -di(cyclic carbonate) telechelic poly(trimethylene carbonate)s," *Green Chem.*, vol. 13, no. 2, pp. 266–271, 2011.
- [10] S. Antoine *et al.*, "Core–Shell Double Gyroid Structure Formed by Linear ABC Terpolymer Thin Films," *Macromol. Rapid Commun.*, vol. 39, no. 9, 2018.
- [11] S. Antoine *et al.*, "Nanoscale Archimedean Tilings Formed by 3-Miktoarm Star Terpolymer Thin Films," *Macromol. Rapid Commun.*, vol. 40, no. 7, pp. 1–6, 2019.
- [12] B. Neises and W. Steglich, "Simple Method for the Esterification of Carboxylic Acids," *Angew. Chemie Int. Ed. English*, vol. 17, no. 7, pp. 522–524, 1978.
- [13] S. Gillier-Ritoit, D. Reyx, I. Campistron, A. Laguerre, and R. P. Singh, "Telechelic cis-1,4-oligoisoprenes through the selective oxidolysis of epoxidized monomer units and polyisoprenic monomer units in cis-1,4-polyisoprenes," *J. Appl. Polym. Sci.*, vol. 87, no. 1 SPEC., pp. 42–46, 2003.
- [14] G. Morandi, N. Kebir, I. Campistron, F. Gohier, A. Laguerre, and J. F. Pilard, "Direct selective reductive amination of carbonyl telechelic oligoisoprenes: elaboration of promising tri- and tetrafunctionalized oligoisoprene intermediates," *Tetrahedron Lett.*, vol. 48, no. 43, pp. 7726–7730, 2007.
- [15] S. Antoine and L. U. D. E. B. Ordeaux, "Synthesis of linear and star miktoarm ABC terpolymers and their self-assembly in thin films To cite this version : HAL Id : tel-01767225 Synthesis of linear and star miktoarm ABC terpolymers and their self-assembly in thin films Synthèse de terpolymères A," no. December 2017, 2018.

Supplementary information:

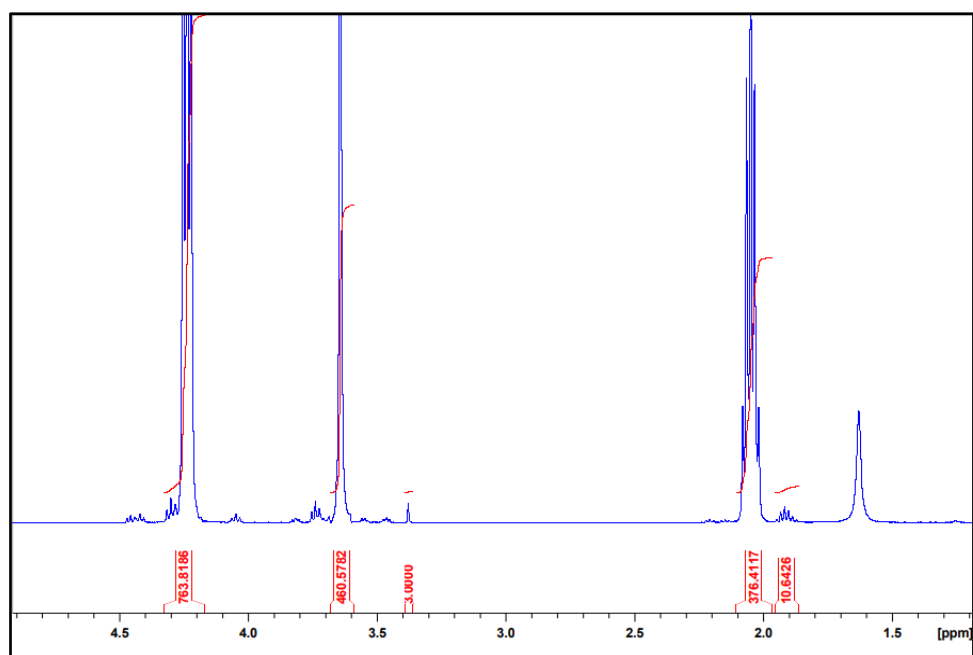


Figure S 5: ^1H NMR in CDCl_3 of $\text{PEG}_{114}\text{-}b\text{-PTMC}_{190}$ (2).

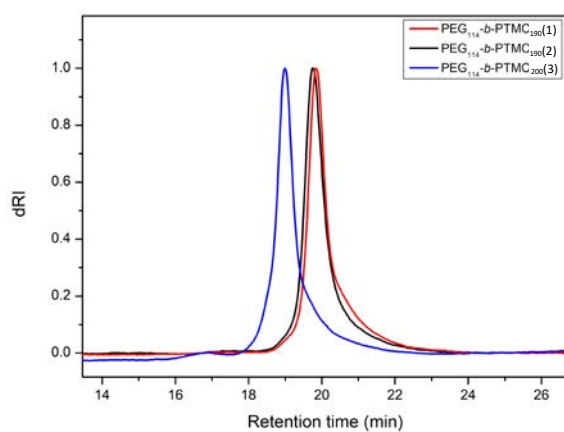


Figure S 6: SEC in THF of $\text{PEG}_{114}\text{-}b\text{-PTMC}_{190}$ (1), $\text{PEG}_{114}\text{-}b\text{-PTMC}_{190}$ (2) and $\text{PEG}_{114}\text{-}b\text{-PTMC}_{200}$ (3).

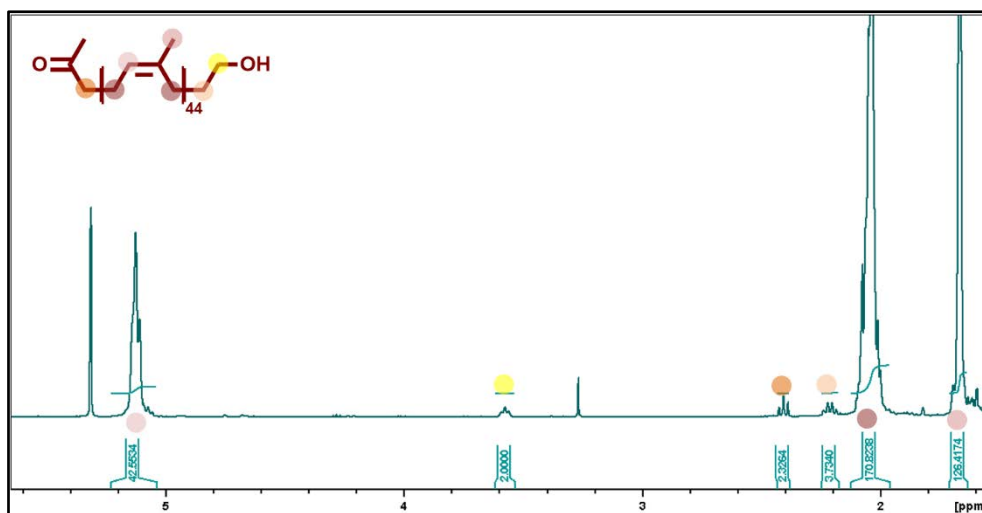


Figure S 7: ^1H NMR in CDCl_3 of the hydroxyl modified poly(isoprene) $\text{PI}_{40}\text{-OH}$ (7).

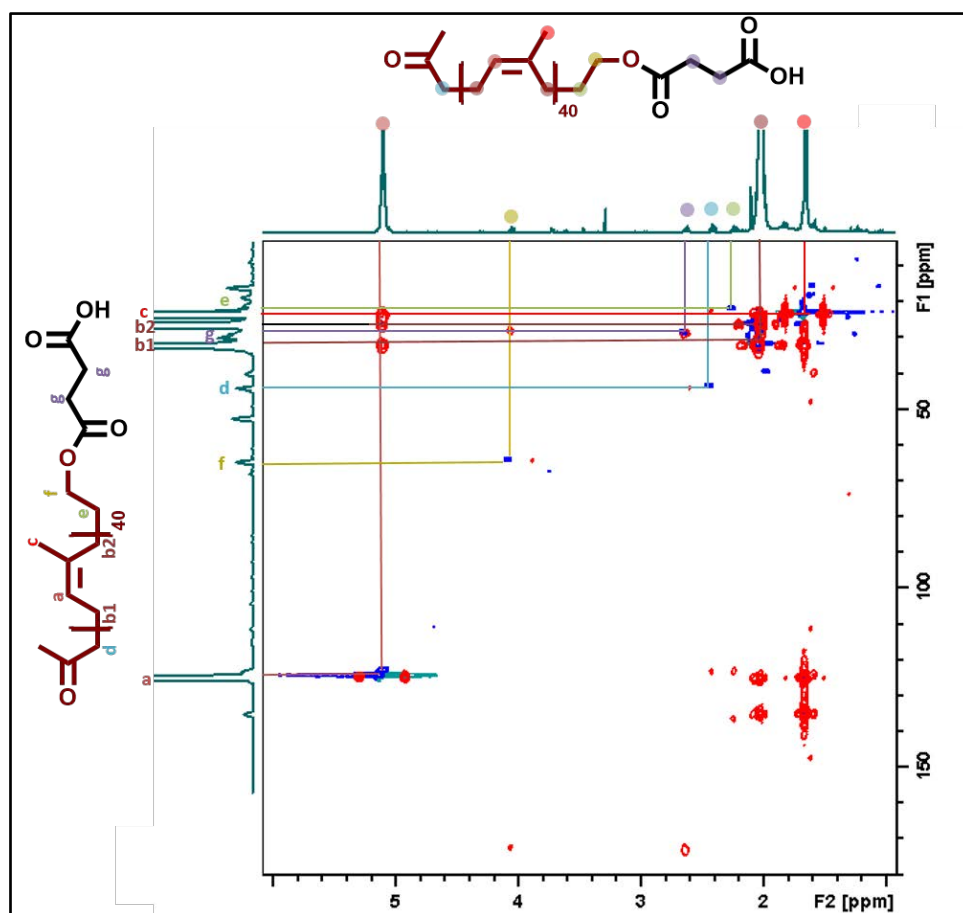


Figure S 8: HSQC (blue spot) and HMBC (red spot) NMR analysis in CDCl_3 of carboxylic functionalized poly(isoprene) $\text{PI}_{40}\text{-COOH}$ (7).

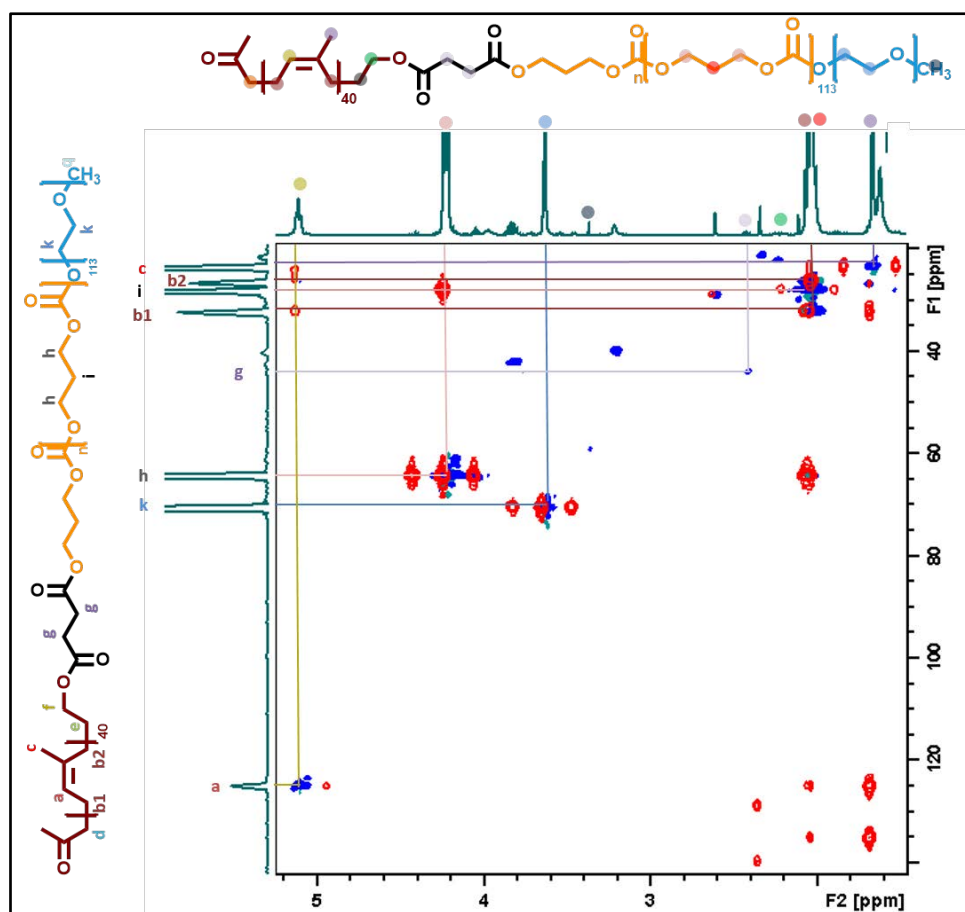


Figure S 9: HSQC (blue spot) and HMBC (red spot) NMR analysis in CDCl₃ of the triblock copolymer PEG₁₁₄-*b*-PTMC₁₉₃-*b*-PI₃₃ (PP3PI7) (5).

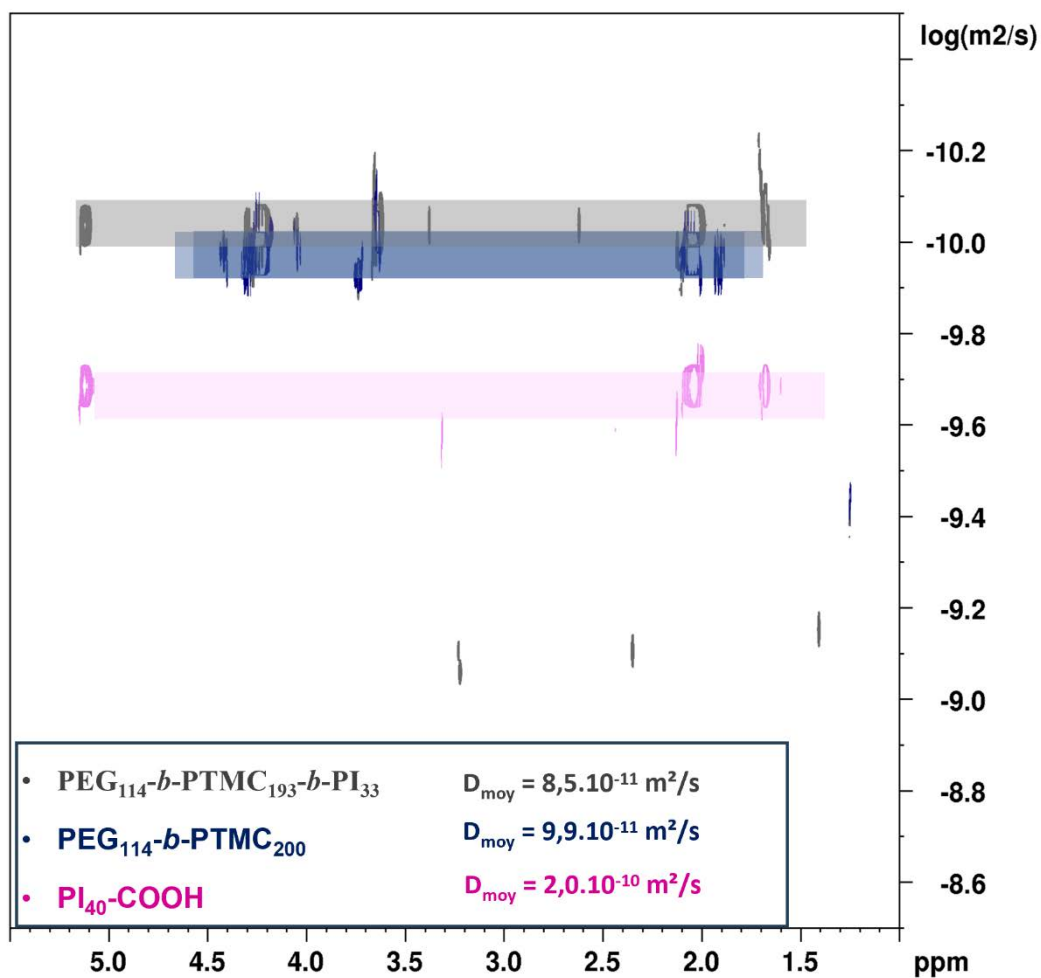


Figure S 10: DOSY NMR analysis of the triblock $\text{PEG}_{114}\text{-}b\text{-PTMC}_{193}\text{-}b\text{-PI}_{33}$ (PP3PI7) (5), 154eblock $\text{PEG}_{114}\text{-}b\text{-PTMC}_{200}$ (3) and $\text{PI}_{40}\text{-COOH}$.

CHAPTER IV: SYNTHESIS OF HYDROPHOBIC IRON OXIDE NANOPARTICLES (IONPs)

Introduction:

This chapter describes the synthesis of hydrophobic chain coated iron oxide magnetic nanoparticles capable of being incorporated within the hydrophobic membrane of polymersomes to produce magnetic polymersomes that elongated under a static magnetic field under the action of dipolar interactions. Iron oxide magnetic nanoparticles (IONPs) have been widely used over the last decades in a variety of systems for medical applications due to their biocompatibility and variety of characteristics [1]. So far, they have been utilized as contrast agents in magnetic resonance imaging (MRI) [2-4], as guided drug delivery systems [5,6], as biosensors and in magnetic hyperthermia [7-10]. More specifically, magnetic hyperthermia is a technique used for cancer treatment, which takes advantage of the ability of IONPs to produce heat while under the application of a high frequency alternating magnetic field (AMF) [11-13]. The local temperature increase can in its turn increase locally the permeability of polymer nanocarriers [14] or trigger the thermal transition of a thermosensitive hydrogel [15]. Recently, more and more literature is being published on another application of IONPs which is magneto-mechanical cell disruption or membrane disturbance by application of a lower frequency magnetic field, which would induce movement of IONPs that were internalized into cancerous cells, for example, and this movement would create targeted lysis of cell membranes due to production of mechanical forces without a production of heat [16-19].

The last example, *i.e.* magneto-mechanical actuation was the goal of this study as presented in Chapter 1, but not directly by introducing free IONPs into a biological system, but by incorporating them into polymersomes that in turn would be able to act as the mechanical-actuators [20-22]. A system as such, has a lot of potential since it is capable of combining magneto-mechanical actuation and drug-delivery [7]. Of course this depends on the properties of the IONPs used, such as their size and morphology which would affect their response to the magnetic field but also first and foremost, their incorporation into the polymersome membranes [23-24].

With this idea in mind, spherical IONPs were synthesized in this study with a small diameter which would allow them to be incorporated into the hydrophobic membrane made of either the triblock copolymer that were described in Chapter 3 or in the graft copolymers, described in Chapter 2. Their size had to be small to ensure a high volume fraction and close packing inside the membrane, furthermore in order for the IONPs to be introduced into the hydrophobic membrane they needed to have a hydrophobic surface [25-26]. Thus, their synthetic process included a functionalization with either oleic acid surfactant molecules, or poly(isoprene) chains with a low molar mass functionalized by an iron-chelating anchor.

To achieve the synthesis of IONPs with a small size polyol route was the main synthetic route that was utilized. The polyol route applied to the production of iron oxide NPs was first introduced by Caruntu *et al.*[25] where the polyol solvent was utilized as a chelating agent and a solvent of high boiling point, around 220 °C. The process described in this chapter results in single-domain superparamagnetic iron oxide nanoparticles, but the polyol route in general can produce a variety of morphologies depending on the parameters of the reaction such as the choice of polyol solvent (pure or mixture), amount of water in the system and the moment when it is introduced in the system, as well as the duration and temperature of reaction and how fast the heating occurs (*i.e.* what is the heating ramp applied) [27-30].

The functionalization of the IONPs occurred either directly with oleic acid or a dopamine functionalized short poly(isoprene), whose synthetic route is described in this chapter as well. Alternatively, the functionalization of IONPs occurred *via* a ligand exchange, *i.e.*, exchange between the oleic acid functionalized IONPs to dopamine functionalized poly(isoprene) according to existing protocol in literature with slight adaptations. The final IONPs were characterized *via* dynamic light scattering (DLS), magic angle spinning (MAS) solid state NMR, thermogravimetric assay (TGA), TEM, FT-IR, static and dynamic magnetization curves (DC and AC magnetometry) and UV spectrometry.

Experimental Section:

Materials:

Iron (II) chloride tetrahydrate ($\text{FeCl}_2 \cdot 4\text{H}_2\text{O}$, 98%), Diethylene glycol (DEG, 99%), sodium hydroxide micropills (NaOH, 98%), were purchased from Alfa Aesar. Iron (III) chloride hexahydrate ($\text{FeCl}_3 \cdot 6\text{H}_2\text{O}$, >97%) was purchased from Panreac. Ethyl acetate (>99.5%) was purchased from Fisher Chemicals. Acetone (technical grade) was purchased from Acros Organics. Ethanol (96%), toluene and methanol were purchased from VWR. Oleic acid $\geq 99\%$ was purchased from Sigma Aldrich. Tetrahydrofuran $\geq 99.6\%$ (THF) was purchased from ThermoFisher scientific and dimethylformamide (DMF) was purchased Alfa Aesar. Dopamine hydrochloride was purchased from Fisher Chemicals. Cis-1,4 poly(isoprene) 96% with an average $M_w = 800.000 \text{ g} \cdot \text{mol}^{-1}$ was purchased from Scientific Polymer Products. Triethylamine (Et_3N) was purchased from Sigma-Aldrich and was dried by CaH_2 and distilled under vacuum. Meta-chloroperbenzoic acid (m-CBPA), periodic acid (H_5IO_6) and sodium carbonate (Na_2CO_3) were purchased from Alfa Aesar (Thermo Fisher). Celite™ (natural diatomaceous earth) was purchased from Alfa Aesar (Thermo Fisher). Sodium triacetoxymethylborohydride ($\text{NaBH}(\text{AcO})_3$) 97% was purchased from Sigma-Aldrich. All solvents were utilized as they were unless previously stated. THF and DMF that were dried by a solvent purification system were utilized when inert atmosphere was required.

Methods:

Synthesis of hydrophobic IONPs functionalized with oleic acid:

Polyol method:

The synthesis of oleic acid functionalized magnetite IONPs was done by following existing report by Caruntu *et al.* [25] to achieve single domain small superparamagnetic iron oxide nanoparticles.

In a 250 mL three-neck round bottom flask, 0.4 g of $\text{FeCl}_2 \cdot 4\text{H}_2\text{O}$ (2 mmol) and 1.08 g of $\text{FeCl}_3 \cdot 6\text{H}_2\text{O}$ (4 mmol) salts were dissolved in 80 mL of diethylene glycol (DEG) and the solution was flushed with nitrogen for 1h. Simultaneously, in a different flask, 0.64 g (16 mmol) of NaOH were dissolved under magnetic stirring in 40 mL of DEG and flushed with nitrogen as well. The NaOH solution was transferred into the iron salts solution at room temperature, changing its color from a dark orange to a deep brown-green. The mixture was left to bubble with nitrogen flow and magnetic stirring for 2 h following a steady increase of temperature over 1.5 h until the final temperature was 210 °C. Once the temperature was reached, it was left at

210 °C for another 2 h. The mixture was left to cool to room temperature and the solid product was separated over a strong permanent ferrite magnet. Following decantation of the phase-separated solution, the black solid was washed with 50 mL of ethanol twice. Finally, the solid was washed with 100 mL of 1:1 (v/v) mixture of ethanol and ethyl acetate another three times. The reaction yield was ~90% (1.8 mmol Fe_3O_4 *i.e.*, ~300 mg, as assessed by UV-vis spectroscopy). At this stage in order to functionalize them with oleic acid, the produced iron oxide nanoparticles were re-solubilized in 20 mL of diethylene glycol and the suspension was heated. At 90 °C, 0.825 mL (2.6 mmol) of oleic acid were added to the colloidal solution. Once the addition was done, the nanoparticles precipitated from the solvent almost immediately and the reaction was left to cool to room temperature again. Following the decantation of the suspension in DEG solvent, the oleic acid capped IONPs were washed with methanol 3 more times by separating them from the supernatant with the help of a permanent magnet, then they were re-suspended in 20 mL of toluene and re-precipitated by 3:1 (v/v) of methanol. Finally, they were re-suspended in THF, resulting in a true (*i.e.* stable) ferrofluid.

FT-IR (cm^{-1}) of IONPs-O. A: broad 3380 ν (OH), 3000 ν (=CH) vinyl, 2954 ν_{as} (CH_3), 2923 ν_{as} (CH_2), 2858 ν_{s} (CH_2), 1520 ν_{as} (COO^-), 1428 ν_{s} (COO^-), 550-580 ν (Fe-O).

Co-precipitation method:

The synthesis of IONPs with the co-precipitation method was not performed in this study but the IONPs produced by a previous student with this method were utilized and further functionalized [31,32]. Briefly, the co-precipitation reaction between 2 Fe^{3+} , 1 Fe^{2+} and 8 OH^- ions (basically the same as in the polyol method) performed in water at room temperature is quasi-instantaneous, but it leads to a very broad distribution of IONP diameters, from very small (2-3 nm) to very large ones (15-20 nm). Therefore a size-sorting process is necessary to reduce the dispersity of diameters, based on multiple phase-separations induced by ionic strength increase, through addition of HNO_3 in excess, followed by washing steps [33]. After this efficient yet time consuming process, a fraction of IONPS with diameters centered around 8-10 nm was isolated and used for this work.

Synthesis of carbonyl heterotelechelic poly (isoprene):

The synthesis of a low molar mass carbonyl heterotelechelic poly(isoprene) followed a protocol published in literature, with a targeted DP =20 ($M_n = 1360 \text{ g}\cdot\text{mol}^{-1}$) [34].

In a 0.5 L round bottom flask, 5 g of commercial high molar mass *cis*-1,4-poly(isoprene) $800000 \text{ g}\cdot\text{mol}^{-1}$ was left to solubilize in 250 mL THF overnight under stirring. 2.7 g (14.7 mmol) of metachloroperbenzoic acid (mCPBA) was solubilized in 50 mL of THF and added dropwise over a period of 15 min into the poly(isoprene) solution. The mixture was left to react for 2 h before 3.5 g (15.4 mmol) of periodic acid (H_5IO_6) which was pre-solubilized in 50 mL of THF was added dropwise in the solution and the reaction was left to stir for another 2 h as well. Finally, 7 g of sodium carbonate (Na_2CO_3) was added into the reaction to react with the produced acids and left to stir for 20 min before the solution was filtered through Celite™ to remove the salts. Next, the THF was distilled under vacuum until the solution reached a smaller volume ~10 mL, which was then precipitated by adding 100 mL of cold methanol under vigorous stirring. A viscous light-yellow precipitate was formed, which was solubilized in diethyl ether and re-filtered through Celite™. Excess diethyl ether was distilled again under vacuum and the remaining solution was precipitated again in cold methanol. The precipitate was solubilized again in THF, the THF was distilled, and the final product was dried under vacuum overnight. The final product was a light yellow, almost transparent viscous polymer, with the weight yield of the reaction ~70%.

^1H NMR (400 MHz, CDCl_3): δ (ppm): 9.74 (t, 1H, $-\text{CH}_2\text{CHO}$), 5.14 (t (broad), 5H $-\text{CH}_2\text{CHv}$), 2.47 (t, 2H, $-\text{CH}_2\text{CHO}$), 2.42 (t, 2H, $-\text{CH}_2\text{COCH}_3$), 2.33 (t, 2H, $-\text{CH}_2\text{CH}_2\text{CHO}$), 2.00–2.12 (m (broad), 20H, $-\text{CH}_2\text{CHv}$ and $-\text{CH}_2\text{C}(\text{CH}_3)\text{v}$), 1.68 (s (broad), 15H $-(\text{CH}_3)\text{CvCH}-$).

Synthesis of dopamine functionalized poly (isoprene):

The dopamine functionalization of the carbonyl heterotelechelic poly(isoprene) was achieved *via* reductive amination between the aldehyde end-group of the poly(isoprene) and the primary amine group of dopamine (5-aminomethyl catechol), initially under hydrochloric salt form [35, 36]. The reaction proceeds as follows:

In a Schlenk tube, 0.406 g (1 eq, 0.289 mmol) of carbonyl heterotelechelic poly(isoprene) was solubilized under a nitrogen flow with 5 mL of dry toluene for 1 h to remove moisture from the system *via* the creation of an azeotrope between the moisture and toluene. In a different Schlenk, similar procedure was applied for 0.06 g (~1.2 eq, 0.338 mmol) of dopamine hydrochloride. After 1 h of stirring for both solutions, the toluene was distilled under vacuum and the reagents were left to dry under vacuum overnight. The following day, carbonyl

heterotelechelic poly(isoprene) was solubilized in 1 mL of dry THF and dopamine hydrochloride was solubilized in 1 mL of dry DMF and 0.05 mL (~1.2 eq, 0.338 mmol) of dry Et₃N, in order to deprotonate the amino group of dopamine, resulting into 1:1 THF: DMF volume ratio in the final reaction. Both solutions were combined under inert atmosphere and the final reaction was left to stir for 2 h under gentle heating at 40 °C. After 2 h, 0.2 g (3.3 eq, 0.986 mmol) of sodium triacetoxyborohydride (NaBH(AcO)₃) was added to the reaction mixture, which was left to stir for another 2 h before termination by precipitation in an excess of cold methanol (40 mL). The product was centrifuged at 4 °C (10 min, 4000 g) and the precipitate was washed another 3 times in order to remove the unreacted dopamine hydrochloride and other byproducts. The final product had a foamy consistency and a yellowish color due to the poly(isoprene) content. The weight yield of the final product was ~70%.

¹H NMR (400 MHz, CDCl₃): δ (ppm): 6.8-6.2 (wide, 3H, -NH₂CH₂CH₂-Ph(C-CHCHCOHCCOHCH)), 5.14 (t (broad), 5H -CH₂CHv), 2.47 (t, 2H, -CH₂CHO), 2.42 (t, 2H, -CH₂COCH₃), 2.33 (t, 2H, -CH₂CH₂CHO), 2.00–2.12 (m (broad), 20H, -CH₂CHv and -CH₂C(CH₃)v), 1.68 (s (broad), 15H -(CH₃)CvCH-).

Methods of characterization of hydrophobically modified IONPs:

Dynamic light scattering (DLS):

Dynamic light scattering was utilized to determine hydrodynamic radius (R_h) and the polydispersity (PDI) of the synthesized IONPs suspensions. A Vasco Flex instrument from Cordouan technologies was utilized for this purpose at an angle of 165° (backscattering angle). The polydispersity (PDI) of the systems was analyzed via a 2nd order Cumulant fit while multi-modal distribution diameters were analyzed by a Pade-Laplace fit.

Transmission electron microscopy (TEM):

A Hitachi H7650 electron microscope with an accelerating voltage from 80 to 120kV was utilized for the determination of the morphology of iron oxide nanoparticles (IONPs). Two different operation modes were utilized *i.e.*, High Contrast Mode (HC) where the magnification could be set between 2000 and 200000 or High Resolution Mode (HR) which could reach higher magnification ranging between 4000 and 600000. The images were captured by a camera SC1000 ORIUS 11Mpx (GATAN). The instrument was provided by the Bordeaux Imaging Center (BIC).

The samples were prepared by depositing dropwise 10 µL of the IONPs sample onto formvar and carbon coated TEM 200 Mesh copper (Cu) grids by Agar Scientific until solvent evaporation with no additional staining.

Thermo-gravimetric analysis (TGA):

The grafting density of the IONPs was calculated via thermo-gravimetric analysis using a Q50 thermogravimetric analyzer (TA Instruments). A sufficient volume of IONPs solution was deposited in a platinum TGA ample pan and dried via a flow of nitrogen until solvent evaporation. The first cycle was performed under nitrogen gas N₂, the heating ramp was 10°C/min from 20°C to 115°C followed with an isothermal heating for 30 min at 115°C. the second cycle continued with an increase of temperature to 450°C at a rate of 10°C/min. Finally, the gas was changed to oxygen and the temperature was increased up to 650°C at 10°C/min.

AC magnetometry:

The mass magnetization in A·m²·kg⁻¹ was calculated for IONPs solutions via AC magnetometry. The dynamic hysteresis loops were produced via a pick-up coil technology by an AC HysterTM setup manufactured by the NanoTech Solutions (NTSOL technologies) company (www.ntsol.es). 40 µL of IONPs solution in the concentration range of 0.5 to 26 g.L⁻¹ was inserted into an NMR tube produced by VWR, France, with a diameter of 3 mm and 4 mm in length. Three measurements of magnetization cycles $M(H)$ were conducted at a magnetic field with an amplitude of 24 kA·m⁻¹ and a frequency (f) of 280 kHz. The final value of mass magnetization in A·m²·kg⁻¹ was determined by averaging and normalization between the three measurements with the weight of iron oxide which was determined by UV titration.

Fourier transform infrared spectroscopy (FTIR):

FTIR was performed to determine the successful grafting of IONPs either by oleic acid or by poly(isoprene). The absorbance spectra were performed with a Bruker Vertex 70 FT-IR spectrometer by addition of a droplet of the IONPs solution on the crystal plate and evaporation of the solvents.

Results and discussion:

Synthesis of IONPs *via* the polyol method and their hydrophobic functionalization with oleic acid:

The synthesis of spherical single-domain iron oxide magnetite nanoparticles was achieved *via* the polyol method following the initial work in literature by Caruntu *et al.* [26]. More precisely, the reaction is utilizing diethylene glycol (DEG) both as a solvent and a chelating agent. DEG has a high boiling point of 245°C which allows the use of high temperature in reactions as well as a high dielectric permittivity $\epsilon=32$ which provides a good medium to solubilize highly polar inorganic compounds, such as in this case iron salts.

As previously stated, DEG acts as chelating agent during the synthesis of IONPs by forming metal chelate complexes consisting of the metal ion coordinated with deprotonated DEG ligand molecules provided by NaOH [37], which replace the chloride ligands through a metathesis reaction. By the presence of water in the system, metal hydroxides $\text{Fe}(\text{OH})_2$ and $\text{Fe}(\text{OH})_3$ are formed, which act as precursors of a polycondensation reaction that finally produces magnetite nanoparticles (Fe_3O_4) after the heating of the system and the water elimination. The rate of the reaction is affected by the rate of heating (applied temperature ramp in °C/min) as well as the initial water content in the system (100 μL corresponds to 5.5 mmol thus ~ 1 eq. as compared to the 6 mmol of total iron) (Figure 85).

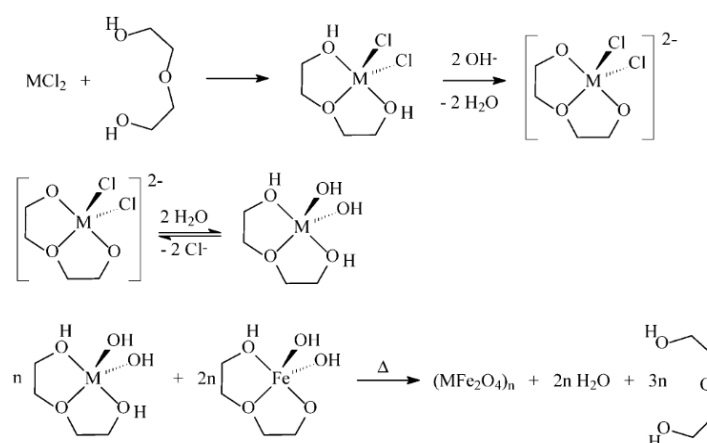


Figure 85: Mechanism of the formation of the metal chelating complexes with DEG and the final formation of IONPs via hydrolysis from Caruntu *et al.*[25].

A representation of the reaction work-up is depicted in Figure 86, where a stoichiometric amount of iron salts ($\text{Fe}^{3+}/\text{Fe}^{2+}$ 2:1) were solubilized in DEG and combined with already solubilized NaOH with DEG.

The mixture was steadily heated for over 3 h until reaching 210°C where it was stabilized for another 2 h. At this stage a black suspension was formed, and the reaction was left to reach room temperature. Once the reaction was cooled down, the formed nanoparticles were separated from the solution by a strong static magnet and washed with first ethanol, and then a mixture of ethanol and ethyl acetate.

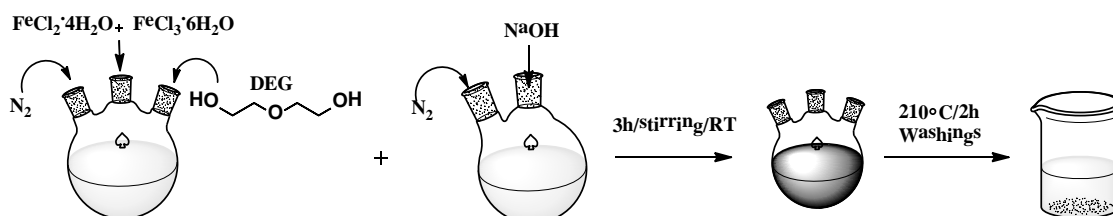


Figure 86: Representation of the IONPs polyol reaction work-up.

Once the iron oxide nanoparticles were isolated, they were re-solubilized in DEG and heated up to 90°C to proceed with their functionalization with oleic acid *via* its carboxylic acid moiety. To do so, 2.6 mmol of oleic acid was added in the system forming immediately a precipitate of nanoparticles. The precipitate was washed several times before recovering the IONPs functionalized with oleic acid that were readily dispersed in THF (Figure 87).

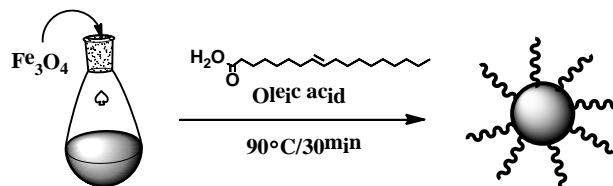


Figure 87 : Representation of the reaction work-up for the functionalization of IONPs with oleic acid.

The final dispersion was analyzed by dynamic light scattering (DLS) and TEM to identify the characteristics of the formed IONPs. The reaction resulted in well-formed spherical iron oxide nanoparticles with a small hydrodynamic diameter which was found in DLS to be $d_H=8.2$ nm with a low polydispersity index $PDI=0.23$, while some aggregation was present as well. Meanwhile, TEM imaging (Figure 88a) revealed a low mean diameter of $d_{TEM}=6$ nm, with a standard deviation of ± 1 nm (Table 13).

Table 13 : Characteristics of IONPs coated with oleic acid provided by DLS, TGA and TEM

Diameter	8.2 nm (57%)
	47.8 nm (27%)
Z-aver	12.2 nm
PDI	0.229
d_{TEM}	6±1 nm (N~7000 particles)
ρ grafting*	5 OA molecules/nm ²
Concentration Fe₂O₃	26 mg·mL ⁻¹

* Estimated from the TGA curve

The grafting density of oleic acid onto the IONPs was calculated via TGA analysis by determining the organic content that was lost during heating up to 650°C by calculating the weight loss fraction. The weight loss % was calculated by the following equation: $\frac{m_1 - m_2}{m_1} * 100$ where m_1 the initial weight after solvent evaporation and m_2 the mass after the organic matter had decomposed.

Figure 88c shows that the main weight loss for OA-coated IONPs occurs between 280°C and 350°C, which corresponds to the decomposition range of oleic acid [38] and yields a 56% ratio of organic to inorganic weight. A second peak in the range 430-470°C might be ascribed to the thermal degradation of OA molecules strongly adsorbed onto the iron oxide cores. From the plateau of TGA curves, one can determine the ratio of organic to inorganic weights.

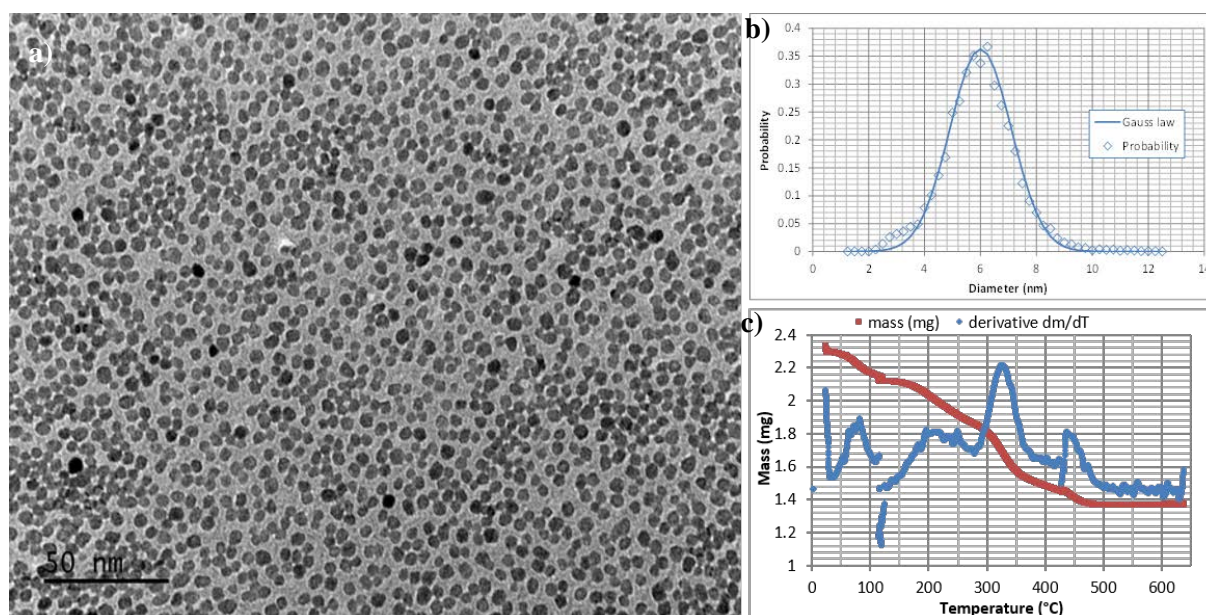


Figure 88 : a) TEM image of Fe_3O_4 coated with oleic acid and their particle size histogram. b) TGA curve enabling to determine the grafting surface density (average number of adsorbed OA molecules/ nm^2).

Further analysis of the oleic acid coated IONPs was done *via* FT-IR spectroscopy, where the binding of the oleic acid onto the iron oxide surface was further proven by the lack of a peak at 1708 cm^{-1} which is attributed to the stretch of $\text{C}=\text{O}$ of free carboxylic groups and the appearance of two peaks at 1520 and 1428 cm^{-1} which were attributed to the asymmetric (ν_{as}) and symmetric (ν_s) stretching of COO^- . The characteristic peak at $550\text{--}580\text{ cm}^{-1}$ of the Fe-O stretch was also observed. Thus, it was concluded that indeed the coating was successfully achieved (Figure 89).

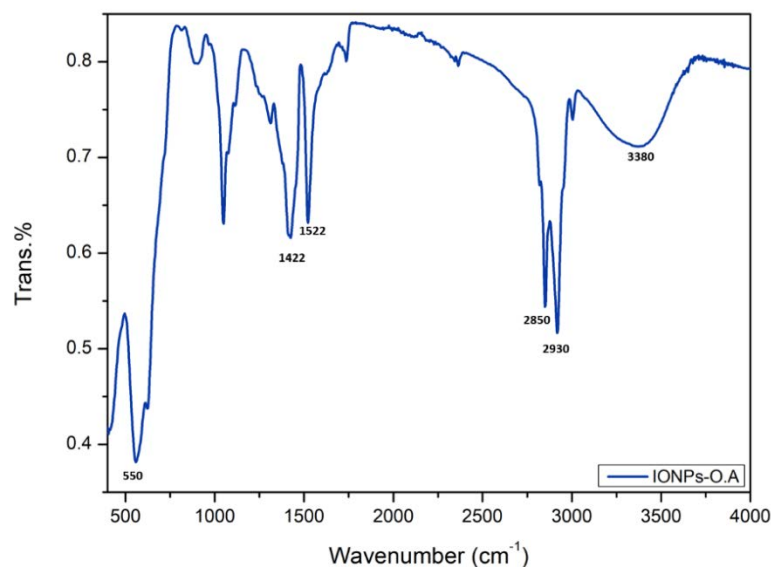
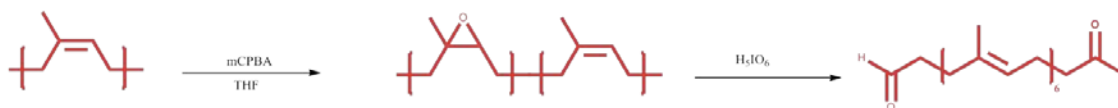


Figure 89 : FT-IR spectra of IONPs-OA (Caruntu method).

Synthesis of carbonyl heterotelechelic poly(isoprene):

The synthesis of carbonyl heterotelechelic poly (isoprene) was achieved via “*one-pot carbonyl telechelic PI (CTPI) preparation via epoxidation (mCPBA) and oxidative degradation of EPI with H_5IO_6* ” following previous publications and is depicted in Scheme 9[34]. A more in-depth description of the synthetic route has been done in Chapter 2, but in short two poly(isoprene) batches with different chain length were synthesized for this part of the study.



Scheme 9 : Scheme of the “one-pot” degradation of long poly(isoprene) to result in a carbonyl telechelic PI is depicted.

Two different lengths of poly(isoprene) were synthesized and studied for the functionalization of magnetic nanoparticles. The targeted DP were 20 and 40 following the report in literature by Berto *et al.* [34,39] modifying the amounts of mCBPA and periodic acid according to each desired degree of polymerization. The polymers were further analyzed by 1H NMR and SEC in THF in order to verify the degree of polymerization as well as the dispersity. The DP of each polymer was determined by integrating the characteristic peak at 9.6 ppm, which is attributed to the proton of the aldehyde end-group and integrated as one (Figure 90 and Figure 91) and are presented in Table 14.

Table 14 : Molecular characteristics of synthesized poly(isoprene) (PI).

PI (97% <i>cis</i> 1,4, MW: 800.000)	$M_{n\text{Theor.}}$ (g·mol) [*]	$M_{n\text{HNMR}}$ (g·mol ⁻¹) ^{**}	DP^{HNMR}	$M_{n\text{SEC}}$ (g·mol ⁻¹) ^{***}	\bar{D}^{**}
PI ₄₀	340	2720	40	2490	1.49
PI ₂₀	340	1360	20	2130	1.19

^{*} $M_{n\text{Theor}}$ from theoretical calculations in literature by Berto *et al.* [34]

^{**} Number-average molar mass (M_n) calculated by ¹H NMR in CDCl₃ using $M_n = I_{5.14\text{ppm}} \times 68 \text{ g}\cdot\text{mol}^{-1}$

^{***} Number-average molar mass (M_n) and dispersity (\bar{D}) obtained by SEC in THF

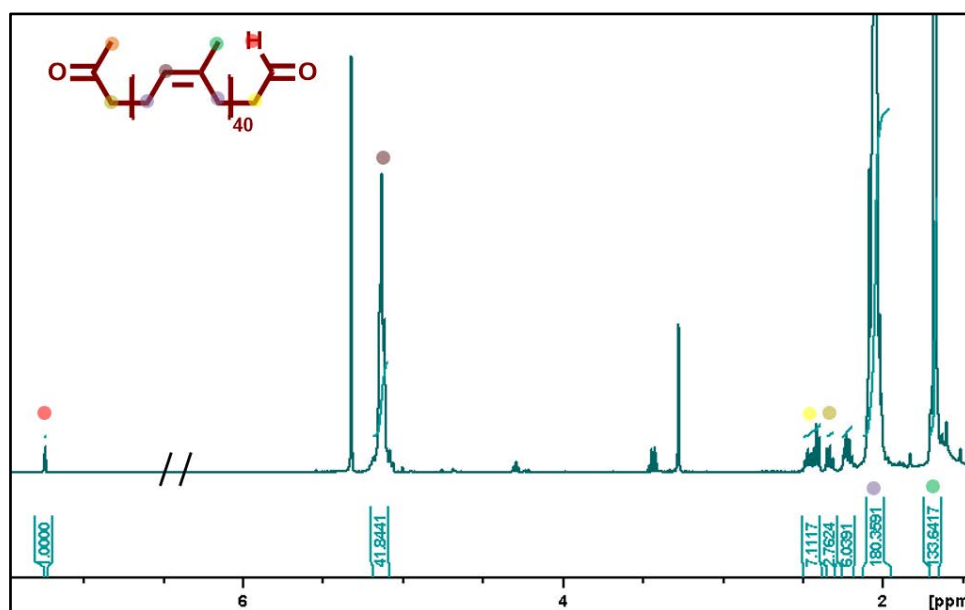


Figure 90 : ¹H NMR in CD₂Cl₂ of poly(isoprene) (PI₄₀) with a $M_{n\text{HNMR}}=2720 \text{ g}\cdot\text{mol}^{-1}$.

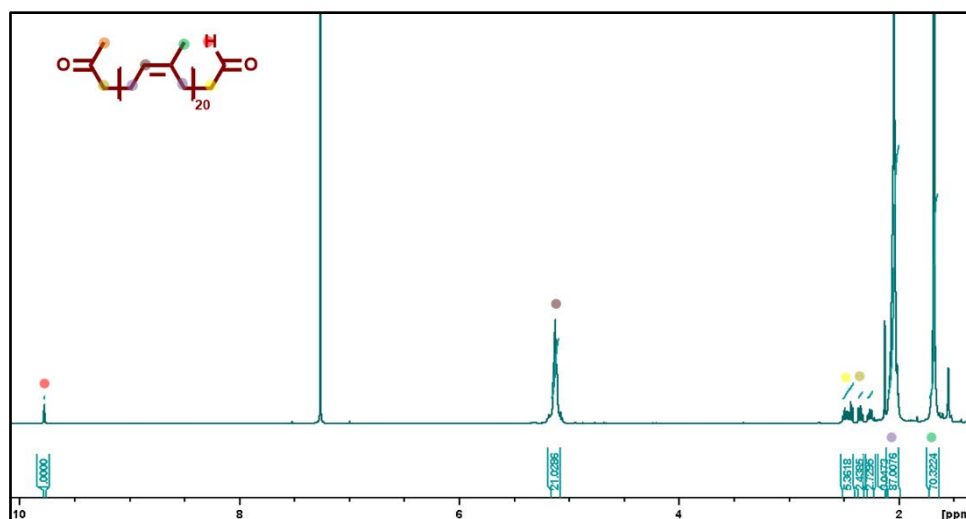
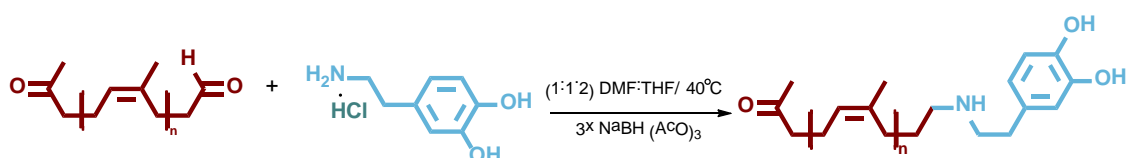


Figure 91 : ^1H NMR in CDCl_3 of poly(isoprene) (PI_{20}) with a M_n ^1H NMR = $1360 \text{ g}\cdot\text{mol}^{-1}$.

Synthesis of dopamine functionalized poly(isoprene):

To produce poly(isoprene) capable of being attached onto IONPs it was important to functionalize it with a functional group that has strong affinity for the IONPs surface. Multiple functional groups could be exploited for such a purpose, such as carboxylic acids, like in this case of oleic acid, phosphonates [40], silanes [41] and catechol groups [42]–[44]. While attempts to attach a phosphonate group on the poly (isoprene) were made, problems with solubility of the amino ethyl phosphonic acid in common solvents with PI resulted in difficulty to functionalize the final polymers and thus a different approach was investigated. In this case dopamine was studied as a functional group due to its catechol moiety which can be taken advantage of to attach it onto IONPs. Moreover, dopamine bears a primary amine group that can be used for further reactions. One way could have been first functionalizing the IONPs with dopamine and then attaching the carbonyl heterotelechelic poly(isoprene), as a post functionalization reaction, but this would result in difficult functionalization control as MAS technique is necessary to obtain NMR spectra of chains grafted on IONPs. Instead, the poly(isoprene) was functionalized first with dopamine and further on the well-characterized functionalized polymer was attached onto the IONPs *via* ligand exchange between the oleic acid and the dopamine functionalized PI.



Scheme 10 : Functionalization of PI with a catechol anchor by reductive amination of heterotelechelic PI with dopamine.

The reaction that was chosen to be performed for the functionalization was a reductive amination between the primary amine group of dopamine and the aldehyde end-group of poly (isoprene) (Scheme 10). The reducing agent of choice was once more sodium triacetoxyborohydride, due to its low toxicity but most importantly due to its inability to reduce ketone groups thus ensuring that the only reaction occurring would be the reduction of the intermediate imine that would be produced during the reaction [45,46].

This reaction has already been studied extensively both in the literature [46], [47] and in this study with different types of polymer functionalization (Chapter 2 and 3). The solvent of the reaction was chosen to be a mixture of THF and DMF due to the insolubility of the dopamine hydrochloride in THF. A mixture of 1:1.2 (v/v) THF:DMF provided a good solubility for both reagents. The reaction was conducted under nitrogen flow to minimize moisture in the system, while all the solvents and reagents were dried as well. Likewise, dry triethylamine was used as a deprotonating agent of the dopamine hydrochloride to render the amine more reactive.

The imine formation step was left to proceed for 2 h before adding the reducing agent in the reaction. The reducing step was left to complete for 24 h to achieve a high functionalization rate with dopamine. The reaction was terminated by precipitation in cold methanol and washed several times to remove unreacted reagents and byproducts. The final polymer was analyzed by ^1H NMR and SEC in THF.

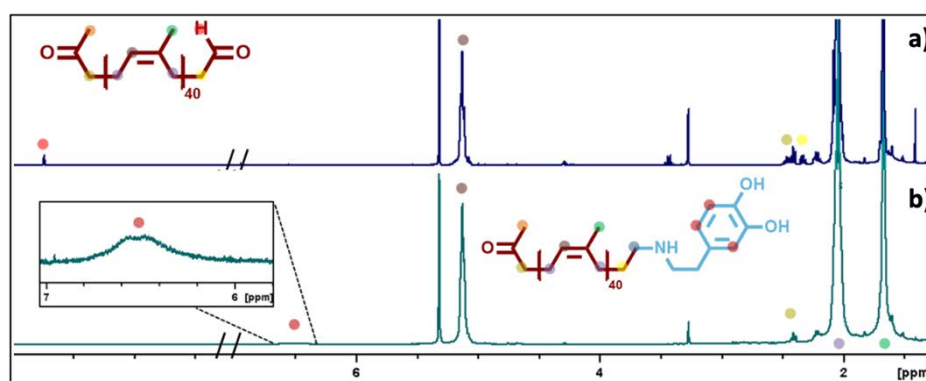


Figure 92 : ^1H NMR in CD_2Cl_2 of a) carbonyl heterotelechelic poly (isoprene) with DP 40 (PI_{40}) and b) dopamine functionalized poly (isoprene) PI_{40} -DOP (C).

The success of the reaction was determined by the lack of the characteristic aldehyde peak of poly(isoprene) at 9.6 ppm in the final spectrum. Moreover, a complete lack of a triple peak at 3.58 ppm suggested that the aldehyde group had not simply been reduced into an alcohol but was indeed functionalized with dopamine. Furthermore, the peak at 2.3 ppm, which was attributed to the 2 protons on the carbon next to the ketone moiety, suggested that the ketone group had not reacted at all and

remained unchanged. Finally, a new broad peak appeared in the final polymers, which was attributed to the catechol ring of dopamine, further verifying that the reaction was successful with 100% functionalization rate and that no side reactions had occurred (Figure 92, Figure 93, Figure 94).

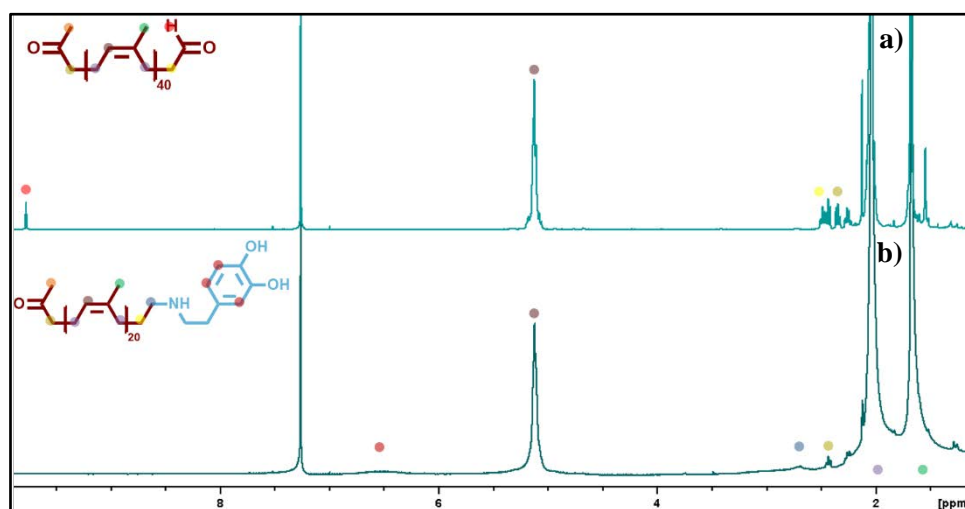


Figure 93 : ¹H NMR in CDCl₃ of a) carbonyl heterotelechelic poly (isoprene) with DP 20 (PI₂₀) and b) dopamine functionalized poly (isoprene) PI₂₀-DOP (D).

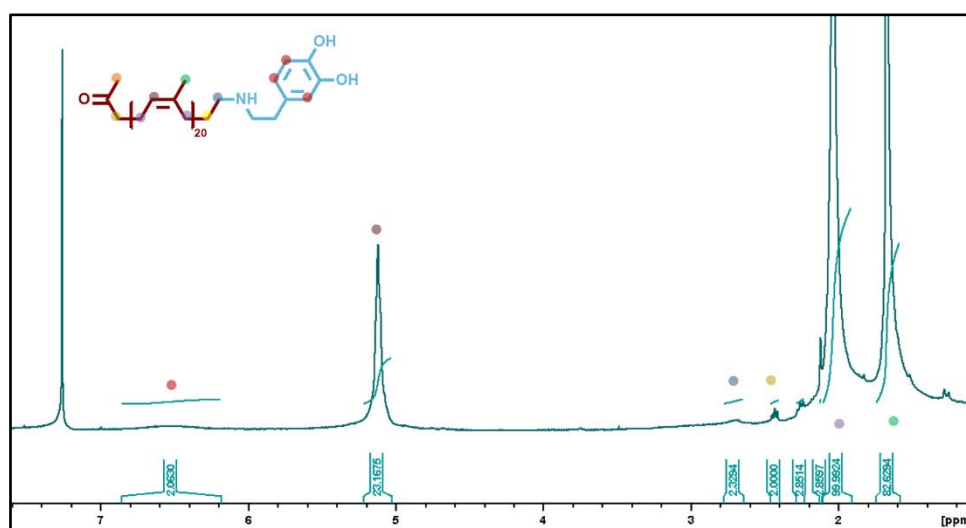


Figure 94 : ¹H NMR in CDCl₃ of dopamine functionalized poly (isoprene) PI₂₀-DOP (D).

Furthermore, all the polymers were analyzed by SEC chromatography in THF where the shift from the original carbonyl heterotelechelic poly(isoprene) was observed for the dopamine functionalized polymers Figure 95. The difference in the final M_n seemed to be substantially higher than the one of the non-functionalized polymers and was attributed to possible interactions between the dopamine moieties, such as π - π stacking between the phenyl rings that could produce an aggregate like effect in SEC. This was further confirmed by ¹H NMR, where no increase in the M_n of the poly(isoprene) chain was observed,

thus verifying that there was no side reaction that would result in a substantial change of molar mass (Table 15).

It is important to notice that the final molar mass measured by SEC analysis did not represent the actual molar mass due to the use of polystyrene standards, whereas absolute molar mass determination by SEC would necessitate to determine first the refractive index increment dn/dc of the functionalized PI in THF.

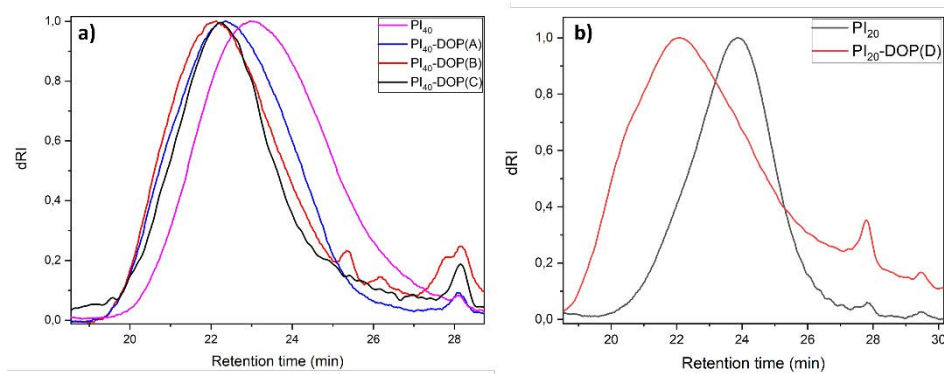


Figure 95 : SEC trace in THF (RI detector) of a) comparison of elution peaks between the non-functionalized PI₄₀ and PI₄₀-DOP (A),(B) ,(C) and b) comparison of elution peaks between the non-functionalized PI₂₀ and PI₂₀-DOP(D).

Further verification of the presence of dopamine was achieved by the UV detector in SEC analysis. Specifically, it was possible to observe the absorption of each polymer in specific wavelengths, such as at 240 nm where poly(isoprene) has a specific absorption, which was present both before and after functionalization. More importantly, the dopamine functionalized polymers presented another absorption signal at 288 nm, which was not present in the non-functionalized PI. This absorption was attributed to the presence of dopamine on the poly(isoprene) chain due to the specific absorption peak of dopamine at 280 nm (Figure 96) [48].

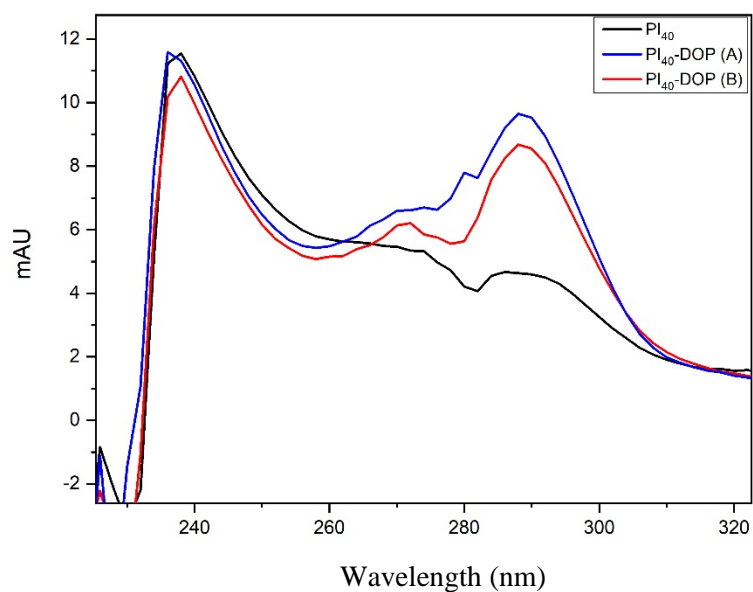


Figure 96 : SEC in THF by UV detector analysis to detect the absorption of the non-functionalized poly (isoprene) and of the dopamine functionalized poly(isoprene).

Table 15 : SEC characteristics of the non-functionalized poly (isoprene) and the library of dopamine functionalized PI-DOP

	M_{nSEC} (g·mol ⁻¹)	\bar{D}
PI₄₀	2490	1.5
PI₂₀	2130	1.2
PI₄₀-DOP (A)	3720	1.4
PI₄₀-DOP (B)	4320	1.4
PI₄₀-DOP (C)	4550	1.3
PI₂₀-DOP (D)	3140	1.6

Grafting of IONPs with dopamine functionalized poly (isoprene)

The coating of IONPs with poly(isoprene) proceeded *via* a ligand exchange between the oleic acid and the dopamine functionalized PI chains. The reaction followed protocol described in literature with modifications according to the solubility of reagents. In short, a desired volume of IONP suspension was added into a vial and the THF was evaporated until the OA-coated IONPs were reduced to a red

paste (owing to the liquid state of oleic acid at room temperature). The IONPs were re-suspended in dry dichloromethane under inert atmosphere. In another vial, twice the amount of weight (w/w) of PI-DOP was solubilized in dry dichloromethane and both solutions were combined under inert atmosphere. Finally, 10 μL of 1 M HCl was added into the mixture, which was finally left to shake overnight (Figure 97, Figure 98).

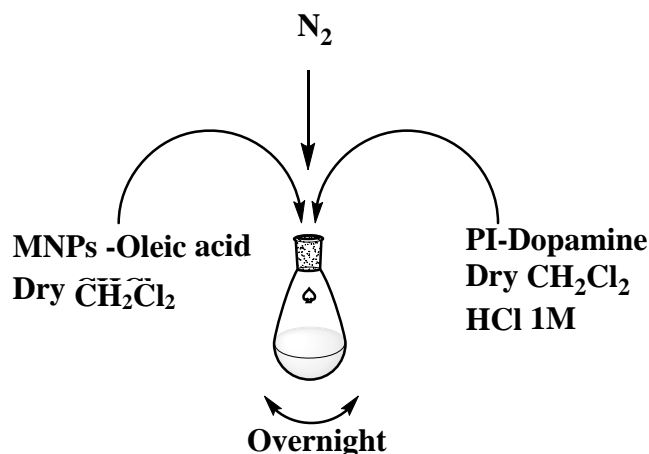


Figure 97 : Schematic representation of the ligand exchange reaction for IONPs-DOP-PI.

The hydrochloric acid played the role of the protonating agent to allow the oleic acid to disengage from the bond with iron oxide, thus allowing the catechol function of dopamine to be attached onto the surface. The final suspension was precipitated into cold methanol and the IONPs were precipitated by the help of a static magnet. The precipitated IONPs were washed many times with methanol to remove oleic acid and further byproducts before full drying by flushing with nitrogen and re-suspending in THF.

The amount of the polymer was chosen to be twice the iron oxide in weight because with a higher amount an excess of polymer was detected in the system, which could not be washed away easily due to the polymer and final nanoparticles being soluble or dispersible in the same solvents.

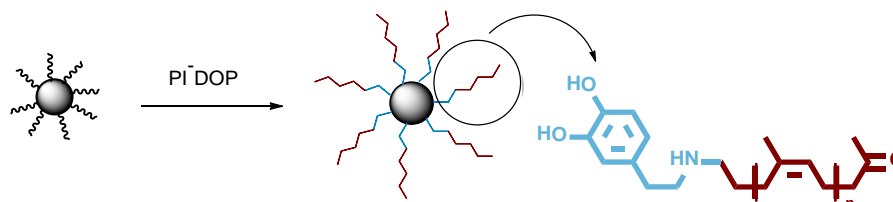


Figure 98: Schematic representation for the final IONPs structure with PI-DOP coating.

The samples can be analyzed by TEM imaging and a strong difference can be seen between the oleic acid coated IONPs and the PI-DOP IONPs: for example, it is visible that the poly(isoprene) functionalized IONPs are more repelled from each other when compared with the oleic acid coated ones.

Furthermore, it is possible to see a white layer in the images around the iron oxide cores in Figure 99, which can be ascribed to the poly(isoprene) brush layer.

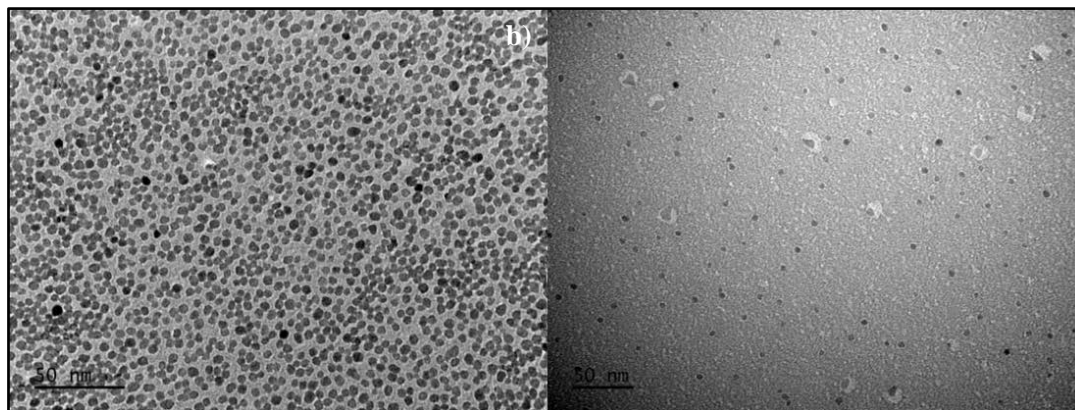


Figure 99 : TEM images of a) IONPs-OA (Caruntu's polyol route) and b) IONPs-PI-DOP (A).

Further verification of the exchange between the layers was performed by comparing FT-IR spectra between the IONPs-OA and the IONPs-PIDOP. There it was possible to see the difference between the two IONPs and identify the peaks (Figure 100). For example, the two main peaks at 3000 cm^{-1} which were representative of the stretching ν ($=\text{CH}$) of the vinyl bonds of oleic acid are clearly exchanged in the final IONPs spectra with a wide peak characteristic for the stretching of the vinyl bonds of poly(isoprene). The two peaks at 1520 and 1428 cm^{-1} which were attributed to the asymmetric (ν_{as}) and symmetric (ν_s) stretching of COO^- , were exchanged with the two peak at 1449 and 1374 cm^{-1} which represent the stretching of the C-C on the phenyl group ($\nu(\text{CC})_{ar}$) as well as the stretching $\nu(\text{CO})_{\text{semiquinone}}$ and in-plane bending ρ (C-C-N), respectively. Furthermore, a transmission peak at 838 cm^{-1} appeared in both PI-DOP and IONPs-PI-DOP representing the γ vibration of $(\text{NH})_{\text{Wag}}$. In the case of Figure 16 the peak at 583 cm^{-1} for $\nu(\text{Fe-O})$ seems smaller than the one for OA-coated IONPs and is attributed to an excess of polymer in this batch of polymer-coated IONPs.

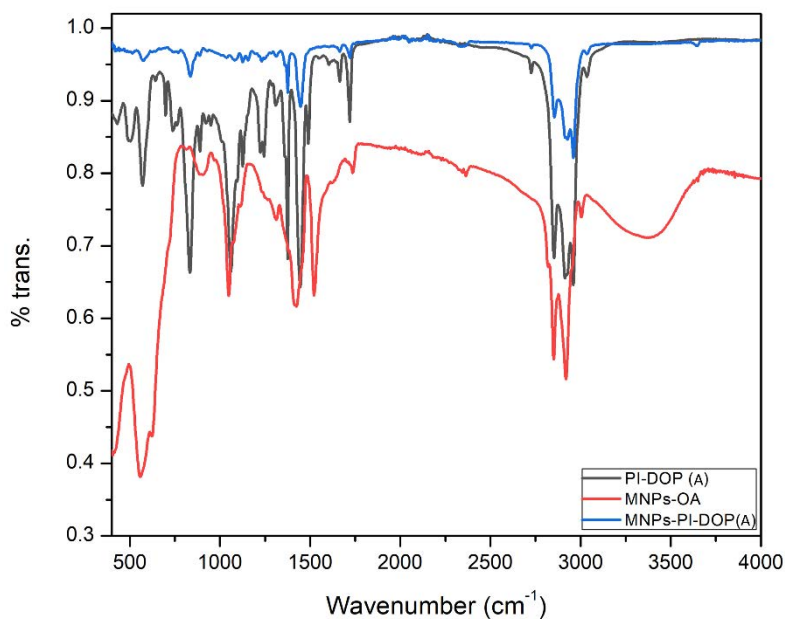


Figure 100 : FT-IR spectra of PI-DOP (B), IONPs-OA and IONPs-PI-DOP (A).

To verify further the efficacy of the ligand exchange, magnetic angle spinning solid state NMR was performed for IONPs-OA and IONPs-PI-DOP (A) (Figure 101). While this batch of IONPs-PI-DOP had an excess of polymer which could be seen in the NMR, the result nonetheless proved the exchange of ligands by the exhibited spectra, the change of the final peaks was apparent, with the characteristic peak of poly(isoprene) being visible and the oleic peaks completely gone. These experiments were kindly performed by Dr. Céline Hénoumont from the NMR and molecular imaging laboratory at the University of Mons in Belgium and were repeated by diluting the suspension in d8-THF in order to attenuate the peak broadening effect caused by the superparamagnetic IONPs on the signal. These spectra are available in Supplementary Information (Figure S 11, Figure S 12, Figure S 13) for three samples, specifically PIDOP(A), PIDOP(B) and PIDOP(D). Figure S 11 and Figure S 12 were diluted 25 times their original volume with d8-THF until the peaks were clearly distinguished. All the samples reinforced the hypothesis that the ligand exchange was successful each time and indeed all the samples were functionalized with PIDOP and not oleic acid.

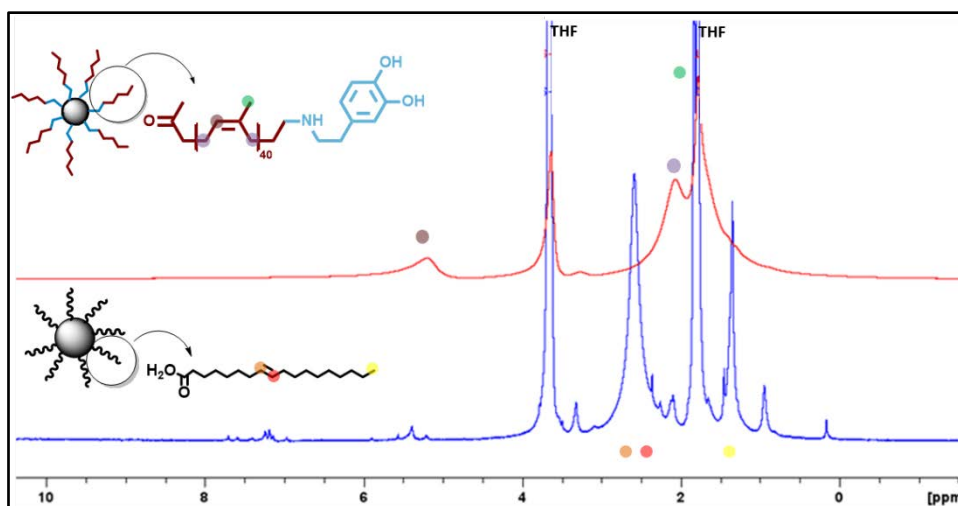


Figure 101 : MAS-ss NMR spectroscopy of IONPs-OA and IONPs-PI-DOP in d8-THF.

The grafting density of IONPs functionalized with PIDOP was calculated as well via TGA analysis by determining the organic content that was lost during heating up to 650°C via calculating the weight loss fraction. From the plateau of TGA curves, it is possible to determine the ratio of organic to inorganic weights (Figure 102).

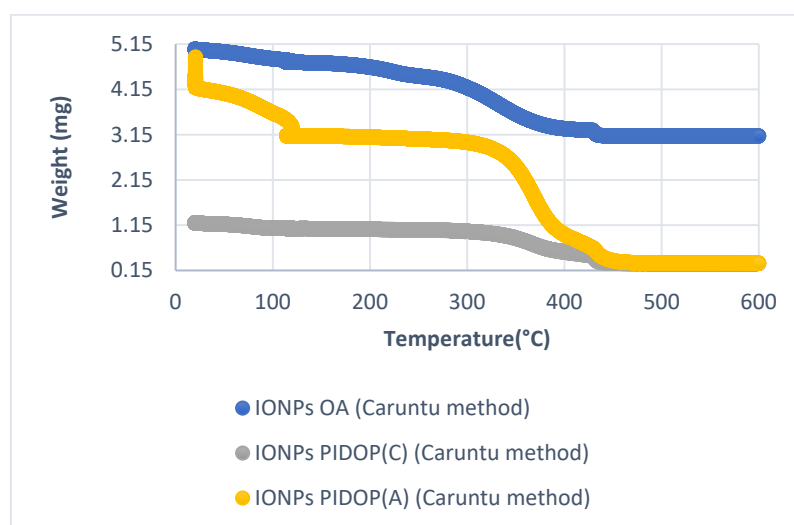


Figure 102 : TGA curve enabling to determine the grafting surface density (average number of adsorbed polymer molecules / nm²).

The degradation of the samples is visibly changed after the ligand exchange between oleic acid and the dopamine functionalized poly(isoprene). After the initial weight loss at the temperature range 0-100°C, which was attributed to solvent still present in all the samples, in this case THF, one can see that the main weight loss appeared to have shifted to higher temperatures for the poly(isoprene) functionalized IONPs. As already described above the degradation range for oleic acid is between 280-350°C while the samples that were functionalized with poly(isoprene) appear to present a different main weight loss

temperature which started after 300°C to 400°C. A second smaller and final weight loss appeared at higher temperatures and reached a maximum at 430°C and could be attributed to either to polymer chains that were strongly adsorbed onto the iron oxide cores or due to the decomposition process of the poly(isoprene).

The IONPs-PIDOP presented a typical profile for PI degradation as has been observed in literature where the main weight loss for *cis*-1,4-poly(isoprene) appeared in the range of 300-400 °C reaching a maximum around 370°C. Of course, it is important to notice that in our case the polymer has a small molar mass and carbonyl end groups that may interfere with the final degradation of the polymer but still the maximum appears to remain the same. The distinction between the maximum degradation temperatures can be observed for the derivative dm/dT where the maximum for the IONPs-OA was indicated to be at 330 °C compared to 380°C which was observed for both IONPs-PIDOP (Figure 103).

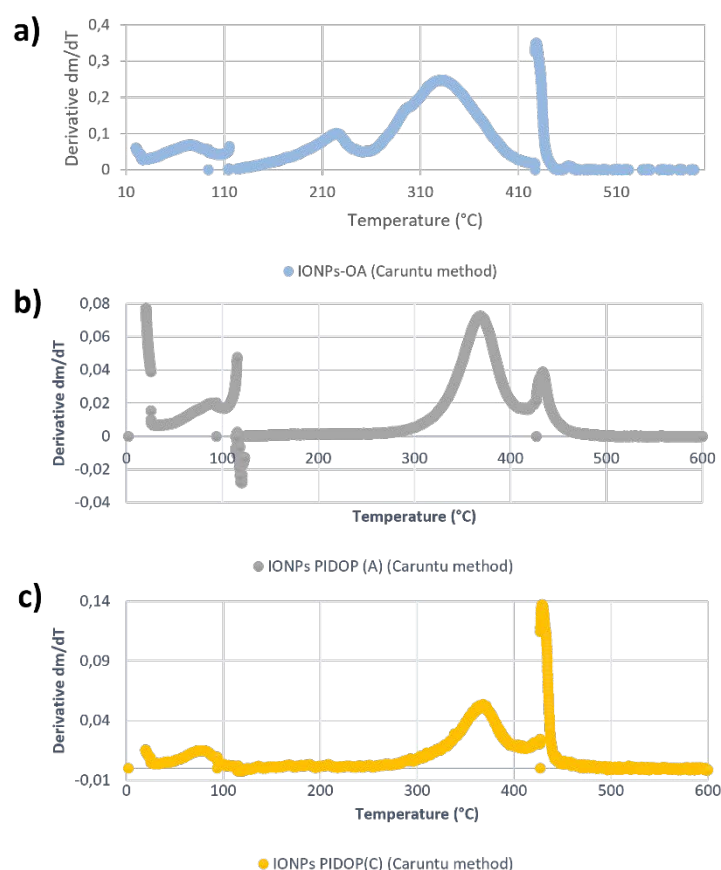


Figure 103 : TGA curve representing the derivative dm/dT for a) IONPs-OA, b) IONPs-PIDOP (A) and c) IONPs-PIDOP (C) from the Caruntu method IONPs.

What can also be observed in Figure 102 is the amount of organic matter for the sample IONP-PIDOP (3) which seems to consist 70% of the original sample and would result in a very high grafting density, 38 chains /nm². From the surface area of the IONPs (estimated geometrically from their mean radius), we estimated the surface grafting density in number of molecules (or chains) per nm². The average

distance between molecules can then be compared to the dimensions of the grafted molecules: ~ 2 nm of extended length for oleic acid and a radius of gyration of 1.8 nm for PI chains of $3 \text{ kg}\cdot\text{mol}^{-1}$ according to law $R_G \cong 1.0308 \times M_n (\text{kg}\cdot\text{mol}^{-1})^{0.49}$ reported in literature [49]. Although the measurement at 38 chains/ nm^2 most likely correspond to an excess of PI (therefore multilayers) and was to be expected for this sample due to the synthetic process, *i.e.* 100x of polymer instead of 2x and was already observed above when characterized with MAS-ss NMR spectroscopy (Figure 101). On the other hand the sample of IONPs-PIDOP(C) which had a 2x of the polymer during the ligand exchange presented 53% of organic to inorganic ratio and a grafted density $\rho=3$ chains / nm^2 was compatible with a monolayer of grafted PI chains in the dense brush [50] regime of tethered chains on a nanoparticle surface.

Furthermore, we were able to see the different mass magnetization $\text{Am}^2\cdot\text{kg}^{-1}$ the IONPs had depending on their coating using AC magnetometry. While this technique is mainly used in magnetic hyperthermia in order to calculate the heating capacity of the magnetic nanoparticles by measuring the magnetization cycles in a variety of magnetic field amplitudes (H_{max}) and different frequencies kHz, herein the heating capacity of the samples was not the primary goal to detect. The samples were measured in the highest amplitude of $24 \text{ kA}\cdot\text{m}^{-1}$ and 280 kHz (Figure 104).

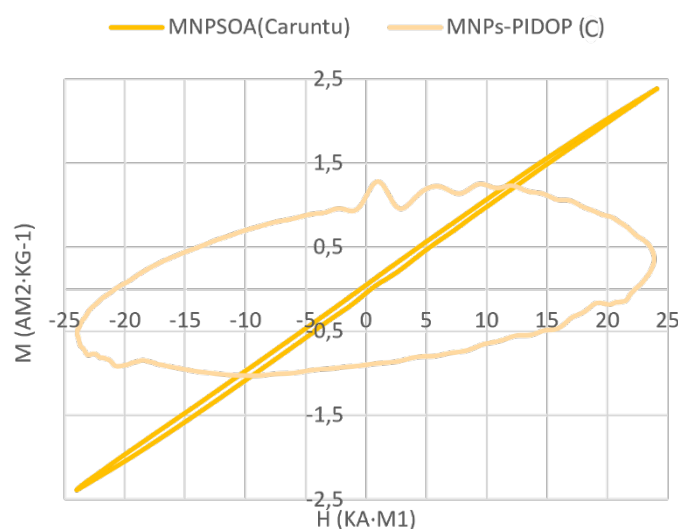


Figure 104 : Dynamic magnetization curves under an alternating magnetic field at 280 kHz measured on the oleic acid and PI-dopamine coated IONPs, both prepared by Caruntu et al polyol method.

The $M(H)$ curve of OA-coated sample showed pure superparamagnetic response (no hysteresis) with a magnetic susceptibility $\chi=M/H=0.1$, in agreement with low diameter IONPs. The hysteresis loop shown for the PI-coated sample could be ascribed to a too low concentration (this method needs an iron oxide $c > 1 \text{ mg}\cdot\text{mL}^{-1}$). While the sample had a concentration of $2.2 \text{ mg}\cdot\text{mL}^{-1}$ the resulting hysteresis loop appeared not well defined and had the same appearance in multiple measurements. It would be possible

to suggest that due to the higher mass of poly(isoprene) of $2700 \text{ g}\cdot\text{mol}^{-1}$ the magnetization of the IONPs was not as effective as it was when they were functionalized with the relatively small oleic acid.

Such behavior has been studied by Majeed *et al.* [51] where ultra-small IONPs with a core diameter of $4.5\pm 0.4 \text{ nm}$ were functionalized with a PTMP-PMAA copolymer with a molar mass of almost $6000 \text{ g}\cdot\text{mol}^{-1}$ and the samples were characterized with Vibrating sample magnetometry in order to determine the saturation magnetization of the IONPs. It was determined then that the samples that had a higher concentration of polymer on their surface had a lower saturation magnetization, when compared to a sample with a lower concentration of polymer or bare IONPs. This phenomenon was attributed to a higher polymer content and while it was a comparison between concentration of polymer in the system it could be prudent to suggest that it can be applied in our case as well if we take into account the huge difference of size between the oleic acid and poly(isoprene) in this case, almost 13 times. Thus we indeed have more polymer in the system even if the grafting density is lower, *i.e.* 3 compared to 5 when it comes to oleic acid.

Same methods of functionalization and characterization were applied to the IONPs that were obtained via the co-precipitation method and fractionated size-sorting. In this case the PI-DOP polymer that was utilized to functionalize the IONPs had a small molar mass of poly(isoprene), with a DP of 20. The final IONPs-PI-DOP were analyzed by DLS, TEM and FT-IR respectively. In Figure 105, we can see the differentiation between the IONPs-OA and IONPs-PI-DOP on TEM images. Specifically, once more when the ligand was oleic acid the IONPs were in close proximity to each other but following the ligand exchange with the dopamine functionalized poly(isoprene) the IONPs were more uniformly dispersed due to the higher molar mass and length of the attached chains. The same phenomenon was observed with the IONPs in the previous section though the poly(isoprene) is smaller compared to the ligand that was functionalized on the IONPs from polyol method, $1360 \text{ g}\cdot\text{mol}^{-1}$ compared to $2720 \text{ g}\cdot\text{mol}^{-1}$.

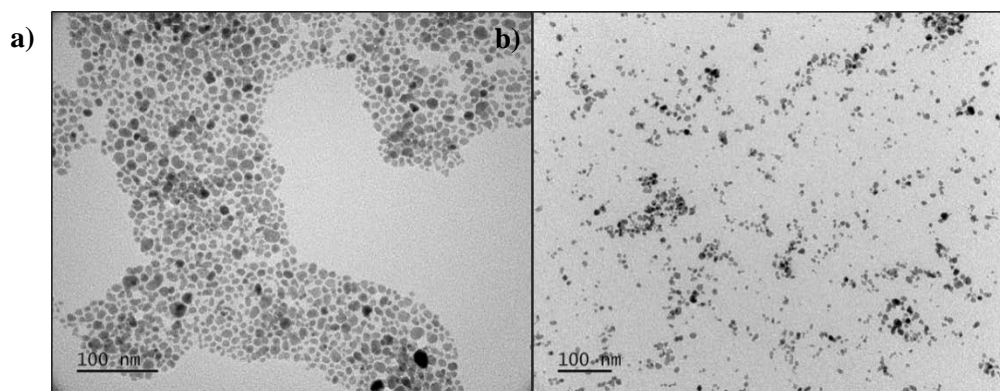


Figure 105 : TEM images of a) IONPs-OA and b) IONPs-PI-DOP (D) both prepared by the coprecipitation route.

Further verification was once more achieved by FT-IR by detecting the characteristic peaks for poly(isoprene) (Figure 106). The main wide peak at 3000 cm^{-1} which was representative of the stretching ν ($=\text{CH}$) of the vinyl bonds of oleic acid is exchanged once more in the final IONs-PIDOP spectra with a wide peak characteristic for the stretching of the vinyl bonds of poly(isoprene). Again, the two peak at 1449 and 1374 cm^{-1} which represent the stretching of the C-C on the phenyl group (ν (CC)_{ar}) as well as the stretching ν (CO)_{semiquinone} and in-plane bending ρ (C-C-N), appeared in the final IONPs-PIDOP spectra. The peak at 580 cm^{-1} for ν (Fe-O) appears in both IONPs spectra verifying the presence of iron oxide nanoparticles.

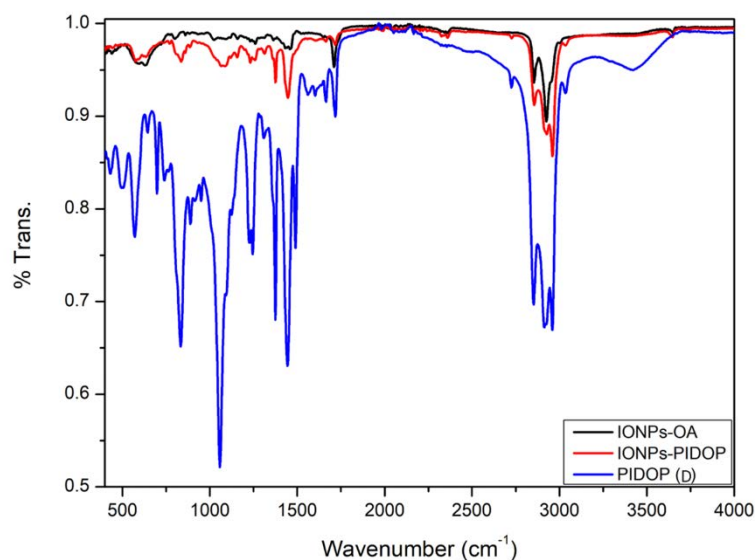


Figure 106 : FT-IR spectra of IONPs-OA and IONPs-PI-DOP (D) both prepared by the coprecipitation route.

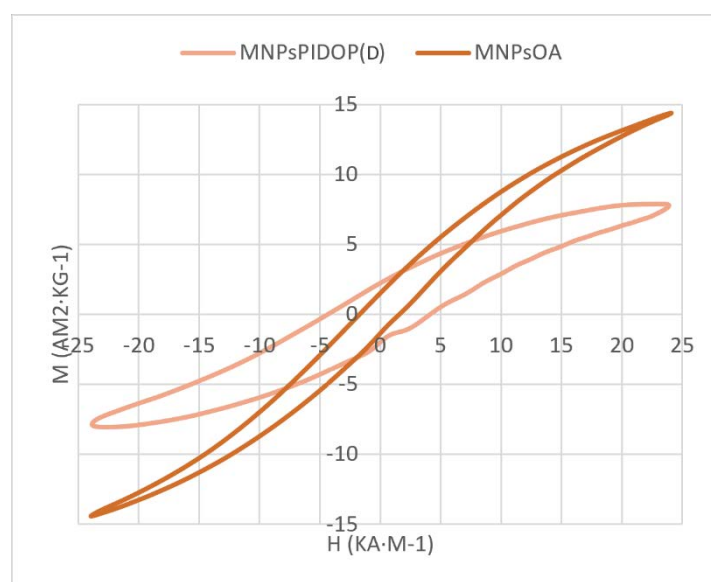


Figure 107 : Dynamic magnetization curves under an alternating magnetic field at 280 kHz measured on the oleic acid and PI-dopamine coated IONPs, both prepared by the coprecipitation route.

AC magnetometry (Figure 107) was performed for these IONPs as well. In comparison to the previous IONPs synthesized by the Caruntu method, these exhibit open hysteresis of the dynamic $M(H)$ curve at this frequency, which is typical for IONPs of larger diameters (8-10 nm for the coprecipitated IONPs as compared to 6 nm for those obtained by the polyol synthesis studied before). But the effect of a lower magnetization could still be observed here after the ligand exchange. While in this case the molar mass of the functionalized poly(isoprene) was smaller than the molar mass in previous samples, i.e. $\sim 1400 \text{ g}\cdot\text{mol}^{-1}$ we could still observe the magnetization drop almost by 50% and the hysteresis loop becoming

less defined. Thus while the polymer is almost 7 times larger than the oleic acid, we could still see a similar effect. Nevertheless, we can anticipate larger magnetic effects also at lower frequencies when these IONPs are incorporated inside polymersomes. The characteristics of all the functionalized iron oxide nanoparticles are describe in **Table 16**.

Table 16 : Table of characteristics of produced IONPs with oleic acid and PI-DOP ligands.

	Concentration (mg·mL ⁻¹)	Diameter (nm)		Z-aver	PDI	$\rho_{\text{grafting}}[\text{Ligand}/\text{nm}^2]$	d _{TEM}
IONPs-OA (Polyol method)	25.8	8	60	12.8	0.3	5	6±1 nm
IONPs-OA (Co-precipitation method)	16	24		-	0.3	8	8±1 nm
(100×polymer/IONPs) IONPs-PI-DOP(A)	1	13	127	45	0.3	38	6±1 nm
(2×polymer/IONPs) IONPs-PI-DOP(C)	2.2	8.96		36	0.5	3	6±1 nm
(2×polymer/IONPs) IONPs-PI-DOP(D)	0.5	29.7		67.7	0.13	4.8	8±1 nm

Conclusion:

In the context of this project, it was important to synthesize iron oxide nanoparticles which had a small diameter to allow them to be easily incorporated into the hydrophobic membrane of polymersomes. Furthermore, it was important to functionalize them with a hydrophobic ligand for the same purpose. Both requirements were met and discussed in this chapter.

To conclude, in this chapter we have demonstrated the synthesis of hydrophobically coated iron oxide nanoparticles. Two types of ligands were utilized for this step *i.e.*, oleic acid and modified poly(isoprene). First iron oxide nanoparticles (IONPs) were produced via the polyol route resulting in small spherical nanoparticles with a diameter of $d=6\text{nm}$. Further on they were functionalized with oleic acid to render them hydrophobic. Dopamine functionalized poly(isoprene) was produced via a reductive amination reaction producing a well functionalized polymer (PI-DOP). PI-DOP was utilized to functionalize the IONPs-OA via a ligand exchange reaction producing well grafted IONPs-PIDOP with high grafting densities ρ . The functionalization of nanoparticles with oleic acid or PI-DOP was verified with FT-IR and TGA.

Another batch of slightly larger nanoparticles, $d=8\text{ nm}$, was functionalized as well with both ligands respectively in order to study the effect of larger nanoparticles in the self-assembly process as will be discussed in the final chapter.

References:

- [1] M. O. Rigo and J. Kleinclauss, “Specific heat of Fe_3O_4 ,” *Philos. Mag. B*, vol. 42, no. 3, pp. 393–407, 1980.
- [2] D. K. Kim *et al.*, “Starch-Coated Superparamagnetic Nanoparticles as MR Contrast Agents,” *Chem. Mater.*, vol. 15, no. 23, pp. 4343–4351, Nov. 2003.
- [3] L. Babes, B. Denizot, G. Tanguy, J. J. Le Jeune, and P. Jallet, “Synthesis of Iron Oxide Nanoparticles Used as MRI Contrast Agents: A Parametric Study,” *J. Colloid Interface Sci.*, vol. 212, no. 2, pp. 474–482, 1999.
- [4] M. I. Papisov *et al.*, “Colloidal magnetic resonance contrast agents: effect of particle surface on biodistribution,” *J. Magn. Magn. Mater.*, vol. 122, no. 1, pp. 383–386, 1993.
- [5] M. K. Yu *et al.*, “Drug-Loaded Superparamagnetic Iron Oxide Nanoparticles for Combined Cancer Imaging and Therapy In Vivo,” *Angew. Chemie Int. Ed.*, vol. 47, no. 29, pp. 5362–5365, 2008.
- [6] J. Liu *et al.*, “Glucose- $\{\}$ pH- and thermo-responsive nanogels crosslinked by functional superparamagnetic maghemite nanoparticles as innovative drug delivery systems,” *J. Mater. Chem. B*, vol. 2, no. 8, pp. 1009–1023, 2014.
- [7] S. Tan *et al.*, “Doxorubicin Loaded Magnetic Polymersomes : Theranostic Nanocarriers for MR Imaging and Magneto-Chemotherapy,” *ACS Nano*, vol. 5, no. 2, pp. 1122–1140, 2011.
- [8] H. S. Huang and J. F. Hainfeld, “Intravenous magnetic nanoparticle cancer hyperthermia,” *Int. J. Nanomedicine*, vol. 8, pp. 2521–2532, 2013.
- [9] Z.-Q. Zhang and S.-C. Song, “Thermosensitive/superparamagnetic iron oxide nanoparticle-loaded nanocapsule hydrogels for multiple cancer hyperthermia,” *Biomaterials*, vol. 106, pp. 13–23, 2016.
- [10] X. L. Liu *et al.*, “Synthesis of Ferromagnetic $\text{Fe}_{0.6}\text{Mn}_{0.4}\text{O}$ Nanoflowers as a New Class of Magnetic Theranostic Platform for In Vivo T1-T2 Dual-Mode Magnetic Resonance Imaging and Magnetic Hyperthermia Therapy,” *Adv. Healthc. Mater.*, vol. 5, no. 16, pp. 2092–2104, 2016.
- [11] M. Bañobre-López, A. Teijeiro, and J. Rivas, “Magnetic nanoparticle-based hyperthermia for cancer treatment,” *Reports Pract. Oncol. Radiother.*, vol. 18, no. 6, pp. 397–400, 2013.
- [12] J. P. Fortin, C. Wilhelm, J. Servais, C. Ménager, J. C. Bacri, and F. Gazeau, “Size-sorted anionic iron oxide nanomagnets as colloidal mediators for magnetic hyperthermia,” *J. Am. Chem. Soc.*, vol. 129, no. 9, pp. 2628–2635, 2007.
- [13] B. Samanta, H. Yan, N. O. Fischer, J. Shi, D. J. Jerry, and V. M. Rotello, “Protein-passivated Fe_3O_4 nanoparticles: low toxicity and rapid heating for thermal therapy,” *J. Mater. Chem.*, vol. 18, no. 11, pp. 1204–1208, 2008.
- [14] S. M. Mirvakili, Q. P. Ngo, and R. Langer, “Polymer Nanocomposite Microactuators for On-Demand Chemical Release via High-Frequency Magnetic Field Excitation,” *Nano Lett.*, vol. 20, no. 7, pp. 4816–4822, Jul. 2020.
- [15] S. Jeong *et al.*, “Hydrogel Magnetomechanical Actuator Nanoparticles for Wireless Remote Control of Mechanosignaling In Vivo,” *Nano Lett.*, May 2023.
- [16] Y. Chen *et al.*, “Hedgehog-Like Gold-Coated Magnetic Microspheres that Strongly Inhibit Tumor Growth through Magnetomechanical Force and Photothermal Effects,” *Small*, vol. 14, no. 45, pp. 1–13, 2018.

- [17] D. Cheng, X. Li, G. Zhang, and H. Shi, "Morphological effect of oscillating magnetic nanoparticles in killing tumor cells," pp. 1–8, 2014.
- [18] A. M. Master *et al.*, "Remote actuation of magnetic nanoparticles for cancer cell selective treatment through cytoskeletal disruption," *Sci. Rep.*, vol. 6, no. April, pp. 1–13, 2016.
- [19] C. Apoptosis, E. Zhang, M. F. Kircher, X. M. Koch, L. Eliasson, and S. N. Goldberg, "Dynamic Magnetic Fields Remote- Rotation," *ACS Nano*, vol. 8, no. 4, pp. 3192–3201, 2014.
- [20] Y. I. Golovin, N. L. Klyachko, M. Sokolsky-Papkov, and A. V. Kabanov, "Single-domain magnetic nanoparticles as force generators for the nanomechanical control of biochemical reactions by low-frequency magnetic fields," *Bull. Russ. Acad. Sci. Phys.*, vol. 77, no. 11, pp. 1350–1359, 2013.
- [21] Y. I. Golovin *et al.*, "The dynamics of magnetic nanoparticles exposed to non-heating alternating magnetic field in biochemical applications: theoretical study," *J. Nanoparticle Res.*, vol. 19, no. 2, 2017.
- [22] Y. I. Golovin, A. O. Zhigachev, N. L. Klyachko, and A. V. Kabanov, "Localizing the Nanodeformation Impact of Magnetic Nanoparticles on Macromolecular Objects by Physical and Biochemical Means," *Bull. Russ. Acad. Sci. Phys.*, vol. 82, no. 9, pp. 1073–1078, 2018.
- [23] A. V. Ryzhkov and Y. L. Raikher, "Numerical Modeling of a Magnetic Polymersome in a Uniform Magnetic Field," *IEEE Magn. Lett.*, vol. 10, no. c, p. 1, 2019.
- [24] A. Ryzhkov and Y. Raikher, "Coarse-grained molecular dynamics modelling of a magnetic polymersome," *Nanomaterials*, vol. 8, no. 10, pp. 1–12, 2018.
- [25] D. Caruntu, G. Caruntu, Y. Chen, C. J. O'Connor, G. Goloverda, and V. L. Kolesnichenko, "Synthesis of Variable-Sized Nanocrystals of Fe₃O₄ with High Surface Reactivity," *Chem. Mater.*, vol. 16, no. 25, pp. 5527–5534, Dec. 2004.
- [26] D. Caruntu, G. Caruntu, and C. J. O'Connor, "Magnetic properties of variable-sized Fe₃O₄ nanoparticles synthesized from non-aqueous homogeneous solutions of polyols," *J. Phys. D. Appl. Phys.*, vol. 40, no. 19, pp. 5801–5809, 2007.
- [27] G. Hemery *et al.*, "Tuning Sizes, Morphologies, and Magnetic Properties of Monocore Versus Multicore Iron Oxide Nanoparticles through the Controlled Addition of Water in the Polyol Synthesis," *Inorg. Chem.*, vol. 56, no. 14, pp. 8232–8243, 2017.
- [28] J. Wan, W. Cai, X. Meng, and E. Liu, "Monodisperse water-soluble magnetite nanoparticles prepared by polyol process for high-performance magnetic resonance imaging," *Chem. Commun.*, vol. 4, no. 47, pp. 5004–5006, 2007.
- [29] B. Zhang, Z. Tu, F. Zhao, and J. Wang, "Superparamagnetic iron oxide nanoparticles prepared by using an improved polyol method," *Appl. Surf. Sci.*, vol. 266, pp. 375–379, 2013.
- [30] W. Cai and J. Wan, "Facile synthesis of superparamagnetic magnetite nanoparticles in liquid polyols," *J. Colloid Interface Sci.*, vol. 305, no. 2, pp. 366–370, 2007.
- [31] R. Massart, "Preparation of aqueous magnetic liquids in alkaline and acidic media," *IEEE Trans. Magn.*, vol. 17, no. 2, pp. 1247–1248, 1981.
- [32] A. B. Chin and I. I. Yaacob, "Synthesis and characterization of magnetic iron oxide nanoparticles via w/o microemulsion and Massart's procedure," *J. Mater. Process. Technol.*, vol. 191, no. 1–3, pp. 235–237, 2007.
- [33] P. Arosio *et al.*, "Hybrid iron oxide-copolymer micelles and vesicles as contrast agents for MRI:

- impact of the nanostructure on the relaxometric properties,” *J. Mater. Chem. B*, vol. 1, no. 39, pp. 5317–5328, 2013.
- [34] P. Berto, S. Grelier, and F. Peruch, “Controlled degradation of polyisoprene and polybutadiene: A comparative study of two methods,” *Polym. Degrad. Stab.*, vol. 154, pp. 295–303, 2018.
- [35] A. V. Radchenko *et al.*, “Facile synthesis of 1,4-: Cis -polyisoprene-polypeptide hybrids with different architectures,” *Polym. Chem.*, vol. 10, no. 19, pp. 2456–2468, 2019.
- [36] K. V Korpany, D. D. Majewski, C. T. Chiu, S. N. Cross, and A. S. Blum, “Iron Oxide Surface Chemistry: Effect of Chemical Structure on Binding in Benzoic Acid and Catechol Derivatives,” *Langmuir*, vol. 33, no. 12, pp. 3000–3013, Mar. 2017.
- [37] G. Hemery *et al.*, “Tuning Sizes, Morphologies, and Magnetic Properties of Monocore Versus Multicore Iron Oxide Nanoparticles through the Controlled Addition of Water in the Polyol Synthesis,” *Inorg. Chem.*, vol. 56, no. 14, pp. 8232–8243, 2017.
- [38] W. Baaziz *et al.*, “Tuning of Synthesis Conditions by Thermal Decomposition toward Core–Shell $\text{CoFe}_{1-x}\text{O}@ \text{CoFe}_3\text{–yO}_4$ and CoFe_2O_4 Nanoparticles with Spherical and Cubic Shapes,” *Chem. Mater.*, vol. 26, no. 17, pp. 5063–5073, Sep. 2014.
- [39] P. Berto, S. Grelier, and F. Peruch, “Telechelic Polybutadienes or Polyisoprenes Precursors for Recyclable Elastomeric Networks,” *Macromol. Rapid Commun.*, vol. 38, no. 22, pp. 2–7, 2017.
- [40] G. Hemery *et al.*, “Monocore vs. multicore magnetic iron oxide nanoparticles: uptake by glioblastoma cells and efficiency for magnetic hyperthermia,” *Mol. Syst. Des. Eng.*, vol. 2, no. 5, pp. 629–639, 2017.
- [41] M. Bloemen, W. Brullot, T. T. Luong, N. Geukens, A. Gils, and T. Verbiest, “Improved functionalization of oleic acid-coated iron oxide nanoparticles for biomedical applications,” *J. Nanoparticle Res.*, vol. 14, no. 9, 2012.
- [42] A. Thakur, S. Ranote, D. Kumar, K. K. Bhardwaj, R. Gupta, and G. S. Chauhan, “Synthesis of a PEGylated Dopamine Ester with Enhanced Antibacterial and Antifungal Activity,” *ACS Omega*, vol. 3, no. 7, pp. 7925–7933, Jul. 2018.
- [43] D. Ling and T. Hyeon, “Chemical Design of Biocompatible Iron Oxide Nanoparticles for Medical Applications,” *Small*, vol. 9, no. 9–10, pp. 1450–1466, 2013.
- [44] A. Ghadban *et al.*, “Bioinspired pH and magnetic responsive catechol-functionalized chitosan hydrogels with tunable elastic properties,” *Chem. Commun.*, vol. 52, no. 4, pp. 697–700, 2016.
- [45] A. F. Abdel-Magid and S. J. Mehrman, “A review on the use of sodium triacetoxyborohydride in the reductive amination of ketones and aldehydes,” *Org. Process Res. Dev.*, vol. 10, no. 5, pp. 971–1031, 2006.
- [46] A. F. Abdel-Magid, K. G. Carson, B. D. Harris, C. A. Maryanoff, and R. D. Shah, “Reductive amination of aldehydes and ketones with sodium triacetoxyborohydride. Studies on direct and indirect reductive amination procedures,” *J. Org. Chem.*, vol. 61, no. 11, pp. 3849–3862, 1996.
- [47] G. Morandi, N. Kebir, I. Campistron, F. Gohier, A. Laguerre, and J. F. Pilard, “Direct selective reductive amination of carbonyl telechelic oligoisoprenes: elaboration of promising tri- and tetrafunctionalized oligoisoprene intermediates,” *Tetrahedron Lett.*, vol. 48, no. 43, pp. 7726–7730, 2007.
- [48] A. Falamaş, A. Petran, A. M. Hada, and A. Bende, “Dopamine Photochemical Behaviour under UV Irradiation,” *Int. J. Mol. Sci.*, vol. 23, no. 10, 2022.

- [49] Z. Zhou and D. Yan, “Improved expression of the mean-square radius of gyration, 3. 1,4-polydienes,” *Macromol. Theory Simulations*, vol. 4, no. 3, pp. 459–470, 1995.
- [50] Daoud, M. and Cotton, J.P., “Star shaped polymers : a model for the conformation and its concentration dependence,” *J. Phys. Fr.*, vol. 43, no. 3, pp. 531–538, 1982.
- [51] M. I. Majeed, J. Guo, W. Yan, and B. Tan, “Preparation of magnetic iron oxide nanoparticles (MIONs) with improved saturation magnetization using multifunctional polymer ligand,” *Polymers (Basel)*, vol. 8, no. 11, pp. 1–16, 2016.

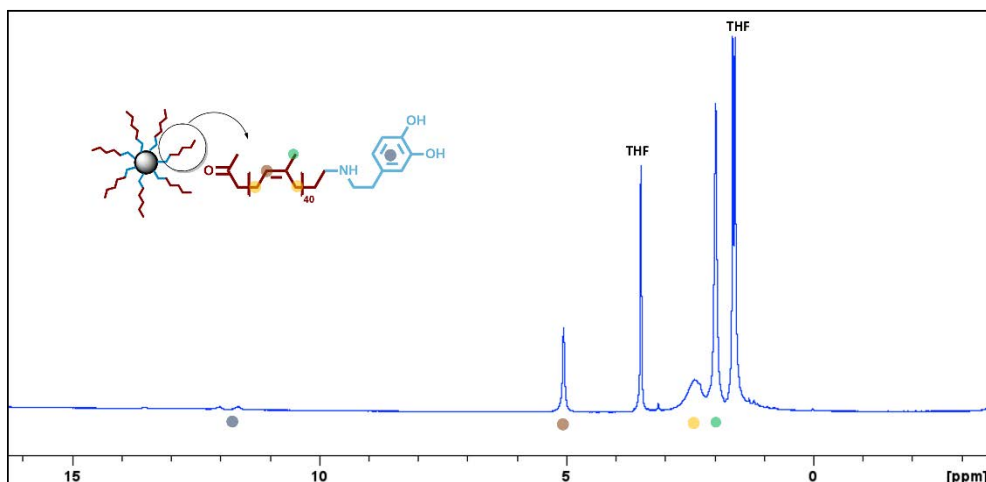
Supplementary information:

Figure S 11: MAS-ss NMR spectroscopy of IONPs-PIDOP(A) diluted in d8-THF 25x its volume.

The spectra in Figure S1 reveals the peaks of poly(isoprene) which can be clearly detected following the dilution of 25x with d8-THF. What is more we can detect the peak of the phenol group at around 12 ppm. While it is quite possible that the excess of polymer that was utilized for this sample is the reason the peak at ~2.5ppm of poly(isoprene) is so wide even if the sample is so diluted.

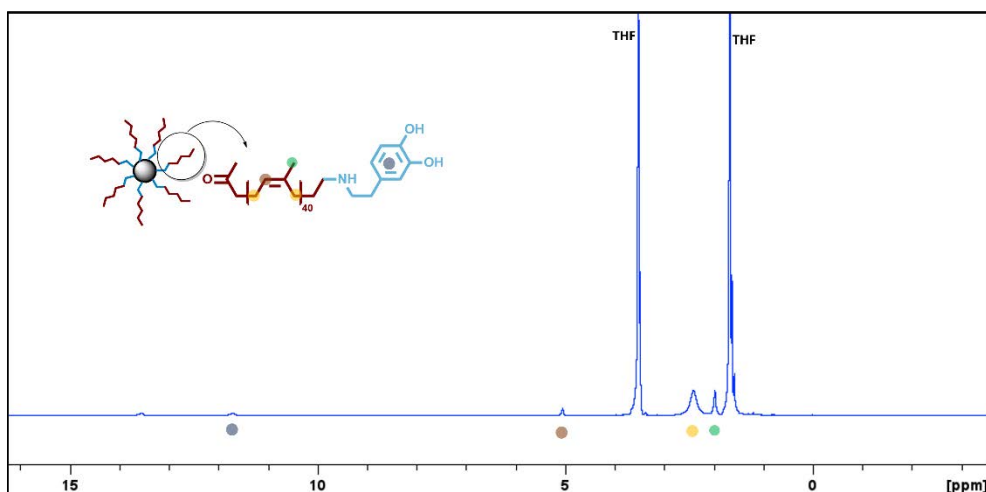


Figure S 12: MAS-ss NMR spectroscopy of IONPs-PIDOP(B) diluted in d8-THF 25x its volume.

In Figure S2 the dilution reveals a clean spectra with the peaks clearly visible and no excess of polymer, as it was expected due to the lower concentration of polymer in the synthetic route of this sample.

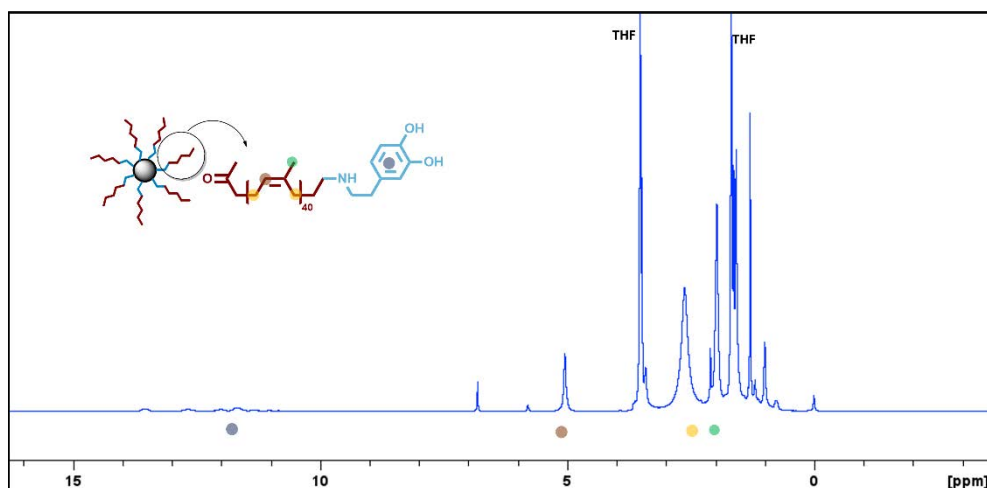


Figure S 13: MAS-ss NMR spectroscopy of IONPs-PIDOP(C) solubilized in d8-THF, no dilution.

In Figure S3 the sample IONPs-PIDOP(C) is depicted, while the proton peaks are present and can be attributed to the functionalized polymer, with no particular excess as expected, we can see some impurities both in the higher and the lower ppm. Cyclohexane may be detected at 1.44ppm as a single peak as it was the original solvent in which the IONPs batch of d=8nm were solubilized pre-ligand exchange.

**CHAPTER V: STUDY OF THE SELF-ASSEMBLY, CROSS-LINKING
UNDER UV AND ELONGATION PROCESS OF MAGNETIC
POLYMERSOMES**

Introduction:

The final step of this study consists of creating magnetic polymersomes which are capable of elongation under a static magnetic field and fixation of their anisotropic shape by membrane cross-linking under UV. In this chapter the self-assembly process will be explored both for the graft copolymers PEG₁₁₄-*b*-PATC_x-*g*-PI_y as well as the triblock copolymers PEG₁₁₄-*b*-PTMC_n-*b*-PI_m with the hydrophobically modified IONPs which were functionalized with either oleic acid or short poly(isoprene) chains. The self-assembly process was done through a fast addition of water into the solution of the polymers in a good solvent, in this case THF. The deformation of the hydrophobic membrane under a static magnetic field of 0.1, 0.2 or 0.4 T was studied, as well as the stability of the deformation after removal from the field once the membrane was cross-linked by irradiation under UV light at 365 nm wavelength.

At first, the self-assembly process of the copolymer without the addition of IONPs was studied by TEM and cryo-TEM to determine the morphology that the copolymers were capable of producing. The addition of IONPs was expected to influence the final morphology, according to literature work by Hickey *et al.*[1] who demonstrated the influence of the addition of hydrophobic iron oxide nanoparticles onto the final morphology of poly(acrylic acid)-*b*-polystyrene (PAA-*b*-PS) copolymers depending on the percentage of the IONPs in the system. Indeed, a different structure could be produced by a variation of the amount of IONPs, as they modify both the hydrophilic-to-hydrophobic ratio and the spontaneous curvature of the membrane.

Furthermore, the cross-linking of the produced morphologies was investigated by exploring the network formation of the poly(isoprene) blocks which were present in both the graft and triblock copolymer. The double bonds of the poly(isoprene) blocks were epoxidized in various amounts and the presence of the epoxides allowed for the use of a cationic photo-initiator in order to induce an epoxide ring opening reaction after UV irradiation, which would result in a network formation [2], [3]. The performance of the UV cross-linking would determine the ability of the self-assembled structures to retain an anisotropic morphology after the end of the exposure to a static magnetic field.

The final step of this chapter was the end goal of the ANR MAVERICK project, which consisted of the deformation of the magnetic polymersomes from spherical into anisotropic structures by taking advantage of the embedded iron oxide nanoparticles in the hydrophobic membrane. The magnetic polymersomes of both copolymers were exposed to a static magnetic field of 0.4T, created by a specially designed arrangement of permanent magnets (so-called “Halbach array”), to induce elongation and were further cross-linked while under the field. In theory, iron oxide nanoparticles with a magnetic moment μ are initially dispersed freely with random orientations within the restriction of being confined in the hydrophobic space of the membrane due to their hydrophobic coating. Once a static magnetic field is applied, their magnetic moments would align parallel to the direction of the magnetic field [4]. Due to the dipole-dipole interactions between the iron oxide nanoparticles, they tend to form aggregates in a

linear fashion. These linear aggregates which would be aligned in the direction of the magnetic field while being restricted in the membrane would theoretically tend to force an elongation of said membrane in the direction of the field [5]. Such experimental examples are few in the literature, which is the point that makes this research novel. One of the experimental results in literature was the work published by Long *et al.* [6] where the group studied the capacity of spherical magnetic nano capsules to transform morphologies under a static magnetic field and how it was possible to achieve controlled drug-release by controlling the elongation-relaxation cycles. The publication demonstrated that indeed it was possible to force an elongation in response to a magnetic field by embedding IONPs in the membrane of the polymeric capsules. Some of the main differences between that publication and our study are, the fact that the size of the IONPs which were utilized in that case was 600 nm, which affects their response to the magnetic field [7] while also that their study did not include the stabilization of the final elongated morphology to avoid its relaxation after removing the field.

The elongation of magnetic polymersomes was explored experimentally and depicted from SANS measurements in previous works by Lecommandoux *et al.* [8] and Sanson *et al.* [9]. Although both cases used different natures of amphiphilic block copolymers – the hydrophobic rubbery block was respectively made of polybutadiene or poly(trimethylene carbonate), while the hydrophilic block was poly(*L*-glutamic acid) instead of poly(ethylene glycol) – they presented anisotropic neutron scattering patterns under an applied magnetic field of 0.1 T, with iron oxide nanoparticles loading rates of 100% for PBut-*b*-PGA vesicles, or 70% for PTMC-*b*-PGA polymersomes.

Experimental Section:

Materials:

THF was purchased from ThermoFisher scientific (Illkirch, France), triaryl sulfonium hexafluorophosphate salts mixed in 50% propylene carbonate and Samarium (III) acetate hydrate were purchased from Sigma-Aldrich (L'Isle-d'Abeau, France). FormvarTM and carbon coated TEM 200 Mesh copper (Cu) grids were purchased from Agar Scientific.

Methods:

Self-assembly of copolymers with IONPs:

A classical nanoprecipitation and co-assembly procedure [10] for the formation of magnetic polymersomes was adjusted depending on the desired feed weight ratio (FWR %) of IONPs in the system as well as the concentration of each IONPs solution. The final polymer concentration was kept at 0.5 mg·mL⁻¹. For example, for a FWR of 70% for the IONPs solution consisting of IONPs functionalized with oleic acid the calculation for the necessary amount of good solvent, in this case THF, as well as the necessary volume of IONPs was as followed:

$$\frac{m_{\text{Fe}_2\text{O}_3(\text{g})}}{m_{\text{polymer}}(\text{g})} = 0.7 \Leftrightarrow m_{\text{Fe}_2\text{O}_3(\text{g})} = 0.7 \times m_{\text{polymer}}(\text{g}) \quad (1)$$

$$\frac{m_{\text{Fe}_2\text{O}_3(\text{g})}}{c(\text{g/L})} = V(\text{L}) \text{ of the desired IONPs' suspension} \quad (2)$$

For a final concentration of polymer 0.5 mg·mL⁻¹, 5mg of polymer needs to be solubilized in 1mL of THF before addition of 10mL of Milli-Q water. As IONPs are solubilized in THF its volume needs to be incorporated into the measurement of the 1mL THF *i.e.*, the final volume of THF is:

$$V_{\text{finalTHF}}(\text{mL}) \text{ of THF} = 1 \text{ mL} - V_{\text{IONPs}}(\text{mL}) \text{ of IONPs calculated from (2)} \quad (3)$$

In the case that the final solution is meant to be cross-linked under UV, an amount of the cationic photo-initiator is necessary to be added in the polymer when it is solubilized in THF. For a chosen concentration of photo-initiator (PhI.) of 6% w/w it was necessary to formulate a new solution of PhI. diluted in THF due to the very low necessary volume that was hard to accurately measure if the photo-initiator was not diluted beforehand. Thus, a solution of 100 µL of photo-initiator in 5 mL in THF was created with 1:50 v/v PhI.: THF and the solution was kept in a dark vial to avoid light exposure.

For a concentration of 6% w/w of PhI. relatively to the polymer, calculations were as follows:

$$0.06 \times m_{\text{Poly}} = m_{\text{Photoinitiator}} \quad (4)$$

$$\frac{m_{\text{Photoinitiator}}}{1.32\text{g/mL}} = V_1 \text{ (mL) Photo-initiator (non-diluted)} \quad (5)$$

$$\text{So the final volume of the initiator form the diluted solution was } V_{\text{final PhI}} \text{ (mL)} = V_1 \text{ (mL)} \times 50 \quad (6)$$

Finally, the final volume of THF that was used to solubilize the polymer was:

$$V_{\text{final THF}} \text{ (mL)} = 1 \text{ mL} - V_{\text{IONPs}} \text{ (mL)} - V_{\text{final PhI}} \text{ (mL)} \quad (7)$$

With V_{IONPs} (mL) being the volume calculated for the IONPs in equation (2) and $V_{\text{final PhI}}$ (mL) the volume of the photo-initiator calculated in equation (6).

In brief, a typical self-assembly process was as follows: In a vial, 5 mg of the chosen polymer was solubilized in $V_{\text{final THF}}$ (mL) of THF which was filtered with a PTFE syringe filter of 0.45 μm pore diameter. Once the polymer was well-solubilized, the volume of IONPs was added together with the calculated amount of the photo-initiator. At this stage, the solution was left to stir mechanically for 1 min to allow all the components to mix adequately. Finally, a fast addition of $10 \times V_{\text{total THF}}$ Milli-Q water was performed, while the solution was stirred via a mechanical stirrer set to enable fast stirring. The water was added manually *via* a plastic syringe while being simultaneously filtered through a cellulose filter in order to add extra pressure, which resulted in a more “chaotic” addition, *i.e.* at a higher Reynolds number, to approach conditions of “flash nanoprecipitation” [11]. The final solution was left to stir overnight to slowly evaporate the THF from the system. The final suspension was characterized by DLS, TEM, cryo-TEM, SAXS and SANS to verify the structural characteristics of the objects formed by the co-assembly in water of the block copolymers and the hydrophobically-coated IONPs.

Methods of characterization:

Transmission electron microscopy (TEM):

The observations were performed at the Bordeaux imaging center (BIC), a core facility of CNRS, Univ. Bordeaux and INSERM and of the national infrastructure “France Life Imaging” (ANR 10-INBS-04), on a Hitachi H7650 electron microscope with an accelerating voltage from 80 to 120 kV for the determination of the morphology of the self-assemblies. Two different operation modes were utilized *i.e.*, High Contrast Mode (HC) where the magnification could be set between 2000 and 200000 or High Resolution Mode (HR) which could reach higher magnification factors ranging between 4000 and 600000. The images were captured by a CCD camera SC1000 ORIUS 11Mpx (GATAN).

Dynamic light scattering (DLS):

The determination of the hydrodynamic radius (R_h) and the polydispersity (PDI) of the synthesized self-assembled solutions was performed by DLS. A VascoTM Flex instrument from Cordouan technologies (Pessac, France) was utilized for this purpose, operating at an angle of 165° (backscattering angle). The polydispersity index (PDI) of the systems was determined by a 2nd order Cumulant fit while multi-modal distribution diameters were analyzed by a multi-exponential decay (Padé-Laplace) fit [12].

Cryo-Transmission Electron Microscopy (Cryo-TEM):

Cryo-TEM was utilized to determine the morphology of copolymer self-assemblies when it was difficult to identify it by regular TEM. The experiments were performed at the laboratory of Chemistry & Biology of Membranes & Nano-objects (CBMN) by a PhD candidate of our team at the LCPO laboratory, Hannah Beuseroy. A Tecnai F20 microscope by Thermo Fischer Scientific operating at 200 kV and equipped with a Gatan 626 cryo-holder was utilized. To visualize the sample, 4 μ L aliquot of the sample was deposited on an EM grid which was coated with a perforated carbon film. A filter paper is utilized to drain the excess of sample and the grids were plunge-frozen into liquid ethane, which was cooled by liquid nitrogen using a Leica EMPC cryo-chamber by Leica Microsystems, Wetzlar, Germany. The grids were loaded onto the cryo-holder before being transferred into the microscope vacuum column. The instrument is equipped with an Eagle 2k CCD camera by FEI, USA to record the images.

Small-angle neutron scattering (SANS):

The measurements of small-angle neutron scattering (SANS) were performed at the Institute Laue–Langevin (ILL) neutron facility in Grenoble, France. The D22 – large dynamic range small-angle diffractometer was utilized to perform the measurements, in collaboration with its local contact, Dr. Lionel PORCAR (EASY-1093 proposal). The neutron wavelength was selected at $\lambda=6$ Å nm and the

beam was collimated with an aperture of 5 mm diameter on the samples. The vacuum tank contains both a large area multidetector (^3He) with a pixel size of 0.8×0.8 cm for the low q range (sample-detector distance $D=17.6$ m), and a second detector at $D = 1.40$ m for the high q range. The neutron beam was collimated through an aperture of 5 mm diameter and the wavelength was selected at 6 \AA , with two sample-detector distances of 17.6 m and 1.40 m respectively, to cover a scattering vector q -range from 2.7×10^{-3} to $6.4 \times 10^{-1} \text{ \AA}^{-1}$ (both detectors measuring simultaneously). The samples which were analyzed with this technique were self-assembled with “heavy” water D_2O and deuterated THF-d8 in order to minimize the incoherent background scattering of samples put in quartz cuvettes of 2 mm length (Thuét, France) and enhance the signal to noise ratio. Sample concentration was $0.5 \text{ mg}\cdot\text{mL}^{-1}$ of polymer in a D_2O :THF-d8 (10:1) mixture matching almost perfectly the nuclear contrast of iron oxide (see calculations further). The scattering signal was thus mostly determined by the copolymer contrast, although one cannot rule out but a contribution also of the magnetic contrast of the IONPs under an applied magnetic field, therefore control experiments of individually dispersed IONPs (without copolymers) under field were done. The acquisition of the spectra was typically performed in 5 min under zero-field to 10 min under field (5 runs of 2 min or 10 runs of 1 min to check the signal stability). The ferrofluids were measured on a longer time (4 runs of 10 min, with or without field perpendicular to beam) as they were dispersed in THF-d8 which almost contrast matched the iron oxide cores (*i.e.* nuclear contrast was very weak yet there was still the magnetic signal of the IONPs under field). Two field configurations were applied on the magnetic polymersome samples, both creating a B field intensity around 0.2 Tesla, one perpendicular to the beam created by two strong FeNdB permanent magnets put in front of each other with a spacer to place the cuvette. The other one has the field oriented parallel to the beam, as created by a Halbach array of many small permanent magnets.

Small-angle x-ray scattering (SAXS):

The measurements of small-angle x-ray scattering (SAXS) were performed at the Paul Pascal Research Center (CRPP, CNRS / Univ Bordeaux joint unit) with acknowledged help of Ahmed Bentaleb. The experiments were performed with a Xeuss 2.0 instrument by Xenocs (Grenoble, France). Data collection was performed by a DECTRIS PILATUS-300k detector which allows for an angle range $0.03^\circ - 50^\circ$ ($0.0025 \text{ \AA}^{-1} - 3.45 \text{ \AA}^{-1}$). Sample concentration was also $0.5 \text{ mg}\cdot\text{mL}^{-1}$, in pure water.

Estimation of the contrast between signals of samples and of solvent in neutron or X-ray scattering

In both SANS and SAXS, it is the difference between the scattering length density (SLD) values – usually noted ρ_{XRays} or ρ_{neutron} – of the objects compared to the SLD of solvent that determines the contrast appearing as pre-factor in the theoretical expression of the scattered intensity curves $I(q)$, where q stands for the scattering vector. In both cases, the values of ρ can be calculated by dividing the sum of

the scattering lengths (b) of each atom of the molecular formula of the compounds, dividing by the molecular V_{mol} (calculated itself from the molar volume in $\text{cm}^3 \cdot \text{mol}^{-1}$, divided by the Avogadro number). The X-ray case is the simplest as one just needs to count the number of electrons in the molecules, as they all count for the same scattering length $b_e = 2.818 \times 10^{-13} \text{ cm}$ [13]. Considering the raw chemical formulas and the mass densities (hence molar volumes) of the different copolymers block (PTMC, PI, PEO), one finds always an X-ray SLD of the polymer part around $\rho_{\text{copolymer}}^{\text{XR}} \sim 10 \pm 2 \times 10^{10} \text{ cm}^{-2}$. In comparison, with its high number of electrons (due to atomic number $Z=26$ of Fe) and its high mass density ($\sim 4.9 \text{ g} \cdot \text{cm}^{-3}$) iron oxide (be it made of $\gamma\text{-Fe}_2\text{O}_3$, Fe_3O_4 or a mixture) presents an SLD $\rho_{\text{IONP}}^{\text{XR}} \sim 40 \times 10^{10} \text{ cm}^{-2}$, which is therefore always the dominant term of contrast in SAXS compared to the SLD of the aqueous solvent ($\rho_{\text{water}}^{\text{XR}} = 9.4 \times 10^{10} \text{ cm}^{-2}$).

The contrast of SANS is a bit more complex [14], as it originates from different origins: on the one hand the nuclear contrast arises from the nature of the atoms (with no correlation with their number of electrons, Z), which itself divides into coherent scattering length b_{coh} and incoherent b_{incoh} , which is particularly high for H atom and contributes only in absorption and incoherent background, *i.e.* not related to the morphology – aka “form factor” – and interactions *i.e.* “structure factor” of the scattering objects); on the other hand, the neutrons are nuclear particles with non-integer spin 1/2, which render them sensitive to magnetic fields.

In practice, the magnetic SLD of a superparamagnetic material like iron oxide is obtained directly from its saturation magnetization, which is nothing less than the volume density of magnetic moments, taking into account that one Bohr magneton, the elementary quantum of magnetic moment of one unpaired electron in d-orbital $\mu_B = 9.274 \times 10^{-24} \text{ J/T}$ ($= \text{A} \cdot \text{m}^2$) counts for $b_{\mu_B} = 2.7 \times 10^{-13} \text{ cm}$ [15]. In the case of IONPs used in this work, they bear values of mass saturation magnetization m_{sat} between $56 \text{ A} \cdot \text{kg} \cdot \text{m}^{-1}$ (for those synthesized by aqueous coprecipitation) and $70 \text{ A} \cdot \text{kg} \cdot \text{m}^{-1}$ (for those obtained by the polyol route that possess less defects in their crystalline structure) [16], corresponding to $2.8 \times 10^5 \text{ A} \cdot \text{m}^{-1}$ to $3.5 \times 10^5 \text{ A} \cdot \text{m}^{-1}$ in volume magnetization or equivalently from 30 to $38 \mu_B/\text{nm}^3$. The magnetic SLD of the IONPs (equal to the contrast because water has no magnetic property) is thus estimated in the range $\rho_{\text{IONP}}^{\text{magnetic}} \sim 9.5 \pm 1.5 \times 10^9 \text{ cm}^{-2}$. In comparison, the nuclear SLD of iron oxide (calculated from neutron scattering lengths $b_{\text{Fe}} = 9.45 \times 10^{-13} \text{ cm}$ and $b_{\text{O}} = 5.80 \times 10^{-13} \text{ cm}$ with molecular volume $V_{\text{mol}} = 5.3 \times 10^{-23} \text{ cm}^3$ for $\gamma\text{-Fe}_2\text{O}_3$) is $\rho_{\text{IONP}}^{\text{nuclear}} = 7.0 \times 10^{10} \text{ cm}^{-2}$ [17]. As a consequence, we can deduce that the magnetic scattering of iron oxide is a minor contribution to the total SANS signal, except when the IONPs are dispersed in a fully deuterated solvent which can compensate almost (but not entirely) the nuclear SLD of $\gamma\text{-Fe}_2\text{O}_3$ with their high SLD values: $\rho_{\text{D}_2\text{O}} = 6.4 \times 10^{10} \text{ cm}^{-2}$ and $\rho_{\text{d}_8\text{-THF}} = 6.4 \times 10^{10} \text{ cm}^{-2}$ (and hence their mixtures) [18].

Finally, we estimated also the nuclear SLD of the different polymers composing the block copolymers in this study from their chemical formulas and their tabulated mass densities: $\rho_{\text{polyisoprene}} = 2.4 \times 10^9 \text{ cm}^{-2}$, $\rho_{\text{PTMC}} = 1.69 \times 10^{10} \text{ cm}^{-2}$ (in its crystalline form, otherwise a bit lower), $\rho_{\text{PEO}} = 6.4 \times 10^9 \text{ cm}^{-2}$, which is close to the hydrophobic copolymer block PATC-*g*-PI_{n=5}, $\rho_{\text{PATC-co-PI}} = 8.4 \times 10^9 \text{ cm}^{-2}$. However, it is usually accepted that PEO blocks do not contribute to the contrast of block copolymers in SANS, as they are highly hydrated, therefore their SLD is much closer to the solvent SLD than calculated in the dry state. In conclusion, the contrast in fully deuterated solvent D₂O:d8-THF (10:1) arises both from the nuclear SLD of block copolymer membranes ($\Delta\rho = (6.40 - 0.84) \times 10^{10} = 5.56 \times 10^{10} \text{ cm}^{-2}$ for the grafted copolymers and $\Delta\rho = (6.40 - 1.69) \times 10^{10} = 4.71 \times 10^{10} \text{ cm}^{-2}$ for the linear terpolymers), and from the magnetic signal of the iron oxide NPs ($\Delta\rho = (6.40 - 0.95) \times 10^{10} = 5.45 \times 10^{10} \text{ cm}^{-2}$). In other words, in SANS experiments in fully deuterated solvent mixture the neutrons “see” all the components of the objects as an approximately homogeneous material, not only the IONPs which have higher electron density like for the X-rays. This is why also in the following part when we present the SANS results of magnetic polymersomes under an applied magnetic field, we will also show the control experiment of the individually dispersed hydrophobically coated IONPs in the same deuterated solvent mixture D₂O:d8-THF (10:1) to check that possible magnetic field effect on the neutron scattering pattern does not arise from the magnetic contrast of the superparamagnetic IONPs themselves.

Results and discussion:

Study of the self-assembly of graft copolymers PEG₁₁₄-*b*-(PATC-*g*-PI_x)_n-*co*-PATC_m

The graft copolymers PEG₁₁₄-*b*-(PATC-*g*-PI_x)_n-*co*-PATC_m whose synthesis and characterization were described in Chapter 2 were further self-assembled with IONPs in the hope of creating magnetic polymersomes. As already mentioned in Chapter 2 an important parameter is the hydrophilic ratio f_{PEG} , which depicts the fraction of molar mass of the hydrophilic block divided by the total molar mass of the blocks of the copolymer:

$$f_{\text{PEG}} = \frac{M_n \text{ hydrophilic block}}{M_n \text{ hydrophilic block} + M_n \text{ hydrophobic block}} \quad (8)$$

This ratio is a critical parameter which can predict the final morphology of a copolymer post its self-assembly process. While it is a good indicator, it is not always accurate since many parameters can intertwine such as the chemical nature or physical state (e.g. rod-like or semi-crystalline) of the blocks as well as the architecture of the copolymers.

In our case, the graft copolymers synthesized in this study exhibit a quite high hydrophilic ratio f_{PEG} considering that a vesicular structure can only be achieved when $20\% < f_{\text{PEG}} < 40\%$. Indeed, the graft copolymer PEG₁₁₄-*b*-(PATC-*g*-PI₃)₁₅-*co*-PATC₅ (G3) has an f_{PEG} of 48%, which lays a bit over the limit for vesicular morphology and falls closer to the range of cylindrical micelles. Such a ratio is a lot higher than the classical $f_{\text{PEG}} < 20\%$ which is usually the aim for poly(trimethylene carbonate) (PTMC) as the hydrophobic block. The graft copolymers do not consist of PTMC but rather of a “PTMC-like” block, poly(amino trimethylene carbonate) (PATC) whose self-assembly process has not been studied yet in literature. While these two polymers look similar, in particular regarding their rubbery (low T_g) state, and it could be assumed that PATC would act as PTMC during self-assembly, yet it might be wrong to ignore the presence of a functional side group of strongly hydrophobic chemical nature such as PI, which could strongly affect the interactions between the chains, and the repulsions with water, in other words the interfacial tension with the solvent, which is known as a strong driving force for self-assembly.

Furthermore, the graft copolymers have two hydrophobic components: PATC, and the poly(isoprene) (PI) oligomers grafted onto it. Poly(isoprene) being a diene polymer allows for the increase of the f_{PEG} allowed for the formation of vesicles according to literature on the self-assembly for diene systems such as PEO-*b*-polybutadiene. Nonetheless, the attached PI has a very small molar mass $340 \text{ g} \cdot \text{mol}^{-1} < M_n < 540 \text{ g} \cdot \text{mol}^{-1}$, deeming it an oligomer another parameter which could affect the self-assembly. Another graft copolymer system studied is PEG₁₁₄-*b*-PATC₂₀-*g*-PI₅ (G4), exhibiting lower hydrophilic ratio of 33%, which falls into the limits of vesicles by the conventional theory for diene systems [19]. Recent theoretical models by Borisov *et al.* [20-21] of the self-assembly of bottlebrush and comb-like

copolymers also indicate that such grafted macromolecular structures self-assemblies exhibit micelle-vesicle phase diagram close to the one of linear block copolymers.

Self-assembly of graft copolymers $\text{PEG}_{114}\text{-}b\text{-(PATC-}g\text{-PI}_x\text{)}_n\text{-}co\text{-PATC}_m$ a TEM study:

To study the resulting morphology of the graft copolymers they were first self-assembled without the addition of magnetic nanoparticles. The chosen final concentration of polymer in solution was $0.5 \text{ mg}\cdot\text{mL}^{-1}$ to keep this parameter stable with the samples that would include the IONPs.

The morphology of the structures was studied by TEM and a variety of morphologies were observed for both $\text{PEG}_{114}\text{-}b\text{-(PATC-}g\text{-PI}_3\text{)}_{15}\text{-}co\text{-PATC}_5$ (G3) and $\text{PEG}_{114}\text{-}b\text{-PATC}_{20}\text{-}g\text{-PI}_5$ (G4). Firstly, G3 was not clearly distinguished by TEM with some spherical objects predominantly appearing without a clear visibility of the structure. Thus, the sample was further analyzed by cryo-TEM in hopes that we could detect the morphology (Image 2: a-b) cryo-TEM image of $\text{PEG}_{114}\text{-}b\text{-(PATC-}g\text{-PI}_3\text{)}_{15}\text{-}co\text{-PATC}_5$ (G3) depicting small micelles (green arrows) and larger vesicles (red arrows)). As can be seen from Image 2, spherical structures were captured that resembled micelles and had a small diameter, while vesicles were also apparent with a higher diameter but a lower probability of appearance.

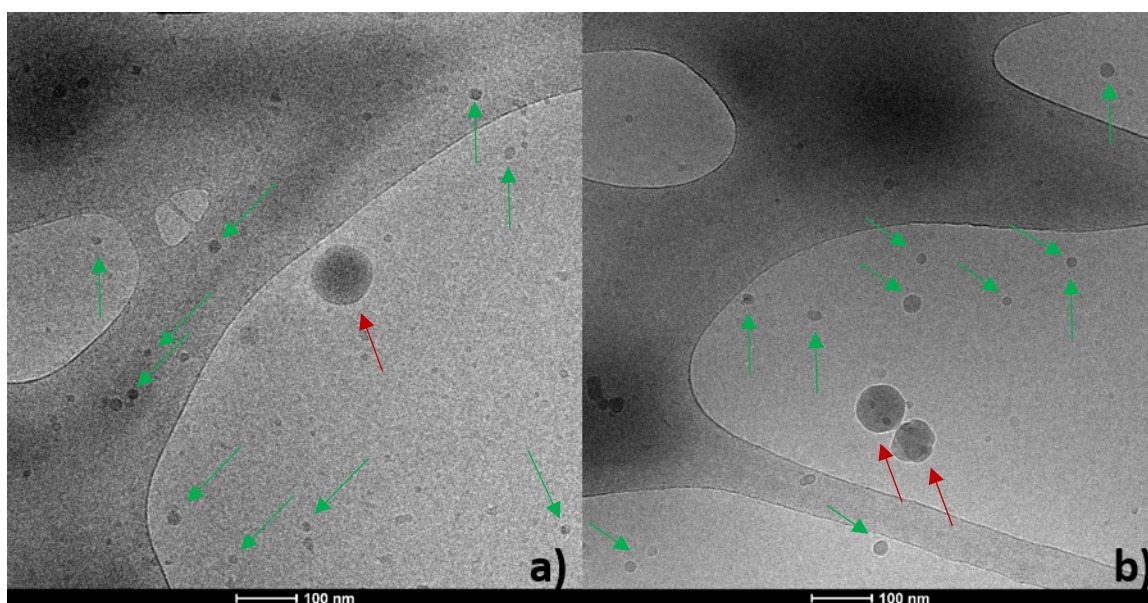


Image 2: a-b) cryo-TEM image of $\text{PEG}_{114}\text{-}b\text{-(PATC-}g\text{-PI}_3\text{)}_{15}\text{-}co\text{-PATC}_5$ (G3) depicting small micelles (green arrows) and larger vesicles (red arrows).

In order to clarify the structures, the polymer was self-assembled along with 3% w/w of the cationic photo-initiator to achieve poly(isoprene) network formation, making it denser to the electrons and perhaps more visible after imaging. After 30 min of UV irradiation, the small spherical micelles which were predominantly apparent were arranged in large aggregates forming “necklace-like” structures, along with some isolated vesicles (Image 3) as those observed in cryo-TEM imaging (Image 2).

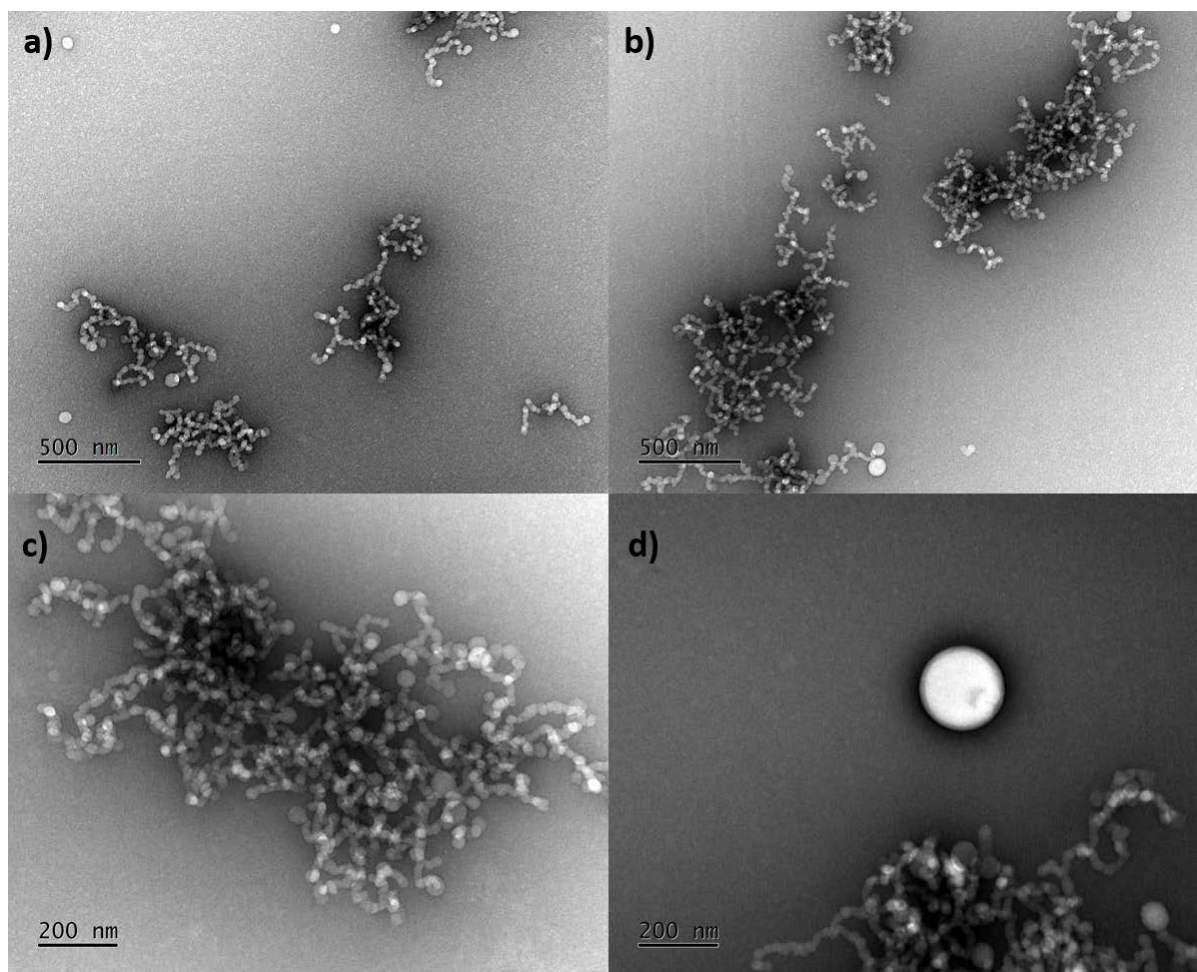


Image 3: a-d) TEM image of PEG₁₁₄-*b*-(PATC-*g*-PI₄)₂₀-*co*-PATC₁₁ (G5) after UV irradiation stained with 2% samarium acetate.

Self-assembly of graft copolymers with hydrophobically-coated IONPs:

After verification that the graft copolymer is capable of self-assembly into tangible structures, the process of adding magnetic nanoparticles was explored. While the structures that were seen during the self-assembly of the copolymers alone suggested that vesicles were not the predominant structures, it was assumed that the addition of magnetic nanoparticles would alter modify the self-assembly process by pushing it towards polymersomes. After all such a concept had already been explored by Hickey et al.[1], who demonstrated the shift of morphologies from micelles to magnetic polymersomes, between the self-assembled PAA₃₈-*b*-PS₇₃ diblock copolymer alone and its morphology following the co-self-assembly with oleic acid functionalized IONPs. Specifically, the publication showed the dependency of mass percentage of magnetic nanoparticles on the resulting morphologies. Such a concept was thus followed here as well, by testing various feed weight ratios (FWR) both to produce polymersomes (Image 4) but also to make them responsive to a magnetic field.

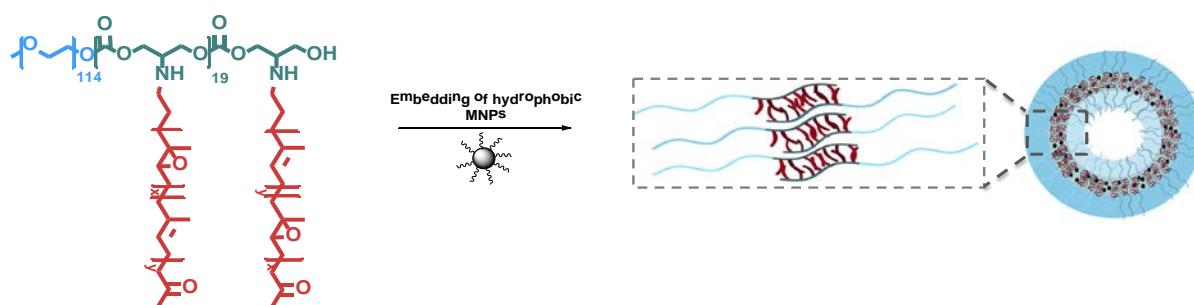


Image 4: Schematic self-assembly process between a graft copolymer and hydrophobic IONPs producing magnetic polymersomes. The FWR is defined as the weight of iron oxide relatively to the weight of copolymer in the feed.

It was possible to confirm the assumption that the addition of hydrophobically coated magnetic NPs would indeed change the final morphology. Various feed weight ratios of IONPs were studied with the graft copolymers. A significant differentiation of the distribution of magnetic NPs within the structures was observed depending on the type of surface functionalization. For example, the IONPs-PIDOP – *i.e.* those bearing short PI chains tethered to their surface through a dopamine anchor (see Chapter IV) – seemed to be dispersed more freely in the membrane with less aggregation present when compared to oleic acid functionalization. This could be attributed to the interactions between the polymers, since the hydrophobic membrane of the graft copolymers has a higher percentage of poly(isoprene). Furthermore, the vesicles seem to be fuller when IONPs-PIDOP were involved suggesting a higher loading capacity of nanoparticles perhaps again due to the better interactions of the PI oligomer tethered to IONPs through a catechol ligand with the copolymer chains.

At first, a 20% FWR of IONPs-PIDOP (D) was tested for self-assembly with a graft copolymer. The morphology as indicated by TEM imaging remained spherical, with a particular propensity to vesicles for the bigger structures (as deduced from a grey corona around them, ascribed to be their membrane) and some magneto-core micelles with a smaller diameter (Image 5).

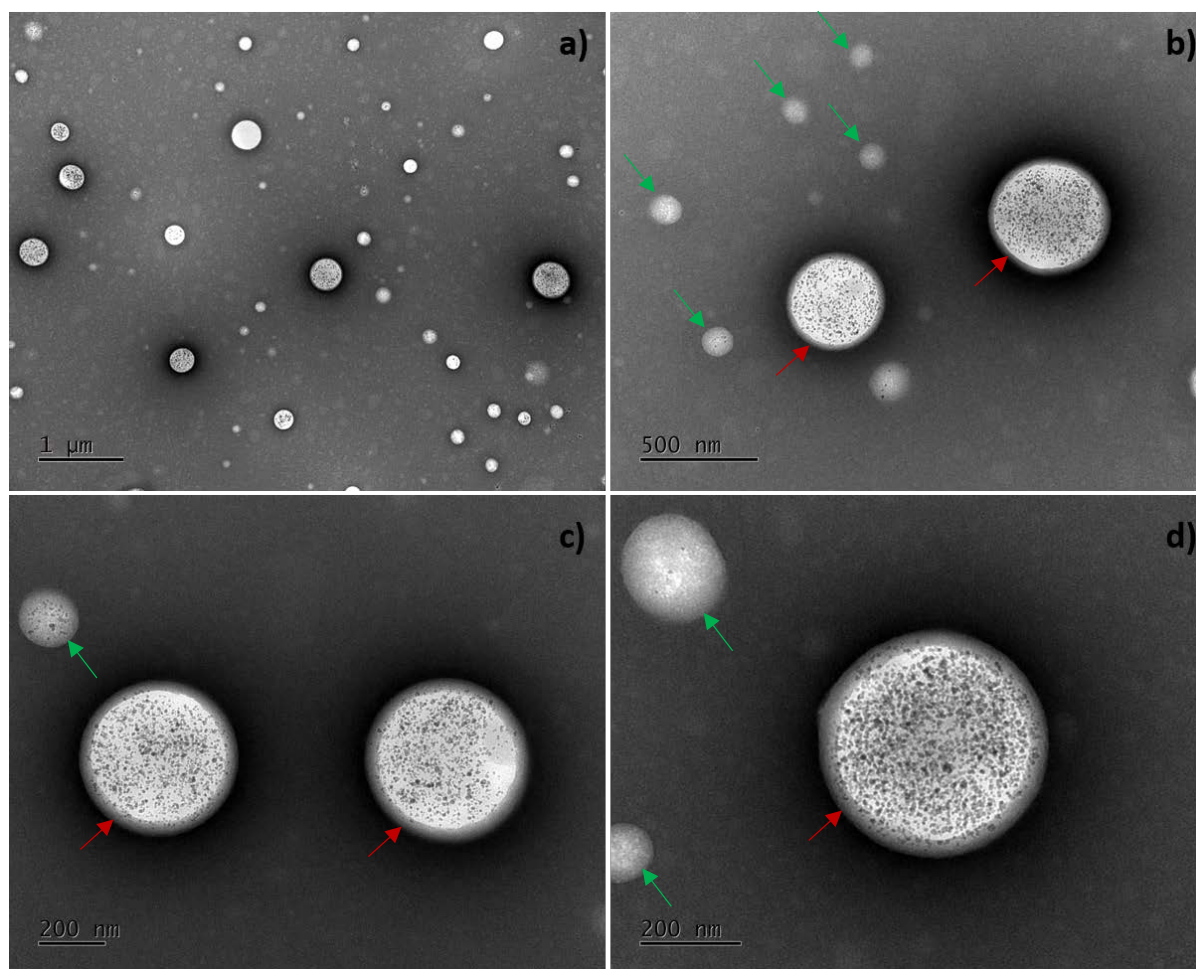


Image 5: a-d) TEM image of PEG₁₁₄-*b*-(PATC-*g*-PI₄)₂₀-*co*-PATC₁₁ (G5) with IONPs-PIDOP (D) FWR=20% stained with 2% samarium acetate showing a mix of micellar (green arrows) and vesicular (red arrows) self-assemblies.

The polymersomes can be distinguished by the visible distribution of magnetic nanoparticles onto the external surface and not in the core of the formed structures. The size of the objects depicted in TEM display a higher diameter than the one calculated by DLS (Table 17) which could be attributed to the deposition and spreading of the structures onto the grid, which is coated by a thin carbon layer and thus hydrophobic. The IONP-PIDOP (D) are functionalized with a low molar mass PI of 1320 g·mol⁻¹, and they appear to be dispersed nicely in the membrane with no aggregates, but the vesicles are obviously not fully packed with IONPs. Thus, further increase of the FWR was tried to see the effect.

For a higher FWR of 30% IONPs, it was possible to detect more vesicular structures but with some micelles present as well. Image 6 presents the graft copolymer which is self-assembled with 30% FWR of IONPs functionalized with poly(isoprene) whose characteristics can be found in Chapter 4. The poly(isoprene) which was used for their functionalization had a molar mass $M_n = 2720$ g·mol⁻¹ which was higher than the molar mass of the poly(isoprene) grafted onto the chains of the graft copolymer by almost 8 times. As can be observed, the final morphology post self-assembly shifts to vesicles of bigger size than the one which was observed for the graft copolymer alone as well as a lower polydispersity

index, as can be seen in Table 17. The morphology again can be attributed to vesicles due to the surface distribution of the IONPs on the exterior membrane for the bigger structures.

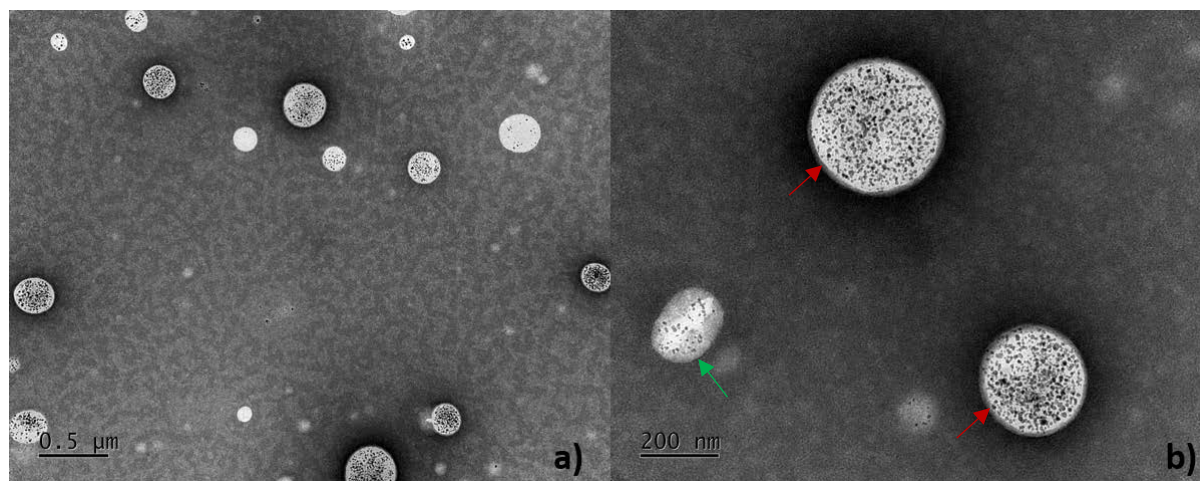


Image 6: TEM image of PEG₁₁₄-*b*-(PATC-*g*-PI₃)₁₅-*co*-PATC₅ (G3) with IONPs-PIDOP (A) FWR=30% stained with 2% samarium acetate, showing micelles (green arrows) and larger vesicles (red arrows).

Table 17 : Characteristics of self-assembled samples with IONPs-PIDOP observed in DLS.

Sample	Diameter (nm)*		z-average (nm) [‡]	PDI [‡]
PEG ₁₁₄ - <i>b</i> -(PATC- <i>g</i> -PI ₃) ₁₅ - <i>co</i> -PATC ₅ (G3)	51 (16%)	301 (78%)	205	0.28
PEG ₁₁₄ - <i>b</i> -(PATC- <i>g</i> -PI ₄) ₂₀ - <i>co</i> -PATC ₁₁ (G5) + 20% FWR IONPs-PIDOP(D)	175 (92%)		166	0.25
PEG ₁₁₄ - <i>b</i> -(PATC- <i>g</i> -PI ₃) ₁₅ - <i>co</i> -PATC ₅ (G3) + 30% FWR IONPs-PIDOP(A)	157 (94%)		157	0.19
PEG ₁₁₄ - <i>b</i> -(PATC- <i>g</i> -PI ₃) ₁₅ - <i>co</i> -PATC ₅ (G3) + 70% FWR IONPs-PIDOP(D)	257 (91%)		269	0.26
PEG ₁₁₄ - <i>b</i> -PATC ₂₀ - <i>g</i> -PI ₅ (G4) + 70% FWR IONPs-PIDOP(D) [†]	196 (82%)		226	0.21

* by Padé-Laplace (multimodal) fit of auto-correlogram (percentage indicates the weight of the mode); [‡] by 2nd order cumulants fit; [†] after UV crosslinking under 0.4 T magnetic field.

An increase of FWR during the self-assembly process up to 70% and using the IONP-PIDOP (7) with a smaller poly(isoprene) molar mass inevitably increased the size of the final polymersomes but provided a lower control in the final structures over the size of the final morphologies and a presence of multiple structures including bigger vesicles and micelles. While the increase in size can be ascribed to a higher amount of IONPs in the feed, perhaps the presence of a smaller size poly(isoprene) on the IONP surface affected the self-assembly in a negative way as regard to the final morphologies. The TEM image presented here depicting this sample is taken post cross-linking and magnetic field (MF) application due to a better visibility of the sample thanks to the cross-linking process, as discussed further in the chapter (Image 7). The larger magnetic polymersomes are quite visible and the IONPs are spread over the exterior membrane, confirming the vesicular morphology with smaller objects being observable as well.

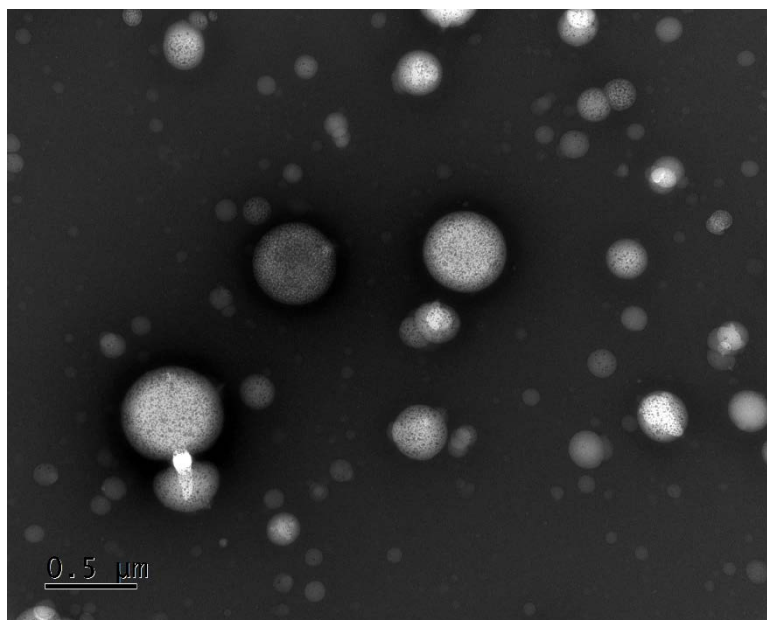


Image 7: TEM image of PEG₁₁₄-*b*-(PATC-*g*-PI₃)₁₅-*co*-PATC₅ (G3) self-assembled with 70% FWR IONPs-PIDOP (D) post UV cross-linking and MF application. Several objects appear close and likely attached to each other.

To study the effect of the IONPs ligand nature, the self-assembly process was investigated with IONPs functionalized by oleic acid as well. A FWR 10% of IONPs, from the Caruntu *et al.*[22] 2004 synthetic method (polyol route), post-functionalized with oleic acid was tested for self-assembly. When combined with a graft copolymer PEG₁₁₄-*b*-(PATC-*g*-PI₄)₂₀-*co*-PATC₁₁ (G5), they resulted in spherical structures that appear to be magnetic polymersomes, with densely hexagonally packed IONPs in their membranes (Image 8).

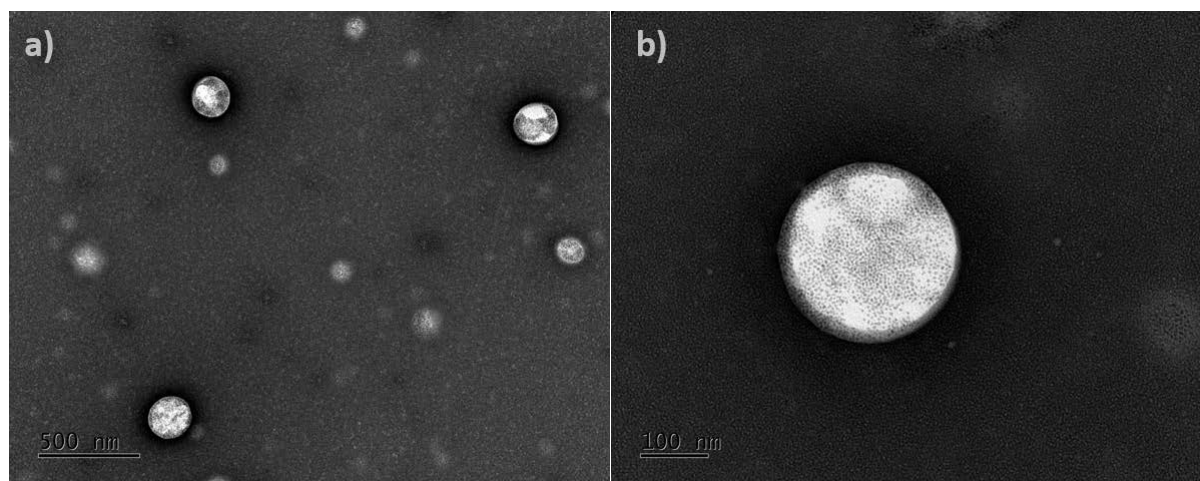


Image 8: a-b) TEM image of PEG₁₁₄-*b*-(PATC₃₁-*g*-PI₄)₃₁ (G5) self-assembled with 10% FWR IONPs-OA (Caruntu synthesis, of ~6 nm core sizes, coated by oleic acid) stained with 2% samarium acetate.

The vesicles seem controlled in size, and close to the sizes detected by DLS (Table 2). The IONPs appear to be on the exterior membrane of the structures, verifying the polymersome morphology. Increasing the FWR of the magnetic NPs up to 70% led to the same result as it was observed above, with the size of the final morphologies increasing both in DLS and TEM characterizations (Image 9). The resulted structures resembled polymersomes which were tightly packed together, like in a foam, with IONPs with a good control over the final size yet with some bigger structures appearing as well.

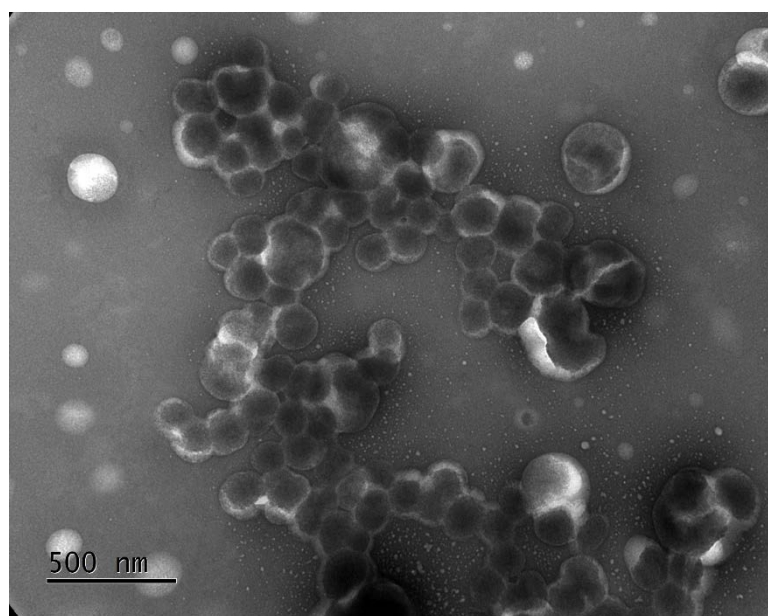


Image 9: TEM image of PEG₁₁₄-*b*-PATC₂₀-*g*-PI₅ (G4) self-assembled with 70% FWR IONPs-OA (Caruntu synthesis, of ~6 nm core sizes, coated by oleic acid) stained with 2% samarium acetate.

Table 18: Characteristics of self-assembled samples with IONPs-OA (Caruntu synthesis of ~6 nm cores) observed in DLS.

Sample	Diameter (nm)*	z-average (nm) [‡]	PDI [‡]
PEG₁₁₄-<i>b</i>-(PATC-<i>g</i>-PI₄)₂₀-<i>co</i>-PATC₁₁ (G5) + 10% FWR IONPs-OA (Caruntu)	158 (88%)	145	0.19
PEG₁₁₄-<i>b</i>-(PATC-<i>g</i>-PI₄)₂₀-<i>co</i>-PATC₁₁ (G5) + 20% FWR IONPs-OA (Caruntu)	178 (94%)	165	0.2
PEG₁₁₄-<i>b</i>-PATC₂₀-<i>g</i>-PI₅ (G4) + 70% FWR IONPs-OA (Caruntu)	250 (94%)	255	0.15

* by Padé-Laplace (multimodal) fit of auto-correlogram (percentage indicates the weight of the mode); [‡] by 2nd order cumulants fit.

All the samples that appear in the table above loaded with oleic acid coated IONPs were self-assembled using smaller magnetic NPs, with a core diameter of 6 nm whose synthesis (so-called Caruntu polyol route) was described in Chapter IV. In order to see how the size of the magnetic NPs embedded affects the structures, self-assemblies with some larger IONPs-OA were attempted, with a core size of 8 nm, synthesized by the aqueous coprecipitation method followed by a size sorting process based on multiple phase-separation induced by ionic strength (see Chapter IV). This larger size of nanoparticles revealed to lead to a less controlled self-assembly. The copolymers indeed form spherical structures that could be attributed as vesicles or magnetic core micelles, whose exact morphology became more apparent on TEM images after UV cross-linking.

A difference between a variety of FWRs was observed as well, from 10% which revealed well-packed structures, to 20% that clearly resulted in vesicles but not-fully packed with IONPs, and aggregation effect inside the membrane was observed. Furthermore, a FWR of 50% resulted in a mixture of final structures, with micelles being more present than vesicles while a 70% FWR did not allow for fully packed structures, with vesicles being present still. It is possible to assume that this size of IONPs was too large for this graft copolymer to incorporate a higher volume fraction, thus a loss of control in self-assembly along with a non-full incorporation of all the IONPs initially present in solution was observed (Image 10), in accordance with previous work by Oliveira *et al.* [10] on the self-assembly of other amphiphilic copolymers (PTMC-*b*-PGA and PEG-*b*-PBLG) with surfactant-coated IONPs of either 6 or 8 nm diameters.

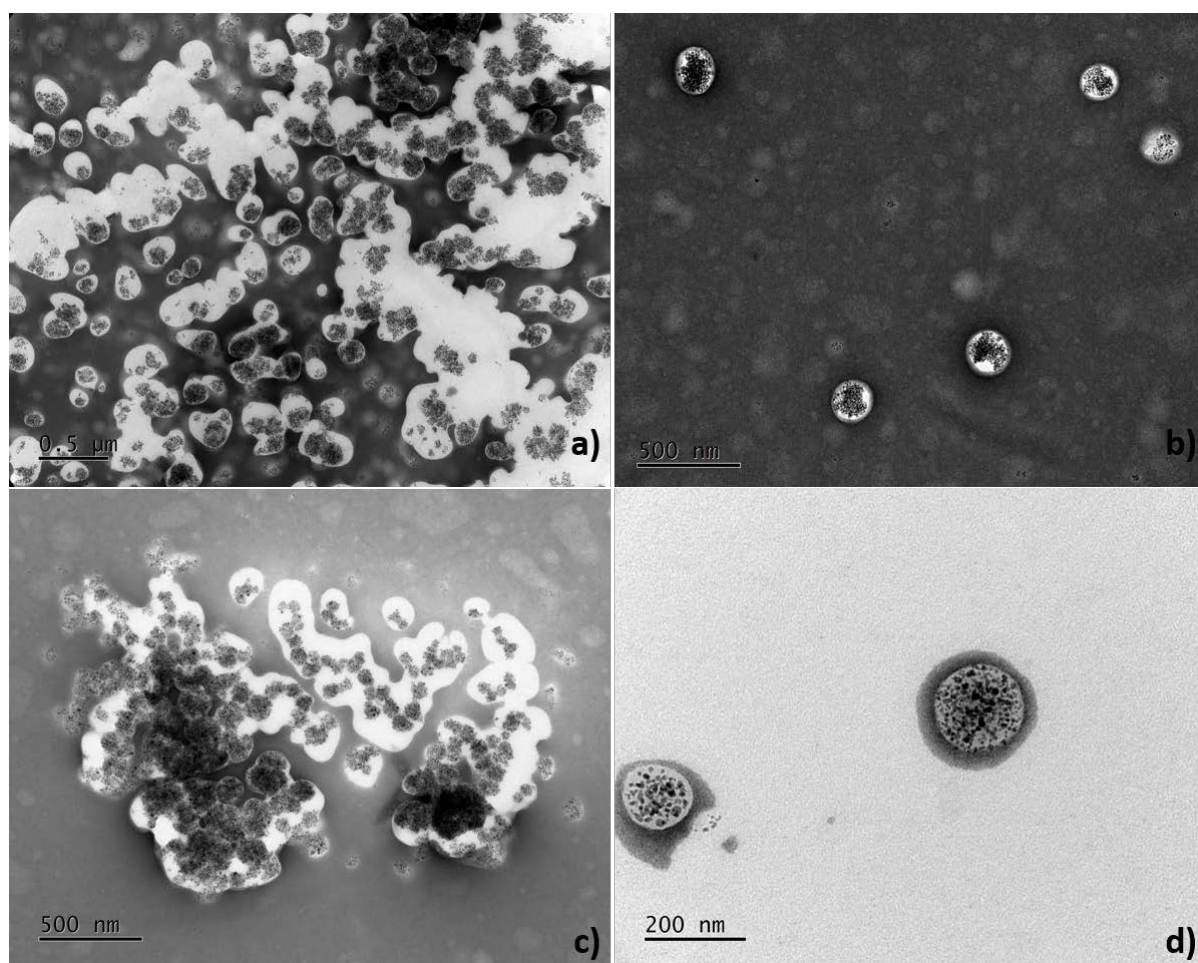


Image 10: TEM images of a) $\text{PEG}_{114}\text{-}b\text{-(PATC-g-PI}_4\text{)}_{20}\text{-co-PATC}_{11}$ (G5) + 10% FWR IONPs-OA, b) $\text{PEG}_{114}\text{-}b\text{-(PATC-g-PI}_4\text{)}_{20}\text{-co-PATC}_{11}$ (G5) + 20% FWR IONPs-OA, c) $\text{PEG}_{114}\text{-}b\text{-PATC}_{20}\text{-g-PI}_5$ (G4) + 50% FWR IONPs-OA and $\text{PEG}_{114}\text{-}b\text{-PATC}_{20}\text{-g-PI}_5$ (G4) + 70% FWR IONPs-OA stained with 2% samarium acetate. The IONPs-OA used here have ~8 nm core sizes.

Table 19: Characteristics of self-assembled samples with IONPs-OA of ~8 nm core sizes observed in DLS.

Sample	Diameter (nm)*		Z-average (nm) [‡]	PDI [‡]
$\text{PEG}_{114}\text{-}b\text{-(PATC-g-PI}_4\text{)}_{20}\text{-co-PATC}_{11}$ (G5) + 10% FWR IONPs-OA	146 (97%)		136	0.18
$\text{PEG}_{114}\text{-}b\text{-(PATC-g-PI}_4\text{)}_{20}\text{-co-PATC}_{11}$ (G5) + 20% FWR IONPs-OA	30 (3%)	176 (97%)	165	0.19
$\text{PEG}_{114}\text{-}b\text{-(PATC-g-PI}_4\text{)}_{20}\text{-co-PATC}_{11}$ (G5) + 50% FWR IONPs-OA	144 (33%)	312 (66%)	218	0.14

* by Padé-Laplace (multimodal) fit of auto-correlogram (percentage indicates the weight of the mode); [‡] by 2nd order cumulants fit.

To conclude on this part of the chapter, it was possible to study the self-assembly process of the various graft copolymers that were synthesized (Chapter II), both with and without the presence of iron oxide NPs in the feed. The graft copolymers alone tended to self-assemble into small micelles with some vesicles present as well. This was expected due to the high hydrophilic ratio which was higher than 30% and was expected to form either vesicles $25\% < f < 40\%$ or cylindrical micelles $40\% < f < 50\%$ if we consider the literature published. What was observed was both expected and not, the graft copolymer PEG₁₁₄-*b*-(PATC-*g*-PI₄)₂₀-*co*-PATC₁₁ (G5) which had an $f_{\text{PEG}}=34\%$ appeared to form mostly small micelles with some vesicles present as well even, although it was in the vesicle forming range according to Disher *et al.* [23] publications for polydiene systems. But if we take into account publications on polyester block (polylactide or polylactone) copolymer systems [24]–[27] the necessary f_{PEG} in order to form vesicles should be lower *i.e.* $< 25\%$ and since one of the blocks involved in the synthesis of the hydrophobic membrane is the PATC polymer, which is in practice a modified poly(trimethylene carbonate) polymer, it was also expected that this would affect the self-assembly by lowering the necessary hydrophilic ratio. Of course, the other block of the hydrophobic membrane is poly(isoprene), which is a diene polymer and was expected to affect the assembly more due to its higher ratio in the system, but perhaps due to the fact that even if the total mass of poly(isoprene) was higher, each grafted chain was small, as an oligomer of poly(isoprene), $340 \text{ g}\cdot\text{mol}^{-1}$, was grafted each time. Thus, it can be concluded that when the polymer was assembled alone with no nanoparticles, the PATC backbone of the hydrophobic block played a bigger role than the PI grafts in influencing the final morphology.

On the other hand, the graft copolymer PEG₁₁₄-*b*-PATC₂₀-*g*-PI₅ (G4) which had similar $f_{\text{PEG}}= 33\%$ formed larger spherical structures, resembling polymersomes, and this could be attributed to the smaller degree of polymerization of the PATC block which perhaps affected less the final morphology and allowed for the poly(isoprene) graft quantity to be a more influencing parameter.

The addition of iron oxide NPs which were modified beforehand with hydrophobic ligands allowed their incorporation into the hydrophobic membrane of the copolymers and shifted the self-assembly into larger structures which appeared like vesicles, each time depending on the hydrophobic ligand used to coat the IONP surface. The feed weight ratio (FWR) of IONPs highly affected the self-assembly as well, even though it was possible to observe that even a FWR of 10% was enough to shift the morphology towards clearly recognized vesicles, while higher FWR appeared problematic if larger core IONPs were used, as observed in Image 10.

Study of the Cross-linking process of the hydrophobic membrane:

After studying the morphology of the self-assembled structures that can be formed between the graft copolymers and IONPs the next step was to investigate whether it was possible to cross-link the hydrophobic membrane after the self-assembly process. In our study the method of cross-linking that was chosen was to use a cationic photo-initiator which would be assembled along with the graft copolymers and IONPs for it to be incorporated into the hydrophobic membrane. The cationic photo-initiator (P.I.) which was chosen for these experiments was triaryl sulfonium hexafluorophosphate salts mixed in 50% propylene carbonate solvent, which was capable of being activated by UV [2-3] (Figure 108).

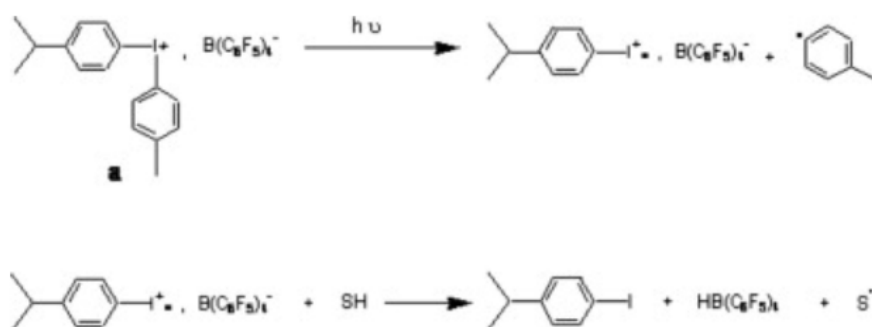


Figure 108: Reaction scheme of the activation of the cationic photo-initiator by UV treatment. From Decker *et al.*[2], [3].

The P.I. is activated under UV at a 300 nm wavelength by producing an acid which in turn is capable to act as ring opening agent of the epoxides that are present on the epoxidized poly(isoprene) block of the graft copolymers. This epoxide ring opening mechanism creates a network between the epoxide rings that are in close proximity upon each other (Figure 109).

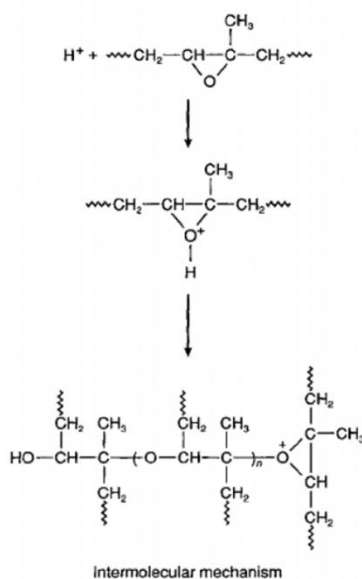


Figure 109: Network formation by cross-linking under UV treatment *via* a ring opening mechanism of the epoxides. From Decker *et al.*[2], [3].

To test whether our graft copolymers are responsive to this type of cross-linking, the reaction was first studied by ^1H NMR spectroscopy. A 3% w/w amount of the photo-initiator was added in a ^1H NMR tube along with the solubilized polymer in CDCl_3 . The tube was exposed to UV *via* the use of a Hamamatsu LC8 LightningcureTM UV lamp (model L9588-02A) with a broad-band filter (ref A9616-03) selecting the 280-400 nm wavelength range and 55% power. At full power, the lamp irradiates more than 500 mW from our measurement with a photodiode (ThorLabs S120VC), but the exact irradiance (mW/cm^2) on the sample depends on the sample-fiber distance and on the outer diameter of either 3.5 or 5 mm of the fused silica guiding fiber used (A10014-35 or -50), as we used either one or the other depending if we needed to irradiate an NMR tube of 5 mm diameter, a capillary of 3 mm, or a quartz cuvette of 10 mm width.

To verify the ring opening of the epoxides, the samples were irradiated for 2 rounds of 5 min each round. The disappearance of the epoxide peaks at 2.7 ppm which corresponded to protons on the carbon bearing the epoxide ring and the shift of the peak initially at 1.3 ppm which corresponded to the methyl group on the epoxide ring were observed after each round. It was obvious that after 10 min of irradiation the epoxides' peaks had completely disappeared and furthermore it was possible to observe the decrease of the intensity of the characteristic poly(isoprene) peak at 5.1 ppm (Figure 110).

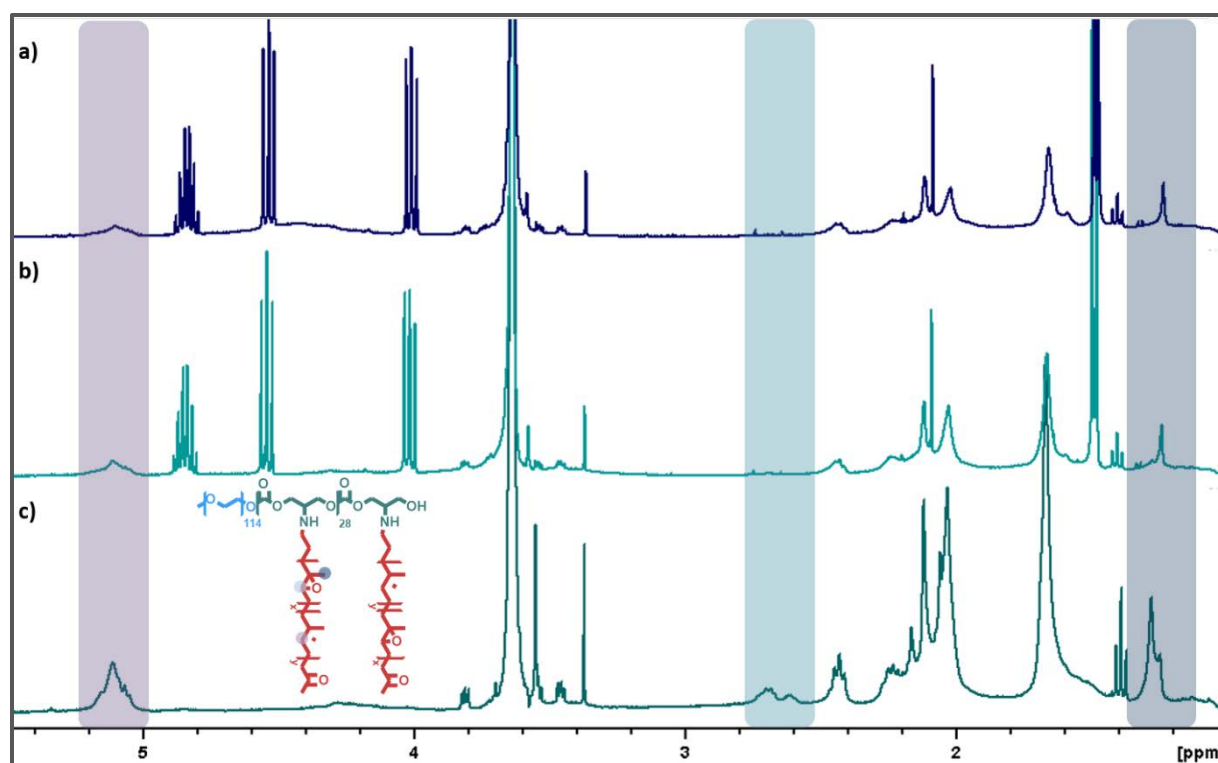


Figure 110: ¹H NMR spectra of a) 40% epoxidized PEG₁₁₄-*b*-(PATC-*g*-PI₃)₁₅-*co*-PATC₅ (G3) + 3% w/w PhI. after 10 min of UV irradiation, b) 40% epoxidized PEG₁₁₄-*b*-(PATC-*g*-PI₃)₁₅-*co*-PATC₅ (G3) + 3% w/w PhI. after 5 min of UV irradiation and c) 40% epoxidized PEG₁₁₄-*b*-(PATC-*g*-PI₃)₁₅-*co*-PATC₅ (G3) with no UV irradiation and no PhI. present.

The disappearance of the peaks that are attributed to the epoxides as well as the decrease of the peak at 5.1 ppm of poly(isoprene) indicates formation of a network which made the poly(isoprene) block more insoluble and thus subtracted from detection, thereby confirming the cross-linking process. Thus, it was possible to continue with studying the cross-linking process on the self-assembled magnetic polymersomes following the same strategy (Figure 111). The process was studied by TEM imaging because it was thought that the network formation would create a visible differentiation on the membrane aspect.

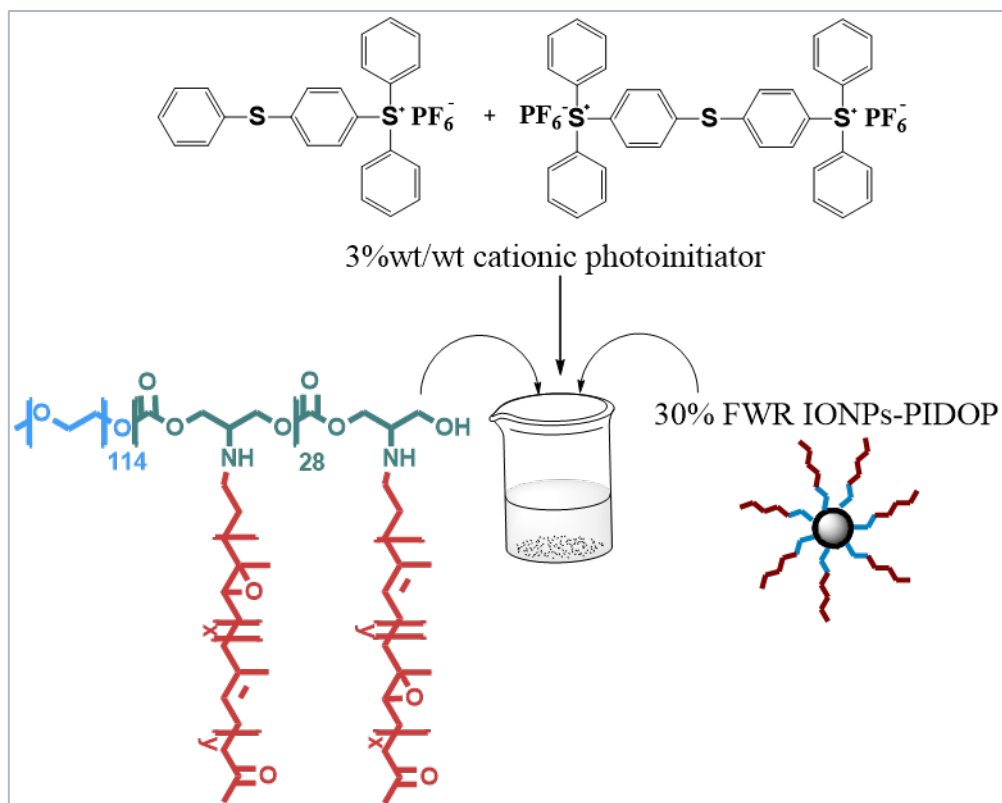


Figure 111: Self-assembly process to produce magnetic polymersomes capable of being cross-linked under UV.

The polymersomes which were studied for the membrane cross-linking were self-assembled *via* a fast water addition process as described in the experimental section. Further on, the sample solution was inserted into a quartz cuvette, which in turn was irradiated at a distance of 1 cm from the UV beam output using the “big” (A10014-50) fiber, for 10, 15, 20, 30 and 40 min equally. The sample was then visualized by TEM imaging to see the differentiation of the membrane (Figure 112). From the imaging it was possible to see a differentiation in the appearance of the membrane, which became darker as the UV irradiation time increased. Furthermore, the structures appeared to be more “concrete” as the time progressed as well, suggesting that the network of poly(isoprene) became denser to the electrons indeed with the UV irradiation dose. A more intense change started to appear particularly after the 30 min mark with the 40 min mark to be the most intensely dark and concrete.

The difference in time of cross-linking between the samples before and after self-assembly can be attributed mainly to the difference of solvent: the sample was initially solubilized in chloroform, while the self-assembled structures were dispersed in water. Consequently, the self-assembled structures have the poly(isoprene) block in the interior of the structures, *i.e.*, within membrane while the PhI. salt was free to diffuse to the aqueous medium, whereas in the non-assembled structures the blocks of poly(isoprene) were fully solubilized thus more approachable by the photoinitiator molecules, thus decreasing the necessary time of UV irradiation.

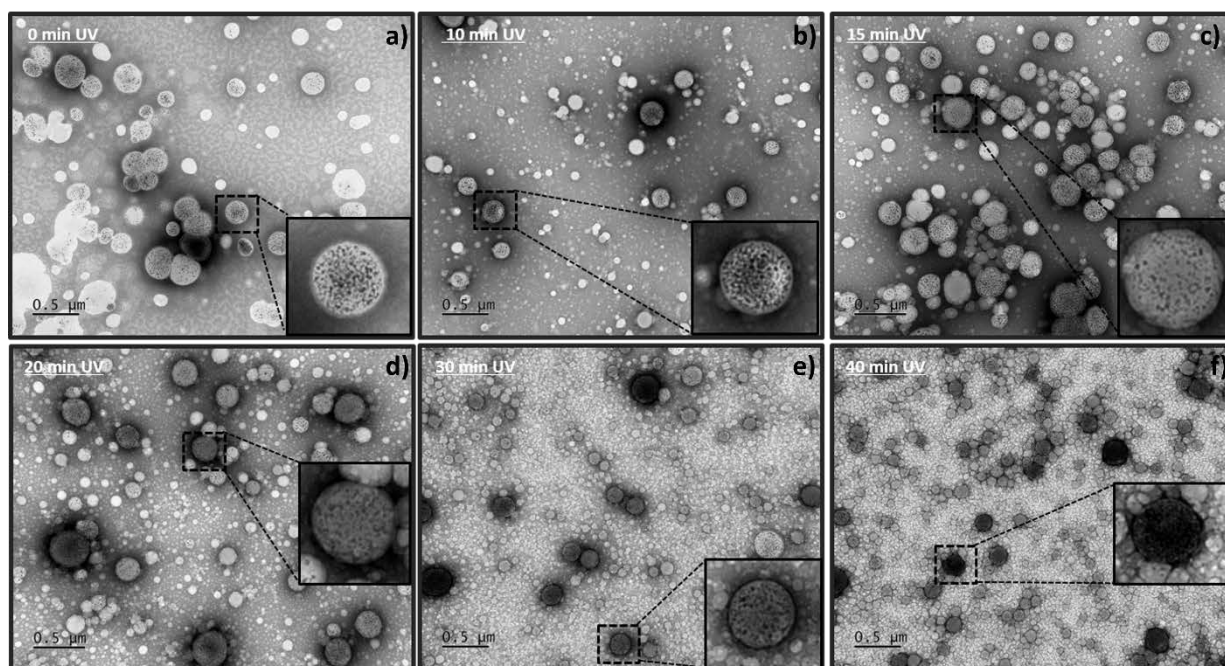


Figure 112: TEM images of the study of cross-linking efficiency depending on the time of irradiation starting with a) 0 min, b) 10 min, c) 15 min, d) 20 min, e) 30 min and f) 40 min of irradiation at 55% of the lamp full power stained with 2% samarium acetate.

Moreover, increasing the intensity of the UV lamp naturally decreased the time necessary for the cross-linking to occur and for a clear difference in the appearance of the structures (Figure 113). Specifically, the graft copolymer $\text{PEG}_{114}\text{-}b\text{-(PATC-g-PI}_4\text{)}_{20}\text{-co-PATC}_{11}$ (G5) was self-assembled with 20% FWR IONPs-PIDOP (D) and 3% w/w PhI. The sample was irradiated with UV in the same procedure as described above but for an intensity at 60% for 15 min. As it can be seen in the image below, before irradiation the sample, even when stained does not show a good definition of the membrane structure, but post-irradiation the structures became more define and concrete once more. In this case an increased intensity resulted in a faster cross-linking kinetics, with the structures resembling more the ones that are depicted in Figure 5 for 30 and 40 min of UV irradiation.

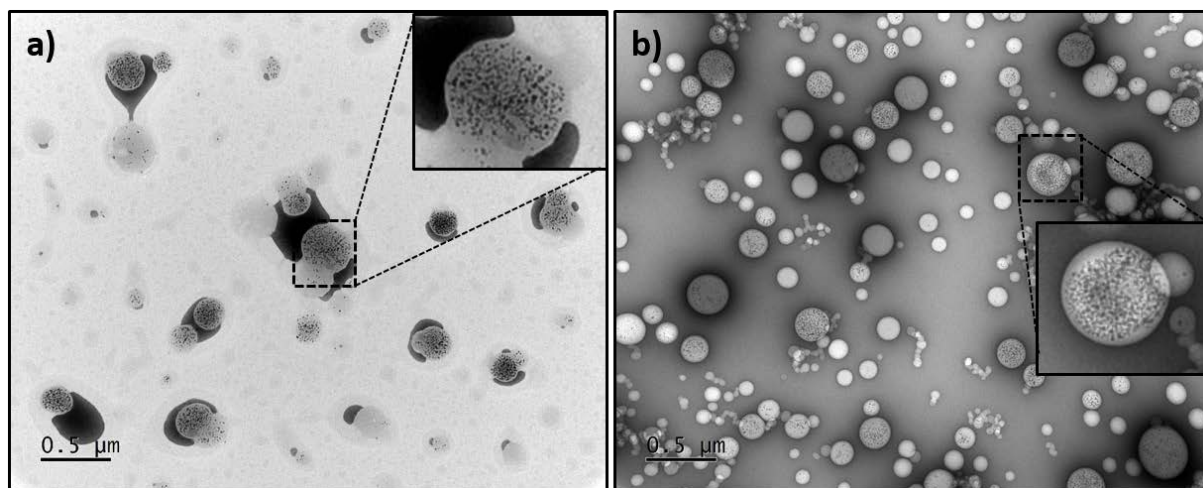


Figure 113: TEM images of a) PEG₁₁₄-*b*-(PATC-*g*-PI₄)₂₀-*co*-PATC₁₁ (G5) +20% FWR IONPs-PIDOP(D) and 3% w/w PI before UV irradiation and b) PEG₁₁₄-*b*-(PATC-*g*-PI₄)₂₀-*co*-PATC₁₁ (G5) +20% FWR IONPs-PIDOP(D) and 3% w/w PhI. after 15 min of UV irradiation at 60% of the lamp full power stained with 2% samarium acetate.

What is interesting is that post-UV irradiation, other smaller structures which had not incorporated IONPs during the self-assembly process and were not visible before, started to appear as ascribed to improved contrast. This suggests that the 20% FWR was not enough to pack the structures fully with IONPs, once more verifying that the graft copolymer G5 forms small micelles if self-assembled alone.

Even when the images remain non-stained, the cross-linking of the membrane could be detected nicely as it can be observed on Figure 114 where the sample was irradiated for 15 min with a 60% UV intensity. As it can be seen on the unstained electron micrographs, the membrane containing the IONPs is the only thing that visibly changes by becoming intensely darker, suggesting a network formation and a denser structure compared to the images of the non-irradiated sample.

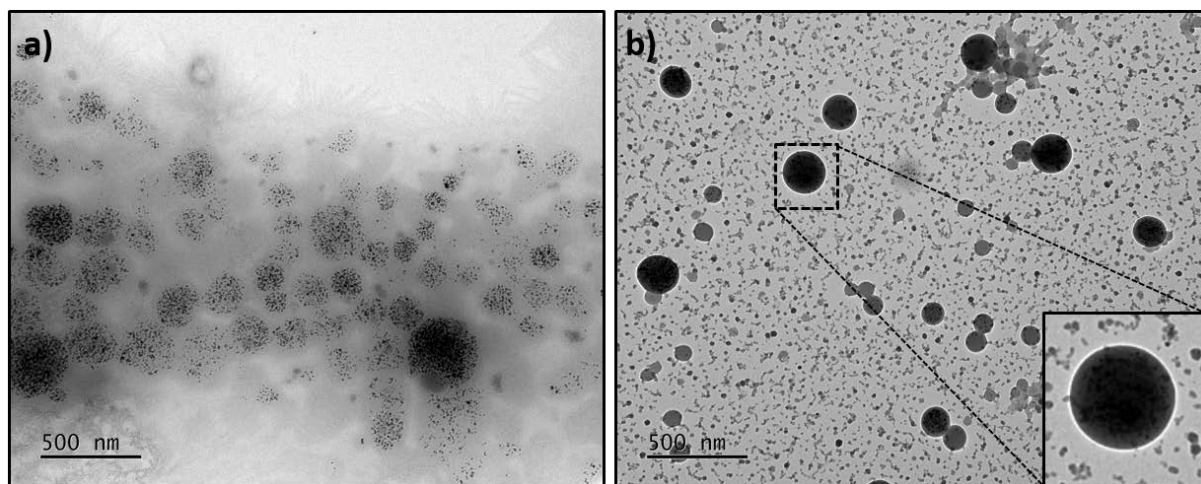


Figure 114: TEM images of a) PEG₁₁₄-*b*-(PATC-*g*-PI₄)₂₀-*co*-PATC₁₁ (G5) +20% FWR IONPs-PIDOP(D) and 3% w/w PhI. before UV irradiation and b) PEG₁₁₄-*b*-(PATC-*g*-PI₄)₂₀-*co*-PATC₁₁ (G5) +20% FWR IONPs-PIDOP(D) and 3% w/w PhI. after 15 min of UV without staining.

In order to see whether DLS can give some further information for the detection of cross-linking, the sample PEG₁₁₄-*b*-PATC₂₀-*g*-PI₅ (G4) + 30% FWR IONPs-PIDOP (D) + 3% PhI. was measured before and after UV irradiation. Specifically, the sample was in this case irradiated for 30 min with a UV lamp intensity of 65%. The sample post-irradiation exhibited a higher hydrodynamic size (both Padé-Laplace and z-average diameters), which could suggest that since the size of the actual structures does not change on the TEM micrographs, what impacts this difference of size is the density of the membrane which became more concrete resulting in a different contribution of the largest objects to the scattering (Table 20). Alternatively, this could also be a sign of some degree of aggregation, which would be induced when PI chains belonging to different vesicles react, attaching the two (or more) vesicles together.

Table 20: DLS characteristics before and after UV irradiation of the sample PEG₁₁₄-*b*-PATC₂₀-*g*-PI₅ (G4) + 30% FWR IONPs-PIDOP (D) + 3% PhI.

Sample	Diameter (nm)*	Z-average (nm) [†]	PDI [†]
PEG ₁₁₄ - <i>b</i> -PATC ₂₀ - <i>g</i> -PI ₅ (G4) + 20% FWR IONPs-PIDOP (D) Control	157 (94%)	157	0.19
PEG ₁₁₄ - <i>b</i> -PATC ₂₀ - <i>g</i> -PI ₅ (G4) + 20% FWR IONPs-PIDOP (D) post 30 min UV irradiation	334 (91%)	243	0.23

* by Padé-Laplace (multimodal) fit of auto-correlogram (percentage indicates the weight of the mode); [†] by 2nd order cumulants fit.

In conclusion for this section of the chapter, the cross-linking of the hydrophobic membrane under UV irradiation by addition of cationic photo-initiator was studied by TEM observations and DLS measurements. It was observed that a differentiation in the appearance of the structures did occur after the irradiation, which resulted in darker structures that were identified as the poly(isoprene) membrane which created a denser network. Depending on the intensity of the UV lamp, different irradiation times were necessary to achieve such an alteration, with a time as low as 15 min in the case of 60% intensity. Following this, we decided to continue with cross-linking, this time under an applied magnetic field.

Study of the behavior of polymersomes under a static magnetic field:

The next step of our study was to investigate the behavior of the self-assembled polymersomes under the influence of an applied static magnetic field. More precisely, the target was the elongation of the polymersomes in the direction of the magnetic field due to the formation of linear aggregates of the IONPs when the field is applied. Due to their restriction in the hydrophobic membrane, these linear aggregates would theoretically force a deformation of the polymersomes which would result in anisotropic vesicles. The examples in literature are limited to a few such as the work that has been performed by Lecommandoux *et al* [8], Sanson *et al.*[9] and recently by Long *et al.*[6], while this concept has been studied extensively with only theoretical studies published by Ryzhkov and Raikher [4], [28] by running coarse grained molecular dynamics models.

Herein, we explored the possible deformation and its stabilization by cross-linking of the hydrophobic membrane following the results described in the above section. More specifically, samples were introduced into a custom made 0.4 T magnetic field which consisted of a Halbach array of magnets and was designed and constructed by Julien Le Mener, engineer within the “Plan de Relance” project [Thetis](#) in collaboration between the LCPO and Cordouan Technologies, Pessac, France. This specific conformation of the magnets resulted in a homogenous field ($\leq 5\%$ variation) oriented in one planar direction in the middle of the structure (Figure 115). This device also has an axial hole to fit a sample (either one tube of 5 or 3 mm diameter, or two tubes of 1.5 mm diameter for SAXS) and a large lateral window, which enables performing UV irradiation and multiangle DLS or SAXS experiments *in situ*, with the incident beam oriented either parallel or perpendicular to the (in-plane) magnetic field direction.

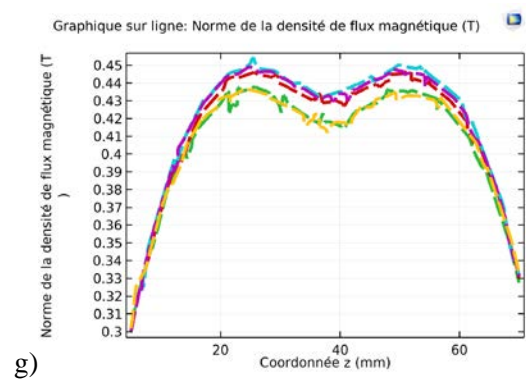
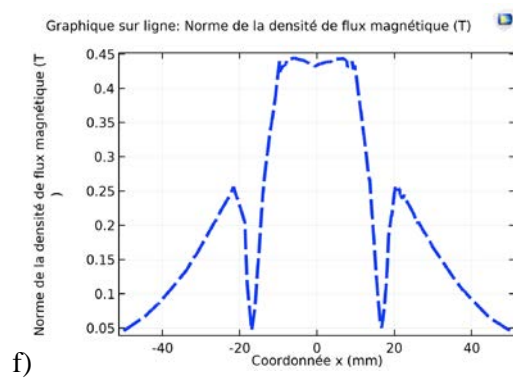
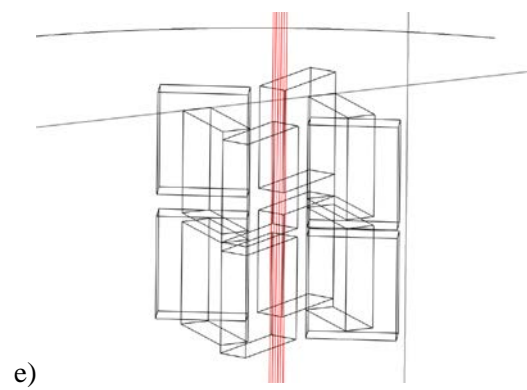
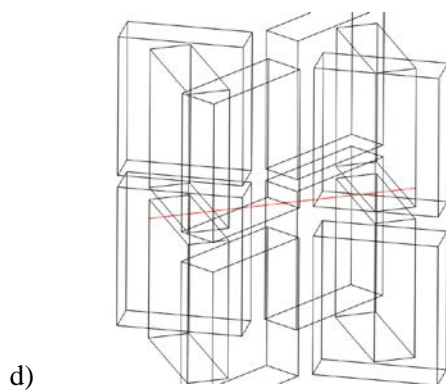
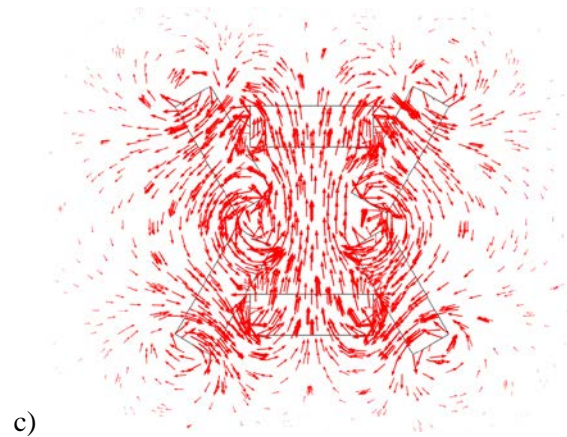
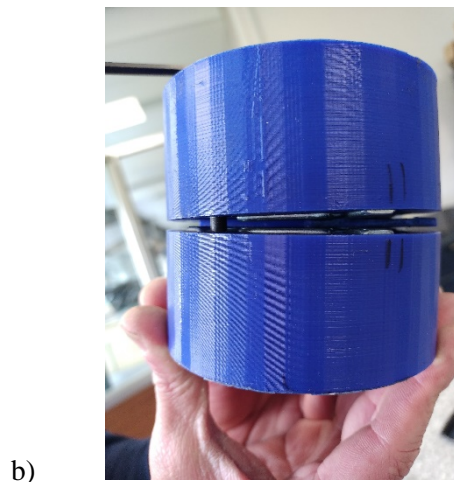
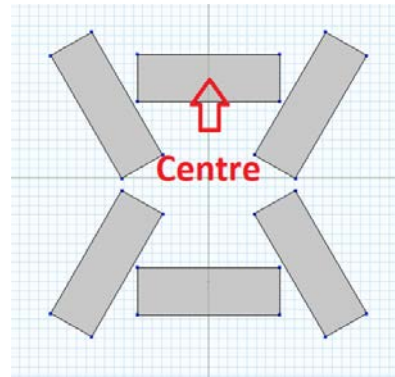
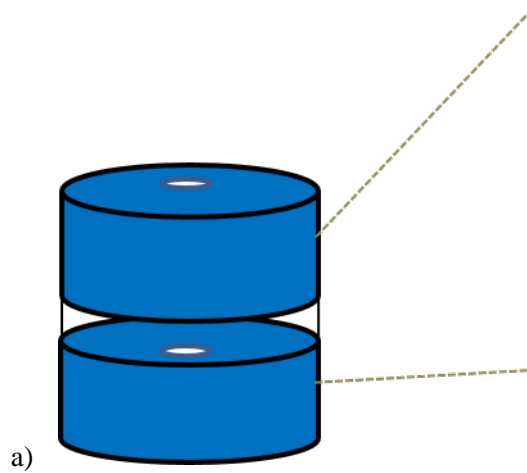


Figure 115: a) Depiction and b) photo of the custom-made Halbach array of strong $\text{Fe}_{14}\text{Nd}_2\text{B}$ ferromagnets creating a magnetic field of $0.43 \pm 0.02\text{T}$, c) directed within the central plane, which was used for the elongation tests; b) The array is composed of 12 parallelepiped magnets in total (arranged as 2 layers of 6), the dimensions of each one being $35 \times 30 \times 10\text{ mm}^3$ ($L \times l \times d$). The magnetic field lines were simulated numerically using COMSOL Multiphysics™ (evaluation license 8079249, 1-15/3/2022).

This set up was utilized for the elongation study changing different parameters such as time of UV irradiation if any and time of exposure to the magnetic field. The way the set up was constructed did not allow for the UV illuminating fiber to reach the sample at a 1 cm distance and the closest it could get was at 3 cm. Thus, it was decided to proceed with the experiments with a higher intensity (70-75%). In summary, each sample was placed in a special tube which had a length of either 3 or 4 inches (approximately 7.5 or 10 cm and an outer diameter of 3 mm (VWR, Rosny-sous-Bois, France). the tube was inserted until it reached the middle of the space between the two cylindrical parts containing the magnets, with the volume of sample in the tube being enough to feel the space but not more so that the magnetic polymersomes would stay in the homogeneous field region of $B=0.43\text{ T}$ at $\leq 1\%$ precision, which is limited to an 8 mm height, hence $40\text{ }\mu\text{L}$ volume. Otherwise the small lateral and axial field gradients (around 5% according to the field profiles on Figure 115) are sufficient to attract the objects onto the walls, disrupting the sample dispersion state and causing (hopefully reversible yet unnecessary) precipitation (Figure 116).

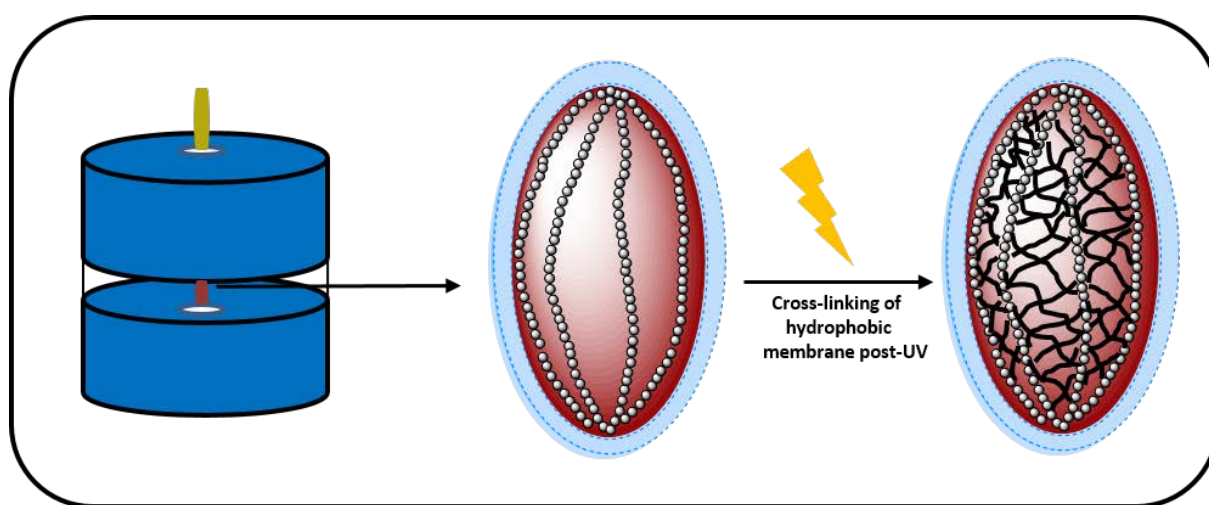


Figure 116: Representation of the interior reaction of the sample which is constrained inside the NMR tube (red cylinder) after elongation of the IONPs in the direction of the field, following with the cross-linking which occurred through UV irradiation, with the fiber inserted from the top (yellow cylinder) at a 3 cm distance from the sample.

It was assumed that the FWR of IONPs in the self-assembled structures would inevitably play a role in the elongation process, naturally the bulk amount and core diameter of the magnetic nanoparticles affects the intensity of the force which is produced by them during the application of a magnetic field. A torque Γ is being produced from magnetic nanoparticles when a magnetic field is applied, and it depends on their magnetic moment $\vec{\mu}$ as well as the amplitude and the direction of the magnetic field,

more specifically through the angle θ between the field and the moment, as it is defined as:

$$\Gamma = \|\vec{\mu} \times \vec{B}\| = \mu \cdot B \sin \theta \cos \theta \quad (8)$$

In addition, if the magnetic field is non-homogeneous, *i.e.* it has a gradient either in the vertical (z) or lateral dimensions (x, y), then the magnetic NPs also experiences a migration force of modulus given by:

$$\|\vec{F}_{\text{mig}}\| = \vec{\mu} \cdot \nabla(B) \quad (9)$$

where the dot sign (unlike the cross sign in previous equation) stands for scalar product of the vectors.

Nonetheless, in this case the nanoparticles would act collectively as linear aggregates which would result in a collective force acting on the membranes, especially at the two magnetic poles of the vesicle, pushing them apart and elongating the shape. Magnetic nanoparticles also present a dipole-dipole interaction, which attracts them to each other when a static magnetic field is applied. It expresses as:

$$\vec{F}_{\text{dip}} = -\nabla(U_{\text{dip-dip}}) \quad (10)$$

Where the magnetic dipole-dipole interaction energy is given by:

$$U_{\text{dip-dip}} = \mu_0 \frac{\vec{\mu}_1 \cdot \vec{\mu}_2}{r^3} \quad (11)$$

With r the distance between the centers of the two magnetic dipoles $\vec{\mu}_1$ and $\vec{\mu}_2$.

Consequently, their magnetic moments $\vec{\mu}$ (assuming to be equal for IONPs of same material and core size) tend to align in parallel direction of the field and the nanoparticles are no longer dispersed freely in the fluid membrane. Due to the constriction that the membrane provides, the IONPs form linear aggregates due to the dipole-dipole interactions, and the mean length of the aggregates depends on the feed weight ratio (FWR), the core diameter and the magnetization of the IONPs, as well as the size of the polymersomes they are embedded in. The importance of dipolar interactions is quantified by a parameter λ defined as the value of the dipolar energy (in kT units) when the IONPs are in close contact with each other (*i.e.* at a distance $r = 2r_{\text{core}} + 2\delta_{\text{shell}}$):

$$\lambda = \frac{\mu_0}{kT} \left(\frac{4\pi}{3}\right)^2 \frac{m_{\text{sat}}^2 r_{\text{core}}^6}{(2r_{\text{core}} + 2\delta_{\text{shell}})^3} \sim \frac{\mu_0 m_{\text{sat}}^2 r_{\text{core}}^3}{2kT} \left(\frac{\pi}{3}\right)^2 \left(1 - 3\frac{\delta_{\text{shell}}}{r_{\text{core}}} + 6\left(\frac{\delta_{\text{shell}}}{r_{\text{core}}}\right)^2 + \dots\right) \quad (12)$$

where $\mu_0 = 4\pi \times 10^{-7}$ is the magnetic permeability of vacuum (in SI units), $kT = 4.1 \times 10^{-21}$ J the thermal energy at 300 K, r_{core} the core radius of the IONPs (either ~ 3 or ~ 4 nm for our two IONP samples, respectively) and δ_{shell} is the thickness of the non-magnetic organic layer, which we can estimated by $\delta_{\text{shell}} \sim 1$ nm for the oleic acid coating and $\delta_{\text{shell}} \sim 2$ nm for the PI-dopamine brush. In their work, Ryzhkov and Raikher [4], [28] consider $\lambda = 3$ as a medium dipolar interaction case ($\lambda = 1$ would mean that dipolar interactions are negligible compared to kT), whereas they take $\lambda = 5$ as a strong dipolar interaction case. In practice, if we assume $m_{\text{sat}} = 3.5 \times 10^5$ A·m⁻¹ as typical saturation magnetization for the IONPs of

$d_{\text{core}} \sim 6$ nm synthesized by the polyol route and $m_{\text{sat}} = 2.8 \times 10^5 \text{ A} \cdot \text{m}^{-1}$ for those of $d_{\text{core}} \sim 8$ nm prepared by the alkaline coprecipitation in water followed by size sorting, we find $\lambda \sim 0.5$ for the Caruntu synthesis IONPs coated by polyisoprene chains, and $\lambda \sim 0.9$ for those coated by OA, whereas for the coprecipitated IONPs which are a bit larger, we estimate $\lambda \sim 1.7$ for those coated by OA and $\lambda \sim 1.0$ for the ones grafted to PI chains. As a conclusion, all of our experiments would be in the weak dipolar interaction regime of magnetic polymersome deformation under a static magnetic field, except for the largest ones with the thinnest organic coating of oleic acid, which exhibit dipolar interactions superior to thermal energy. Please note also that these estimates were made for IONPs free to move in 3D, whereas in our case the IONPs are confined in the membranes by their hydrophobic coating, thus the dipole-dipole interaction might play a more prominent role, explaining why the IONPs exhibit surface crystallization as hexagonal arrays on TEM micrographs.

Examining the structures that were created by the self-assembly process between the graft copolymer PEG₁₁₄-*b*-PATC₂₀-*g*-PI₅ (G4) + 70% FWR IONPs-OA (Caruntu) + 6% PhI. it was visible that spherical structures containing IONPs inside the hydrophobic membrane were created. The sample was put in the magnetic field and irradiated with UV for 5 min at an intensity of 70%, then the irradiation stopped, and the sample was left for 15 min in the MF with no irradiation following with another irradiation of 15 min while in the MF and finally stopping it and letting the sample to settle in the MF for another 5 min. The rationale in this way of working was done with the idea that the initiation of the cross-linking was to be started from the very beginning of entering the magnetic field in order to stabilize the structure a little, so the samples do not “break” into smaller structures, like in the Rayleigh “pearling” instability of a fluid cylindrical droplet, which is also experienced by tubular vesicles[29]. Further on, the sample was left in the MF for 15 min to allow the magnetic nanoparticles to orientate in the direction of the field by forming linear aggregates and forcing slowly an elongation. Finally, the irradiation started again for another 30 min without taking the sample outside of the field to keep the chains of the nanoparticles intact as well as to keep the structure which was formed stable.

As it can be seen in Figure 117 the final morphology of the structures appears elongated (Figure 117b-j) when compared to the control group (Figure 117a). The larger structures seem to be more affected than the medium size ones, with smaller structures also presenting a slight elongation. With no irradiation or inadequate irradiation, the magnetic nanoparticles return to their freely dispersed state thus relaxing the morphology back to its original form. This could be one of the reasons that not all structures are elongated, but it is not the only reason. Smaller structures may not allow the linear aggregates to form longer chains which are necessary for a noticeable elongation of the structures which they are embedded in.

Of course this goes somehow against what has been found theoretically by Ryzhkov *et al.*[30] who studied the dependency of the possible elongation of magnetic polymersomes on their size. More

specifically, *via* coarse grain computer simulations, they were able to detect that smaller polymersomes would tend to elongate more when compared to ones with a larger diameter. This was attributed to a steric parameter, meaning that the smaller polymersomes would increase the tendency of the magnetic nanoparticles to align in a linear aggregate more than a bigger polymersome would. Due to the higher freedom that the latter would provide for the IONPs, they would prefer to remain in smaller chains and not be restricted into the longer aggregates which would aid the elongation process. These calculations were performed for a relatively low loading capacity of polymersomes, with the volume fraction of IONPs within the polymer membrane being $\phi=11\%$, and not for highly packed structures. However, in our case, although the packing looks very high, the FWR is 70% (in weight), but it corresponds to $\phi\sim 12\%$ in volume, given the high mass density of iron oxide $\rho^{\gamma\text{-Fe}_2\text{O}_3}\sim 4.9\text{ g}\cdot\text{cm}^{-3}$.

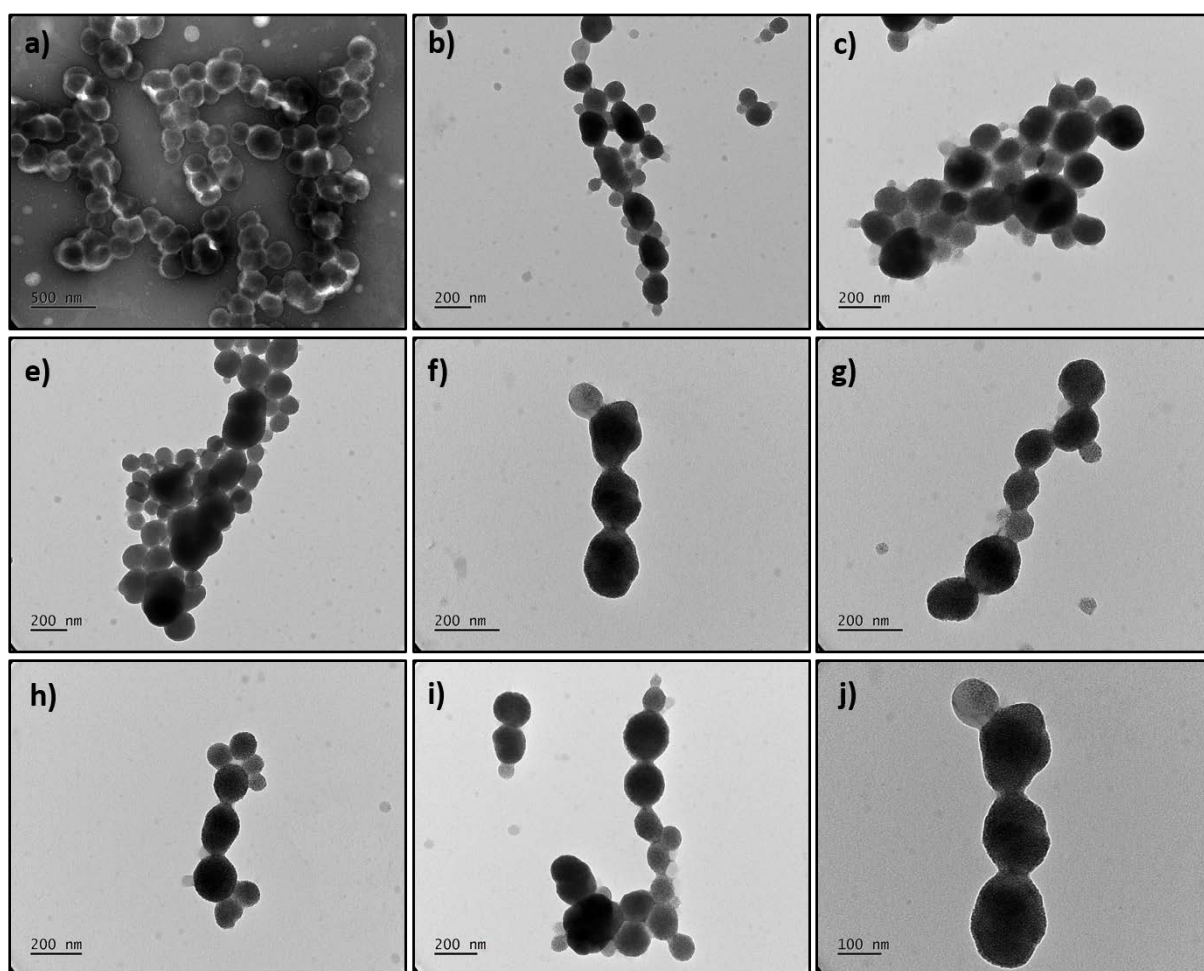


Figure 117: TEM images of PEG₁₁₄-*b*-PATC₂₀-g-PI₅ (G4) + 70% FWR IONPs-OA (Caruntu) + 6% PhI. a) before application of MF or UV irradiation, b-j) post the deformation process with application of a 0.4T MF and UV irradiation through the “5.15.30.5” protocol (5 min UV on out of field, 15 min in field UV off, 30 min in field UV on). Stained with 2% samarium acetate.

During the imaging process, the linear aggregates of IONPs within membranes cannot be detected due to the lack of a magnetic field in the TEM and their tendency to relax and return to a freely dispersed state. To stabilize the linear aggregates in that position, the cross-linking should have been performed in between the magnetic nanoparticles themselves, *i.e.* using epoxidized PI-dopamine instead of OA as surface ligand, nevertheless the elongation is quite prominent for this intensity of magnetic field.

In order to demonstrate whether the elongated structures in the sample post MF+UV exposure prevail against the spherical structures an anisotropic parameter R , where $R=b/a$ with b standing for the length of the long axis and a standing for the length of the short axis and was calculated *via* ImageJ analysis of the TEM images. While this R parameter can be accurate, in this case it can't be taken as absolute as the amount of sample in the images is not enough to statistically demonstrate accurately the anisotropy. Nonetheless it can be considered in the cases described in this manuscript as an indicative parameter which could at the very least suggest that an alteration does indeed occur during the UV/MF process.

As it can be observed on Figure 118 the R parameter shifts to higher value after the elongation and cross-linking process of the sample has occurred. Specifically, in the control group the average value for R is 1.05 ± 0.02 , while the average value for R for the UV+MF sample is 1.3 ± 0.06 . As a spherical morphology would inevitably result in an $R=1$, thus the higher value indicates a deviation from the spherical morphology into an axially anisotropic structure. Another important observation which can be made is the fact that a chaining effect can be observed post UV/MF, perhaps demonstrating a cross-linking between the polymersomes.

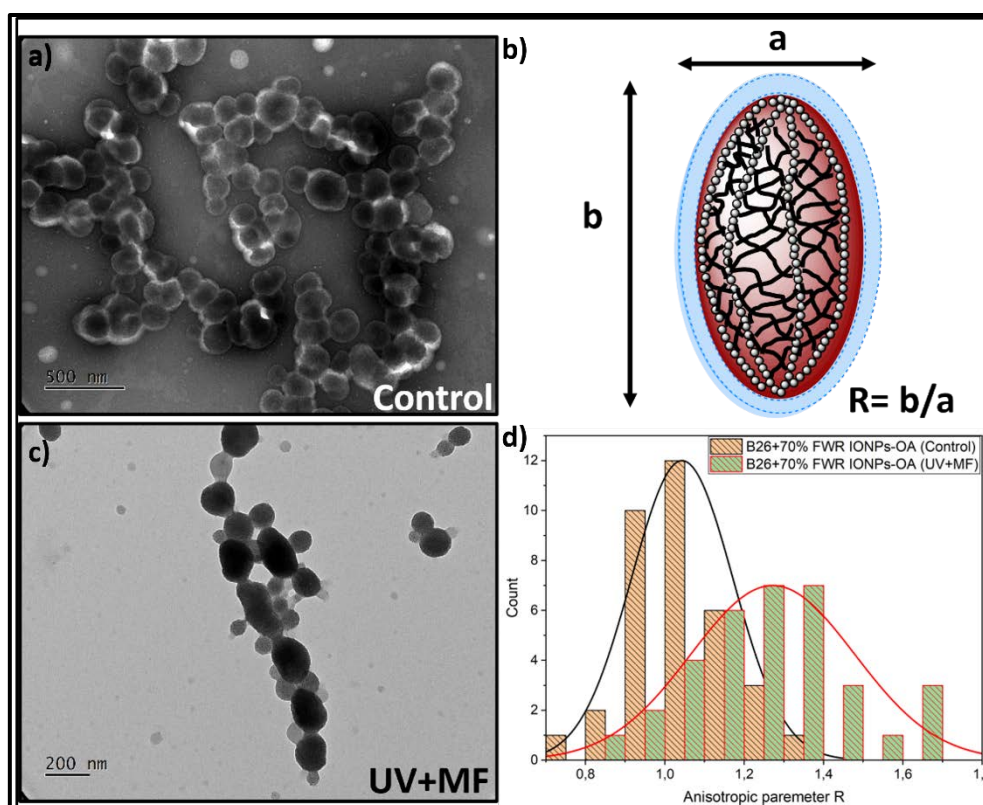


Figure 118: a) TEM image of the sample PEG₁₁₄-*b*-PATC₂₀-g-PI₅ (G4) + 70% FWR IONPs-OA (Caruntu's polyol route sample of $d_{\text{core}} \sim 6$ nm) + 6% PhI. before (Control), b) Schematic demonstration of the R anisotropic parameter calculated from the TEM images of vesicles c) TEM image of the sample PEG₁₁₄-*b*-PATC₂₀-g-PI₅ (G4) + 70% FWR IONPs-OA (Caruntu) + 6% PhI. after magnetic field and UV exposure (UV+MF) and d) diagram of the anisotropy parameter R for both samples (Control, UV+MF) calculated from the TEM images of the samples.

Another example where slight deformation was able to be observed was for a lower feed weight ratio of IONPs, specifically 50% but the IONPs utilized in this sample had a bigger magnetic core diameter, near 8 nm (sample prepared by aqueous coprecipitation followed by size sorting). This sample of IONPs appeared to bear higher magnetic susceptibility, as calculated from the AC-magnetometry measurements, and was expected to result in a higher elongation due to a better response to the magnetic field. The same graft copolymer was self-assembled with 50% FWR of IONPs and was left overnight in the magnetic field, the following day it was irradiated with UV for 30 min. The TEM images present a difference before and after the application of the magnetic field and the UV irradiation. The change mainly affects the visibility of the membrane due to the cross-linking process but also some visible elongation. Once more the elongation can be only seen mainly in polymersomes with a larger size and a higher packing density of IONPs (Figure 119).

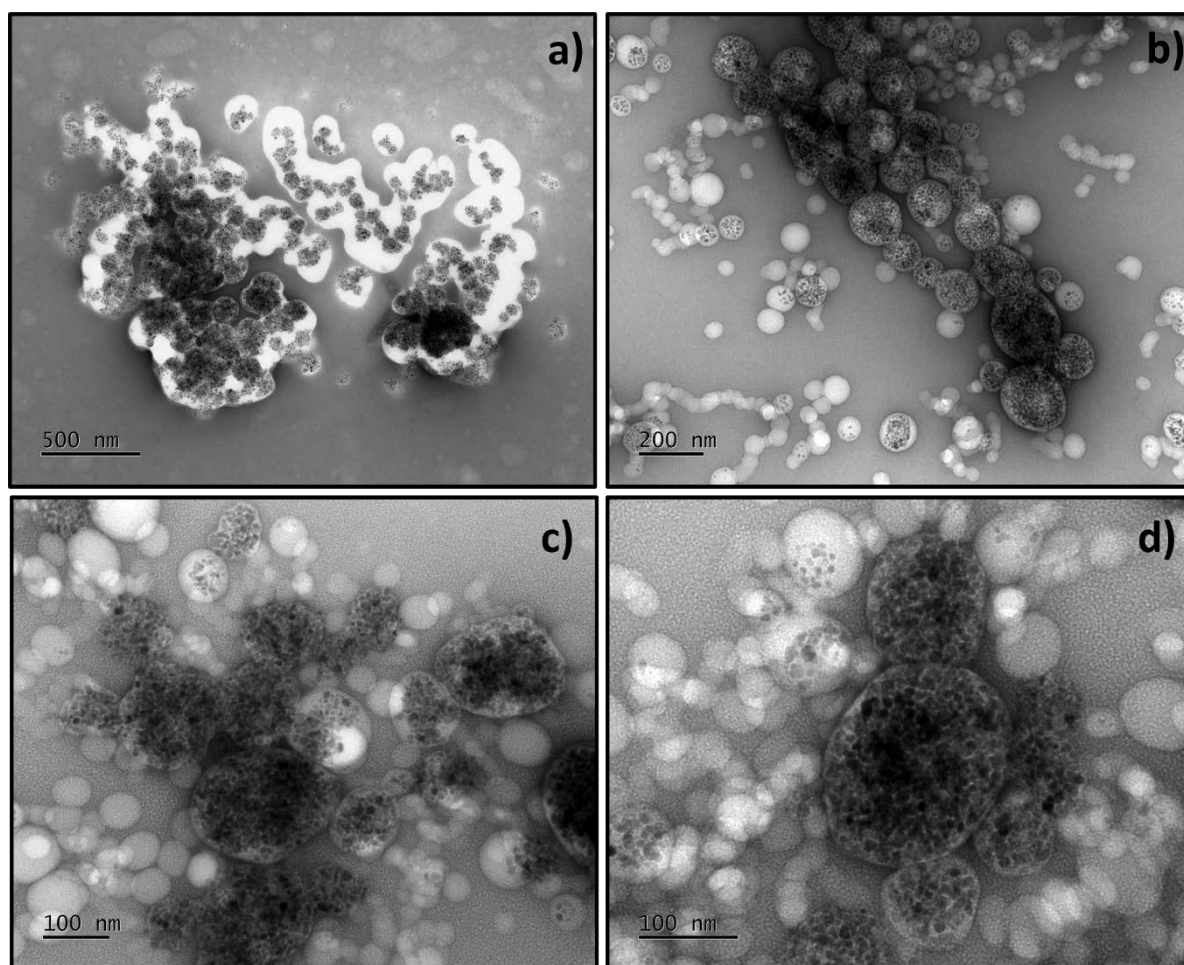


Figure 119: TEM images of PEG₁₁₄-*b*-PATC₂₀-*g*-PI₅ (G4) + 50% FWR IONPs-OA (coprecipitated sample of $d_{\text{core}} \sim 8$ nm) + 6% PI a) before application of MF or UV irradiation, b-d) post the deformation process with application of a 0.4 T MF overnight and 30 minutes UV irradiation. Stained with 2% samarium acetate.

The appearance of the membrane post-UV is visible enough as it was expected: in the control image (Figure 119a), it was only possible to observe the IONPs, but post irradiation the membrane became visible, and it became easier to detect the actual morphologies of the structures. Furthermore, it was possible to observe that not all the vesicles were magnetic as some of them appeared empty post irradiation (Figure 119b-d). As seen before, this was likely due to some of the IONPs not being incorporated during the initial self-assembly process. More precisely, it has been observed that when higher FWR of IONPs with this larger diameter were utilized for co-assembly, not all the IONPs were incorporated in the vesicles and some precipitation of the hydrophobically coated IONPs in water occurred. On the contrary, for the samples that had managed to incorporate a high amount of the IONPs, which resulted in larger vesicles, it was possible to stabilize a slight elongation post-crosslinking (by UV irradiation for 30 min).

While anisotropy was visible for some polymersomes, it was not as prominent as it was expected for this sample. Once more, the largest samples seem to present some visible elongation while the smallest

ones remain spherical. The calculation of the anisotropic ratio R from TEM images in Figure 12, produced an $R = 1.15 \pm 0.025$ which was slightly higher than 1, suggesting that while anisotropy was present it was not prevalent throughout the depicted sample (Figure 120). Due to the lack of clear limits in the control group of the sample (Figure 119a), the anisotropic parameter was difficult to identify accurately but it is possible to observe that some anisotropic structures exist already.

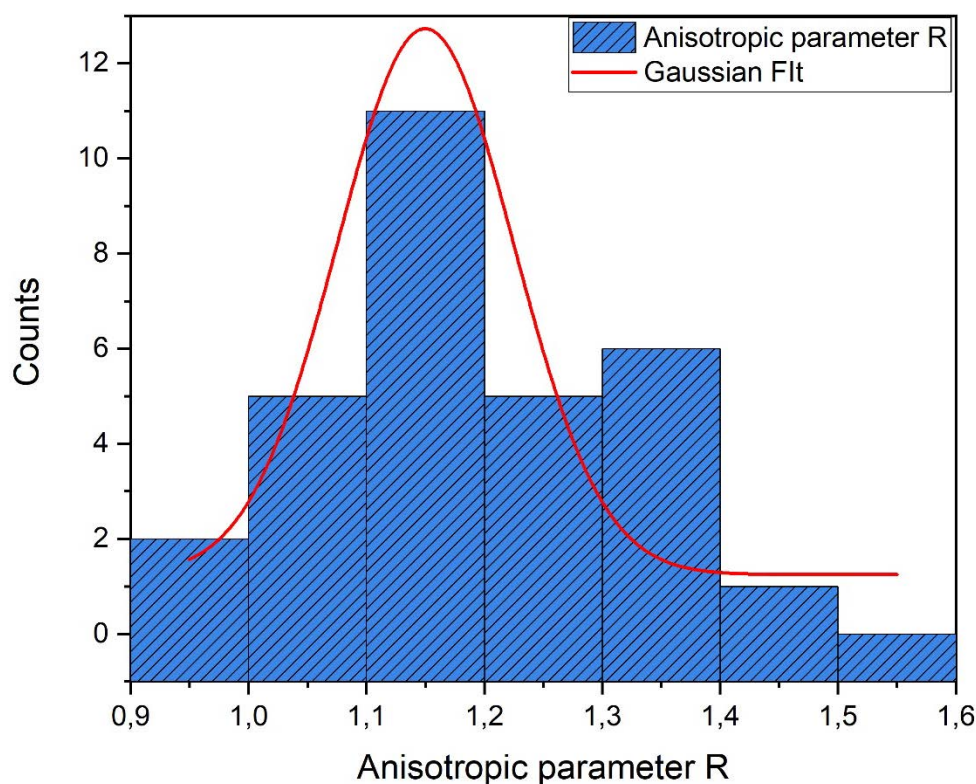


Figure 120: Anisotropy parameter R of PEG₁₁₄-*b*-PATC₂₀-*g*-PI₅ (G4) + 50% FWR IONPs-OA (coprecipitated sample of $d_{\text{core}} \sim 8$ nm) + 6% PhI. after UV and MF exposure.

Unfortunately, these were the only cases where it was possible to detect some type of deformation or/and elongation. For samples with smaller FWR of IONPs both with the small diameter of 6 nm and the bigger ones of 8 nm, no visible elongation was able to be stabilized. This was not due to lack of cross-linking, since all the samples had a visual confirmation in TEM that the cross-linking indeed occurred, by presenting a darker membrane as has already been discussed in the cross-linking section. It is believed that the lower FWR did not allow for the elongation to be strong enough either due the formation of shorter linear aggregates of the magnetic nanoparticles, which did not allow for a visible elongation, or the volume fraction of the nanoparticles in the membranes was not enough to produce an adequate number of chains which would produce vesicle elongation. Nonetheless, the 50% FWR and most importantly and noticeably the 70% FWR led to a good result, which produced a stabilized image of elongation.

Chapter V

To study the elongation in real-time, in situ DLS, SAXS and SANS analyses were employed. In all the experiments, the same samples were analyzed both inside and outside of the magnetic field, in order to see whether it was possible to detect the elongation process in real time. The main results of these preliminary and somehow delicate experiments will be reported in the last part of this chapter.

Triblock copolymers:

Study of the self-assembly of the triblock PEO-*b*-PTMC-*b*-PI copolymers:

The same study on the self-assembly behavior was done as well for the triblock copolymers. Once more the hydrophilic ratio f_{PEG} was considered to study the self-assembly process of the copolymers. The f_{PEG} of PP1PI7 sample was 17.8% as already discussed in Chapter III, which is in the range of ideal values to produce polymersomes by self-assembly through nanoprecipitation for copolymers that contain poly(trimethylene)carbonate, as indicated by literature. To study whether the hydrophobic block of poly(isoprene) would affect the self-assembly process, the triblock was first studied without any addition of iron oxide nanoparticles by TEM and cryo-TEM observations.

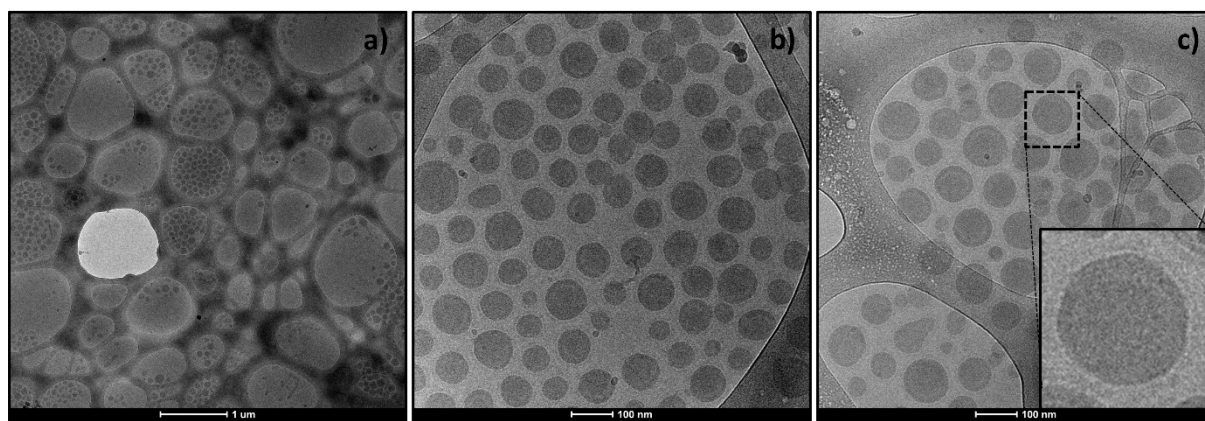


Figure 121: Cryo-TEM (a-c) of the triblock copolymer PEG₁₁₄-*b*-PTMC₂₀₀-*b*-PI₄₀ self-assembled alone.

As it can be observed from Figure 121, the cryo-TEM images revealed that when the triblock copolymer was self-assembled alone with no presence of IONPs, it resulted in spherical structures with a visible membrane. In our case the ABC terpolymer consists of the block of PEG (A) which is hydrophilic and two hydrophobic blocks B and C, PTMC and PI respectively, which are soft, *i.e.* in a rubbery physical state, membrane-forming blocks.

In all cases the corona forming block is PEG, as was expected due to its hydrophilic nature, with the white corona being visible in all cases. Further on we can see a dark grey membrane of around 10 nm thickness which corresponds to the hydrophobic blocks. A thin darker gray line can be detected as well, and it is attributed to the presence of the poly(isoprene) block, denser in electrons than PTMC owing to its double bonds. Using image analysis with ImageJ software, it was possible to determine the average diameter of the polymersomes as well as the average thickness of their membrane, the average diameter being 95 ± 2 nm and the average bilayer thickness 11.0 ± 0.7 nm (Figure 122). When compared to scaling law reported by Lebleu *et al.*[31] one would expect a thickness ~ 20 nm for a PTMC block length of 200 units, as found also in a previous thesis in the team[32]. The discrepancy might arise from a higher degree of chain interpenetration between the two leaflets of the bilayer, maybe due to PI end-block

entanglements, or just because polymer dimensions are systematically underestimated by TEM image analysis because the chains are collapsed in the vacuum column of the electron microscope. Nonetheless, the thickness of the membrane is still large enough to enable the incorporation of the IONPs that were synthesized in this project, of $d_{\text{core}} \sim 6$ or 8 nm (Chapter 4).

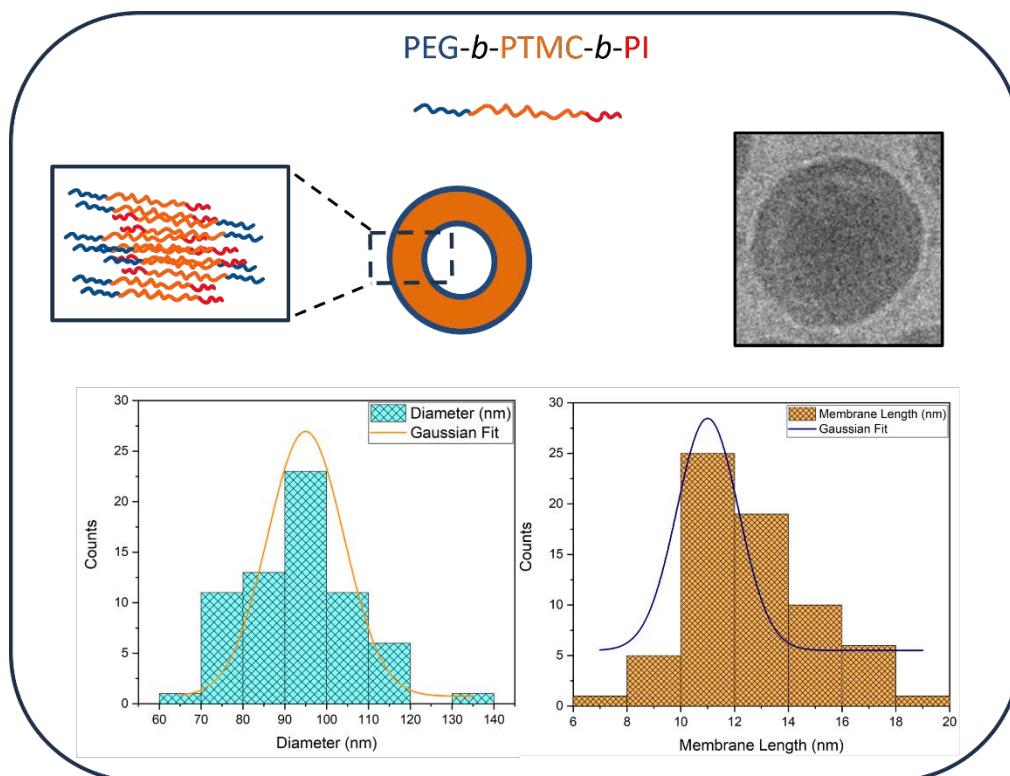


Figure 122: Determination of the average diameter of the vesicles as observed in cryo-TEM and of the average membrane thickness (nm).

While unilamellar vesicles can be detected on the micrographs, it is impossible to ignore the internal hydrophobic membrane that is visible inside some of the depicted structures in Figure 121. More specifically, it appears that smaller vesicles exist inside larger vesicles, suggesting the presence of so-called “nested vesicles”, which for other rubbery state copolymer (Pbut-*b*-PEO and PDMS-*b*-PEO) polymersomes were shown by Salva *et al* [33] to originate from a spherical-to-stomatocyte-to-nested vesicle transformation caused by osmotic chocks. In our case, the osmotic pressure was not controlled as we used pure water for nanoprecipitation instead of a buffer or sugar solution of known osmolarity. Nevertheless, when we later study polymersome crosslinking, such osmotic shock is plausible to occur because the UV-induced cleavage of the photoinitiator (Figure 108) produces liberation of solutes in the interval aqueous cores of the vesicles, which can cause the hypertonic shock at the origin of such morphological transition to nested vesicles. In addition, a fraction of bilamellar vesicles (*i.e.*, vesicles with a double membrane) were observed as well (Figure 123). Usually; vesicles need to be passed through filter of given porosity (typically 0.1 or 0.2 μm) to retrieve only unilamellar vesicles, a process called “extrusion” initially developed for liposomes, but that works also for polymersomes [34].

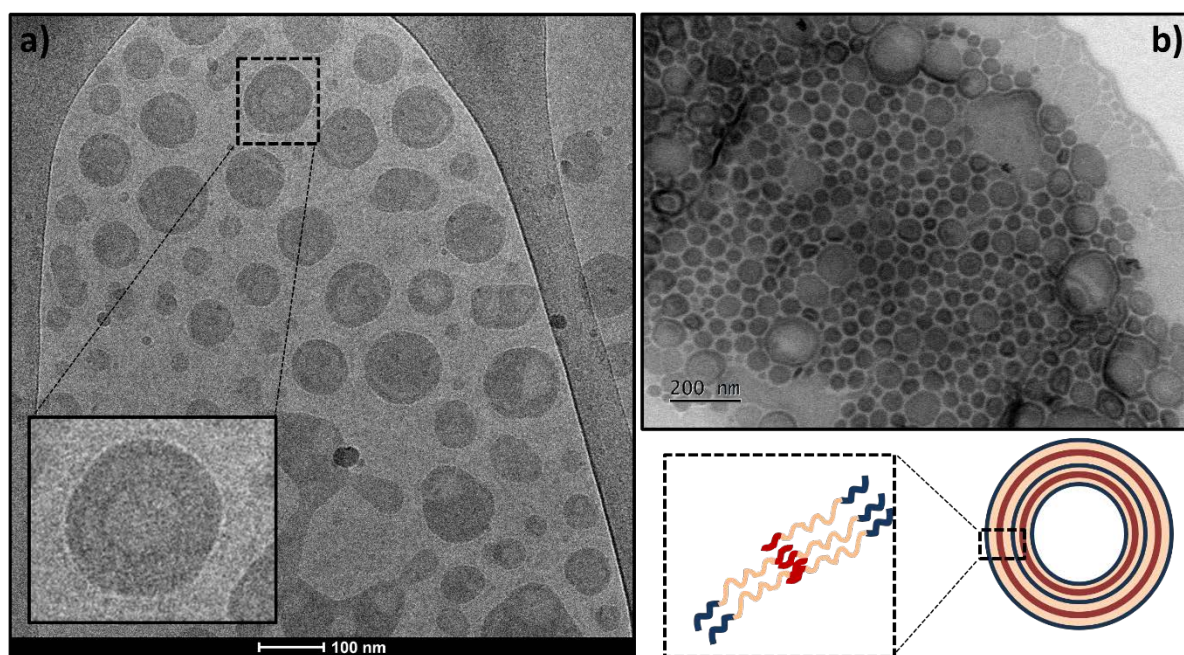


Figure 123: Comparison of a) cryo-TEM image of the triblock copolymer and b) TEM image stained by osmium oxide OsO_4 . The sketch represents a bilamellar vesicle (*i.e.* having a double-membrane).

Self-assembly of triblock copolymers with IONPs:

After confirming that the triblock copolymer could produce vesicular structures and that the hydrophobic membrane had enough capacity to encapsulate hydrophobically coated IONPs, their common self-assembly by nanoprecipitation was studied.

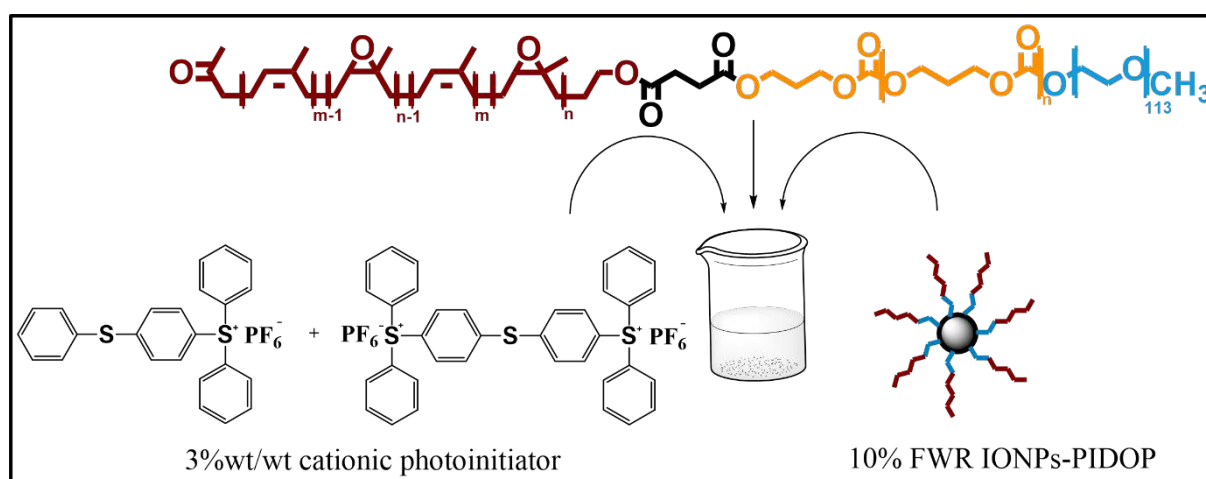


Figure 124: Sketch of the fast self-assembly process by nanoprecipitation of the triblock copolymer, together with 10% FWR IONPs-PIDOP, and 3% w/w cationic photo initiator.

At first, the terpolymer was self-assembled with 10% FWR of IONPs of core diameter $d_{\text{core}} \sim 6$ nm functionalized with short poly(isoprene) oligomers (PIDOP (C)) (Figure 124), producing nicely

spherical structures whose mean diameter was 130 ± 0.7 nm, as calculated from TEM image analysis with ImageJ (Figure 125). However, the TEM grids were stained with 2% samarium acetate and the sample was a bit too concentrated, thus, a lot of vesicles were stacked on top of each other. Nonetheless, the IONPs seem to be dispersed along the hydrophobic membrane with the PEG corona clearly visible, especially when there was an excess of staining on the image. Although the large outer diameters were indicative of polymer vesicles, it was difficult to claim the vesicular structure only from these TEM images, since the structures could also be filled magneto-core micelles.

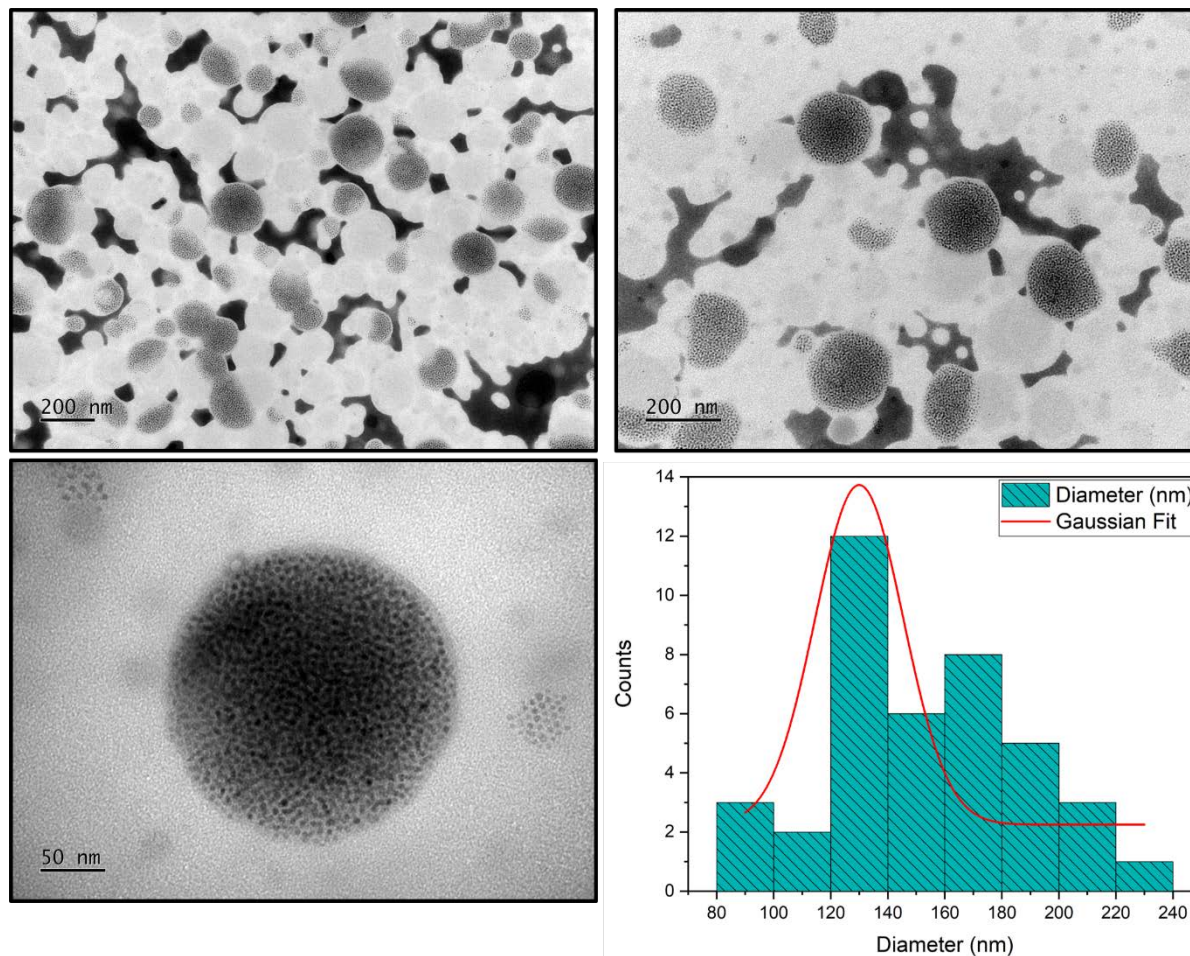


Figure 125: TEM images of PEG₁₁₄-*b*-PTMC₂₀₀-*b*-PI₄₀ self-assembled with 6% FWR of IONPs-PIDOP(C) of core diameter $d_{\text{core}} \sim 6$ nm +3% PhI, stained with 2% samarium acetate. The figure demonstrates the average diameter of the structures as determined by TEM image analysis using ImageJ.

To study how the functionalization of IONPs affected the self-assembly process, the triblock copolymers were also self-assembled with IONPs-OA functionalized with oleic acid. Both the smaller IONPs with a core diameter of 6 nm (polyol route) and the larger IONPs with a core diameter of 8 nm (coprecipitated ones) were self-assembled with a FWR of 70% and are presented in the images below. Figure 126 depicts the triblock copolymer PEG₁₁₄-*b*-PTMC₂₀₀-*b*-PI₄₀ (PP1PI7) with 70% FWR of IONPs-OA with a core diameter of 8 nm. The structures appeared to be spherical and almost “fluid” under the electron

beam, without a clear retention of their structures, thus the sample was unable to be characterized with electron microscopy techniques.

On the other hand, when the triblock copolymer was self-assembled with 70% FWR of IONPs-OA with a core diameter $d_{\text{core}}=6$ nm, much more defined structures were observed, as on Figure 127. The structures appeared more defined and well-packed. It was possible to calculate an average diameter of the structures by analyzing the TEM images, which was determined to be 65 ± 7 nm. The diameter calculated from TEM images was lower than the diameter determined from DLS measurements (Table 21), as the average hydrodynamic diameter appeared to be 167 nm. At this stage, the morphology of the structures was unclear from TEM imaging only, and more insight will arise later from small angle X-ray and neutron scattering experiment results (see the last part of this Chapter V).

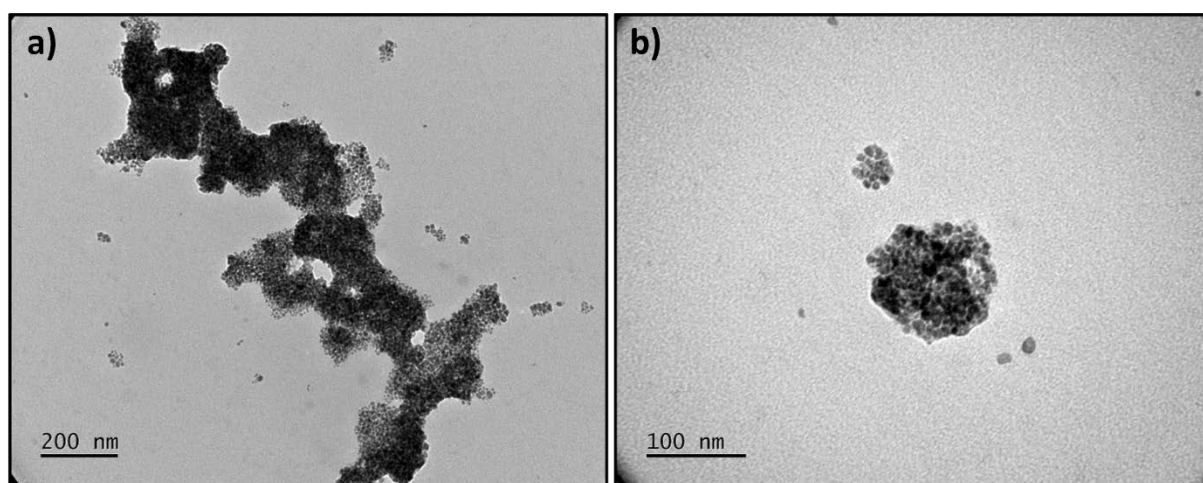


Figure 126: TEM images of (a, b) PEG₁₁₄-*b*-PTMC₂₀₀-*b*-PI₄₀ (PP1PI7) + 70% FWR IONPs-OA ($d_{\text{core}}=8$ nm).

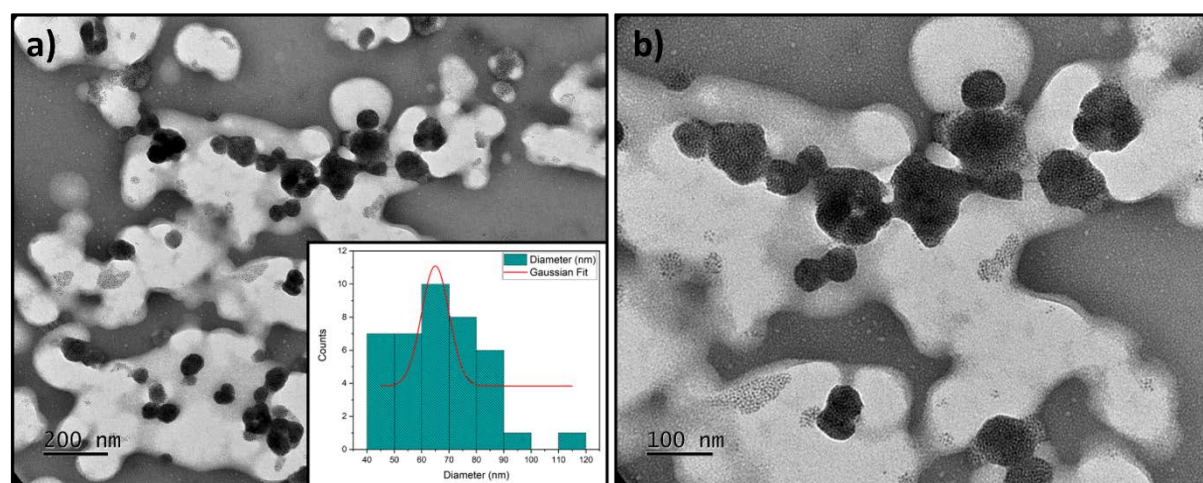


Figure 127: TEM images of (a, b) PEG₁₁₄-*b*-PTMC₂₀₀-*b*-PI₅₀ (PP14PI7) + 70% FWR IONPs-OA (Caruntu, $d_{\text{core}}=6$ nm), and histogram of outer sizes fitted with a Gaussian law of average diameter $d_{\text{TEM}}=65$ nm.

Table 21: DLS characteristics of the self-assembled triblock copolymers with IONPs

Sample	Diameter (nm)*	Z-average (nm) [‡]	PDI [‡]
PEG₁₁₄-<i>b</i>-PTMC₂₀₀-<i>b</i>-PI₄₀ (PP1PI7) +70% FWR IONPs-OA (<i>d</i>_{core}=8 nm)	210 (93%)	216.5	0.122
PEG₁₁₄-<i>b</i>-PTMC₂₀₀-<i>b</i>-PI₅₀ (PP14PI7) +70% FWR IONPs-OA (<i>d</i>_{core}=6 nm)	167 (87%)	183	0.173
PEG₁₁₄-<i>b</i>-PTMC₂₀₀-<i>b</i>-PI₅₀ (PP14PI7) +6% FWR IONPs- PIDOPC (<i>d</i>_{core}=8 nm)[†]	160 (94%)	161	0.118

* by Padé-Laplace (multimodal) fit of auto-correlogram (percentage indicates the weight of the mode); [‡] by 2nd order cumulants fit; [†] after UV crosslinking under 0.4 T magnetic field.

Study of the cross-linking process of the hydrophobic membrane of vesicles made of the triblock copolymer and their elongation under a static magnetic field:

The cross-linking process of the triblock copolymer was studied in a similar matter as described above for the graft copolymers. The poly(isoprene) block of the triblock copolymer was functionalized with epoxide groups in order to deem it capable of being cross-linked *via* a ring opening reaction of the epoxides by the use of a cationic photo-initiator. The same photo-initiator (PhI.), triaryl sulfonium hexafluorophosphate salts mixed in 50% propylene carbonate solvent, was used in this case. The activation mechanism and cross-linking process were already described in Figure 1 and 2 respectively.

To verify that the triblock copolymer can react with the PhI. after exposure to UV light at a wavelength around 300 nm, the reaction was studied by ¹H NMR spectroscopy in a similar matter as it was described in the sub-chapter above regarding the cross-linking of the graft copolymers. In short, the triblock copolymer was solubilized in deuterated chloroform with 3% w/w of PhI. and the NMR tube was exposed to UV for a duration of 5 min, twice, to initiate the ring opening reaction of the epoxides. The figure (Figure 128) below reveals that after 5 min of exposure, the network formation was initiated, and post 10 min of UV exposure, the epoxides were no longer present, a fact which was verified by the disappearance of the peaks at 2.65 and 1.15 ppm. Moreover, a visible decrease of the peak at 5.15 ppm (ethylenic protons of the poly(isoprene)) suggests formation of a dense network which obstructed the protons from being visible and detected by classical liquid state NMR.

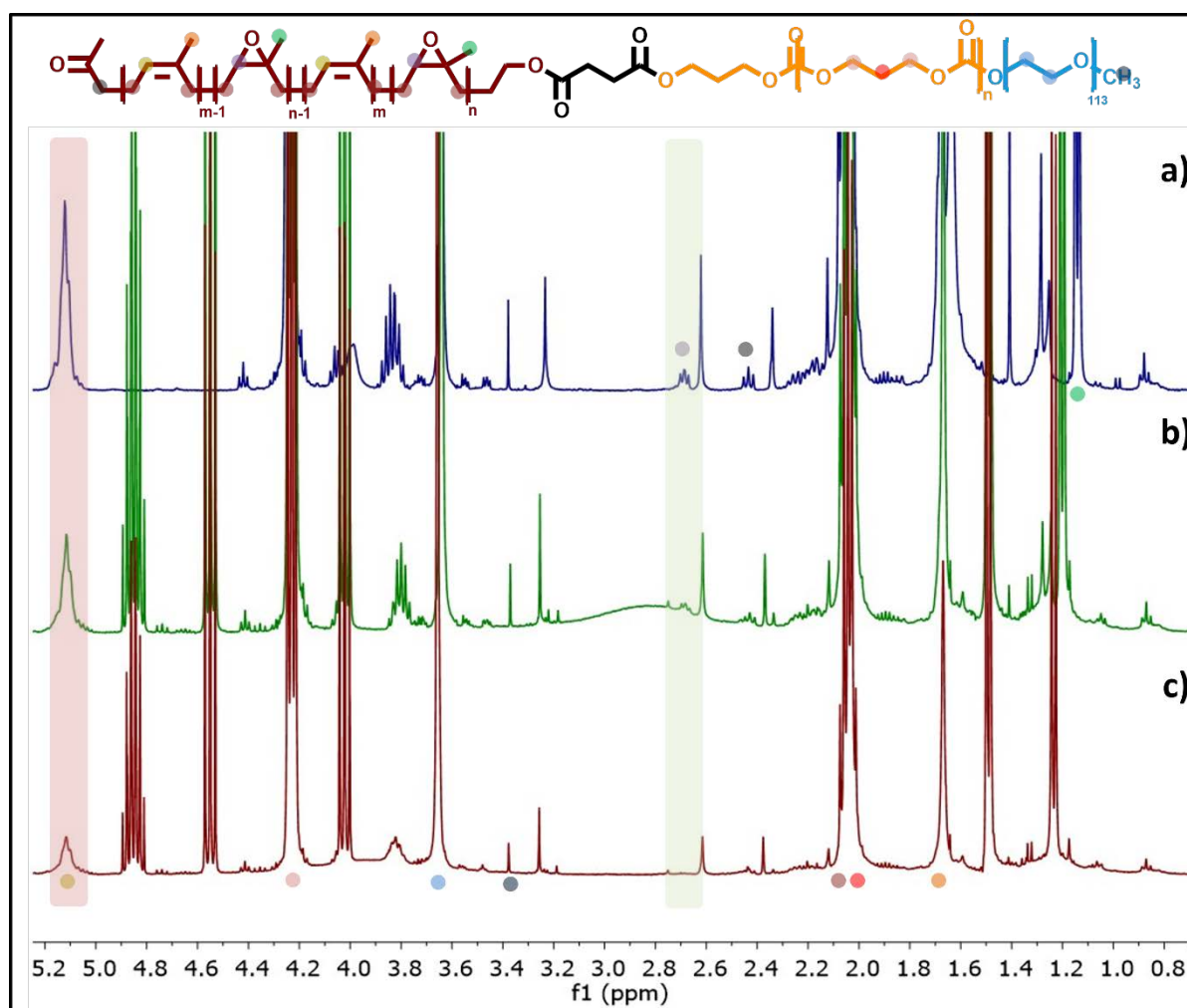


Figure 128: ^1H NMR spectra of a) 9% epoxidized $\text{PEG}_{114}\text{-}b\text{-PTMC}_{200}\text{-}b\text{-PI}_{40}$ + 3% w/w PhI. with no UV irradiation, b) 8% epoxidized $\text{PEG}_{114}\text{-}b\text{-PTMC}_{200}\text{-}b\text{-PI}_{50}$ + 3% w/w PhI. after 5 min of UV irradiation and c) 8% epoxidized $\text{PEG}_{114}\text{-}b\text{-PTMC}_{200}\text{-}b\text{-PI}_{40}$ + 3% w/w PhI. after 10 min of UV irradiation.

Thus, it was concluded that the triblock copolymer indeed responded to UV as expected and even 5 min of irradiation at 75% lamp intensity was enough to initiate the cross-linking. The cross-linking of the self-assembled triblock copolymer along with IONPs was investigated by TEM imaging, as HR-MAS NMR was possible only through collaboration, therefore not for a kinetic.

The self-assembled sample of $\text{PEG}_{114}\text{-}b\text{-PTMC}_{200}\text{-}b\text{-PI}_{50}$ with an epoxidation rate of 9% mixed at 70% FWR with IONPs-OA (Caruntu synthesis, of $d_{\text{core}}=6$ nm) was irradiated with UV light for 10 min and 20 min equally, with a Hamamtsu UV lamp with a 280-400nm wavelength range and 70% power, at 1 cm distance. Following the irradiation, the sample was imaged by TEM. Unfortunately, no clear visible transformation was observed on the spherical structures. While this could be expected since the poly(isoprene) block is not truly visible with this imaging technique, one can observe that the space that the IONPs take in the self-assembled structure became slightly denser and more defined, especially after 20 min of irradiation (Figure 129c). Another observation is that the grey matter of the corona where the

IONPs are embedded in seems to fuse between adjacent objects, although this is not fully conclusive that the crosslinking was successful.

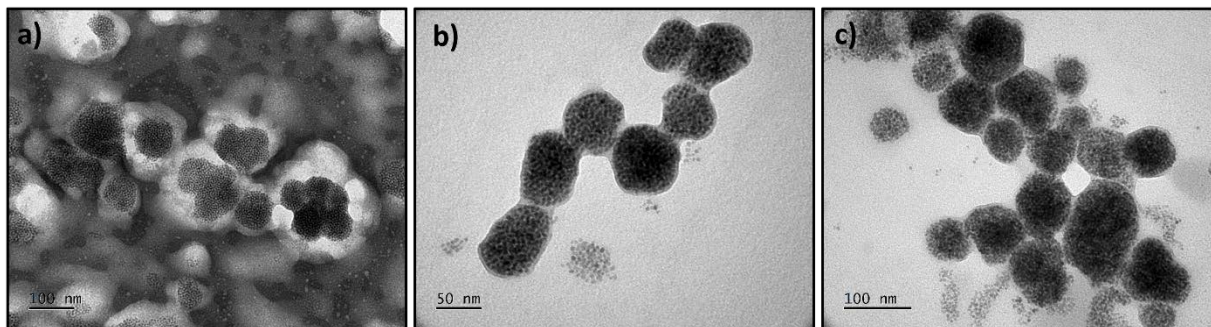


Figure 129: TEM images of 8% epoxidized PEG₁₁₄-*b*-PTMC₂₀₀-*b*-PI₅₀ + 6% w/w PhI. + 70% IONPs-OA (Caruntu synthesis, $d_{\text{core}}=6$ nm) a) control with no UV irradiation, b) 10 min UV irradiation and c) 20 min of UV irradiation.

It was decided to continue with the application of a magnetic field onto these structures nonetheless, since the ^1H NMR (without IONPs) does reveal that the cross-linking mechanism indeed works. An increase of irradiation time was implemented as well to strengthen the cross-linked network in the case that 20 min was not enough, in view also of the UV absorption by the IONPs. As such, the sample was inserted into the static magnetic field created by the Halbach array of magnets, whose structure is depicted in Figure 115. The sample was irradiated with a 70% intensity of the UV lamp for 40 min while being in the magnetic field of 0.4 T. The images of the sample presented remarkable results, with a visible stabilized elongation of the structures (Figure 130). While some spherical structures were still visible, the majority seemed to be of an anisotropic nature. To characterize the elongated nature of the structures, the long axes were measured to determine the average length of the final structures (Figure 131). Due to the fact that the sample before an application of a static magnetic field already had structures that presented some anisotropy, the images were analyzed with ImageJ by calculating the anisotropy parameter $R=b/a$ where b stands for the length of the long axis of the structures while a stands for the length of the short axis (Figure 132).

By comparing the control group and the UV+MF exposed sample, it was observed that the R parameter shifted to higher values post MF exposure. The average value R for the control group was determined to be 1.1 ± 0.05 while the average R for the MF+UV group was 1.3 ± 0.1 , while in general structures with higher R parameter had a higher frequency of appearing when compared with the control group. It is important to note that if the R parameter equals to 1 then no anisotropy is observed, *i.e.* $a=b$. This measurement as already mentioned above is not definitive, due to the small amounts of samples and unclear limits of the membranes in some cases, nonetheless this result can still be utilized as it is at the very least indicative of an anisotropic sample.

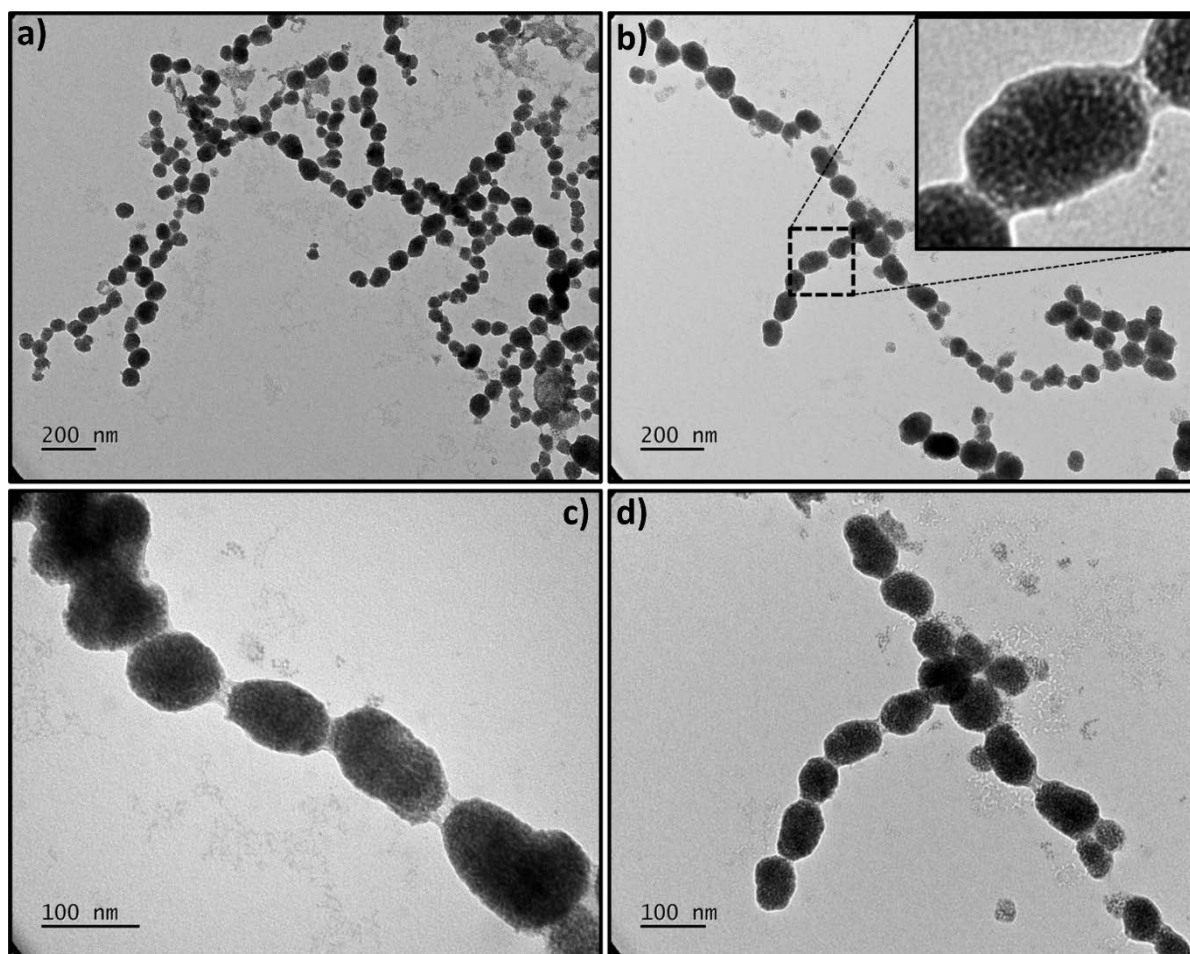


Figure 130: TEM images of (a-d) $\text{PEG}_{114}\text{-}b\text{-PTMC}_{200}\text{-}b\text{-PI}_{52}$ + 6% w/w PhI. + 70% IONPs-OA (Caruntu synthesis, $d_{\text{core}}=6$ nm) post UV and MF application through the “5.15.30.5” protocol (5 min UV on out of field, 15 min in field UV off, 30 min in field UV on). The TEM grid was stained with 2% samarium acetate.

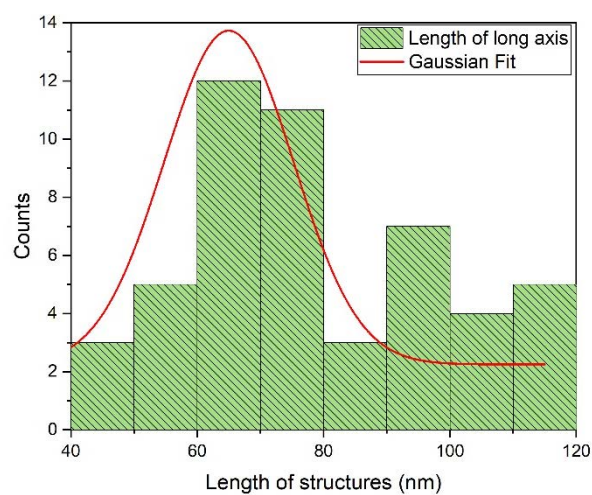


Figure 131: Determination *via* ImageJ of the length of the long axis of the elongated structures, indicating an average length of 65.0 ± 3.4 nm.

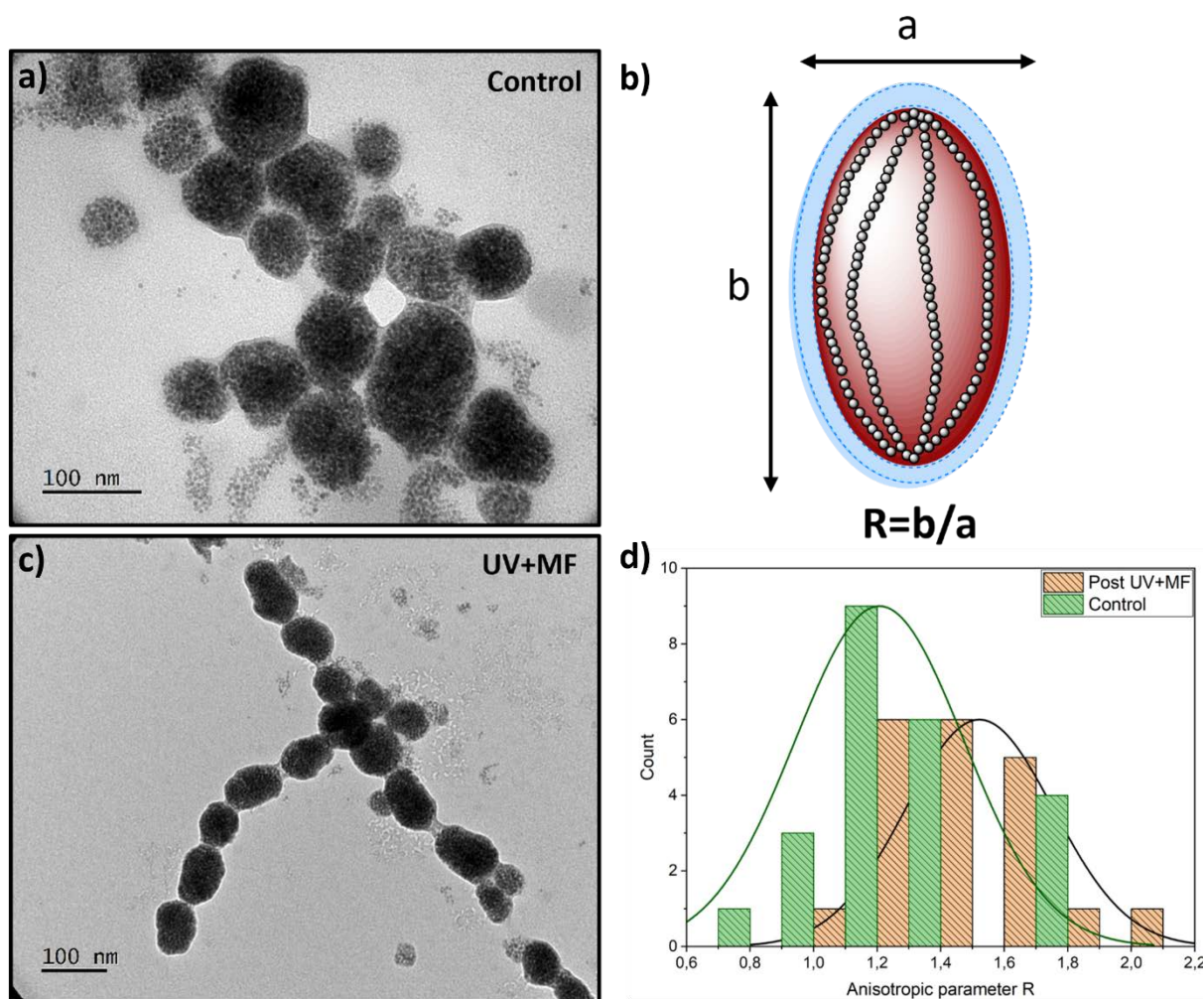


Figure 132: Determination of the anisotropy parameter R before and after application of a static MF and UV, with a) a TEM image of the magnetic polymersomes before UV+MF exposure (control), b) a schematic representation of the R parameter, c) TEM image of the magnetic polymersomes post UV+MF irradiation (UV+MF) through “5.15.30.5” protocol and d) a graph of the anisotropy parameters which were calculated from the TEM images of the control and UV+MF groups, respectively.

The length of the long axis (Figure 131) of the final elongated structures in Figure 130 has an average of $65.0 \pm 3.4 \text{ nm}$ which is similar to the initial diameter which was calculated for the control sample before UV and MF application, as can be seen in Figure 127, which demonstrates the structures with an average diameter of $65.0 \pm 7 \text{ nm}$. These results suggest that while elongation occurs, the average size of the structures does not change overall, with the main difference to appear in the short axis which becomes shorter post MF, resulting into a structure which resembles elongated (prolate) ellipsoids. While interestingly we can observe the chaining effect being present in these samples as well, suggesting perhaps a cross-linking between the membranes of the polymersomes.

Similar procedures were implemented on the triblock copolymer which had larger IONPs embedded in it. More specifically PEG₁₁₄-*b*-PTMC₂₀₀-*b*-PI₄₀ (PPIPI7) which had an epoxidation rate of 15% was self-assembled with 6% w/w PhI. and a 70% FWR of IONPs-OA with larger core diameter $d_{\text{core}}=8$ nm. Figure 126 depicts the control group of the resulted from this self-assembly process, but as already discussed in that section the sample did not present a clear image, with the structures to appear almost “broken” and not depicting a clear morphology due to aggregates. From individual images the structures appeared spherical, but it was not clear whether they represented vesicles or magneto-core micelles.

In this case, the sample was irradiated in a similar manner that was described in the graft copolymer section, *i.e.* the method “5.15.30.5” where it was first irradiated for 5 min while in the MF, then left in the field with no irradiation for 15 min, proceeding with 30 min of UV irradiation while still in the MF and finally 5 minutes of MF alone in order to let the structure settle. The total amount of irradiation was 35 min, slightly lower than the time above, while the MF exposure was a total of 55 min.

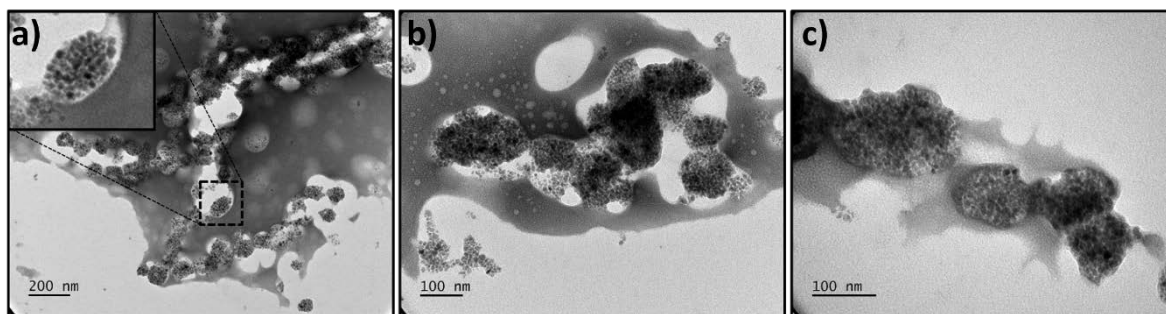


Figure 133: a-c) TEM images of PEG₁₁₄-*b*-PTMC₂₀₀-*b*-PI₄₀ (PPIPI7) triblock with an epoxidation rate of 15% + 6% w/w PhI. + 70% FWR of IONPs-OA (coprecipitation route, $d_{\text{core}}=8$ nm). The TEM grid was stained with 2% samarium acetate.

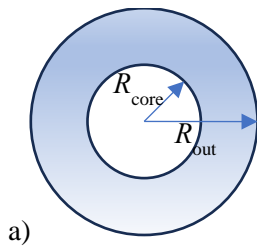
While the images revealed more defined structures compared to the control sample from Figure 126 and some elongation was indeed visible, it was not possible to accurately calculate the size of the structures nor the anisotropy parameter due to poor image definition. Nonetheless, a lot of anisotropic structures were observed but it was difficult to determine the differences between the control group and the one post MF+UV, perhaps the only certain parameter that can be observed is the fact that the structures seem more defined, suggesting that the cross-linking process indeed took place, thus stabilizing the structures.

DLS, SAXS and SANS study of magnetic polymersomes, out and in B_{DC} magnetic field

In order to decipher whether the magnetic polymersomes actually deform under an applied magnetic field, samples representative of the two systems (graft copolymers or linear triblock) were studied by small angle X-ray and neutron scattering techniques, with both sizes of IONPs $d_{core} \sim 6$ or 8 nm, in the case of the OA coating, at FWR values of 70 or 50%, respectively. The first performed were the SAXS experiments, as a Xenocs Xeuss 2.0 instrument is available on campus, with the aim to do SANS later one, which is possible only at an international neutron source like the ILL, in Grenoble. As our initial beam time requirement was not accepted by the reviewing committee (due to important load on the SANS instruments and a said insufficient justification by us in our proposal of the need of neutron scattering as compared to X-ray beam at a synchrotron), we had only a test experiment during the FAN2021 workshop for new trainees in neutron scattering, and an EASY experiment of 24 hours allocated by ILL direction on June 20th 2023. Nevertheless, this beam time was sufficient to improve our knowledge of our systems under magnetic field, as will be presented thereafter.

Structural study by X-ray (SAXS) and neutron (SANS) small angle scattering of grafted and triblock copolymers self-assemblies, with or without co-assembled IONPs:

To start with, SANS curves of “blank” amphiphilic diblock and triblock copolymers (*i.e.* not loaded with IONPs) self-assembled by fast nanoprecipitation in deuterated solvent mixture (D_2O : d_8 -THF 10:1) were acquired on D22 spectrometer of the ILL during the FAN2021 training school on neutron scattering (EASY-1045 experiment). The curves are plotted in I vs. q and $I \times q^2$ vs. q representations on Figure 135a) and b), the latter plot enabling to highlight vesicle shape [35]. To get insight on morphology and mean dimensions of the self-assemblies, the SANS intensity curves were fitted by a polydisperse shell form factor, as described by Jan S. Pederson [36], which formula is illustrated on Figure 134.



$$H_{shell} = R_{out} - R_{core}$$

$$R_{shell} = (R_{out} + R_{core})/2$$

$$b) I(q) = \phi(\rho_{polymer} - \rho_{solvent})^2 P(q, R_{core}, R_{out})$$

$$\text{with } P(q, R_{core}, R_{out}) = \left[\frac{V(R_{out})F(q, R_{out}) - V(R_{core})F(q, R_{core})}{V(R_{out}) - V(R_{core})} \right]^2 \quad (13)$$

$$\text{where } V(R_{out}) = \frac{4}{3}\pi R_{out}^3 \text{ is the outer volume of the vesicle,}$$

$$V(R_{core}) = \frac{4}{3}\pi R_{core}^3 \text{ is the volume of its internal compartment,}$$

$$\text{and } F(q, R) = 3 \frac{\sin(qR) - (qR) \cos(qR)}{(qR)^3} \quad (14)$$

$$c) P(R, R_0, \sigma_R) = \frac{1}{R\sigma_R\sqrt{2\pi}} e^{-\frac{(\ln R/R_0)^2}{2\sigma_R^2}} \quad (15)$$

$$d) P(H, H_0, \sigma_H) = \frac{1}{H\sigma_H\sqrt{2\pi}} e^{-\frac{(\ln H/H_0)^2}{2\sigma_H^2}} \quad (16)$$

Figure 134: a) Sketch and b) theoretical shell form factor used to fit the SANS curves. The formula is convolved with log-normal distribution laws of median radius R_0 , median thickness H_0 , and broadness values σ_R and σ_H for the shell **radius c)**

$P(R_{\text{shell}}, R_0, \sigma_R)$ and the shell thickness $d) P(H_{\text{shell}}, H_0, \sigma_H)$, respectively. In particular, $P(q \rightarrow 0) = \frac{\langle V_{\text{shell}}^2 \rangle}{\langle V_{\text{shell}} \rangle}$, where $V_{\text{shell}} = V(R_{\text{out}}) - V(R_{\text{core}})$ is the volume of the hydrophobic copolymer blocks constituting the vesicle membranes, and $\langle \rangle$ represents ensemble averaging on the two distributions.

In practice, we chose to set the neutron SLD contrast $\Delta\rho = \rho_{\text{objects}} - \rho_{\text{solvent}}$ and volume fraction ϕ of objects at their theoretical values (the former at the calculated value of semicrystalline PTMC, the latter computed from the hydrophobic block concentration and mass density. Then to find the four geometrical parameters describing the distribution of vesicle radii and thicknesses R_0^{fit} (σ_R^{fit}) and H_0^{fit} (σ_H^{fit}), we proceeded with the following systematic method. At first, we determined the radius of gyration of the objects (independent on any assumption on their shape) R_G from a Guinier plot of the first data plot at lowest scattering vectors q :

$$\lim_{q \rightarrow 0} \ln I(q) \cong \ln I(0) - \frac{q^2 R_G^2}{3} \quad (17)$$

$$\ln[I(q) \times q^2] \propto -\frac{q^2 H_{\text{KP}}^2}{12} \quad (18)$$

The R_G value was taken from a low number of points (usually less than 5) so as to insure a coefficient of determination $R^2 \geq 0.95$ for the linear regression of the $I(q \rightarrow 0)$ curve in the Guinier plateau Eq. (17). Then we plotted the data in the so-called Kratky-Porod representation [37] $\ln[I(q) \times q^2]$ vs. q^2 for the intermediate q -range. Again, the data points were carefully chosen to maximize the R^2 value when fitting them with Eq. (18), which enables to determine an average membrane thickness H_{KP} . Those two characteristic dimensions were determined unequivocally though with some experimental uncertainty. Then the whole $I(q)$ curve was fitted with the set of Eqs. (13-16). In practice, we used a home-made MS Excel spread sheet calculating a numerical integral of Eqs. (13-14) convoluted with Eqs. (15-16). More precisely, the double integral was approximated by trapeze formulas in each interval δR and δH over a 60×60 matrix of $[R, H]$ values chosen on sufficiently broad ranges to describe the two statistical distributions of shell radius and shell thickness. Our numerical method to assess the theoretical form factor of polydisperse vesicles has been compared to results obtained with the well-known SASview software (<https://www.sasview.org/>) to be sure that there was no mistake in the calculation.

The reason why we preferred to use Excel to fit the experimental curves $I(q)$ rather than SASview is because we can better check the physical relevance of the fits. As previously stated, we set the contrast and the volume fraction of objects to their theoretical values, thus we left four parameters R_0^{fit} , σ_R^{fit} , H_0^{fit} , and σ_H^{fit} to be varied. We defined two quadratic error functions $\chi_1 = \sum_i (I_{q_i}^{\text{exp}} - I_{q_i}^{\text{fit}})^2$ and $\chi_2 = \sum_i (I_{q_i}^{\text{exp}} \times q_i^2 - I_{q_i}^{\text{fit}} \times q_i^2)^2$ (where the i index varies over the whole set of experimental data points, which can be reduced to ~120 by a preliminary sliding average process) and we asked the Solver tool of Excel to minimize their sum $\chi_1 + \chi_2$ so that the curve is fitted both in the low- q and the high- q ranges. An important point is that we ask the Solver to verify three constraints so that the optimal values of the four variable parameters are physically relevant. To do so, we computed the “intensity-averages” (also

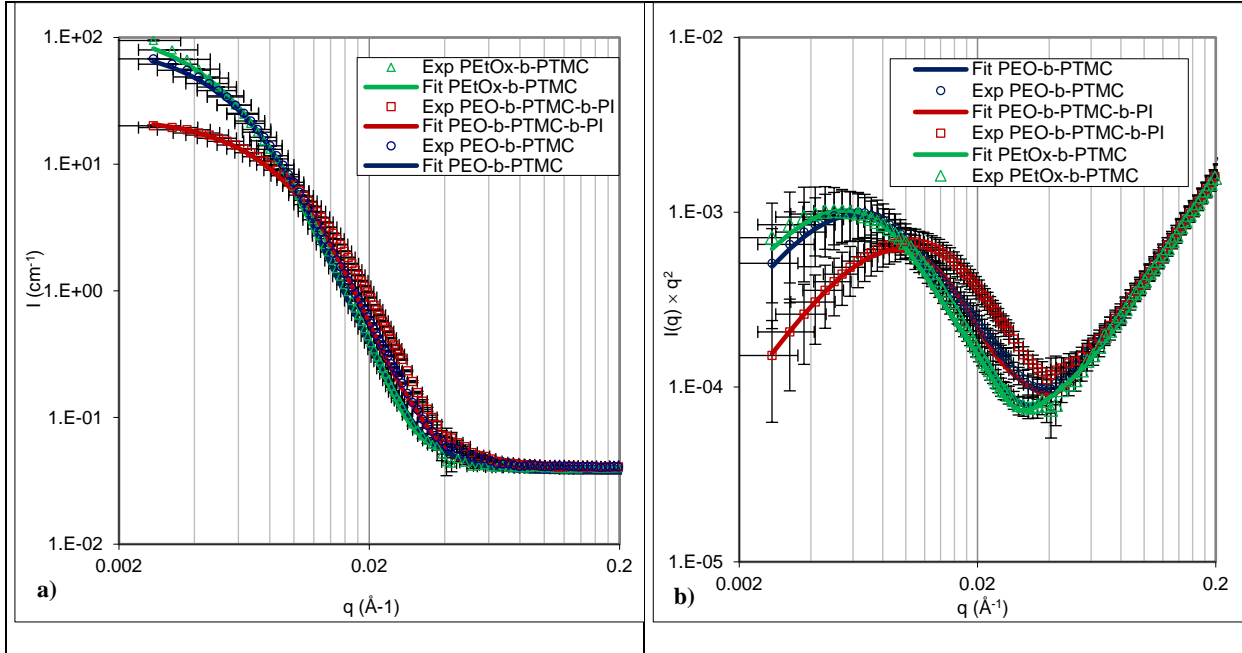
called “Z-averages”) of the two distributions R_Z^{fit} and H_Z^{fit} (easily computed from the standard formulas of the n^{th} order statistical momentums of the log-normal distribution law). The first physical constraint is then that the Z-average internal core radius of the vesicles is positive, meaning that the objects really show an aqueous compartment, otherwise if they were totally filled, they would be micelles. The two other constraints are that the R_Z^{fit} and H_Z^{fit} calculated values of the fitted curves match exactly with the two experimentally determined values R_G and H_{KP} , respectively. The first equality $R_Z^{\text{fit}} = R_G$ is a well-known property of vesicle morphology[38] (their hydrodynamic and gyration radii are equal as all the points of the shape have identical distance to the center of mass). As for the second constraint $H_Z^{\text{fit}} = H_{KP}$, we are not sure if it has theoretical grounds, but we used it by analogy to the first one, and it always led to good results. The efficacy of our fitting method can be appreciated on Figure 135 with the relatively good accordance between experimental and fitted curves in both $I(q)$ vs. q and $I(q) \times q^2$ vs. q representations (the latter better highlighting the high- q region). The determined fitted parameters are listed in Table 22.

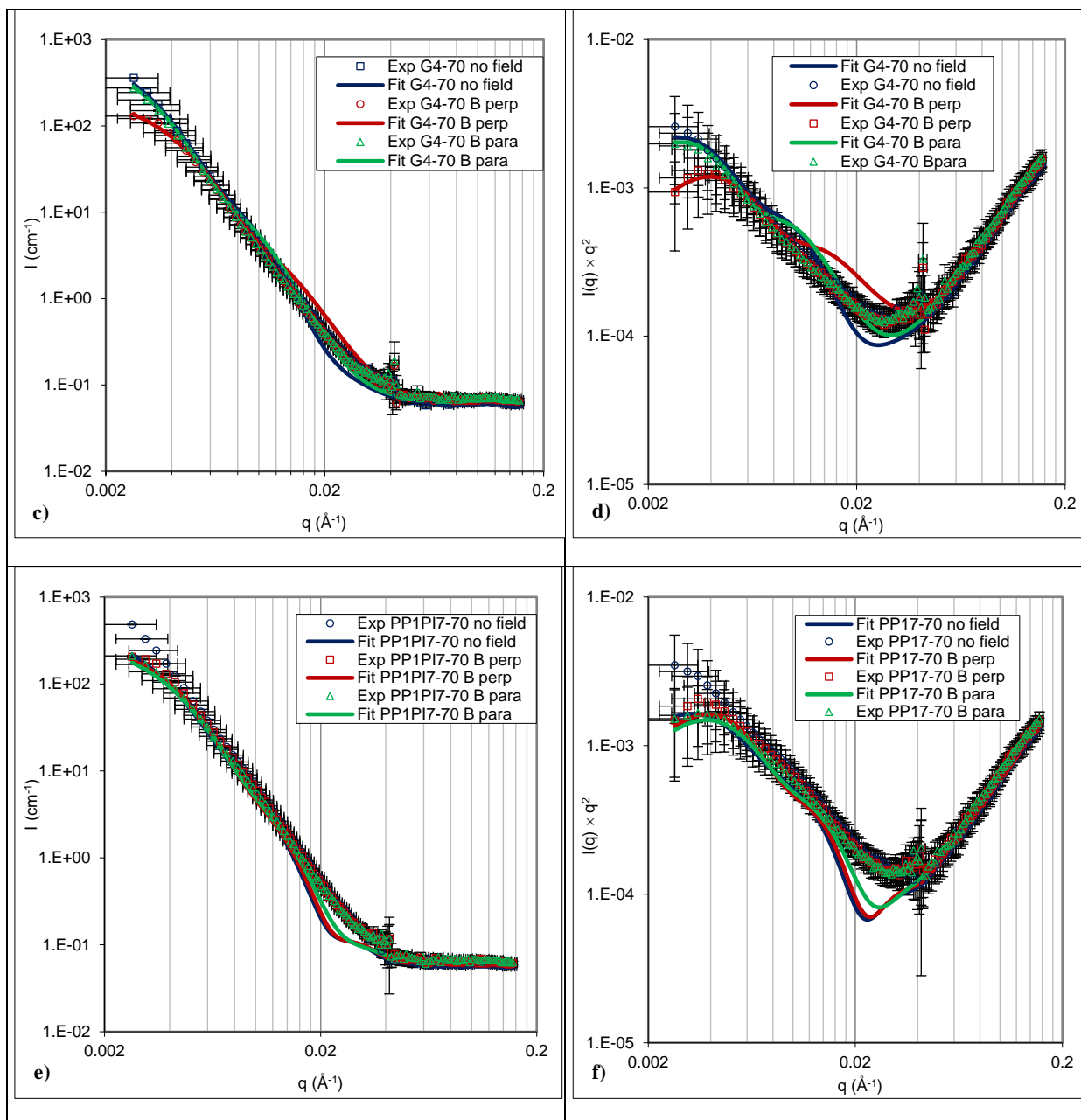
As a first result, we see that two diblock copolymers POXP3 and PP5 exhibit analogous SANS curves, evidencing that they both self-assemble into vesicular objects with a membrane thickness $H_{KP}=25 \pm 1$ nm that is close to expectation from the scaling law derived by Lebleu *et al.* [31] for PTMC-based amphiphilic copolymers with a DP of TMC around 160. Instead of PEG, POXP3 has a different hydrophilic block, which is a poly(2-ethyl-2-oxazoline) also of $M_n=5$ kg·mol⁻¹, which was provided to us (with an amino chain-end) by Katerina Mathianaki, who is doing her PhD thesis with Pr Guillaume Delaittre at the University of Wuppertal in Germany in order to perform the ROP of TMC as described in Chapter IV. Although we were not able to demonstrate that the synthesis of a diblock copolymer was successful in that case, we observed that the final product self-assembled into vesicles. The third blank copolymer studied by SANS, PEG₁₁₄-*b*-PTMC₁₆₇-*b*-PI₄₄ (PP3PI5), shows significantly lower size, both by its hydrodynamic radius in DLS and its gyration radius measured by SANS. The shell thickness also is smaller, $H_{KP}=16$ nm, although the central PTMC block had the same degree of polymerization than the two previous diblock copolymers. This can be ascribed to higher compaction and entanglement degrees of the chains as ascribed to a higher hydrophobic interaction expected for the PI end-block as compared to the more polar PTMC block.

The second SANS experiment (EASY-1093) was performed on two copolymers, respectively PEG₁₁₄-*b*-PTMC₂₀₀-*b*-PI₄₀ (PP1PI7) and PEG₁₁₄-*b*-PATC₂₀-*g*-PI₅ (G4), both being loaded at either 70% FWR with IONP@OA^{6nm} (polyol synthesis) or at 50% FWR with IONP@OA^{8nm} (coprecipitation). As before, the solvent was fully deuterated (D₂O: d8-THF 10:1), therefore the signal was detected at full contrast, *i.e.* with the contributions of the nuclear contrast of the hydrophobic copolymer blocks and of the magnetic contrast of the IONPs, both of them with solvent being $\Delta\rho \sim 5.1 \pm 0.4 \times 10^{10}$ cm⁻² (see the exact values of SLD calculations in the Methods of characterization part). This can explain why the values of

membrane thicknesses H_{KP} reported in Table 22 appear systematically larger for these IONP-loaded vesicles as compared to the blank ones, from 25 nm for G4 graft polymer loaded at 50% FWR with 8 nm core IONPs to 44 nm for G4 embedding 6 nm core IONPs at 70% FWR, while PP1PI7 triblock led to shells of $H_{KP} \sim 32$ nm thickness with both combinations of IONP type and FWR value. We can deduce that the hydrophobically coated IONPs are efficiently embedded in the hydrophobic leaflets of the membranes, forming one or two layers at most of IONPs. In addition, from the entries of Table 22, the hollow shell morphology is maintained for all the IONP-loaded self-assemblies as there is always a large radius R_{core} of internal aqueous compartment, ranging from 37 to 47 nm, this core size increase compared to blank objects being correlated with the increase of hydrodynamic size in DLS.

The effect of an applied magnetic field and its direction relatively to the incident neutron beam on these four samples will be discussed in detail in a forthcoming part, but the quality of the numerical fitting procedure described beforehand can already be appreciated on the graphs shown on Figure 135. Globally, the SANS curves are rather well fitted in the low and intermediate q -ranges, with some discrepancies tough in the high- q region (better seen in the Kratky-Porod plot of $I \times q^2$), as presumably ascribed to a degree of roughness of the IONP-loaded membranes (at a scale lower than their diameter *i.e.* at $q \geq 2\pi/d_{core} \sim 0.1 \text{ \AA}^{-1}$) as compared to perfectly flat interfaces assumed in the model Eqs. (13-16).





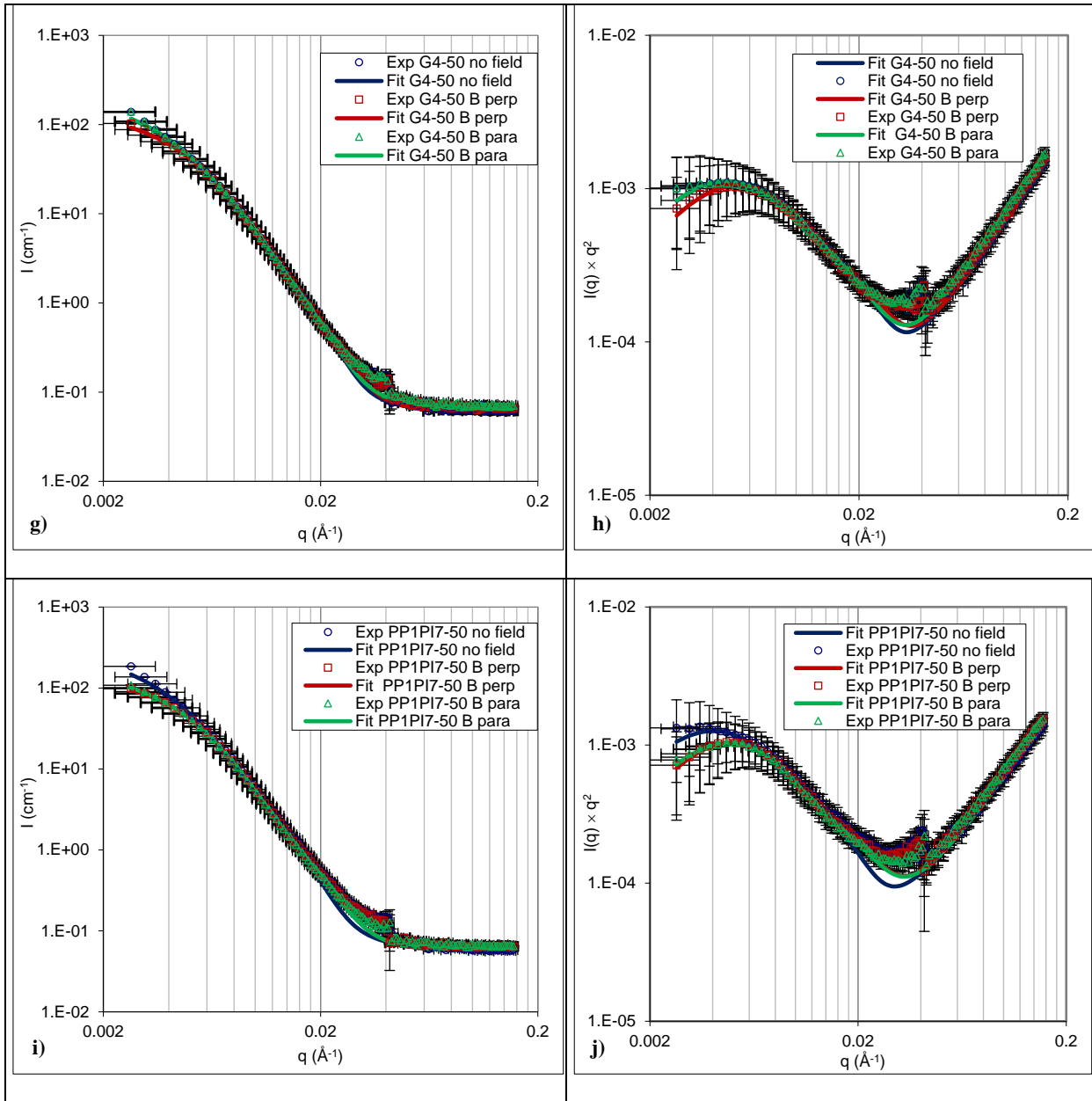


Figure 135: a), c), e), g), i) SANS curves $I(q)$ and b), d), f), h), j) SANS data in “Kratky-Porod like” representation $I \times q^2$ vs. q of different copolymer self-assemblies with and without IONPs: a), b) PEO₅₀-*b*-PTMC₁₆₇ (POXP3), PEG₁₁₄-*b*-PTMC₁₅₇ (PP5), and PEG₁₁₄-*b*-PTMC₁₆₇-*b*-PI₄₄ (PP3PI5); c), d) PEG₁₁₄-*b*-PATC₂₀-*g*-PI₅ (G4) + 70% IONP@OA^{6nm}; e), f) PEG₁₁₄-*b*-PTMC₂₀₀-*b*-PI₄₀ (PP1PI7) + 70% IONP@OA^{6nm}; g), h) PEG₁₁₄-*b*-PATC₂₀-*g*-PI₅ (G4) + 50% IONP@OA^{8nm}; i), j) PEG₁₁₄-*b*-PTMC₂₀₀-*b*-PI₄₀ (PP1PI7) + 50% IONP@OA^{8nm}. The solid lines correspond to least-square numerical fits to polydisperse vesicle shell form factor assuming a theoretical neutron SLD of hydrophobic block $\rho_{\text{PATC-g-PI}} = 8.4 \times 10^9 \text{ cm}^{-2}$ for grafted copolymer and $\rho_{\text{PTMC}} = 1.7 \times 10^{10} \text{ cm}^{-2}$ for linear terpolymer and volume fraction $\phi = C_{\text{pol}} \times (1-f)/d$ where f is the hydrophilic weight fraction of the given copolymer and d is its mass density, taken as the one of semi-crystalline PTMC, $d = 1.33 \text{ g} \cdot \text{cm}^{-3}$ for both the linear and the grafted terpolymers. Polydispersity was modelled by convolving the theoretical form factor $P(q, R_{\text{core}}, R_{\text{out}})$ with log-normal distributions of widths σ_R for the radius R_{shell} and σ_H for the shell thickness H_{shell} (see sketch on Figure 134). The total polymer concentration C_{pol} was always kept constant at $0.5 \text{ mg} \cdot \text{mL}^{-1}$ (even for measurements under \perp or \parallel magnetic field), corresponding to volume fractions $\phi = 3.1 \times 10^{-4}$ for PP1PI7 linear terpolymer ($f=18\%$) and $\phi = 2.5 \times 10^{-4}$ for G4 grafted copolymer ($f=33\%$).

Table 22: DLS characteristics and structural parameters determined by SANS on samples out of magnetic field.

Sample (code, hydrophilic weight fraction f)	Main diameter (nm) [*]	Z-ave diameter (nm) (PDI) [⊥]	$R_G = R_Z^{\text{fit}}$ (nm) [†]	$H_{\text{KP}} =$ H_Z^{fit} (nm) [‡]	R_0^{fit} (nm) [¶] (σ_R^{fit}) [¶]	H_0^{fit} (nm) [¶] (σ_H^{fit}) [¶]	$R_{\text{core}} = R_Z^{\text{fit}}$ $- H_Z^{\text{fit}}/2$ (nm) [¶]
PEtOx₅₀-<i>b</i>-PTMC_{NA} (POXP3, 23%)**	145.5	145 (0.016)	37.4	26.3	13.1 (0.48)	21.3 (0.22)	24.2
PEG₁₁₄-<i>b</i>-PTMC₁₅₇ (PP5, 23%)	134	125 (0.13)	31.0	28.0	11.8 (0.46)	20.0 (0.27)	17.0
PEG₁₁₄-<i>b</i>-PTMC₁₆₇-<i>b</i>- PI₄₄ (PP3PI5, 20%)	87	88 (0.006)	20.0	16.0	8.5 (0.44)	14.9 (0.12)	12.0
PEG₁₁₄-<i>b</i>-PATC₂₀-<i>g</i>- PI₅ (G4, 33%) + 70% IONP@OA^{6nm}	159 (86%)	142.5 (0.17)	65.0	44.1	33.8 (0.38)	28.5 (0.31)	42.9
PEG₁₁₄-<i>b</i>-PATC₂₀-<i>g</i>- PI₅ (G4, 33%) + 50% IONP@OA^{8nm}	229 (77%)	223 (0.17)	49.9	24.9	16.4 (0.50)	16.8 (0.29)	37.5
PEG₁₁₄-<i>b</i>-PTMC₂₀₀-<i>b</i>- PI₄₀ (PP1PI7, 18%) + 70% IONP@OA^{6nm}	282 (65%)	239 (0.22)	63.3	31.6	26.5 (0.44)	28.2 (0.16)	47.5
PEG₁₁₄-<i>b</i>-PTMC₂₀₀-<i>b</i>- PI₄₀ (PP1PI7, 18%) + 50% IONP@OA^{8nm}	146 (63%)	172 (0.29)	53.0	32.8	19.4 (0.47)	20.9 (0.32)	36.6

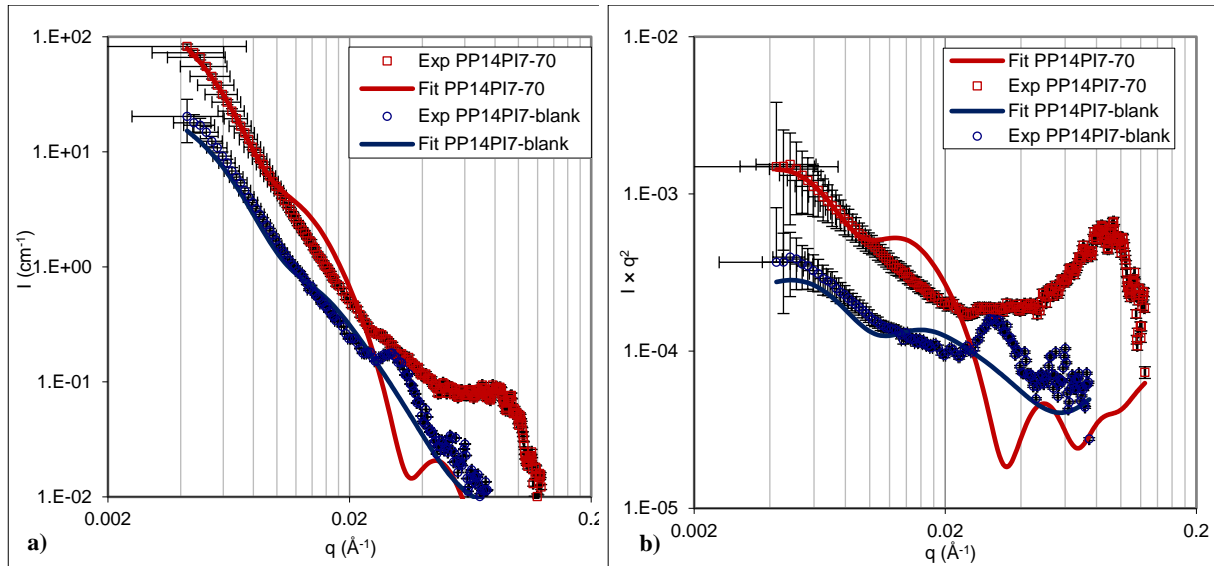
^{*} by Padé-Laplace (multimodal) fit of auto-correlogram (percentage indicates the weight of the mode); **NA: Not available; [⊥] by 2nd order cumulants fit, measured in deuterated solvent mixture D₂O:d8-THF (10:1) of viscosity $\eta=1.286 \times 10^{-3}$ Pa·s and refraction index $n=1.341$; [†] Gyration radius from Guinier fit at low q ; [‡] Mean shell thickness from Kratky-Porod fit at intermediate q range; [¶] obtained from fitting to polydisperse vesicle form factor assuming a theoretical neutron SLD of hydrophobic copolymer block $\rho_{\text{PTMC}}=1.7 \times 10^{10}$ cm⁻² for linear copolymer PP1PI7 and $\rho_{\text{PATC-g-PI}}=8.4 \times 10^9$ cm⁻² for grafted copolymer G4. Volume fraction is $\phi=C_{\text{pol}} \times (1-f)/d$ where f is the hydrophilic weight fraction of the given copolymer and d is its mass density, taken as the one of semi-crystalline PTMC, $d=1.33$ g·cm⁻³. Polydispersity was modelled by log-normal distributions of widths σ_R^{fit} for the radius and σ_H^{fit} for the shell thickness, and C_{pol} was kept at 0.5 mg·mL⁻¹. The Z-average

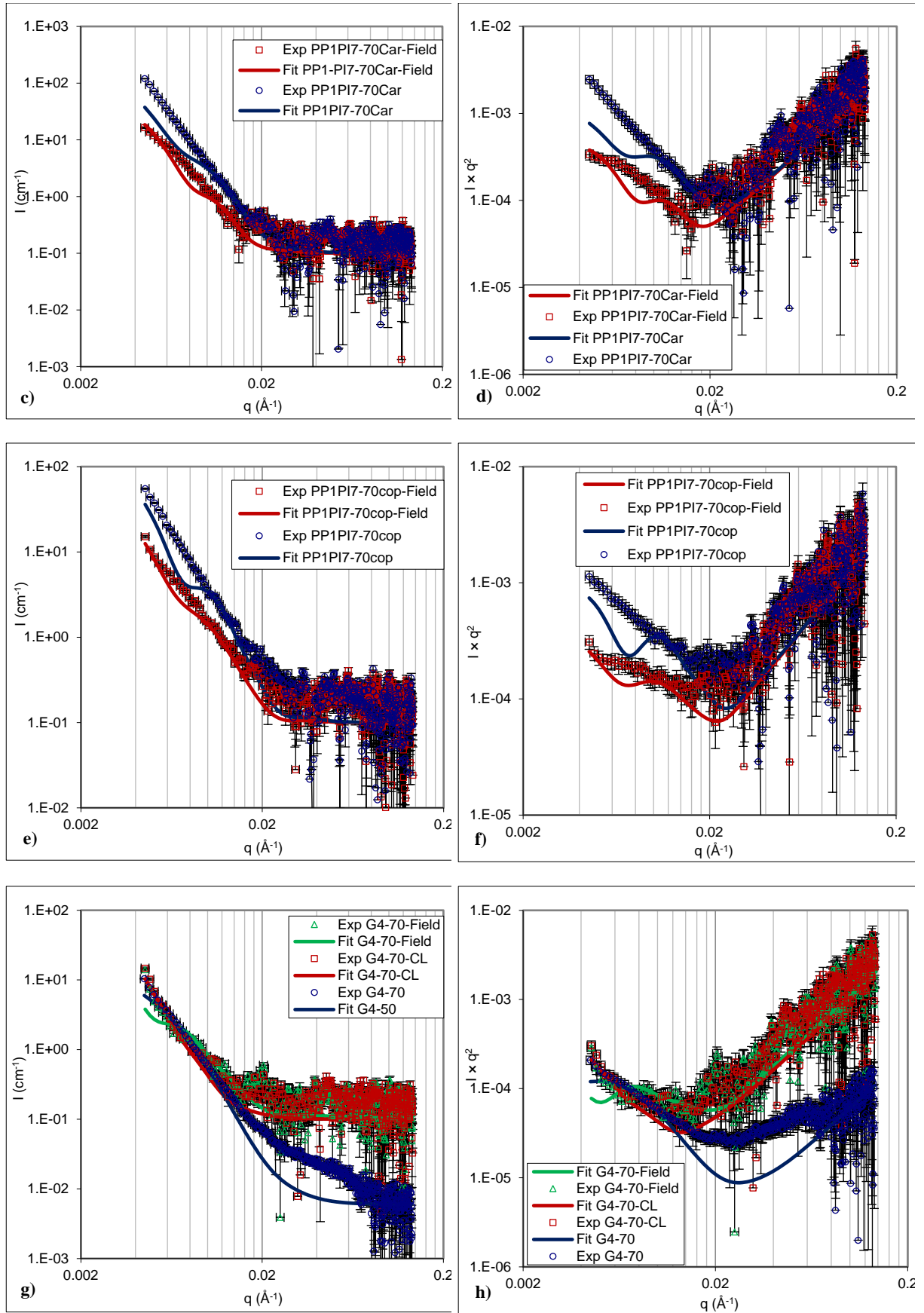
values of radius and thickness were computed from usual momentums of log-normal law: $R_Z^{\text{fit}} = \left(\frac{\langle R^6 \rangle}{\langle R^3 \rangle} \right)^{\frac{1}{3}} = R_0^{\text{fit}} e^{\frac{9}{2} \sigma_R^2}$ and $H_Z^{\text{fit}} = \left(\frac{\langle H^6 \rangle}{\langle H^3 \rangle} \right)^{\frac{1}{3}} = H_0^{\text{fit}} e^{\frac{9}{2} \sigma_H^2}$.

The same methodology was applied to fit the SAXS curves of our samples, except the concentration of copolymers that was not set at its nominal value of $0.5 \text{ mg}\cdot\text{mL}^{-1}$ because we were unsure that the scattered intensity was retrieved in absolute cm^{-1} unit like in SANS, thus these experiments were less quantitative. Nevertheless, we were still able to fit the curves with polydisperse vesicle form factors. As we have a fifth parameter to fit (namely the copolymer concentration C_{pol} or the volume fraction ϕ of IONPs which are dominating the contrast), we imposed another constraint which is that the theoretical contrast (of copolymer for blank objects or of iron oxide) is identical to the experimental contrast provided by the conservation law usually called the “scattering invariant”[14], [39]:

$$Q = \int_{q_{\min}}^{q_{\max}} [I(q) - I_{\text{background}}] q^2 dq = 2\pi^2 (\Delta\rho)^2 \phi (1 - \phi) \quad (19)$$

To be convergent, this integral Q needs proper subtraction of the background in the high- q domain, therefore an additional constant $I_{\text{background}}$ was subtracted to the signal when subtraction of a capillary filled by pure solvent was not enough to reach the expected Porod regime $I(q) \propto \frac{1}{q^4}$ in the high- q part. Then using $\rho_{\text{PTMC}}^{\text{XR}} \sim 1.2 \times 10^{11} \text{ cm}^{-2}$ for blank objects or $\rho_{\text{IONP}}^{\text{XR}} \sim 4 \times 10^{11} \text{ cm}^{-2}$ for those incorporating IONPs, we subtract $\rho_{\text{water}}^{\text{XR}} = 9.4 \times 10^{10} \text{ cm}^{-2}$ to get the theoretical contrast $(\Delta\rho)^2$, and from the value of Q computed from the experimental SAXS curve, we can unambiguously deduce the volume fraction ϕ of objects to use in the numerical fitting with the polydisperse vesicle form factor.





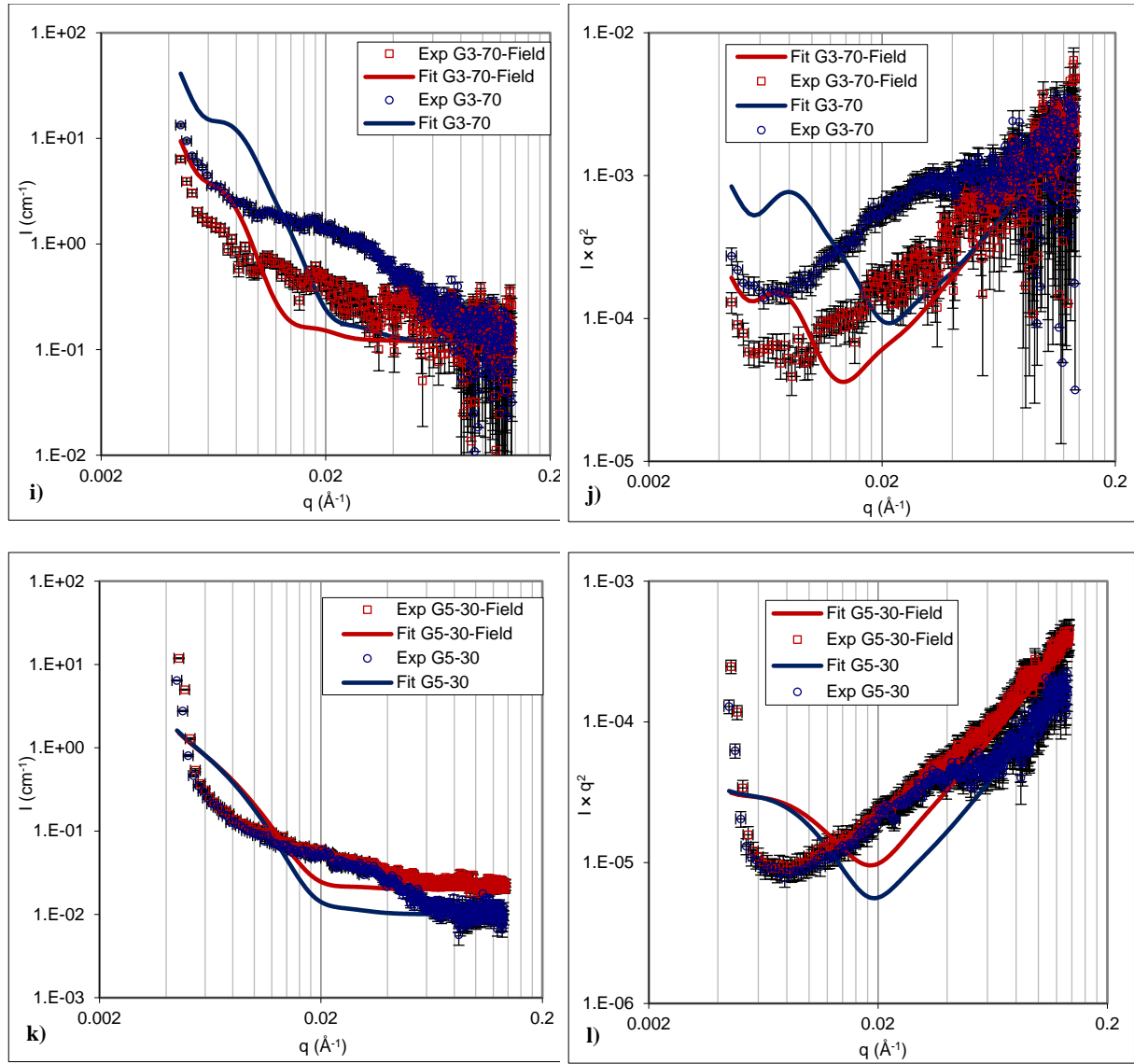
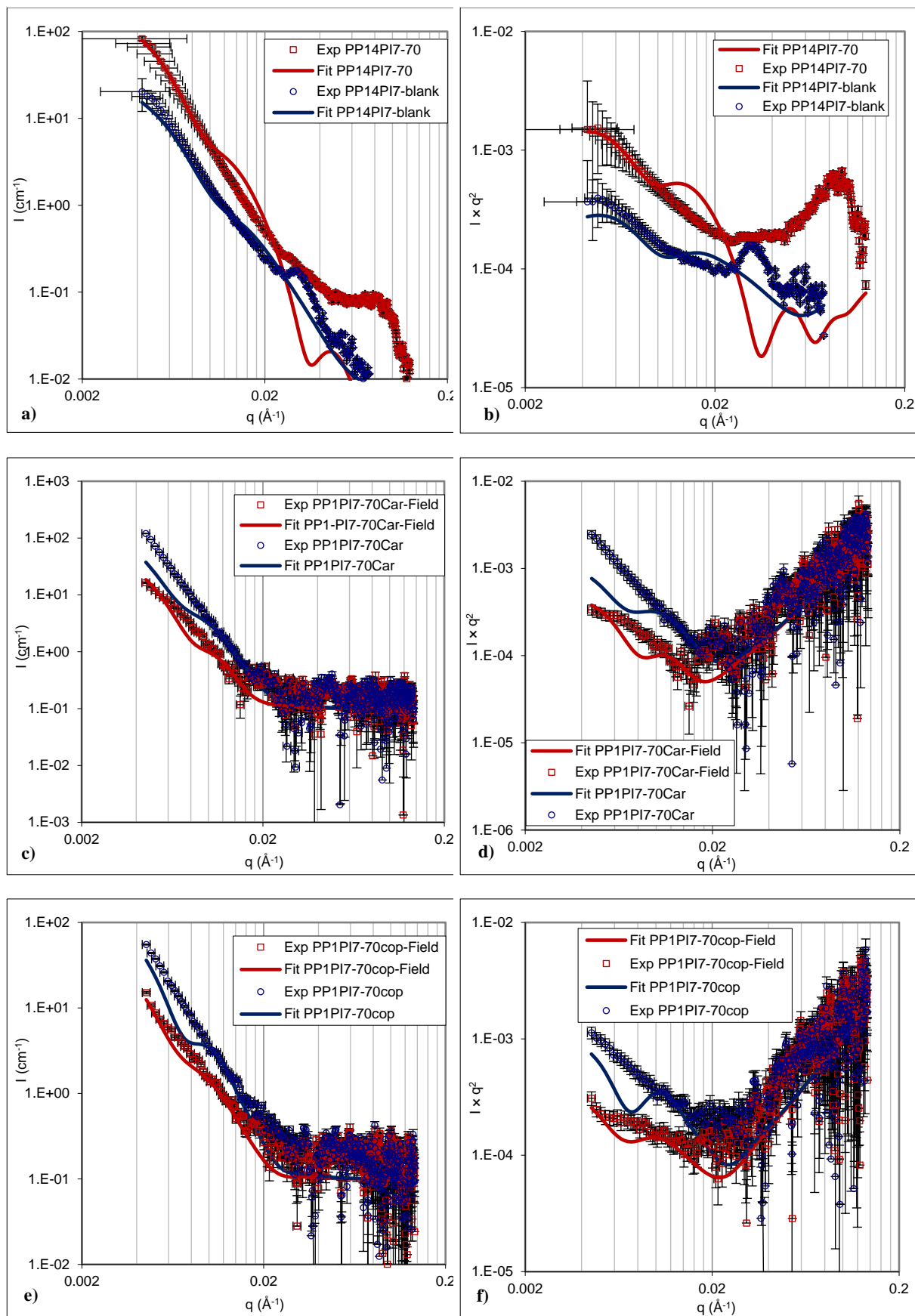


Figure 136: a), c), e), g), i), k) SAXS curves $I(q)$ and b), d), f), h), j), l) SAXS data in “Kratky-Porod like” representation $I \times q^2$ vs. q of different copolymer self-assemblies with and without IONPs, under zero-field or $B_{DC}=0.43$ T applied static magnetic field: a), b) $\text{PEG}_{114}\text{-}b\text{-PTMC}_{190}\text{-}b\text{-PI}_{44}$ (PP14PI7) and $\text{PEG}_{114}\text{-}b\text{-PTMC}_{190}\text{-}b\text{-PI}_{44}$ (PP14PI7) + 70% IONP@OA^{6nm}; c), d) $\text{PEG}_{114}\text{-}b\text{-PTMC}_{200}\text{-}b\text{-PI}_{40}$ (PP1PI7) + 70% IONP@OA^{6nm} (Caruntu) under no-field and $B_{DC}=0.43$ T; e), f) $\text{PEG}_{114}\text{-}b\text{-PTMC}_{200}\text{-}b\text{-PI}_{40}$ (PP1PI7) + 50% IONP@OA^{8nm} (coprecipitation) under no-field or $B_{DC}=0.43$ T; g), h) $\text{PEG}_{114}\text{-}b\text{-PATC}_{20}\text{-}g\text{-PI}_5$ (G4) + 70% IONP@OA^{6nm}, before and after UV crosslinking (CL) and under $B_{DC}=0.43$ T; i), j) $\text{PEG}_{114}\text{-}b\text{-}(\text{PATC-}g\text{-PI}_3)_{15}\text{-co-PATC}_5$ (G3) + 70% IONP^{6nm}@dop-PI₂₀ (D) under no-field or $B_{DC}=0.43$ T applied static magnetic field; k), l) $\text{PEG}_{114}\text{-}b\text{-}(\text{PATC-}g\text{-PI}_4)_{20}\text{-co-PATC}_{11}$ (G5) + 30% IONP^{6nm}@dop-PI₂₀ (D) under no-field or $B_{DC}=0.43$ T applied static magnetic field.



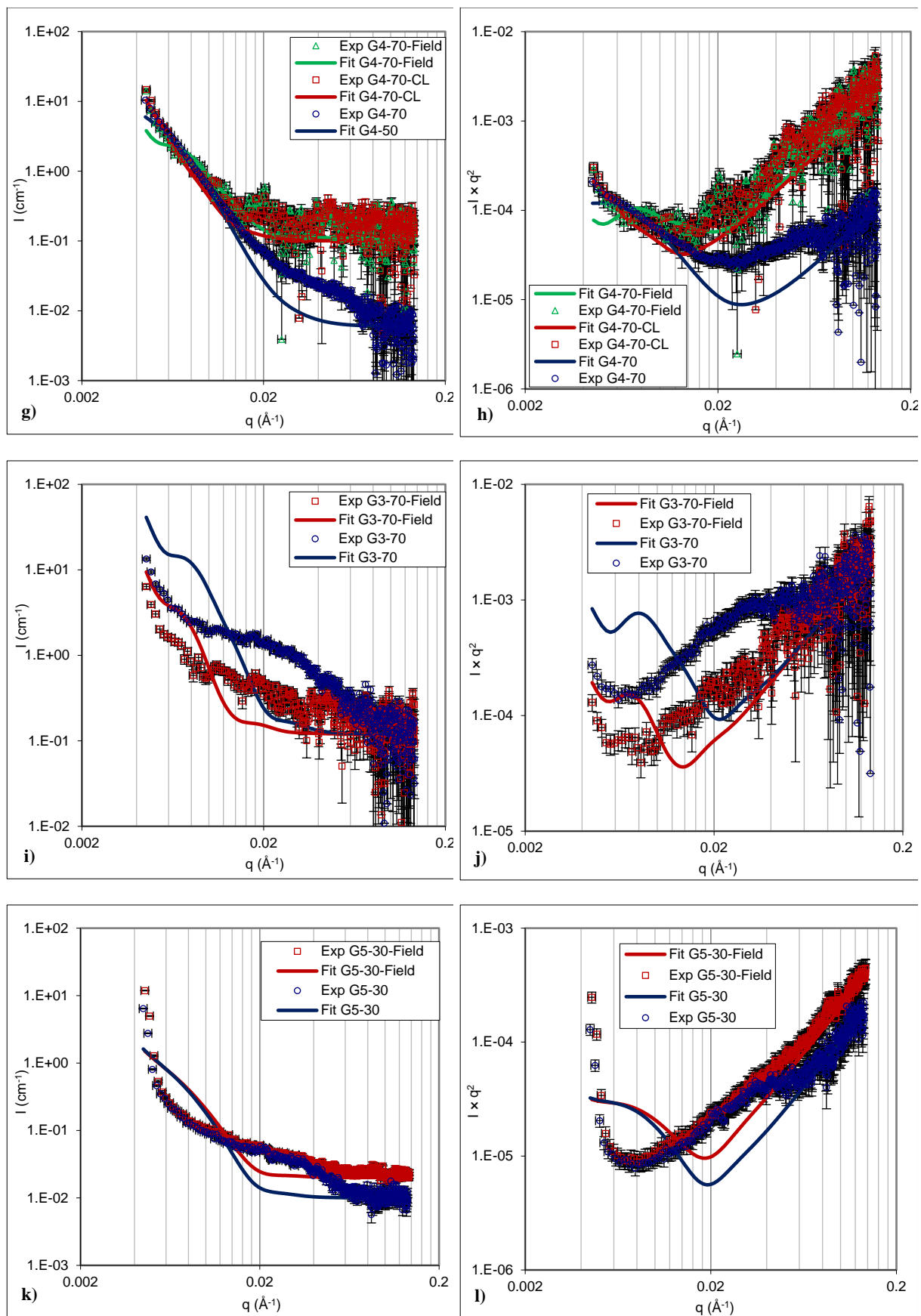


Figure 136 and Table 23, demonstrate that the fit of the SAXS curve of the blank PP14PI7 self-assemblies is globally correct, except the peak observed about scattering vector $q^* \sim 3 \times 10^{-2} \text{ \AA}^{-1}$ that is not reproduced by the polydisperse shell form factor. The same feature was observed when this triblock copolymer was loaded at a FWR=5% with polyol made IONPs of $d_{\text{core}}=6 \text{ nm}$ coated by oleic acid. Looking at the TEM images on Figure 123 for which we already discussed the presence of multilamellar vesicles in these PEO-*b*-PTMC-*b*-PI samples, we can ascribe this structure peak to the correlation length between adjacent membranes and estimate their mean distance $L^* = 2\pi/q^* \sim 210 \text{ \AA}$. Simulating this structure peak can very likely be made with the multiple-shell fit of SASview software, but we have not implemented it yet in our Excel spread sheet. Again, extruding the vesicles through pores after their self-assembly should be sufficient to solve this issue of multi-lamellarity of their membranes. The same PP14PI7 sample loaded with IONPs also exhibits a peak that shifts to $q^* \sim 8.5 \times 10^{-2} \text{ \AA}^{-1}$, from which we deduce an inter-membrane distance $L^* = 2\pi/q^* \sim 74 \text{ \AA}$, very close to the mean diameter of the IONPs: one can easily imagine them to act as “pinning centers” that bridge the membranes owing to their hydrophobic coating, as described by S. Förster and coll. [40], [41] for PEO-*b*-PI bilayers decorated with IONPs.

Table 23: DLS characteristics and structural parameters determined by SAXS on samples out of magnetic field.

Sample (code, hydrophilic weight fraction <i>f</i>) $C_{\text{pol}}^{\text{fit}}$ (mg·mL ⁻¹) [¶]	Main diameter (nm) [*]	Z-ave diameter (nm) (PDI) [⊥]	$R_G = R_Z^{\text{fit}}$ (nm) [†]	$H_{\text{KP}} =$ H_Z^{fit} (nm) [‡]	R_0^{fit} (nm) [¶] (σ_R^{fit}) [¶]	H_0^{fit} (nm) [¶] (σ_H^{fit}) [¶]	$R_{\text{core}} = R_Z^{\text{fit}}$ $- H_Z^{\text{fit}}/2$ (nm) [¶]
PEG ₁₁₄ - <i>b</i> -PTMC ₂₀₀ - <i>b</i> - PI ₅₀ (PP14PI7, 17%) $C_{\text{pol}}^{\text{fit}}=0.66 \text{ mg·mL}^{-1}$	130 (55%)	142 (0.12)	36.6	13.7	23.3 (0.32)	7.9 (0.35)	29.7
PEG ₁₁₄ - <i>b</i> -PTMC ₂₀₀ - <i>b</i> - PI ₅₀ (PP14PI7, 17%) + 5% IONP@OA ^{6nm} $C_{\text{pol}}^{\text{fit}}=0.06 \text{ mg·mL}^{-1}$	180 (47%)	175 (0.21)	39.9	18.8	26.6 (0.30)	18.2 (0.084)	30.5
PEG ₁₁₄ - <i>b</i> -PTMC ₂₀₀ - <i>b</i> - PI ₄₀ (PP1PI7, 18%) + 70% IONP@OA ^{6nm} $C_{\text{pol}}^{\text{fit}}=0.029 \text{ mg·mL}^{-1}$	393 (93%)	338 (0.25)	>52.1	33.3	35.0 (0.30)	25.0 (0.25)	35.5
PEG ₁₁₄ - <i>b</i> -PTMC ₂₀₀ - <i>b</i> - PI ₄₀ (PP1PI7, 18%) + 70% IONP@OA ^{8nm} $C_{\text{pol}}^{\text{fit}}=0.028 \text{ mg·mL}^{-1}$	246 (89%)	229 (0.19)	>46.3	25.5	36.8 (0.23)	22.5 (0.17)	33.5

PEG₁₁₄-<i>b</i>-PATC₂₀-<i>g</i>-PI₅ (G4, 33%) + 70% IONP@OA^{6nm} $C_{pol}^{fit}=0.005 \text{ mg}\cdot\text{mL}^{-1}$	264 (70%)	279 (0.13)	50.8	43.7	11.3 (0.58)	27.7 (0.32)	29.0
PEG₁₁₄-<i>b</i>-PATC₂₀-<i>g</i>-PI₅ (G4, 33%) cross-linked + 70% IONP@OA^{6nm} $C_{pol}^{fit}=0.007 \text{ mg}\cdot\text{mL}^{-1}$	237 (58%)	288 (0.28)	63.5	65.0	30.0 (0.41)	50.0 (0.24)	5.0
PEG₁₁₄-<i>b</i>-(PATC-<i>g</i>-PI₃)₁₅-<i>co</i>-PATC₅ (G3, 48%) + 70% IONP@PI_{dop}^{6nm} $C_{pol}^{fit}=0.048 \text{ mg}\cdot\text{mL}^{-1}$	238 (83%)	270 (0.26)	>61.1	33.1	48.3 (0.23)	28.0 (0.19)	44.6
PEG₁₁₄-<i>b</i>-(PATC-<i>g</i>-PI₄)₂₀-<i>co</i>-PATC₁₁ (G5, 36%) + 30% IONP@PI_{dop}^{6nm} $C_{pol}^{fit}=0.004 \text{ mg}\cdot\text{mL}^{-1}$	247.5 (94%)	225 (0.17)	>109	35.9	52.8 (0.40)	28.9 (0.22)	90.5

* by Padé-Laplace (multimodal) fit of auto-correlogram (percentage indicates the weight of the mode); [†] by 2nd order cumulants fit; [‡] Gyration radius from Guinier fit at low q (the sign > indicates that a Guinier plateau was not observed at the lowest q that the SAXS bench can reach); [§] Mean shell thickness from Kratky-Porod fit at intermediate q range; [¶] obtained from fitting to polydisperse vesicle shell form factor assuming a theoretical X-ray SLD of block copolymer $\rho_{PTMC}^{XR}=1.2\times 10^{11} \text{ cm}^{-2}$ for blank copolymer PP14PI7 and $\rho_{IONP}^{XR}=4.0\times 10^{11} \text{ cm}^{-2}$ for all copolymers loaded with IONPs. Polydispersity was modelled by log-normal distributions of widths σ_R^{fit} for the radius and σ_H^{fit} for the shell thickness. The Z-average values of radius and thickness were computed from usual momentums of log-normal law: $R_Z^{fit} = \left(\frac{\langle R^6 \rangle}{\langle R^3 \rangle}\right)^{\frac{1}{3}} = R_0^{fit} e^{\frac{9}{2}\sigma_R^2}$ and $H_Z^{fit} = \left(\frac{\langle H^6 \rangle}{\langle H^3 \rangle}\right)^{\frac{1}{3}} = H_0^{fit} e^{\frac{9}{2}\sigma_H^2}$. The volume fraction of scattering objects – $\phi=C_{pol}/d$ where d is taken as the mass density of semi-crystalline PTMC, $d=1.33 \text{ g}\cdot\text{cm}^{-3}$, for blank copolymer, or $\phi=C_{pol}\times\text{FWR}/d$ where $d=4.9 \text{ g}\cdot\text{cm}^{-3}$ is the mass density of iron oxide for those loaded with IONPs – was fitted (and hence also the C_{pol}) under the constraint that the experimental SLD contrast, deduced by computing the scattering invariant Q , is equal to the theoretical contrast $\Delta\rho$ with $\rho_{water}^{XR}=9.4\times 10^{10} \text{ cm}^{-2}$. *Values in italics are subject to caution because the SAXS curves were not well fitted with the polydisperse shell form factor.*

In the case of PEG₁₁₄-*b*-PTMC₁₉₀-*b*-PI₄₄ (PP14PI7) copolymer self-assemblies, the SAXS curves show a fair quality of the fits in the intermediate and high q ranges, but not at low q where the intensity is underestimated, for both sizes of embedded IONPs (*i.e.*, both syntheses, Caruntu or coprecipitation). In addition, the polymer concentration retrieved by the scattering invariant method is $C_{pol}\sim 0.03 \text{ mg}\cdot\text{mL}^{-1}$, much lower than the nominal concentration $C_{pol}^o=0.5 \text{ mg}\cdot\text{mL}^{-1}$. These two observations can both be explained by a degree of aggregation of the objects (thus their partial sedimentation in the capillary), explaining both the steep increase of $I(q)$ at low q and high hydrodynamic diameters $\sim 300 \text{ nm}$ or more.

The colloidal stability appears better for PEG₁₁₄-*b*-PATC₂₀-*g*-PI₅ grafted copolymer (G4), which can be loaded at 70% FWR with the 6 nm core IONPs while still exhibiting a Guinier plateau at low q . For this sample, the membrane thickness derived by the Kratky-Porod plot is the same in SAXS (Table 23) than previously obtained by SANS (Table 22), $H_{KP} \sim 44$ nm. Such thick membrane can be ascribed to its high loading rate with IONPs, which is indeed a favorable factor to orient the self-assembly towards vesicles as the IONPs are coated with hydrophobic oleic chains. Once cross-linked by UV irradiation with the “5.15.30.5” protocol, the thickness gets even larger, $H_{KP} \sim 65$ nm, which can be correlated to the higher membrane visibility by electron microscopy of the crosslinked objects, although it goes along with smaller internal compartment. With other synthesized grafted copolymers PEG₁₁₄-*b*-(PATC-*g*-PI₃)₁₅-*co*-PATC₅ (G3) and PEG₁₁₄-*b*-(PATC-*g*-PI₄)₂₀-*co*-PATC₁₁ (G5), of larger hydrophilic fractions respectively $f_{PEG}=48\%$ (G3) and $f_{PEG}=36\%$ (G5), the incorporation of IONPs – grafted with short catechol functionalized PI₄₀-dop (C) chains of $M_n=3140$ g·mol⁻¹ (Chapter IV) – both led to objects that were most likely not vesicles, as the fits with polydisperse shell form factor were very poor, as seen from the last entries, i) an j), k) and l), of Figure 136. The aspect of these two SAXS curves where $I(q) \propto \frac{1}{q^4}$ both at low q and at high q , with an intermediate range where $I(q) \propto \frac{1}{q^2}$ or $\frac{1}{q}$ resembles more to a random coil form factor. The structure of these self-assemblies would rather be a string of small objects, like a necklace whose pearls would be spherical micelles like observed for empty copolymers G3 (Image 2) and G5 (Image 3), except that they would be filled with IONPs coated by PIDop chains.

Finally, the effect of a static magnetic field was studied *in situ* by DLS, SAXS and SANS during field application on certain of these samples, in view of the objective of this thesis that was the obtention of elongated polymersomes and the fixation of such anisotropic shape by UV-induced crosslinking of the membranes, to impede their relaxation to spherical shape when the sample is removed from the field.

Structural study by DLS, SAXS and SANS of the grafted and triblock copolymers co-assembled with hydrophobically coated IONPs under a static magnetic field:

During this thesis, we had the opportunity to use dedicated sample environments to apply a static (DC) magnetic field *i.e.*, of constant intensity ($B_{DC}=0.2$ or 0.4 T) and relatively homogeneous intensity ($\pm 5\%$) while making *in situ* structural measurements by DLS, SAXS or SANS. The goal was to evidence the deformation of magnetic polymersomes under constant field, while setting up definitively the shape (without relaxation when the field is removed) by simultaneous UV irradiation and photo-crosslinking. The $B_{DC}=0.4$ T is a Halbach array of magnets originally built to perform depolarized DLS experiments at different angles (between 30° and 150°) under an applied field (Thetis project), which was adapted to shine an X-ray beam and measure the scattering pattern at low angle with a commercial Xenocs Xeuss

SAXS bench. For the SANS experiment under field, two setups were built by Dr Lionel Porcar and technical staff of the ILL in Grenoble to hold a usual 2 mm thick quartz cuvette on the D22 spectrometer in either parallel (Halbach array) or perpendicular (2 facing magnets) field configuration, applying in both cases an intensity $B_{DC}=0.2$ T. The different setups are photographed on Figure 137, together with samples after their under-field measurements by SANS.

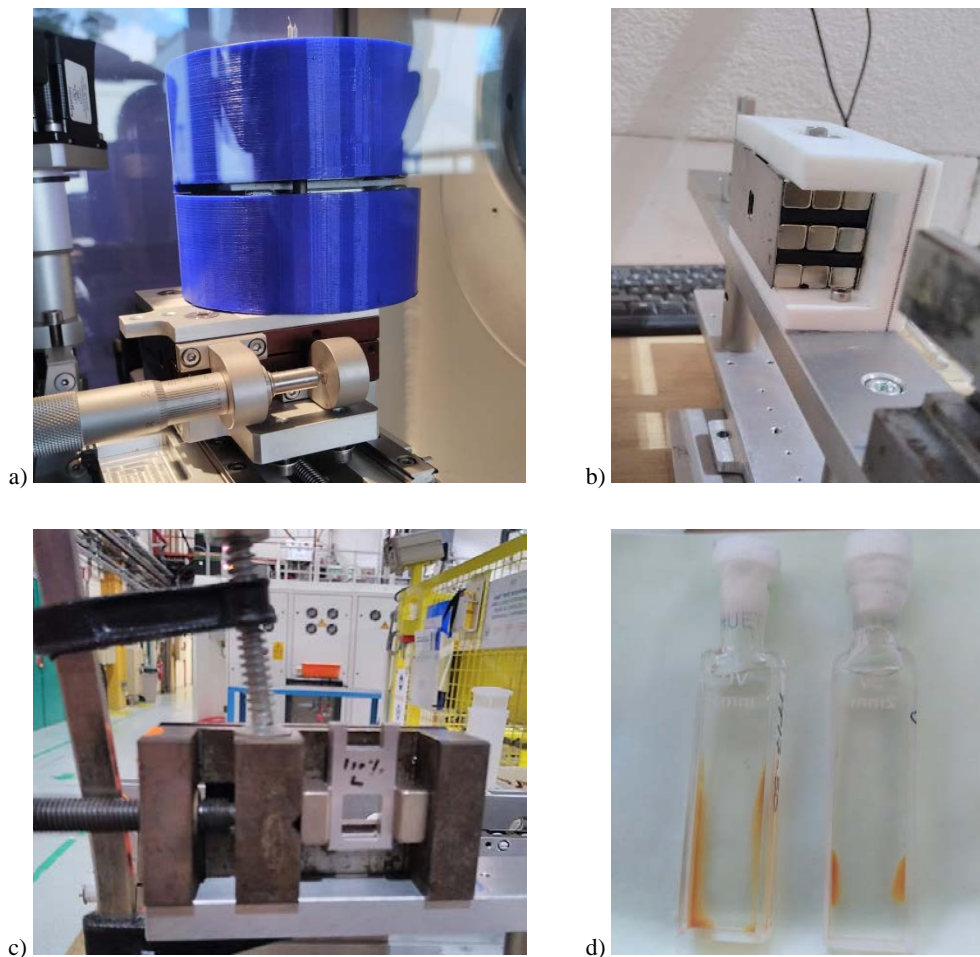


Figure 137: a) Picture of the SAXS parallel/perpendicular field experiment and of the SANS sample holder with magnetic field either b) parallel or c) perpendicular. Unfortunately, the homogeneity of the field was not good enough, and d) some migration of the samples occurred during the 40 min of measurements, due to the magnetophoretic force given by Eq. (9).

We used all the methods described before (Halbach array or doublet of magnets) to apply a constant (and hopefully homogeneous enough) magnetic field on the samples while performing *in situ* (*i.e.*, in-field) measurements by a scattering technique, either light (DLS), X-ray (SAXS) or neutron (SANS). The results of all measured dimensions (hydrodynamic diameter, gyration radius, membrane thickness, and internal aqueous core radius) are presented in Table 24.

Table 24: DLS characteristics and structural parameters determined by SAXS and SANS on samples under magnetic field B_{DC} .

Sample (code, f)	Main diameter (nm)*	Z-ave diameter (nm) (PDI) [⊥]	$R_G = R_Z^{\text{fit}}$ (nm) [†]	$H_{KP} =$ H_Z^{fit} (nm) [‡]	R_{fit}^0 (nm) [¶] (σ_R^{fit}) [¶]	H_0^{fit} (nm) [¶] (σ_H^{fit}) [¶]	$R_{\text{core}} = R_Z^{\text{fit}}$ $- H_Z^{\text{fit}}/2$ (nm) [¶]
PEG₁₁₄-<i>b</i>-PATC₂₀-<i>g</i>- PI₅ (G4, 33%) + 70% IONP@OA^{6nm} $B_{DC} \parallel$ beam (SANS)	-	-	59.3	53.4	34.1 (0.35)	22.5 (0.44)	32.7
$B_{DC} \perp$ beam (SANS)	237 (58%) **	288 (0.28) **	45.0	43.9	24.4 (0.37)	11.6 (0.54)	23.1
$B_{DC} \perp$ beam (SAXS)			76.7	25.1	54.0 (0.24)	22.3 (0.16)	57.4
PEG₁₁₄-<i>b</i>-PATC₂₀-<i>g</i>- PI₅ (G4, 33%) + 50% IONP@OA^{8nm} $B_{DC} \parallel$ beam (SANS)	120 (63%)	137 (0.12)	50.6	28.5	16.1 (0.50)	16.3 (0.35)	36.3
$B_{DC} \perp$ beam (SANS)	164 (81%)	168 (0.25)	40.2	25.7	15.6 (0.46)	15.1 (0.34)	27.3
PEG₁₁₄-<i>b</i>-PTMC₂₀₀-<i>b</i>- PI₄₀ (PP1PI7, 18%) + 70% IONP@OA^{6nm} $B_{DC} \parallel$ beam (SANS)	-	-	49.2	30.3	23.7 (0.40)	24.4 (0.22)	34.0
$B_{DC} \perp$ beam (SANS)	358 (76%) **	367 (0.22) **	45.5	30.3	24.1 (0.38)	27.5 (0.15)	30.4
$B_{DC} \perp$ beam (SAXS)			41.6	37.0	30.0 (0.27)	30.0 (0.22)	23.1
PEG₁₁₄-<i>b</i>-PTMC₂₀₀-<i>b</i>- PI₄₀ (PP1PI7, 18%) + 50% IONP@OA^{8nm} $B_{DC} \parallel$ beam (SANS)	-	-	42.8	33.3	16.0 (0.47)	16.6 (0.39)	26.2
$B_{DC} \perp$ beam (SANS)	306 (53%)**	292 (0.23)**	37.8	32.6	16.6 (0.43)	16.3 (0.39)	21.5
$B_{DC} \perp$ beam (SAXS)			55.1	24.2	36.8 (0.30)	22.5 (0.13)	43.0

* by Padé-Laplace (multimodal) fit of auto-correlogram (percentage indicates the weight of the mode); [†] by 2nd order cumulants fit; in both cases (Padé or Cumulant fit) the correlograms were measured after 15 min application of B_{DC} (parallel or perpendicular to incident beam); ** after UV crosslinking under 0.4 T magnetic field (through the “5.15.30.5” protocol); [‡] Gyration radius from Guinier fit at low q ; [§] Mean shell thickness from Kratky-Porod fit at intermediate q ; [¶] obtained from fitting to polydisperse vesicle shell form factor assuming a theoretical neutron SLD of hydrophobic copolymer block $\rho_{PTMC}=1.7\times 10^{10}$ cm⁻² for linear copolymer PP1PI7 and $\rho_{PATC-g-PI}=8.4\times 10^9$ cm⁻² for grafted copolymer G4. Volume fraction is $\phi=C_{pol}\times(1-f)/d$ where f is the hydrophilic weight fraction of the given copolymer and d is its mass density, taken as the one of semi-crystalline PTMC, $d=1.33$ g·cm⁻³. Polydispersity was modelled by log-normal distributions of widths σ_R^{fit} for the radius and σ_H^{fit} for the shell thickness, and C_{pol} was kept at 0.5 mg·mL⁻¹. The Z-average values of radius and thickness were computed from usual momentums of log-normal law: $R_Z^{fit} = \left(\frac{\langle R^6 \rangle}{\langle R^3 \rangle}\right)^{\frac{1}{3}} = R_0^{fit} e^{\frac{9}{2}\sigma_R^2}$ and $H_Z^{fit} = \left(\frac{\langle H^6 \rangle}{\langle H^3 \rangle}\right)^{\frac{1}{3}} = H_0^{fit} e^{\frac{9}{2}\sigma_H^2}$.

Interestingly, PEG₁₁₄-*b*-PATC₂₀-*g*-PI₅ grafted copolymer (G4) measured by SANS under B_{DC} field showed no membrane thickness variation when the field was oriented perpendicularly to the beam, *i.e.* H_{KP} stayed ~44 nm when the copolymer was loaded at 70% FWR with IONP@OA^{6nm} and ~25 nm with 50% FWR of IONP@OA^{8nm}. On the contrary, the membrane thickness increased to respectively ~53 nm and ~28.5 nm when the field was directed along the neutron beam, which would mean that the IONPs make somehow longer chains at the poles of the vesicles (which would be ellipsoidal, instead of spherical). The effect is exactly opposite on the radius of gyration: Initially $R_G\sim 65$ nm for G3 copolymer loaded at 70% FWR with IONP@OA^{6nm} and $R_G\sim 50$ nm with 50% FWR of IONP@OA^{8nm} out of the magnetic field (Table 22); under a $B_{DC}\sim 0.2$ T these values become almost unchanged when the field is oriented parallelly to the neutron beam, but they decrease respectively to $R_G\sim 45$ nm and $R_G\sim 40$ nm when the field is perpendicular, meaning that the cross-sectional area of the objects became smaller (perpendicularly to field), which is compatible with prolate (*i.e.* elongated) ellipsoidal vesicles.

In the case of PEG₁₁₄-*b*-PTMC₁₉₀-*b*-PI₄₄ (PP14PI7) linear triblock copolymer, the effect of magnetic field application was weaker than for the grafted G3 copolymer, as the membrane thickness remained approximately unchanged compared to the no-field condition, for both IONP core sizes of 6 and 8 nm, and in both directions parallel or perpendicular to the beam, *i.e.* it stayed at $H_{KP}\sim 30$ nm for 70% FWR loading with IONP@OA^{6nm} and at $H_{KP}\sim 33$ nm for 50% FWR with IONP@OA^{8nm}. Nevertheless, a similar “contraction” effect of the vesicles was observed, this time in both magnetic field orientations, but more specifically in the perpendicular direction: The values dropped from $R_G\sim 63$ nm in no-field for 70% FWR IONP@OA^{6nm} loading to $R_G\sim 49$ nm || field and $R_G\sim 45$ nm \perp field, and from $R_G\sim 53$ nm in no-field for 50% FWR IONP@OA^{8nm} to $R_G\sim 43$ nm || field and $R_G\sim 38$ nm \perp field.

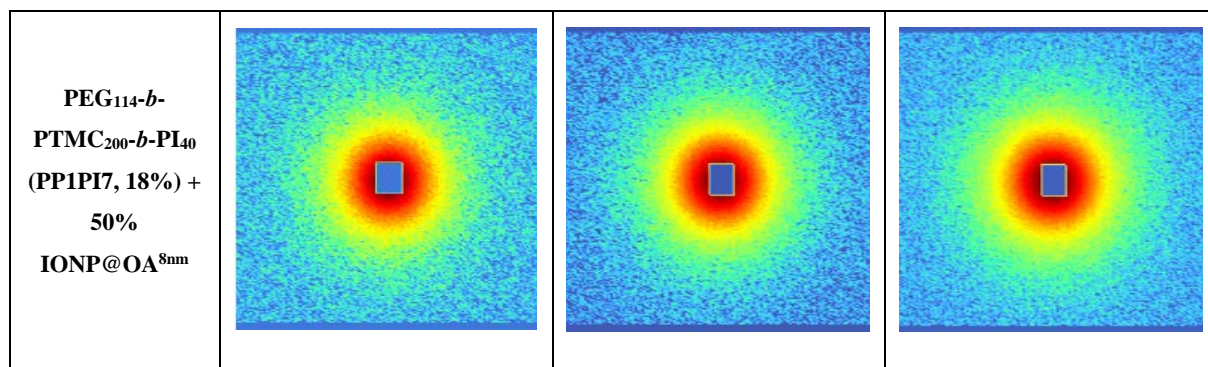
This “shrinking” effect of the vesicles under the applied B_{DC} might be concomitant with another parasitic phenomenon, which is the migration induced by unavoidable field gradient, especially in the 2-magnet perpendicular field (less homogeneous than the field created by a Halbach array of more numerous magnets). Even if limited (as we did not observe a decrease of the concentration of scattering objects during the SANS signal acquisition for 10 to 15 min by steps of 1 or 2 min runs), this migration effect can be responsible of a global decrease of the self-assemblies, because the biggest ones would move at

a higher speed away from the neutron beam, explaining a small drift of R_G measured, whatever the field direction.

To determine if such different variation of the isotropic curve $I(q)$ in the parallel and the perpendicular field directions was caused by non-isotropic shapes, we looked closely at the raw scattering patterns acquired by the planar detector located at 17.6 m away from sample for low q measurements (Table 25). All those patterns look globally isotropic. However, close insight of the lowest scattering vectors q , *i.e.*, at the closest distance from the beam center (covered by a rectangular beam-stop, corresponding to the wave front of the neutron beam collimated by a wave guide of rectangular cross-section) leads to observation of a non-circular scattering pattern, more specifically diamond-shape, in particular for G4.

Table 25: Raw neutron scattering patterns on the low q 2D detector for samples outside and under a magnetic field $B_{DC} \sim 0.2$ T. In each condition, the SANS data were acquired during 10 min (average of 10×1 min, 5×2 min or 2×5 min acquisitions).

Sample (code, f)	No-field	$B_{DC} \parallel \text{beam}$	$B_{DC} \perp \text{beam}$
PEG₁₁₄-<i>b</i>- PATC₂₀-<i>g</i>-PI₅ (G4, 33%) + 70% IONP@OA^{6nm}			
PEG₁₁₄-<i>b</i>- PATC₂₀-<i>g</i>-PI₃ (G4, 33%) + 50% IONP@OA^{8nm}			
PEG₁₁₄-<i>b</i>- PTMC₂₀₀-<i>b</i>-PI₄₀ (PP1PI7, 18%) + 70% IONP@OA^{6nm}			



This diamond shape of the scattering pattern at the lowest q range is particularly visible for G4 grafted copolymer loaded at 70% FWR with 6 nm sized IONPs, and exclusively for the configuration where the magnetic field is oriented perpendicularly to the neutron beam (red arrow). This diamond pattern is the signature of elongated structures, which have the particularity to be oriented in two directions (both perpendicular to the beam), parallel or perpendicular to the field. Although limited to one sample under SANS (but no SAXS that has not small enough q_{\min}), this observation is very encouraging, and it clearly demonstrates that an anisotropic shape of vesicles under DC field has finally been achieved.

Conclusion:

In conclusion, in this final chapter of our PhD work we have explored the self-assembly properties of all the synthesized copolymers throughout this project, and tried to demonstrate how the addition of IONPs with different sizes and functionalization affected the final structure. Furthermore, once the self-assembled structures were verified, we have evidenced the cross-linking potential of the hydrophobic membranes of the copolymers *via* UV irradiation using a cationic photo-initiator. Finally, as the most important step and the end point of the project, we have demonstrated the elongation of the magnetic polymersomes under a static magnetic field, and ability to stabilize these structures *via* the cross-linking process so that we can depict the final anisotropic structure by TEM imaging, which would be used for biological experiments in the following of the MAVERICK project.

More precisely, we have demonstrated that graft copolymers when self-assembled alone tended to form mostly into small micelles, with the presence of a few vesicles but which were not the main morphology. On the contrary, once the copolymers were self-assembled along with hydrophobically coated IONPs in a concentration-dependent way, but no matter the nature of the functionalization (oleic acid surfactants or short poly(isoprene) chains ended by a catechol anchor), the observed morphology shifted mostly to vesicles. Next, we have managed to demonstrate on TEM imaging the signature of the cross-linking process of the hydrophobic membrane after UV irradiation. We have captured images which clearly showed the difference of the outlook of the membrane before and after the cross-linking process, which forced a network formation between the epoxidized poly(isoprene) block, with the membrane appearing darker and more “concrete”.

The success of this step was imperative for our end goal which was the deformation process under the magnetic field. Indeed, the graft copolymers were submitted under a static magnetic field of up to $B_{DC}=0.4$ T which induced an elongation due to the presence of tightly packed IONPs with a FWR of 70%. An anisotropy parameter $R=1.3$ was calculated through the processing of the TEM images and compared to the control group which demonstrated almost no anisotropy (R parameter close to 1), suggesting that the graft copolymer has shifted morphologies post UV and MF application from spherical to slightly anisotropic. Another FWR of IONPs was experimented with, specifically, 50% FWR IONPs-OA with a somehow larger diameter $d_{core}=8$ nm, which was self-assembled with a graft copolymer and the sample was exposed to MF and UV, with an optimized sequential manner called “5.10.15.30.5” (where the figures represent times in min of MF and UV applications, either successive or combined). With this treatment, the sample exhibited a slight deformation as well, albite it being a less prominent one. These results show that the deformation was possible for the graft copolymer with two different IONPs mean diameters, and two different FWRs.

Furthermore, the second copolymer, *i.e.*, the triblock copolymer, was self-assembled alone and a vesicular morphology was formed, as was expected due to its very low hydrophilic fraction $f_{\text{PEG}} < 20\%$. When IONPs were added to the system, the structures depicted on TEM were neither clearly magnetic polymersomes nor magneto-core micelles. It was difficult to determine the exact morphology by TEM but nonetheless, the deformation step was still pursued. A 60% FWR was utilized both for IONPs-OA of $d_{\text{core}}=6$ nm and $d_{\text{core}}=8$ nm, and both exhibited an anisotropic stabilized morphology post MF+UV, with the IONPs-OA $d_{\text{core}}=6$ nm appearing to have a more anisotropic stabilized morphology with an anisotropy parameter $R=1.3$ while the control group exhibited an $R=1.1$.

Finally, both polymer morphologies, *i.e.*, graft and triblock were studied with both SAXS and SANS in order firstly to verify the morphology of the magnetic self-assembled structures, and secondly to study the elongation process under the magnetic field in real time by SANS under an applied B_{DC} , either parallel to the incident beam or in the perpendicular direction. In the end it was shown that both copolymer architectures, grafted or linear, lead to magnetic vesicles of membrane thickness that could be evaluated by so-called “Kratky-Porod” plots of the SANS or SAXS data, H_{KP} , varying from 25 nm to 44 nm depending on the copolymers and IONPs, *i.e.* higher than for the pristine copolymersomes which thicknesses are $H_{\text{KP}}^{\circ} \sim 15 \pm 1$ nm (from SANS and SAXS measurements on triblock copolymer vesicles without added IONPs). In addition, both types of copolymers gave magnetic field responsive polymersomes, as evidenced by the anisotropy of the radius of gyration R_G which becomes smaller in the direction perpendicular to the magnetic field, as ascribed to ellipsoidal deformation of the vesicles. An even more direct signature of the shape anisotropy of the vesicles under magnetic field was observed for one sample (G4 grafted copolymer loaded at 70% FWR with 6 nm diameters IONPs coated by oleic acid): in that case the scattering pattern at very low q exhibited diamond-like instead of circular shape, which was interpreted as a mixed population of elongated vesicles, presenting both orientations, either parallel or perpendicular to the magnetic field.

References:

- [1] R. J. Hickey, A. S. Haynes, J. M. Kikkawa, and S. J. Park, "Controlling the self-assembly structure of magnetic nanoparticles and amphiphilic block-copolymers: From micelles to vesicles," *J. Am. Chem. Soc.*, vol. 133, no. 5, pp. 1517–1525, 2011.
- [2] C. Decker, H. Le Xuan, and T. N. Thi Viet, "Photocrosslinking of functionalized rubber. II. Photoinitiated cationic polymerization of epoxidized liquid natural rubber," *J. Polym. Sci. Part A Polym. Chem.*, vol. 33, no. 16, pp. 2759–2772, 1995.
- [3] C. Decker, H. Le Xuan, and T. N. T. Viet, "Photocrosslinking of functionalized rubber. III. Polymerization of multifunctional monomers in epoxidized liquid natural rubber," *J. Polym. Sci. Part A Polym. Chem.*, vol. 34, no. 9, pp. 1771–1781, Jul. 1996.
- [4] A. V. Ryzhkov and Y. L. Raikher, "Numerical Modeling of a Magnetic Polymersome in a Uniform Magnetic Field," *IEEE Magn. Lett.*, vol. 10, no. c, p. 1, 2019.
- [5] A. V. Ryzhkov and Y. L. Raikher, "Field-Induced Deformation and Structure Changes in a Magnetic Polymersome: Many-Particle Simulation," *IOP Conf. Ser. Mater. Sci. Eng.*, vol. 581, no. 1, 2019.
- [6] Y. Long, C. Liu, B. Zhao, K. Song, G. Yang, and C. H. Tung, "Bio-inspired controlled release through compression-relaxation cycles of microcapsules," *NPG Asia Mater.*, vol. 7, no. 1, p. e148, 2015.
- [7] A. Ryzhkov and Y. Raikher, "Size-dependent properties of magnetosensitive polymersomes: Computer modelling," *Sensors (Switzerland)*, vol. 19, no. 23, pp. 1–11, 2019.
- [8] S. Lecommandoux, O. Sandre, F. Chécot, J. Rodriguez-Hernandez, and R. Perzynski, "Magnetic nanocomposite micelles and vesicles," *Adv. Mater.*, vol. 17, no. 6, pp. 712–718, 2005.
- [9] S. Tan *et al.*, "Doxorubicin Loaded Magnetic Polymersomes : Theranostic Nanocarriers for MR Imaging and Magneto-Chemotherapy," *ACS Nano*, vol. 5, no. 2, pp. 1122–1140, 2011.
- [10] P. Arosio *et al.*, "Hybrid iron oxide-copolymer micelles and vesicles as contrast agents for MRI: impact of the nanostructure on the relaxometric properties," *J. Mater. Chem. B*, vol. 1, no. 39, pp. 5317–5328, 2013.
- [11] A. Nikoubashman, V. E. Lee, C. Sosa, R. K. Prud'homme, R. D. Priestley, and A. Z. Panagiotopoulos, "Directed Assembly of Soft Colloids through Rapid Solvent Exchange," *ACS Nano*, vol. 10, no. 1, pp. 1425–1433, Jan. 2016.
- [12] J. S. Bowers, R. K. Prud'homme, and R. S. Farinato, "An assessment of the Padé-Laplace method for transient electric birefringence decay analysis," *Comput. Chem.*, vol. 16, no. 3, pp. 249–259, 1992.
- [13] T. Li, A. J. Senesi, and B. Lee, "Small Angle X-ray Scattering for Nanoparticle Research," *Chem. Rev.*, vol. 116, no. 18, pp. 11128–11180, 2016.
- [14] F. Cousin, "Small angle neutron scattering," *EPJ Web Conf.*, vol. 104, 2015.
- [15] C. Kittel, *Introduction to solid state physics*. John Wiley & sons, inc, 2005.
- [16] M. Bejko *et al.*, "Optimal sizes of iron oxide nanoflowers for magnetic hyperthermia depend on the alternating magnetic field conditions," 2023.
- [17] V. F. Sears, "Neutron scattering lengths and cross sections," *Neutron News*, vol. 3, no. 3, pp. 26–37, 1992.

- [18] M. Fauquignon *et al.*, “In situ monitoring of block copolymer self-assembly through controlled dialysis with light and neutron scattering detection,” 2022.
- [19] H. Bermudez, A. K. Brannan, D. A. Hammer, F. S. Bates, and D. E. Discher, “Molecular weight dependence of polymersome membrane structure, elasticity, and stability,” *Macromolecules*, vol. 35, no. 21, pp. 8203–8208, 2002.
- [20] E. B. Zhulina and O. V Borisov, “Micelles Formed by an AB Copolymer with Bottlebrush Blocks: Scaling Theory,” *J. Phys. Chem. B*, vol. 125, no. 45, pp. 12603–12616, 2021.
- [21] E. B. Zhulina, S. S. Sheiko, and O. V Borisov, “Theoretical advances in molecular bottlebrushes and comblike (co)polymers: solutions{,} gels{,} and self-assembly,” *Soft Matter*, vol. 18, no. 46, pp. 8714–8732, 2022.
- [22] D. Caruntu, G. Caruntu, Y. Chen, C. J. O’Connor, G. Goloverda, and V. L. Kolesnichenko, “Synthesis of Variable-Sized Nanocrystals of Fe₃O₄ with High Surface Reactivity,” *Chem. Mater.*, vol. 16, no. 25, pp. 5527–5534, Dec. 2004.
- [23] D. E. Discher and A. Eisenberg, “Polymer Vesicles,” *Science (80-.)*, vol. 297, no. 5583, pp. 967–973, 2002.
- [24] R. Šachl, M. Uchman, P. Matějček, K. Procházka, M. Štěpánek, and M. Špírková, “Preparation and characterization of self-assembled nanoparticles formed by poly (ethylene oxide)-block-poly (ϵ -caprolactone) copolymers with long poly (ϵ -caprolactone) blocks in aqueous solutions,” *Langmuir*, vol. 23, no. 6, pp. 3395–3400, 2007.
- [25] D. J. Adams *et al.*, “On the mechanism of formation of vesicles from poly (ethylene oxide)-block-poly (caprolactone) copolymers,” *Soft Matter*, vol. 5, no. 16, pp. 3086–3096, 2009.
- [26] S. Hocine *et al.*, “Polymersomes with PEG corona: structural changes and controlled release induced by temperature variation,” *Langmuir*, vol. 29, no. 5, pp. 1356–1369, 2013.
- [27] W. Qi, P. P. Ghoroghchian, G. Li, D. A. Hammer, and M. J. Therien, “Aqueous self-assembly of poly (ethylene oxide)-block-poly (ϵ -caprolactone)(PEO-b-PCL) copolymers: Disparate diblock copolymer compositions give rise to nano-and meso-scale bilayered vesicles,” *Nanoscale*, vol. 5, no. 22, pp. 10908–10915, 2013.
- [28] A. Ryzhkov and Y. Raikher, “Coarse-grained molecular dynamics modelling of a magnetic polymersome,” *Nanomaterials*, vol. 8, no. 10, pp. 1–12, 2018.
- [29] G. Boedec, M. Jaeger, and M. Leonetti, “Pearling instability of a cylindrical vesicle,” *J. Fluid Mech.*, vol. 743, pp. 262–279, 2014.
- [30] A. Ryzhkov and Y. Raikher, “Size-dependent properties of magnetosensitive polymersomes: Computer modelling,” *Sensors (Switzerland)*, vol. 19, no. 23, pp. 1–10, 2019.
- [31] C. Lebleu, L. Rodrigues, J. M. Guigner, A. Brûlet, E. Garanger, and S. Lecommandoux, “Self-Assembly of PEG-b-PTMC Copolymers: Micelles and Polymersomes Size Control,” *Langmuir*, vol. 35, no. 41, pp. 13364–13374, 2019.
- [32] E. AYDINLIOGLU, “Auto-assemblages à base de polypeptides sensibles au pH en tant que supports de délivrance de médicaments et de gènes pH-responsive polypeptide-based self-assemblies as drug and gene delivery carriers,” 2020.
- [33] R. Salva *et al.*, “Polymersome shape transformation at the nanoscale,” *ACS Nano*, vol. 7, no. 10, pp. 9298–9311, 2013.
- [34] J. E. Bartenstein, J. Robertson, G. Battaglia, and W. H. Briscoe, “Stability of polymersomes

- prepared by size exclusion chromatography and extrusion,” *Colloids Surfaces A Physicochem. Eng. Asp.*, vol. 506, pp. 739–746, 2016.
- [35] F. Chécot, A. Brûlet, J. Oberdisse, Y. Gnanou, O. Mondain-Monval, and S. Lecommandoux, “Structure of polypeptide-based diblock copolymers in solution: stimuli-responsive vesicles and micelles,” *Langmuir*, vol. 21, no. 10, pp. 4308–4315, May 2005.
 - [36] J. S. Pedersen, “Analysis of small-angle scattering data from colloids and polymer solutions: modeling and least-squares fitting,” *Adv. Colloid Interface Sci.*, vol. 70, pp. 171–210, 1997.
 - [37] P. Balgavý, M. Dubničková, N. Kučerka, M. A. Kiselev, S. P. Yaradaikin, and D. Uhríková, “Bilayer thickness and lipid interface area in unilamellar extruded 1,2-diacylphosphatidylcholine liposomes: a small-angle neutron scattering study,” *Biochim. Biophys. Acta - Biomembr.*, vol. 1512, no. 1, pp. 40–52, 2001.
 - [38] D. Kunz, A. Thurn, and W. Burchard, “Dynamic light scattering from spherical particles,” *Colloid Polym. Sci.*, vol. 261, no. 8, pp. 635–644, 1983.
 - [39] B. Abécassis, F. Testard, Q. Kong, B. Francois, and O. Spalla, “Influence of Monomer Feeding on a Fast Gold Nanoparticles Synthesis: Time-Resolved XANES and SAXS Experiments,” *Langmuir*, vol. 26, no. 17, pp. 13847–13854, Sep. 2010.
 - [40] V. B. Leffler *et al.*, “Controlled Assembly of Block Copolymer Coated Nanoparticles in 2D Arrays,” *Angew. Chemie Int. Ed.*, vol. 58, no. 25, pp. 8541–8545, 2019.
 - [41] M. Krack, H. Hohenberg, A. Kornowski, P. Lindner, H. Weller, and S. Förster, “Nanoparticle-loaded magnetophoretic vesicles,” *J. Am. Chem. Soc.*, vol. 130, no. 23, pp. 7315–7320, 2008.

CONCLUSIONS AND PERSPECTIVES:

Conclusions and Perspectives:

The aim of this PhD project was the synthesis of magnetic polymersomes which were capable of deforming under a static magnetic field and produce anisotropic morphologies following the needs of the MAVERICK project 2019. While magnetic polymersomes have been studied extensively in the past decades for a multitude of reasons in the biomedical community mostly for their capabilities of controlled drug release due to the ability of iron oxide nanoparticles to release heat when under the magnetic field, thus if pared with thermos-responsive copolymers capable to control the release of the drug by changing the state of the polymers. Nonetheless, these studies kept one thing certain and that was the spherical morphology of the polymersomes. Spherical morphology has been the prevailing morphology in almost all studies when it comes to drug-delivery systems since it does offer many advantages such as high circulation time, biocompatibility, granted the choice of polymers. But lately, morphology in itself has become a point of interest and investigation since it has been found that it plays an important role in the way that a potential drug delivery system circulates in the blood stream and accumulates in the cells. It has been found that a higher targeting capacity can be achieved when different morphologies other than spheres were introduced, with some presenting higher deposition in specific organs. Furthermore, studies on cell loading have demonstrated to present a higher depositing rate for elongated structures when compared to spherical ones.

In principle, iron oxide nanoparticles have been studied on their own as a possible anticancer treatment called magnetic hyperthermia, using their heat releasing properties when an alternating magnetic field of high frequencies is applied. But lately, their use has been expanded in other areas, such as the magneto-mechanical destruction of cells from the inside. In this method iron oxide nanoparticles when internalized by the targeted cells perform mechanical rotations when a low frequency magnetic field is applied, and their produced torques create disruptions in the cell's membrane capable of resulting in controlled cell apoptosis without heat production.

Such a concept of mechanical destruction from within is an interesting concept and the idea of combining magnetic polymersomes which can act as drug delivery agents and magnetic nanoparticles which can react to the magnetic field is what has been studied in our case. Magnetic polymersomes which can respond to a magnetic field by deforming their shape is a new concept that has not been studied extensively in literature. Only a few publications have taken advantage to study this opportunity. Iron oxide nanoparticles embedded in the hydrophobic membrane responding to a low frequency magnetic field would elongate in the direction of the field thus causing elongation of the polymersome. Such a concept of an elongated polymersome thus could act as a drug delivery system or as a mechanical system is a novel idea and the experimental study on this subject is what is described in this research.

The first three experimental chapters described the synthesis of the building blocks of the project and demonstrated the synthesis of the copolymers and iron oxide nanoparticles which were finally all

combined in the final chapter which explored the elongation of the polymersome and stabilization of their morphology under a static magnetic field.

In the Chapter II we discuss the synthesis of a graft copolymer $\text{PEG}_{114}\text{-}b\text{-PATC}_m\text{-}g\text{-PI}_n$ consisting of poly(ethylene) glycol ($\text{CH}_3\text{-PEG-OH}$, $M_n=5000\text{g}\cdot\text{mol}^{-1}$) as a hydrophilic block which acted a macroinitiator of the ring opening polymerization (ROP) of the tert-butyl (2-oxo-1,3-dioxan-5-yl) carbamate monomer, which acted a one of the hydrophobic blocks of the copolymer. The synthesis of the monomer is described according to literature. The one-pot degradation of poly(isoprene), the second hydrophobic block which is utilized in this study, is described. The reaction includes the degradation of an industrial poly(isoprene) with a high molar mass of $800.000\text{g}\cdot\text{mol}^{-1}$ by using mCBPA and periodic acid as means of degrading the polymer into smaller molar mass blocks of a carbonyl hetero-telechelic poly(isoprene) with a controlled final M_n , whose value depended on the needs of each reaction. Further on a “grafting to” reaction of reductive amination is described between the deprotected diblock copolymer $\text{PEG}_{114}\text{-}b\text{-PATC}_m$ and the aldehyde group of the carbonyl hetero-telechelic poly(isoprene) by the use of sodium triacetoxyborohydride ($\text{NaBH}(\text{AcO}_3)$) as a reducing agent. This reducing agent was chosen due to its low toxicity and specificity to only reduce aldehydes and not ketone groups. Herein, we managed to produce a variety of grafted copolymers with different hydrophilic ratios f_{PEG} in order to provide the base for the magnetic polymersomes. The poly(isoprene) block was further epoxidized to some degree in order to provide the opportunity of cross-linking once the magnetic polymersomes were formed and stabilize the elongated structure.

In Chapter III the synthesis of another copolymer was discussed, more specifically a triblock copolymer $\text{PEG}_{114}\text{-}b\text{-PTMC}_m\text{-}b\text{-PI}_n$ was synthesized in two steps. First poly(ethylene) glycol ($\text{CH}_3\text{-PEG-OH}$, $M_n=5000\text{g}\cdot\text{mol}^{-1}$) was used as a macroinitiator of the ROP of the trimethylene carbonate monomer in order to produce the diblock copolymer $\text{PEG}_{114}\text{-}b\text{-PTMC}_m$ whose DP was targeted as 200 in order to produce a polymer whose hydrophilic ratio f_{PEG} was $\leq 20\%$, and would decrease even more once the addition of the second hydrophobic block poly(isoprene) would be added. The ROP polymerization was achieved in a controlled manner by the use of a DBU/TU catalytic system. By increasing the amount of catalyst in the system the polymerization reaction time was decreased from 8.5 hours to 5 hours while retaining the control of the polymerization. The addition of poly(isoprene) was a necessary component in order to add a cross-linkable moiety onto the copolymer. More specifically, the carbonyl hetero-telechelic poly(isoprene) was modified with a carboxyl moiety using succinic anhydride and the reaction achieved an 85% conversion. The final modified poly(isoprene) was attached onto the diblock copolymer via a Steglich esterification reaction using DPTS/DIC as the catalytic system. The reaction was deemed successful by confirmation via SEC, HNMR, HMBC/HSQC and DOSY NMR analysis. The reaction produced side reactions which were minimized by changing the equivalents of the carboxyl modified poly(isoprene) from 3 to 1.5 and 1.2 respectively. Furthermore, it was possible to decrease the reaction time to 2 days instead of 3.

Conclusion and Perspectives

In Chapter IV the synthesis of hydrophobically functionalized iron oxide nanoparticles was discussed. Iron oxide nanoparticles with a magnetic core diameter $d=6\text{nm}$ were synthesized via a polyol route and were functionalized with oleic acid. Another batch of IONPs was functionalized with a poly(isoprene) layer via a fast ligand exchange. The synthesis of the poly(isoprene) layer was described as well, where its aldehyde group was functionalized with dopamine in order to allow it to attach onto the IONPs surface. The dopamine modification proceeded via a reductive amination following the same synthetic route that was utilized in the graft synthesis chapter. Highly functionalized iron oxide nanoparticles were produced, and their properties were confirmed via FT-IR and TGA.

The final chapter, Chapter V, explored the self-assembly properties of the copolymers with the produced iron oxide nanoparticles. The produced morphologies were cross-linked via UV irradiation and their membrane deformation was depicted via TEM imaging. Finally, the elongation of the magnetic polymersomes was achieved via exposure under a magnetic field of 0.4T and was confirmed via TEM imaging as well. The morphology was stabilized via cross-linking with UV irradiation.

The final goal of the project was the stabilization of an elongated morphology which had resulted due to an application of a static magnetic field, which indeed was achieved for both the graft copolymer and the triblock copolymer. The triblock copolymer exhibited a stronger elongation as can be seen from the images but nonetheless both copolymer systems had a desirable result.

For further study of the elongation process SAXS and SANS experiments were performed while the polymersomes were under a magnetic field and it was possible to detect an anisotropy due to magnetization of the structures by the magnets. In particular, one of our samples, G4 with 70% IONPs-OA ($d=6\text{nm}$) presented more prominent elongation features in SANS analysis while under the magnetic field, which was observed by the scattering pattern at low q which was no longer spherical in neither perpendicular nor parallel field. These experiments should be repeated with more diluted solutions or a different experimental set-up, which would not allow for the sample to come in direct contact with the magnets. While the project indeed achieved its goal of elongation and stabilization of the morphology many more experiments can be performed to verify the anisotropic morphology.

Further on, the elongated structures which were produced should be studied for biological applications to verify if indeed they offer more benefits over the spherical structures and if they can act as magneto-mechanical actuators and react under a rotating field forcing them to rotate in a way which is capable of inducing disturbances in the cell environment and causing cell apoptosis. While in our case some studies in biological media have been conducted, they were regarding the toxicity of the spherical magnetic polymersomes and not the elongated structures.

Finally, the project could expand in the formation of already elongated structures [1], since the self-assembly of many copolymers allow for the direct formation of ellipsoid nanoparticles with a variety of

techniques [2]–[5], thus skipping the step of elongation in the magnetic field and directly studying the mechanism of magneto-mechanical destruction of said nanoparticles in biological medium.

References:

- [1] S. Matsumura *et al.*, “Stability and Utility of Pyridyl Disulfide Functionality in RAFT and Conventional Radical Polymerizations,” *J. Polym. Sci. Part A Polym. Chem.*, vol. 46, no. April, pp. 7207–7224, 2008.
- [2] T. Chidanguro and Y. C. Simon, “Bent out of shape: towards non-spherical polymersome morphologies,” *Polym. Int.*, vol. 70, no. 7, pp. 951–957, 2021.
- [3] R. M. Perera, S. Gupta, T. Li, M. Bleuel, K. Hong, and G. J. Schneider, “Influence of NaCl on shape deformation of polymersomes,” *Soft Matter*, vol. 17, no. 16, pp. 4452–4463, 2021.
- [4] C. Katterman, C. Pierce, and J. Larsen, “Combining nanoparticle shape modulation and polymersome technology in drug delivery,” *ACS Appl. Bio Mater.*, vol. 4, no. 4, pp. 2853–2862, 2021.
- [5] C. K. Wong, M. H. Stenzel, and P. Thordarson, “Non-spherical polymersomes: Formation and characterization,” *Chem. Soc. Rev.*, vol. 48, no. 15, pp. 4019–4035, 2019.

Curriculum Vitae

Nom : Kazaryan

Prénom : Diana

Laboratoire : LCPO

Téléphone Labo : -

E-mail personnel : dianakazar@gmail.com

Directeur(s) de thèse: Dr Olivier Sandre and Dr Frédéric Peruch

Date de début de la thèse :13/01/20

Type de Financement : ANR Maverick 2019

Spécialité de la thèse : Chimie des Polymères

Date de la soutenance de thèse :03/10/23

Situation après la soutenance de la thèse : recherche de post-doc ou de poste dans l'industrie

Thèse en cotutelle : Non

Production scientifiques et techniques

1) Publications dans des journaux internationaux avec comité de lecture (préciser titre, auteurs, journal et références. Pour les publications soumises, joindre au formulaire le mail de l'éditeur confirmant la soumission)

Kaklamani, G., Kazaryan, D., Bowen, J., Iacovella, F., Anastasiadis, S.H. and Deligeorgis, G., 2018. On the electrical conductivity of alginate hydrogels. *Regenerative biomaterials*, 5(5), pp.293-301.

Stavroulaki, D., Kyroglou, I., Skourtis, D., Athanasiou, V., Thimi, P., Sofianopoulou, S., Kazaryan, D., Fragouli, P.G., Labrianidou, A., Dimas, K. and Patias, G., 2023. Influence of the Topology of Poly (L-Cysteine) on the Self-Assembly, Encapsulation and Release Profile of Doxorubicin on Dual-Responsive Hybrid Polypeptides. *Pharmaceutics*, 15(3), p.790.

2) Brevets ou dépôts de brevets (préciser titre, dates, auteurs et références)

3) Chapitre d'ouvrage (préciser titre du chapitre, auteurs, titre de l'ouvrage, éditeurs et références)

“Hybrid magnetic-polymer nanoparticles as actuators on cell membranes under low frequency alternating or rotating magnetic fields”, Diana Kazaryan, Frédéric Peruch, Véronique Gigoux, Olivier Sandre, in *Magnetoresponsive soft nanosystems: Engineering and biomedical applications*, Ladislau Vekas and Sophie Laurent Eds., to appear in 2024, [RSC book series on Nanoscience & Nanotechnology](#), ISSN: 1757-7136

4) Communications à des colloques/congrès avec actes (préciser intitulé, dates, lieu, auteurs et références)

- “*Biological cell killing induced by anisotropic magnetic polymersome rotation under low frequency alternating magnetic field*”, D. Kazaryan, F. Peruch, O. Sandre, C’Nano Great South West Young Scientists Meeting, June 21st 2021, Toulouse (on-line oral)
- “*UV-induced cross-linking of magnetic polymersomes deformed under a static magnetic field to study magnetically induced cell mortality*” (on-line oral), D. Kazaryan, F. Peruch, S. Lacomme, E. Gontier, A. Abdelhamid, V. Gigoux, and O. Sandre, 13th Hellenic Polymer Society International Conference, 12-16th December, 2021, Athens, Greece
- “*Deformation of magnetic polymer vesicles (polymersomes) under magnetic field and photo-crosslinking of their membrane in their deformed state*”, D. Kazaryan, S. Lacomme, E. Gontier, L. Laib, V. Gigoux, F. Peruch, O. Sandre, ACS Spring 2023 Meeting, Division of Colloid & Surface Chemistry: Colloids Intended for Biological Applications, March 26-30th 2023, Indianapolis IN, USA et acte du colloque: [hal-04059215](https://hal.archives-ouvertes.fr/hal-04059215)

5) Présentations par voie d’affiches (préciser intitulé, date, lieu de la réunion scientifique et auteurs de l’affiche en soulignant l’auteur présentant la communication)

- “*UV-induced cross-linking of magnetic polymersomes deformed under a static magnetic field to study magnetically induced cell mortality*”, D. Kazaryan, F. Peruch, S. Lacomme, E. Gontier, A. Abdelhamid, V. Gigoux, and O. Sandre, Meeting annuel de la Société Française de Nanomédecine ([SFNano 2021](https://www.sfnano.fr/)), Session Nanochemistry, Angers, 6-8 décembre 2021
- “*Biological cell killing induced by anisotropic magnetic polymersome rotation under low frequency alternating magnetic field*”, D. Kazaryan, S. Lacomme, E. Gontier, A. Abdelhamid, L. Kehal, V. Gigoux, F. Peruch, O. Sandre, [EPF European Polymer Congress](https://www.epf-congress.com/), “Polymers for Biological and Medical Applications” Session, Prague, June 26th – July 1st 2022
- “*Deformation of magnetic polymer vesicles (polymersomes) under magnetic field and photo-crosslinking of their membrane in their deformed state*”, D. Kazaryan, S. Lacomme, E. Gontier, L. Laib, V. Gigoux, F. Peruch, O. Sandre, [SFNano 2022](https://www.sfnano.fr/) Annual Meeting, 5-7th December 2022, IRCAD, Strasbourg, France

6) Autres (article de vulgarisation (ex : actualité chimique), communications grand public...)

Bande dessinée par Naïs Coq (dessinatrice d’Angoulême) dans le cadre du projet ANR MAVERICK et de l’AAP « Sciences Avec et Pour la Société » dont le CNRS-DR15 et l’Université de Bordeaux sont lauréats. La BD sera mise en ligne à la fin du mois de juillet à l’adresse <https://www.lcpo.fr/anr-maverick>.

DIANA KAZARYAN

Chemist, MSc, PhD.

Contact information :



Bordeaux, France



dianakazar@gmail.com



www.linkedin.com/in/diana-kazaryan

Research experience:

2020-2023: Ph.D. in Polymers:

Ph.D. at the Laboratoire de Chimie des Polymères Organiques (LCPO), University of Bordeaux, France

Thesis: "Synthesis of amphiphilic linear and comb-like terpolymers with epoxidized double-bonds and their self-assembly into magnetic vesicles with shape fixing ability under UV cross-linking"

2017-2019: Master in Science:

Master in Science, Laboratory of Industrial Chemistry (Polymer Lab), Group of Prof. Hermis Iatrou, Chemistry Department, National and Kapodistrian University of Athens, Greece.

Title: "Synthesis and Characterization of multi-Responsive Graft-Polypeptides for Controlled Drug Release"

2013-2017: Bachelor:

Diploma Thesis, Group Hybrid Nanostructures of Prof. Spiros.H.Anastasiadis, Foundation of Research and Technology (FORTH), Institute of Electronic structure and Laser (IESL), Heraklion, Crete.

Education:

- **2020-2023: Ph.D. in Polymers:** Graduate Research School of the University of Bordeaux, LCPO, ENSCBP, Bordeaux, France.
- **2017-2019: Master in Science:** "Polymer Science and Its Applications", Chemistry Department, National & Kapodistrian University of Athens, Greece.
- **2013-2017: Bachelor:** Chemistry Degree, University of Crete, Department of Chemistry, Greece

Publications and conferences:

- ❖ Kaklamani, G., Kazaryan, D., Bowen, J., Iacovella, F., Anastasiadis, S.H. and Deligeorgis, G., 2018. On the electrical conductivity of alginate hydrogels. *Regenerative biomaterials*, 5(5), pp.293-301.
- ❖ Stavroulaki, D., Kyroglou, I., Skourtis, D., Athanasiou, V., Thimi, P., Sofianopoulou, S., Kazaryan, D., Fragouli, P.G., Labrianidou, A., Dimas, K. and Patias, G., 2023. Influence of the Topology of Poly (L-Cysteine) on the Self-Assembly, Encapsulation and Release Profile of Doxorubicin on Dual-Responsive Hybrid Polypeptides. *Pharmaceutics*, 15(3), p.790.
- May 2017: 19th Chemistry Postgraduates' Conference Heraklion, Crete
- September 2017: Chemical Biology Disease Conference, FORTH, Crete
- October 2018: Poster Participation in 12th Hellenic Polymer Society
- International Conference 2018, Ioannina
- June 2019: Poster Participation at the European Polymer Congress 2019, Heraklion, Crete.
- June 2021: Oral presentation at the "Rencontres Jeunes du C'Nano Grand-Sud-Ouest - C'Nano Great South West Young Scientists Meeting 2021"
- December 2021: Oral presentation at the 13th Hellenic Polymer Society International Conference
- June 2022: Poster presentation at the EPF European Polymer Congress, Prague
- December 2022: Poster presentation at SFNano 2022 Strasbourg, France
- March 2023: Oral presentations at the ACS 2023 Meeting, Indianapolis USA

General Skills:

- Ring Opening polymerization
- Organic synthesis
- Monomer synthesis
- Synthesis of Iron oxide Nanoparticles
- Polymer self-assembly
- Polymer Characterization (TEM, DLS, SLS, NMR, SEC, SANS, IR, UV-Vis, TGA)
- Completed a Transmission electron microscopy (TEM) training
- Office, Excel, Origin, MestRenova, Astra

Languages:

- Greek (Native)
- English (Proficient C2)
- Russian (Native)
- French (Elementary)
- Italian (B2)

References:

Dr.Olivier Sandre:

olivier.sandre@enscbp.fr

Dr.Frédéric Peruch:

frederic.peruch@enscbp.fr